Method development for the MALDI MS imaging of drug compounds and biomolecules in Tuberculosis research

DISSERTATION

zur Erlangung des akademischen Grades eines

Doktors der Naturwissenschaften (Dr. rer. nat.)

in der Bayreuther Graduiertenschule für Mathematik und Naturwissenschaften (BayNAT)

der Universität Bayreuth

vorgelegt von

Axel Treu

aus *Leer in Ostfriesland*

Bayreuth, 2021

Die vorliegende Arbeit wurde in der Zeit von (11/2016) bis (08/2021) in Bayreuth am Lehrstuhl für Bioanalytik und Lebensmittelanalytik unter Betreuung von Herrn Professor Dr. Andreas Römpp angefertigt.

Vollständiger Abdruck der von der Bayreuther Graduiertenschule für Mathematik und Naturwissenschaften (BayNAT) der Universität Bayreuth genehmigten Dissertation zur Erlangung des akademischen Grades eines Doktors der Naturwissenschaften (Dr. rer. nat.)

Dissertation eingereicht am: 13.08.2021

Zulassung durch das Leitungsgremium: 14.09.2021

Wissenschaftliches Kolloquium: 04.02.2022

Amtierender Direktor: Prof. Dr. Hans Keppler

Prüfungsausschuss:
Prof. Dr. Andreas Römpp (Gutachter)
Prof. Dr. Rainer Schobert (Gutachter)
Prof. Dr. Stefan Schuster (Vorsitz)
Prof. Dr. Klaus Ersfeld

Table of contents

Zusammenfassung

Matrix unterstütze Laser Desorption/Ionisation Massenspektrometrie Imaging (MALDI MSI) ist eine physikalisch-chemische Analysetechnik, welche die molekulare Spezifizität der Massenspektrometrie mit räumlicher Information verknüpft. Sie ist in der Lage, die Verteilung von Analyten auf einer Probenoberfläche wie z.B. Gewebedünnschnitten sichtbar zu machen. Da MALDI MSI keiner Radionuklidmarkierung bedarf, ist sie besonders geeignet zur Untersuchung der Verteilung von Wirkstoffen. In diesem Feld wird MALDI MSI neben diversen anderen Anwendungen in der Tuberkuloseforschung eingesetzt. Tuberkulose (TB) ist eine Infektionskrankheit des pulmonalen Systems verursacht, in den meisten Fällen, von *Mycobacterium tuberculosis* (Mtb). Im Menschen führt eine aktive TB zur Bildung von nekrotischen Granulomen in der Lunge. Für eine erfolgreiche Behandlung von TB müssen Wirkstoffe die gegen TB eingesetzt werden, sog. Antituberkulotika, in der Lage sein in die Granulome einzudringen um die Mykobakterien abzutöten. Daher korreliert die substanzspezifische Fähigkeit von Antituberkulotika in Granulome einzudringen direkt mit ihrer *in vivo* Wirksamkeit

Das Ziel dieser Dissertation war die Entwicklung eines MALDI MSI Workflows mit dem die Verteilung von Antituberkulotika bei therapeutischer Dosierung in Mauslungengewebe mit hoher räumlicher Auflösung und hoher Massengenauigkeit untersucht werden kann. Der entwickelte Workflow wurde im Folgenden dazu verwandt, das Eindringverhalten von Antituberkulotika in pulmonale Granulome von TB infizierten IL-13^{tg} Mäusen zu untersuchen. Die Entwicklung des Workflows erfolgte mit nicht infiziertem Lungengewebe von BALB/c Mäusen. Um die Delokalisierung vor allem von wasserlöslichen Analyten zu vermindern, wurde eine Methode zum Anfertigen von Kryoschnitten aus uneingebetteten, unbefüllten intakten Lungenlappen entwickelt. Eine Herangehensweise zur Matrixoptimierung für das Imaging von niedrigkonzentrierten Wirkstoffen in Gewebeschnitten wird vorgestellt. Zur Erhöhung der Detektionssensitivität für Antituberkulotika sowie der Reduzierung des Probenbedarfs wurden MALDI MSI Messungen mit alternierender selected ion monitoring (SIM) und full scan Akquisition in einer Messung durchgeführt. Die Identität von Analyten in Gewebeschnitten wurde mithilfe von Messungen mit hoher Massenauflösung und Massengenauigkeit sowie MS/MS bestätigt. Auf diese Weise konnte ein Strukturvorschlag für das bislang nicht bestätigte doppelt protonierte Molekülion von Pyrazinamid gemacht werden. Die Verteilung aller vier Erstrang-Antituberkulotika (Pyrazinamid, Isoniazid, Ethambutol und Rifampicin) und die der Zweitrang-Antituberkulotika Moxifloxacin und Clofazimin konnten erfolgreich in therapeutischen Konzentrationen in Mauslunge untersucht werden. Messungen mit einer Pixelgröße von 10 x 10 µm zeigten des Weiteren eine Anreicherung von Clofazimin in Fettablagerungen welche an die Atemwege angrenzen.

Zur direkten Identifizierung von Analyten aus Imagingdaten ist eine hohe Massengenauigkeit unerlässlich. Diese kann mithilfe von interner oder externer Massenkalibrierung, basierend auf Referenzmassenlisten, erreicht werden. Eine gute Quelle für Referenzmassen sind omnipräsente Matrixionen, deren Summenformel bekannt ist. Parallel zur Entwicklung des Imaging Workflows wurden daher elf MALDI Matrizes hinsichtlich der von ihnen generierten Ionen untersucht und Listen von Ionen erstellt, die für eine Verwendung als Referenzmasse geeignet sind. Insgesamt konnten etwa 450 individuelle Matrixionen identifiziert werden.

Der Umgang mit tuberkulösem Probenmaterial erfordert ein der biologischen Sicherheitsstufe (BSL) 3 entsprechendes Labor. Zur Verwendung in einem Labor ohne biologische Sicherheitsstufe wurden

Lungenschnitte von TB infizierten IL-13^{tg} Mäusen mittels Gammabestrahlung inaktiviert. Nach der Verifizierung, dass die Bestrahlung keinen Einfluss auf die Verteilung von Analyten hat, wurde der MALDI MSI Workflow auf diese Schnitte angewendet. Neben der Detektion und Identifizierung von Lipiden, die charakteristisch für das Granulom und das umliegende Gewebe sind, zeigten die Imagingmessungen, dass das Antituberkulotikum Pyrazinamid in der Lage ist in Granulome einzudringen, Clofazimin und Rifampicin aber nicht. Mithilfe eines neu entwickelten Datenanalysetools konnten „Penetration Plots“ erstellt werden. Diese zeigten eine Akkumulation von Clofazimin in den zellulären Bereichen von TB Granulomen welches mithilfe von Imaging mit einer Pixelgröße von 5 x 5 µm verifiziert werden konnte. Die beobachteten Verteilungen von Pyrazinamid und Clofazimin stimmen mit Daten aus klinischen Studien überein. Dies zeigt, dass das IL-13^{tg} Mausmodell für präklinische Tests von Antituberkulotika geeignet ist. Neben dem Eindringverhalten von Pyrazinamid, Clofazimin und Rifampicin wurde auch das sich momentan in der klinischen Phase 1 und 2 befindliche Antituberkulotikum BTZ-043 mit dem entwickelten Workflow in TB infizierter IL-13^{tg} Lunge untersucht. Messungen an mehreren Zeitpunkten nach Verabreichung zeigten, dass nach anfänglicher Anreicherung in den zellulären Bereichen der Granulome BTZ-043 vier Stunden nach Verabreichung im Inneren der Granulome detektierbar ist. Im weiteren Verlauf verblieb BTZ-043 in den Granulomen länger als im umliegenden Gewebe. In Korrelation mit pharmakokinetischen und histologischen Daten wurde somit eine mögliche Erklärung für die hohe Wirksamkeit von BTZ-043 gefunden.

Diese Arbeit liefert eine umfassende analytische Methode mit der die Verteilung und damit eine der Voraussetzungen für die Wirksamkeit von Antituberkulotika in einem human-ähnlichen Tiermodell mit bisher nicht erreichter räumlicher Auflösung und Spezifizität untersucht werden kann. Die Entwicklung der Methode erfolgte in Kooperation mit dem Forschungszentrum Borstel im Rahmen eines Projekts des Deutschen Zentrums für Infektionsforschung (DZIF). Nach Integrierung der Methode in die Entwicklungspipeline für neue Antituberkulotika des DZIF kann sie die zukünftige Entwicklung von neuen Antituberkulotika beschleunigen und somit ein Beitrag zur Bekämpfung der TB Pandemie leisten. Darüber hinaus hat die entwickelte analytische Technik ein potentiell sehr breites Anwendungsspektrum und ist nicht auf den Einsatz in der Tuberkuloseforschung limitiert.

Abstract

Matrix assisted Laser Desorption/Ionization mass spectrometry imaging (MALDI MSI) is a physico-chemical analytical technique which combines the molecular specificity of mass spectrometry with spatial information. It does not require radioactive labelling and can visualize the distribution of analytes on sample surfaces such as thin tissue sections making it ideally suited for investigating the distribution of pharmacological compounds in tissue. Among various other applications in this field, MALDI MSI is currently employed in Tuberculosis (TB) research. TB is an infectious disease of primarily the pulmonary system with *Mycobacterium tuberculosis* (Mtb) as its main causative agent. In humans, TB leads to the formation of necrotic granuloma in the lung. Antimicrobial agents used against TB must be able to penetrate into the granuloma to locally eliminate the mycobacteria. As such, the *in vivo* efficacy of anti-Tuberculosis drugs correlates directly with their penetration behavior, which is compound-specific. The goal of this thesis was the development of a complete MALDI MSI workflow capable of imaging the distribution of current and novel anti-TB drugs at therapeutic concentration in murine lung tissue with both high spatial resolution and mass accuracy and use it to investigate the penetration of drug compounds into granuloma of TB infected IL-13^{tg} mice. The workflow was established on uninfected BALB/c mouse lung tissue. A cryosectioning methodology that minimizes the delocalization of water-soluble drug compounds was established for unembedded, uninflated murine lung lobes. A matrix optimization technique for the detection of low concentrated drugs is described. To increase detection sensitivity for drug compounds and to reduce the consumption of scarce sample material, MALDI MSI measurements were conducted with alternating selected ion monitoring (SIM) and full scan acquisition windows in one measurement. The identity of drug compounds was confirmed via accurate mass measurements and on-tissue MS/MS. This also led to a structural proposal for the previously unconfirmed double protonated molecular ion of pyrazinamide. All four first line anti-TB drugs (pyrazinamide, isoniazid, ethambutol and rifampicin) and the second line antibiotics moxifloxacin and clofazimine could be imaged at therapeutic concentrations in murine lung sections. High spatial resolution measurements with 10 x 10 µm pixel size showed an accumulation of clofazimine in lipid deposits around major airways.

Identification of drug compounds directly from imaging data requires high mass accuracy, which can be achieved with internal or external mass calibration using well-known *m/z* values. These reference masses can be supplied by ubiquitous matrix ions, if their sum formula is known. In parallel with the development of the imaging workflow, an investigation was conducted on eleven MALDI matrices to identify the ions generated by these matrices on tissue and determine if these ions are suitable for use in mass calibration. Identified matrix ions were compiled into tables for each matrix. In total, around 450 ions could be identified.

TB infected sample material must be handled in a biosafety level (BSL) 3 facility. For use outside of BSL 3 conditions, sections of TB infected IL-13^{tg} lung were inactivated via γ irradiation. After verification that the irradiation has no effect on the drug distribution, the workflow was applied on TB infected IL-13^{tg} lung tissue. Characteristic lipid species for the granuloma and surrounding tissue areas could be identified. Pyrazinamide was found able to penetrate into granuloma whereas clofazimine and rifampicin were not. Drug penetration plots generated by a newly developed data analysis tool showed an accumulation of clofazimine in the cellular regions of TB granuloma. This could be confirmed in 5 x 5 µm pixel size measurements. These findings were in accordance with results from clinical trials thus validating the IL-13^{tg} model as suitable for pre-clinical drug trials. In addition to these findings the

novel anti-TB drug BTZ-043, which is currently in clinical Phase 1 and 2 trials, was investigated in TB infected IL-13^{tg} lung regarding its ability to penetrate into TB granuloma. MALDI MSI measurements conducted at different time points post dose showed that after initial accumulation in the cellular regions of the granuloma BTZ-043 is able to penetrate into TB granuloma 4 h after administration and to persist there for longer than in the surrounding areas. In correlation with pharmacokinetic and histological data, these results delivered a possible explanation of the high efficacy of BTZ-043.

This thesis delivers a powerful analytical method with which the distribution of anti-TB drugs can be investigated and evaluated in a human like animal model with unprecedented spatial resolution and specificity. The method was developed in cooperation with the Research Center Borstel as part of a joint project from the German Center for Infection Research (DZIF). Following integration into the established drug screening and development procedures of the DZIF, the developed method can accelerate the development of novel anti-TB drugs and contribute to fight the TB pandemic. Furthermore, the method has a broad range of possible applications and is not limited to Tuberculosis research.

Abbreviation index

AUC	area under the curve
BSL	biological safety level
BTZ-043	benzothiazinone-043
CFU	colony forming units
CFZ	clofazimine
CHCA	*alpha*-cyano-4-hydroxycinnamic acid
CMC	carboxymethyl cellulose
DCTB	2[(2E)-3-(4-tert-butylphenyl)-2-methylprop-2-enylidene]malononitrile
DESI	desorption electrospray ionization
DHAP	2,6-dihydroxyacetophenone
DHB	2,5-dihydroxybenzioc acid
EMB	ethambutol
ESI	electrospray ionization
FT	Fourier transform
FT-ICR	Fourier transform ion cyclotron resonance
FWHM	full width at half maximum
HE	haematoxylin and eosin stain
HR-MS	high resolution mass spectrometry
IL-13^{tg}	interleukin 13 overexpressing transgenic
INH	isoniazid
LC-MS	liquid chromatography mass spectrometry coupling
LDI	laser desorption/ionization
LPC	lysophosphatidylcholine
m/z	mass to charge ratio
MALDI	matrix-assisted laser desorption/ionization
MALDI MSI	matrix-assisted laser desorption/ionization mass spectrometry imaging
MIC	minimum inhibition concentration
MS	mass spectrometry
MSI	mass spectrometry imaging
Mtb	*Mycobacterium tuberculosis*
MXF	moxifloxacin
Orbitrap	orbital trapping mass analyzer or an instrument equipped with this analyzer
PC	phosphatidylcholine
PI	phosphatidylinositol
PK	pharmacokinetic
pNA	4-nitroaniline
ppm	parts per million
PS	phosphatidylserine
PZA	pyrazinamide
R	mass resolution when used in regard to a mass spectrum; resolving power when used as an instrumental parameter
RIF	rifampicin
RMSE	root mean square error

SIM	selected ion monitoring
SIMS	secondary ion mass spectrometry
TB	Tuberculosis
UV	ultraviolet
WHO	World Health Organization
ZN	Ziehl-Neelsen stain

1 Motivation

Mass spectrometry imaging (MSI) is a physico-chemical analytical method that combines the molecular specificity of mass spectrometry with spatial information, and is capable of visualizing the distribution of analyte molecules on a surface.[1] Among the available MSI techniques, only matrix assisted laser desorption/ionization mass spectrometry imaging (MALDI MSI) features a soft ionization capable of producing intact pseudo molecular ions of organic molecules and the potential for high spatial resolution.[2] MALDI MSI is superior to classic molecular imaging techniques such as autoradiography as it detects analyte ions based on their mass to charge ratios (*m/z*) and does not require a radioactive labelling of targeted compounds. This makes MALDI MSI ideally suited for imaging the distribution of drug compounds in small anatomical structures in thin tissue sections. Apart from numerous successful applications in drug imaging[3, 4], MALDI MSI is currently being employed in Tuberculosis (TB) research.

Tuberculosis is an infectious disease of the pulmonary system with *Mycobacterium tuberculosis* (Mtb) as its main causative agent. WHO estimates suggest, that one in three humans carries a latent TB infection. In 2020, TB was the leading cause of death (above HIV/AIDS) from a single infectious agent with over 10 million new active TB cases and 1.2 million recorded deaths among HIV negative people.[5] This is despite the fact, that TB can be cured, whereas HIV/AIDS cannot. TB treatment relies on long term combination chemotherapy with specialized antibiotics[6, 7] which can last for more than a year. The long duration of treatment which suffers from compliance issues in combination with the specific pathology of TB fosters the development of antibiotic resistant Mtb strains, which ultimately creates a demand for novel anti-TB drugs.

In humans, an active TB infection leads to the formation of centrally necrotic granuloma in the lung. A granuloma is an inflammatory hot spot, walled off by the immune system, containing a large number of extracellular Mtb. To successfully treat and eventually cure TB, an anti-TB drug must be able to penetrate into these granuloma to eliminate the mycobacteria.

As the penetration behavior of anti-TB drugs is highly compound specific, a major hurdle in the development of novel anti-TB drugs is to determine their ability to penetrate into TB granuloma.

MALDI MSI is among the only techniques with the potential to visualize the penetration of anti-TB drugs thus enabling an evaluation of a drugs *in vivo* effectiveness.[8] However, current pre-clinical inbred animal models such as BALB/c mice, the most commonly used animal model in pre-clinical drug testing[9, 10], fail to replicate human TB pathology. This means that predictions derived from MALDI MSI studies using these animal models are of limited credibility.

The goal of this work was the development of a MALD imaging workflow capable of visualizing the distribution of various anti-TB drugs in lung tissue of a special mouse model[11] that mimics human TB pathology at therapeutic concentrations with high spatial resolution, mass resolution and mass accuracy. As part of a joint project of the German Center for Infection Research (DZIF), the developed workflow was then to be used as a platform inside the regular drug development piepeline of the DZIF to investigate and evaluate the penetration behavior of current and novel anti-TB drugs into TB granuloma to accelerate the screening and development process of novel anti-TB drugs.

2 Introduction

2.1 Mass spectrometry

Mass spectrometry (MS) is a versatile physico-chemical analytical technique. It is based on the separation of purposefully generated gaseous ions in high vacuum conditions based on their mass to charge ratio (*m/z*). In simple terms, a mass spectrometer can be described as a scale for atoms and molecules which is several million times more precise than any commercial kitchen scale. MS can (potentially) differentiate the molecular composition of any ionizable sample or sample mixture and even enable the structural elucidation of previously unknown compounds. The first mass spectrometers were devised by Joseph John Thompson at the onset of the 20th century.[12] Among other applications, these early instruments were used to show that stable Neon contains two different weight atoms (^{20}Ne and ^{22}Ne), which was the first proof of isotopy in stable elements.[13] Today, over 100 years later, mass spectrometry has matured from an experimental curiosity into a rugged, highly sensitive and precise tool for chemical analysis. The field of mass spectrometry has a large user base and is present in almost all fields of modern science, industry and law enforcement.

2.2 The mass spectrometer

All mass spectrometers operate under vacuum conditions. This is necessary to enable a sufficient mean free path of ions from the ion source towards the analyzer and detector without collisions with residual gas molecules. According to the kinetic theory of gases, the mean free path of ions is given as

$$L = \frac{kT}{\sqrt{2}p\sigma} \tag{2.1}$$

where *k* is the Boltzmann constant, *T* the temperature, p the pressure and *σ* the collision cross section of the ion.

According to equation 2.1, a longer flight path of the ions inside the mass spectrometer necessitates a higher-grade vacuum, i.e. a lower pressure. The flight distance of ions varies depending on the operating principle of the mass analyzer from meters in reflectron time of flight and sector analyzers to several kilometers in orbital trapping or FT-ICR analyzers.

Independent of mass spectrometer type and ionization methods, a classic mass spectrometer theoretically consist of five parts: Sample inlet, ion source, mass analyzer, detector and data system, Fig. 1 A. The main working components of the mass spectrometer are connected by ion optics. Ion optics is a general term for a series of different components whose main function is to maintain or guide a stream of ions, i.e. an ion beam, via electric or magnetic fields. Ion optical components used in many mass spectrometers include quadrupoles, hexapoles, octupoles or apertures.[14] Modern mass spectrometers normally feature an ambient ionization source which negates the need for a dedicated sample inlet system. Some of these instruments, such as the orbital trapping mass spectrometer used in this dissertation combine mass analyzer and detector in one working piece, Figure 1 B.

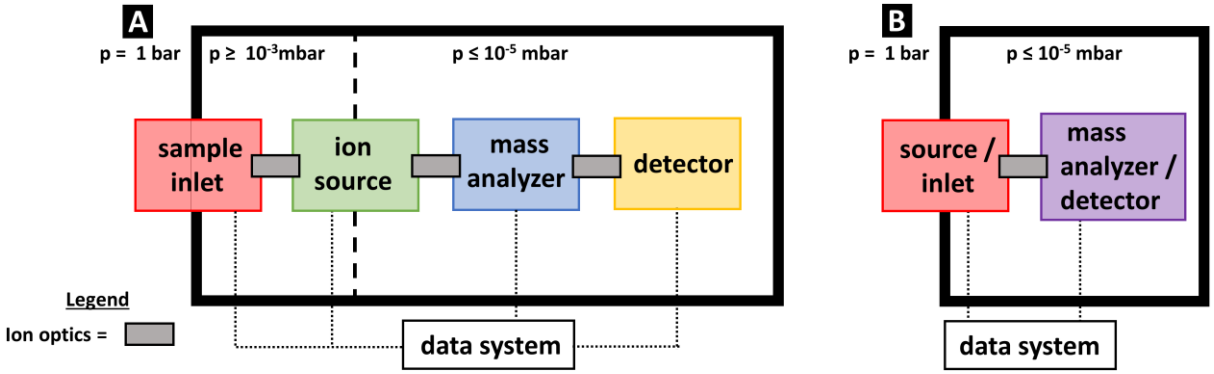

Figure 1. Schematic overview of the main working components of a mass spectrometer. **A)** Classic layout featuring a dedicated sample inlet and vacuum lock combined with separate working pieces for the mass analyzer and detector comparable to a time of flight mass spectrometer or magnetic sector instrument. **B)** Mass spectrometer with an atmospheric pressure ion source and combined mass analyzer/detector working piece comparable to an orbital trapping or FT-ICR instrument coupled to an electrospray ion source.

The purpose of a sample inlet is the transfer of sample material from ambient conditions into the vacuum of the mass spectrometer without breaking the vacuum inside the machine.

The ion source, an essential part in every mass spectrometer, produces desolvatized gaseous ions from condensed sample material. It is important to note, that in any given ion source, only a fraction of the available sample molecules are ionized and transferred into the mass analyzer. Usually, ionization techniques are described as hard or soft ionization. Hard ionization techniques, such as the classic electron impact ionization generates molecular ions with an uneven number of electrons ($M^{+\cdot}$, $M^{-\cdot}$), so called odd electron ions, and impart them with high quantities of internal energy (10 - 20 eV).[15] These ions, as a result of their energetic state, are unstable and tend to fragment according to well-studied fragmentation mechanisms.[16] The larger the analyte molecule, the more unlikely it is to generate an intact molecular ion with hard ionization methods. The defining characteristic of soft ionization techniques is the ability to produce intact molecular ions of high mass molecules with little or no fragmentation. Soft ionization techniques generate ions by protonation or the addition of other cations (Na^+, K^+) to the neutral analyte molecule. In the negative ion mode, ions are usually formed via deprotonation. A large number of soft ionization techniques are available.[17] The most commonly used soft ionization techniques are the electrospray ionization (ESI) and the matrix-assisted laser desorption/ionization (MALDI), the latter will be described on more detail in Section 2.4.The mass analyzer, which separates ions according to their *m/z* ratio, is the central working piece of the mass spectrometer. There are a number of different mass analyzer types[18] utilizing different physical principles for ion separation. For example, the time of flight analyzer, one of the most simple analyzer designs, separates ions based on the flight time of ions with different that are *m/z* accelerated with the same amount of energy. The orbital trapping mass spectrometer used in this work is discussed in more detail in Section 2.3**.** Ionic currents produced by the ions in the mass analyzer are very low (nA to µA range)[19]. The purpose of the detector is to amplify the ionic currents generated by the analyte ions and to convert the analogue signal into digital form for data processing. Detectors used for signal amplification can be distinguished as discreet and continuous dynodes. A discreet dynode detector is the secondary ion multiplier. Continuous dynode type detectors include the channeltron, microchannel plate and faraday cup.[20] Despite the different makeup, these detectors use the same operating principle. Analyte ions accelerated out of the mass analyzer impact on a defined voltage carrying area of the detector. The impact triggers an electron cascade with a measurable current. Some

types of mass spectrometers, i.e. the FT-ICR and orbital trapping mass spectrometers, feature a combined mass analyzer / detector setup. In these mass spectrometers, the repeated movement of ions in a strong magnetic (FT-ICR) or electric field (Orbitrap) is used to generate an image current inside electrodes, which is used for *m/*z determination as well as detection. The fifth component of modern mass spectrometers is the data system. It is connected to all other components to control and monitor the functions of the mass spectrometer. Furthermore it is used for the processing and analysis of mass spectral data.

2.3 The orbital trapping mass analyzer/detector

The orbital trapping or simply Orbitrap mass analyzer is the latest mass analyzer / detector to be introduced that gained widespread adoption in the field of mass spectrometry. In this work it is used for the majority of all MS work. The Orbitrap uses image current detection and FT for ion detection and signal processing and can achieve high mass resolution without the need for strong magnetic fields and superconducting magnets at comparatively low cost. This means orbital trapping mass spectrometers are cheaper, require less space, maintenance and upkeep while delivering comparable or superior performance than other mass spectrometers capable of achieving high mass resolution, i.e. FT-ICR and certain time of flight instruments.

In 1923, Kingdon suggested the use of electrostatic fields to trap ions in a low-pressure tube between the inner wall of the tube and a central electrode, a tungsten wire.[21] The modern day orbital trapping mass analyzer uses a similar operating principle[22] as reported by Kingdon and was mainly developed by Alexander Makarov and coworkers during the 1990s and early 2000s.[23] The first commercially available orbital trapping mass spectrometers were introduced in 2005.[24] A standard high field Orbitrap, as used in this thesis and depicted in Figure 2 (left panel) has roughly the size and shape of a walnut and consist of three parts; an inner spindle electrode surrounded by two cup shaped outer electrodes that face each other divided by a very thin isolator.

As the Orbitrap is conceptually an ion trap, it requires a pulsed ion injection. In Orbitrap instruments, a specialized ion trap the so called ‘c-trap’, is used for ion accumulation and pulsed injection of ion packages into the Orbitrap.[25] After ion injection, a voltage is applied between the inner and outer electrodes of the Orbitrap generating a radial electric field. This electric field bends the trajectory of injected ions towards the central electrode. This is counteracted by the tangential movement of ions around the central electrode, which creates an opposing centrifugal force and keeps the ion packages in a stable spiraling movement around the inner electrode (Figure 2 right panel), analogous to a celestial body orbiting its star. Hence the name Orbitrap. Due to the conical shape of the outer electrodes, an axial electric field pushes the ion spirals along the z-axis, i.e. the inner electrode, towards the widest part of the Orbitrap. The resulting oscillation of ion spirals between the narrowest (outside) and widest part (middle) of the Orbitrap along the *z*-axis (central electrode) is detected via the generation of an image current in a set of outer electrodes.

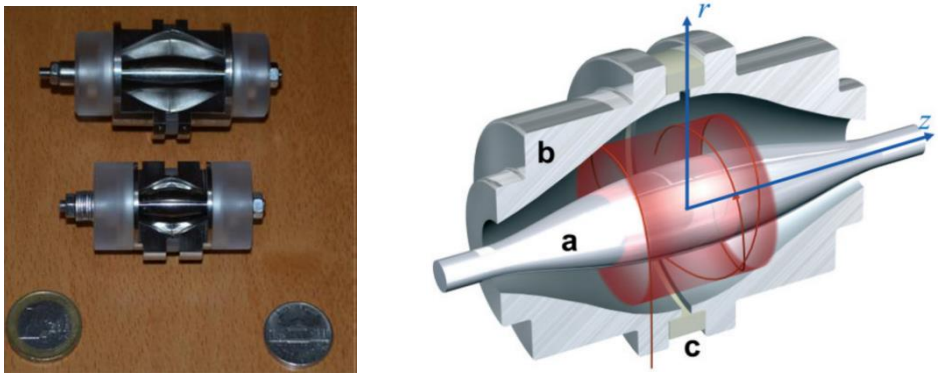

Figure 2. Left panel) Cutaways of a regular (top) and high field (bottom) orbital trapping mass analyzer. Shown for scale a one euro coin and a US quarter.[24] **Right panel)** Schematic representation of an orbital trapping mass analyzer showing the movement of ion packages during signal acquisition.[26]

The frequency of this oscillation ω is only related to the charge *z* and the mass *m* of the oscillating ions according to

$$\omega = \sqrt{k\frac{z}{m}} \tag{2.2}$$

with *k* as a set instrumental constant. For ion detection, the *ω* of oscillating ion packages is recorded for a certain amount of time by the outer electrodes simultaneously for all ion packages present in the Orbitrap. The resulting ion transient is very convoluted as it contains the *ω* values and the corresponding intensities of all ion species present in the Orbitrap. The transient is converted into a frequency spectrum via FT which is then converted into a regular deconvoluted mass spectrum via a two-point calibration.[27] The mass resolving power R of the Orbitrap scales inversely proportional to the square root of the mass to charge ratio. For comparison, the mass resolving power of FT-ICR instruments, the only other commercially available high resolution capable mass spectrometer using FT, is inversely proportional to the mass to charge ratio. This means that if plotted against the mass of the ions, the mass resolution curve of the FT-ICR declines steeper towards higher masses than that of the Orbitrap. Accordingly, the mass resolving power of an Orbitrap is superior past a certain *m/z* threshold at higher masses while FT-ICR instruments provide higher resolution at lower mass ranges.

2.4 Matrix-assisted laser desorption/ionization

Matrix assisted laser desorption/ionization 'MALDI' is a soft ionization method and is the ionization technique used for all imaging work done as part of this dissertation The basic principle of MALDI is the irradiation of sample material with focused laser light. The irradiation transfers energy into the sample, which causes the ablation and instant evaporation of material in the laser focus. Through a series of reaction chains taking place in the ejection plume, i.e. the MALDI plume located above the sample, some sample molecules are eventually ionized and extracted. Laser irradiation as a means of ionization was used as early as the 1960s[28] in a process now referred to as laser desorption/ionization (LDI). LDI is classified as hard ionization technique as the unmitigated exposure of sample molecules to focused laser light leads to fragmentation. Furthermore, an efficient energy transfer onto sample molecules without a chromophore, which is able to absorb light of the same wavelength as the laser,

is difficult.[29] As a result, LDI works very well for chromophore containing compounds such as anthocyanins[30], but struggles to ionize other compounds.

As an advancement of LDI, MALDI uses an excess of highly light absorbing compounds to shield sample molecules from direct laser exposure and to facilitate energy transfer onto sample molecules without a chromophore to assist the ionization process. These light absorbing compounds are called matrices. MALDI is mostly performed with UV lasers. Ionization in MALDI does not occur below a laser irradiance of 10^6 Wcm^{-2}.[31] Above this threshold, ion abundances rapidly rise until they a reach a plateau at which an increase of laser irradiance does not result in higher ion yields.[32] The position of this plateau depends greatly on the matrix and the sample to matrix ratio. Matrices used for UV MALDI are crystalline organic solids with a chromophore able to absorb UV light. Many common UV MALDI matrices contain a delocalized π-electron system, usually in form of a central aromatic structure as a chromophore, and are often derivatives of small aromatic acids such as nicotinic or phenolic acid. Side chains and substituents connected to the central aromatic structure such as $–CO_2H$ or $–NH_2$ exert –M or +M effects which influence the chemical properties of the matrix and define its usability range. In regular MALDI, the analyte is mixed with a vast excess (10.000 : 1) of matrix in a suitable solvent. Dried droplets of this mixture are applied on a target plate, which is transferred into the ion source for measurement. In the dried droplets, the analyte molecules are incorporated 'co-crystallized' into the crystal lattice of the matrix. In the laser focus, matrix and co-crystallized sample molecules are immediately evaporated following the laser shot. The ejected material forms an inverted-drop shaped ejection cloud over the sample, the so-called MALDI plume. From the MALDI plume, positive and negative ions in both even- and odd-electron configuration are released at the same time, regardless of the polarity setting of the mass spectrometer. In comparison to other soft ionization techniques, MALDI generates predominantly singly charged ions. Molecular ions generated in positive mode are usually protonated or adducts with alkali metal cations. In negative mode, molecular ions are mainly deprotonated. While the exact ionization mechanism of MALDI is not fully understood yet, several plausible theories explaining this behavior have been published. Among the most commonly cited is the 'lucky survivor' model.[33] It postulates that analyte ions (cations and anions) and their respective counterions are pre-formed in the matrix and merely released into the gas phase by the laser. Inside the plasma of the MALDI plume which has a net charge of zero, cations and anions are present as separated isolated ions. Depending on the polarity of the acceleration potential, either cations or anions are extracted from the plume by the mass spectrometer. Most of the isolated ions however, lose their charge through re-neutralization via recombination with counterions or collisions with neutral particles. The ions that retain their charge and are transferred into the mass spectrometer are referred to as the lucky survivors. The chance of re-neutralization is greater for multiple charged ions, which explains their lack in MALDI MS spectra. However, the lucky survivor model completely disregards the possibility of direct photoionization[34], especially for UV light absorbing analytes, and thermal ionization[35] trough sample heating by the laser. Another popular model, the coupled chemical and physical dynamics model or 'pooling' model suggests that ionization in MALDI takes place through energy pooling reactions between electronically exited species within the ion plume.[36, 37] In summary, it should be noted that there is no singular pathway of ion formation and that ionization in MALDI is a combination of numerous processes leading to the observed ion configurations.

2.5 Mass spectrometry imaging

Mass spectrometry imaging (MSI) is the main analytical technique used in this work. MSI combines the molecular specificity of mass spectrometry with imaging capabilities.[1, 38] In comparison to classic molecular imaging techniques such as autoradiography, MSI does not require radioactive labelling as analytes are detected based on their mass to charge ratio rather than radioactive decay emissions. This allows MSI to detect and distinguish multiple analytes simultaneously. In MSI, the spatial information required to reconstruct the distribution of an analyte can be obtained using two approaches which are called microscope and microprobe mode.

2.5.1 Microscope mode

Microscope mode utilizes a position sensitive detector, e.g. a microchannel plate, to obtain spatial information.[39] The ions generated on the surface of the sample by the ionization beam are directed onto the position sensitive detector via microscopic ion optics. The spatial resolution in microscope mode is therefore dependent of both the quality of the employed ion optics as well as the resolution of the detector. Furthermore, microscope does not require the sample to be moved during analysis. Similar to regular optical microscopes which have a limited depth of vison, the ion optics used for microscope mode also have a limited depth of vision.[40] As a consequence, microscope mode MSI requires very even sample surfaces.

2.5.2 Microprobe mode

In comparison to microscope mode, the microprobe mode is conceptually more simple and by far the most commonly used approach for MSI. In this mode, which can be described as position correlated mass spectrometry[1], a mass spectrum is recorded at one position of the sample surface after which the sample is moved to the next position with defined spacing in x and y direction (step size) to create an array of mass spectra.[41] The spatial resolution in microprobe mode is therefore directly dependent on diameter of the ionization beam as well as the accuracy with which the sample can be moved in either direction. The spatial distribution of an analyte within the field of view can be visualized by plotting the intensity of said analyte in every measured spectrum against the respective x y coordinates. The resulting intensity heat map is commonly referred to as an ‘ion image’. In the ion image, each pixel represents the intensity of a selected ion in the mass spectrum recorded at that particular coordinates. The color of the pixel represents the intensity of the chosen analyte in that particular mass spectrum. Using appropriate software[42, 43], the ion images of different analytes can be overlayed in a composite image (RGB overlay) which allows the comparison of different analyte distributions in one image.

2.5.3 Ionization techniques

While an MSI ion source can be coupled to a number of different mass analyzers, the three main ionization techniques used in MSI are secondary ion mass spectrometry (SIMS), desorption electrospray ionization (DESI) and MALDI. A schematic overview of these 3 techniques is given in Figure 3.

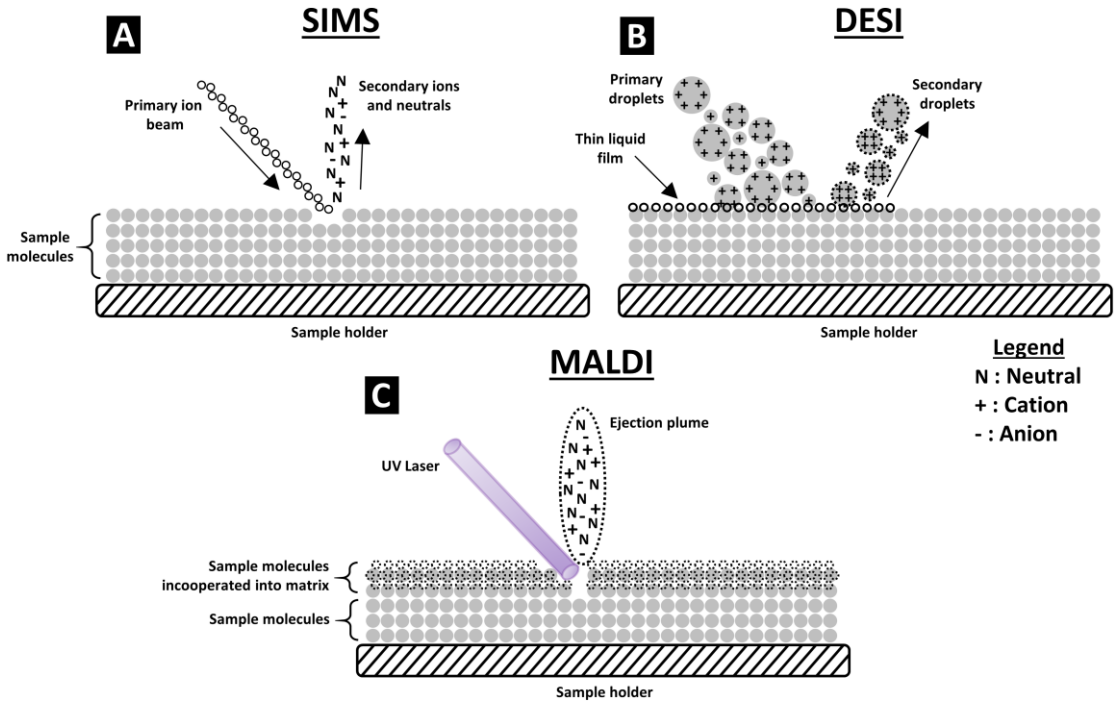

Figure 3. Comparison of the ionization mechanics of A) SIMS, B) DESI and C) MALDI.

SIMS

Secondary ion mass spectrometry or SIMS uses a discrete beam of primary ions to generate secondary analyte ions from a sample surface. The impact of the primary ions on the sample surface causes the ejection (sputtering) of sample material from the surface and the release of both positive and negative secondary ions at the same time.[44] It must be noted that the majority of the sputtered sample material consist of neutrals, which are lost to the analysis.[45] The primary ion beam used in SIMS is generated by an ion gun and can consist of single atom ions such as Cs^+, Bi^+, Ar^+, polyatomic ions (SF_5^+, C_{60}^+) or cluster ions (Bi_n^+, $(H_2O)_n^+$).[46] Inside the ion gun, the primary ions are generated from the neutral base substance via thermal or field ionization and then focused onto the sample by ion optics. SIMS offers the possibility for depth profiling and 3D analysis by sputtering a thin layer of material from the sample surface via the ion gun itself or by an additional sputter gun and then analyze and sputter the next layer and so on.[47, 48] In contrast to DESI or MALDI, which can operate under ambient conditions, SIMS ion sources operate under vacuum conditions only, meaning samples must be introduced into the ion source via a dedicated inlet system and must not contain volatile materials. The primary ions transfer a large amount of energy onto sample molecules (keV range), making SIMS a hard ionization method and thus unable to produce intact molecular ions of high mass biomolecules.[49] SIMS is however well suited for the analysis of inorganic samples. In this capacity, SIMS was the first ionization technique used for imaging and predates other imaging techniques by several decades.[50] Further non-biological applications for SIMS include for example the investigation of semiconductor plates.[51] SIMS imaging of biological samples such as thin tissue sections requires the use of polyatomic primary ions, which offer a somewhat softer ionization.[52] Inherent to the working principle of SIMS is the small diameter of the ionization beam, i.e. the primary ion beam. As a result, SIMS offers the highest possible spatial resolution of all available MS imaging techniques (<100 nm).[53]

DESI

Similar to SIMS, DESI is based on the generation of secondary ions by projecting a stream of ions onto a sample surface. In DESI, this is achieved via an electrospray ionization (ESI) sprayer pointed onto the sample surface. Regular DESI sources operate under atmospheric pressure conditions and require little to no additional sample preparation. The ESI spray cone directed at the sample consist of highly charged solvent droplets, 'primary droplets'. These droplets consist mainly of neutral solvent molecules, e.g. MeOH, ACN or H_2O, intermixed with ionized solvent molecules and solvent clusters. The stream of primary droplets coats the sample surface with a thin liquid layer which extracts analytes from the sample. Further primary ions impacting the liquid layer in conjunction with pneumatic assistance from the spray gas cause the ejection of secondary droplets from the liquid layer which are accelerated towards the inlet of the mass spectrometer placed opposite of the ESI sprayer and angled to the sample surface.[54] From the secondary droplets, analyte ions are desolvatized and released into the gaseous phase according to the well-known ESI mechanics.[55] For imaging, a sample stage is moved continuously during the DESI process with a defined speed in x and y direction. DESI transfers only a small amount of energy onto sample molecules and is classified as a soft ionization technique. In comparison to SIMS, DESI is therefore capable of producing intact ions of organic molecules such as drugs[56], lipids[57] and peptides[58] similar to MALDI. However, while MALDI is more suited to unpolar analyte molecules, DESI is well suited for the analysis of water-soluble, polar analytes. Inherent to the design of DESI is a wide diameter of the ionization beam, i.e. the ESI spray, which means DESI is not capable of achieving SIMS or MALDI level spatial resolution. Achievable spatial resolution in regular DESI MS imaging is around 40 µm.[59]

MALDI

In the repertoire of available MSI techniques, MALDI MSI is by far the most commonly used.[38] In MALDI MSI, a thin layer of matrix is deposited onto the sample surface. The matrix substances used in MALDI MSI are similar to those used in regular MALDI. Commonly used matrices in MALDI MSI are for example 2,5-dihydroxybenzoic acid or *alpha*-cyano-4-hydroxycinnamic acid. During the MALDI MSI measurement, the matrix covered sample surface is irradiated by a laser with defined spacing in x and y direction to create a raster of laser spots. A mass spectrum is recorded at every spot in the raster to create an array of mass spectra which contain molecular and spatial information, Figure 4.[2] Note that the ionization process of MALDI MSI is the same as in regular MALDI, which is described in Section 2.4. MALDI MSI requires a more elaborate sample preparation than DESI and SIMS, see Section 2.6. In terms of spatial resolution, MALDI MSI is superior to DESI due to the smaller diameter of the ionization beam, i.e. the laser beam. Current commercially available MALDI MSI instruments are capable of a achieving a spatial resolution < 1.5 µm[60, 61], which is still several times below the resolution achievable with SIMS imaging. However, as a soft ionization technique, MALDI MSI can produce ions of intact large biomolecules, which presents a significant advantage over SIMS. Thus, MALDI MSI delivers a good compromise between achievable spatial resolution and soft ionization making it ideally suited for imaging the distribution of organic molecules in small anatomical structures. One of the main application fields of MALDI MSI, apart from imaging lipids[62], proteins[63]or peptides[64] is drug imaging. Among various other applications in this field[3, 4], MALDI MSI is used for imaging of drug compounds in cancer[65], HIV/AIDS[66] or Malaria research[67]. The ability of MALDI MSI to image intact organic molecules with high spatial resolution was also employed in several studies. In 2011, Römpp et al. have reported imaging of imatinib with a pixel size of 10 µm in murine kidney tissue.[68] More recently published works have shown MALDI MSI with 5 µm pixel size of ezogabine and cabotegravir in rat retina[69] and muscle

tissue[70]. Bäckström et al. have investigated the differing distributions of inhaled intravenously administered salmeterol in rat lung tissue with 10 µm pixel size, which is so far the highest reported spatial resolution for MALDI MSI of drug compounds in lung tissue.[71]

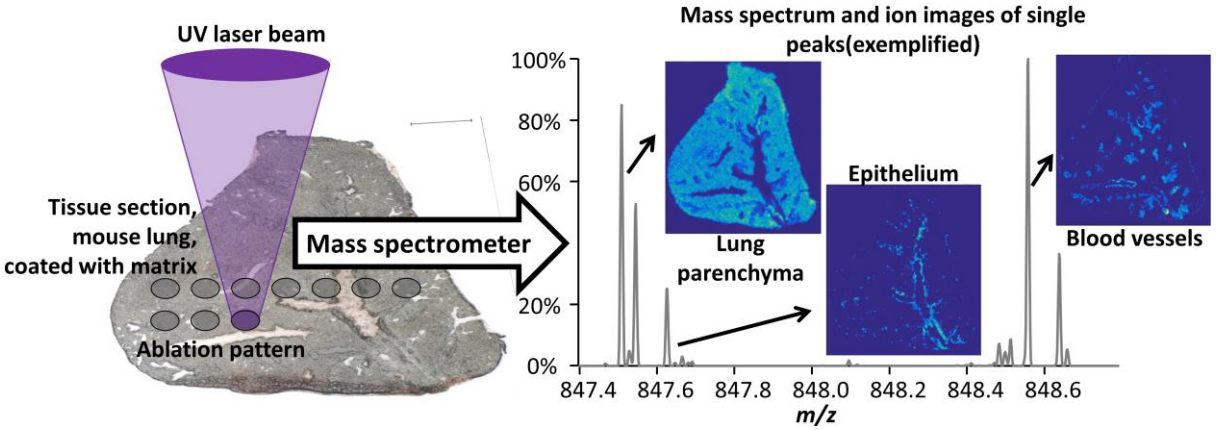

Figure 4. Schematic showing MALDI MSI in microprobe mode of a murine lung section.

2.5.4 imzML: A common data format

MSI experiments produce very large datasets containing thousands of mass spectra which usually all share the same experimental parameters. Every major vendor uses its own proprietary data format which severely limits the possibility for cross site data sharing and the range of available software tools for data analysis. Furthermore, these existing data formats are not sufficient to describe imaging data and can lack, for example, a means to record imaging parameters such as the number of pixels per line, number of lines or the step size. The imzML format[72, 73] was developed to overcome the shortcomings of existing formats and enable easy data sharing and accessibility without the limitations of proprietary formats and software. Development of the format was headed by Prof. Römpp within the framework of the EU funded project COMPUTIS. An imzML file consist of two parts, an XML file (.imzML) containing metadata and a binary file containing the mass spectral data (.ibd). Both files are connected by a universally unique identifier (UUID). Proprietary data formats can be converted to imzML using a number of available software tools[74].

2.6 Sample preparation for MALDI MSI of biological tissues

Sample preparation for MALDI MSI of biological samples is more elaborate than for other imaging applications but is just as important as the actual measurement itself. Generally, sample preparation for MALDI MSI includes three stations; Sample collection, sectioning and matrix application. Collected sample material must be kept in deep freeze conditions to avoid tissue degradation. A cryotome is used for the preparation of thin tissue cryosections. Section thickness depends on the application and the tissue type. The two main challenges of sample preparation for MALDI MSI are maintaining tissue histology within the sections during cryosectioning and minimizing analyte delocalization. Many sample types such as murine brain possess a rigid quality when frozen and can be sectioned without further preparation[75,76] steps. Delicate sample material, or samples that cannot be sectioned without structural support, can be embedded to preserve sample histology during cryosectioning. This approach has been used for a number of samples such as plant tissues[77] or whole insects[78]. Sectioning of murine lung tissue, which is the primary sample material used in this dissertation has been reported

with inflation methods.[79-81] While embedding or inflation simplifies sectioning, the mostly aqueous embedding media can promote the delocalization of water soluble analytes. Application of the matrix layer can be done with a number of different techniques such as pneumatic spraying[62] or sublimation[82]. It can be adapted to produce small matrix crystals, which are required for measurements with small pixel sizes, or to provide good analyte extraction, which is required for imaging of low concentrated compounds but usually yields larger matrix crystals and can cause the delocalization of analytes.[83, 84] Ultimately there is no singular way for sample preparation as the procedure is adapted to fit the experimental goals which often includes compromises such as sample histology vs analyte delocalization or crystal size vs analyte extraction.

2.7 High resolution mass spectrometry and MSI

High resolution mass spectrometry (HR-MS), as it is employed in this dissertation, includes both mass resolution and mass accuracy.[85]

Mass resolution

The mass resolution (R) is a dimensionless quantity indicating the degree of separation in a mass spectrum. It is defined as the smallest difference in the mass to charge ratio (Δ*m/z*) that is still separated for a given peak at a given *m/z*. For any given peak, R is calculated as follows

$$R = \frac{m}{\Delta m} = \frac{m/z}{\Delta m/z} \tag{2.3}$$

The ability of a mass spectrometer to separate neighboring peaks, i.e. differences in *m/z*, is referred to as the mass resolving power. Today, the most commonly used definition for mass resolution or resolving power is the full width at half maximum (FWHM) definition.[86] According to the FWHM definition, R is the mass or *m/z* of a single peak divided by its width at 50 % of its intensity, Figure 5.

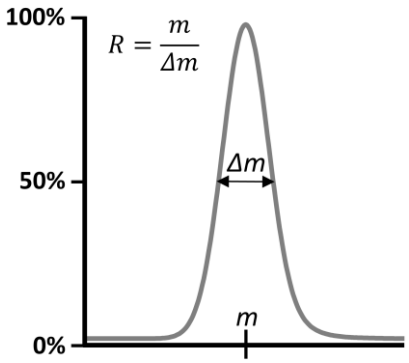

Figure 5. Graphical depiction of the full width at half-maximum definition used to calculate the mass resolution of a peak.

The 10 % valley definition, which is another definition for mass resolution, is mainly used for magnetic sector instruments and will not be discussed here. Mass resolution values are often classified as either high or low resolution. While there is no set limit to distinguish between high and low mass resolution, a value below 3000 is considered as low resolution. A mass resolution above 5000 is considered as high resolution.[87] The mass resolving power of mass spectrometers depends on the mass range. As a general trend, the mass resolving power of any instrument decreases with an increasing mass range.

The exact mathematical correlation between mass range and resolving however depends on the type of the mass analyzer.

Mass accuracy

While mass resolution is needed to separate neighboring peaks, mass accuracy is required to measure the theoretical masses and subsequently determine the elemental composition of the unknown analytes. The mass accuracy of a measured peak can be given as the absolute mass accuracy, which is the difference between the measured mass and the (calculated) theoretical mass. A more meaningful way to report mass accuracy of a peak is the relative mass accuracy (*δm/z*) in parts per million (ppm), which is the absolute mass accuracy divided by the theoretical mass and multiplied by a factor of 10^6.

$$\delta m/z\ [ppm] = \frac{m/z_{measured} - m/z_{theo.}}{m/z_{theo.}} x10^6 \tag{2.4}$$

According to Equation 2.4, the relative mass accuracy is dependent on the mass range, meaning the same absolute mass deviation leads to different relative mass accuracies depending on the mass range. For example: A peak of an imaginary analyte measured at *m/z* 1000 with a total mass deviation of 0.001 u leads to a relative mass accuracy of 1 ppm. An imaginary peak at *m/z* 100 measured with the same total mass deviation results in a relative mass accuracy of 10 ppm.

Equation 2.4 applies to single mass spectra. When reporting the mass accuracy of a peak across numerous mass spectra, it is reported as the root mean square of the individual *δm/z* values and is often referred to as the RMS error or RMSE. It is calculated as follows:

$$RMSE\ [ppm] = \sqrt{\frac{\sum_1^n (\delta m/z - \overline{\delta m/z})^2}{n}} \tag{2.5}$$

with *n* as the number of individual spectra containing the peak and $\overline{\delta m/z}$ as the arithmetic mean of all calculated *δm/z* values.

Mass calibration

Apart from certain instrument specific influences, e.g. the dynamic range of orbital trapping mass analyzers[27], the mass accuracy depends largely on the quality of the mass calibration. For mass calibration, a number of known *m/z* values (reference masses) are measured by the mass spectrometer. The received experimental values (measured *m/z* values) are subsequently matched against the theoretical *m/z* values of the reference masses. If the mass accuracy of the measured *m/z* values is not sufficient, they can be adjusted to restore mass accuracy.[88]

In practice, mass calibration can be carried out as external or internal mass calibration. In external mass calibration, reference masses are measured separately and the calibration data applied to future measurements or retroactively to past measurements (recalibration). In internal mass calibration reference masses and sample are measured at the same time, i.e. they are contained in the same mass spectra, which allows an online mass calibration. Internal mass calibration generally yields better results than external mass calibration and is often used to supplement the external mass calibration.

Ideally, the reference masses used for mass calibration are distributed evenly over the mass range of interest. Reference masses required for mass calibration can be generated by reference compounds.

A number of different reference compounds are available that fit the specific needs of different ionization techniques.[89-92] Especially for internal mass calibration, reference masses may also be generated by ubiquitous impurities[93] present in almost all mass spectra such as phthalate based plasticizers or UV stabilizers. Similarly, ions generated by known endogenous substances or ions generated by MALDI matrices can serve as reference masses for mass calibration.[94]

2.7.1 High resolution MSI

Biological tissues are among the most complex sample materials and contain a very large number of isobaric species. When performing MSI of such samples, the entire bandwidth of molecules contained in the sampling area is transferred into the mass spectrometer without further chromatography based separation steps. This leads to the superposition of isobaric ions in low mass resolution mass spectra and makes an identification of specific analytes from this data alone impossible. As such, one of the biggest challenges of MSI is the identification of analytes directly from imaging data. Apart from MS/MS multiple reaction monitoring[8] or ion mobility separation for imaging[95], only high resolution MSI enables an identification of analytes from regular full scan imaging data based on their accurate masses. As stated above this requires both a high mass resolution to separate isobaric peaks and mass accuracy to determine the elemental composition of the analyte. Accordingly, high resolution MSI is restricted to imaging systems that are capable of high mass resolution, i.e. FT-ICR, orbital trapping or certain time of flight instruments.

2.7.2 The AP-SMALDI Orbitrap imaging system

All MALDI MSI work of this dissertation was conducted using an Orbitrap mass spectrometer (Section 2.3) in combination with the atmospheric pressure scanning microprobe MALDI imaging source (AP-SMALDI 10) originally developed at the University of Giessen.[41] Further development of this source led by Prof. Römpp enabled its application on biological samples, i.e. thin tissue sections, which is the instrumental basis for all MALDI imaging work conducted in this thesis.[2] A schematic representation of the source is given in Figure 6. The base plate of the source containing the nitrogen laser and the laser attenuator is mounted on top of the Q Exactive HF™ orbital trapping mass spectrometer. Through a lens/mirror assembly the laser beam is directed into the ion source mounted to the atmospheric pressure interface of the mass spectrometer. Here, the widened laser beam is directed through a focusing lens and onto the sample by a second mirror. The sample is mounted on a sample stage movable in x/y/z direction. The unique feature of this setup is the centrally bored second mirror which allows that both laser and the inlet capillary are arranged orthogonal to the sample. This allows a better laser focusing resulting in a better spatial resolution. This system has the distinction of being the first available MSI system capable of both HR-MS and high spatial resolution at the same time.

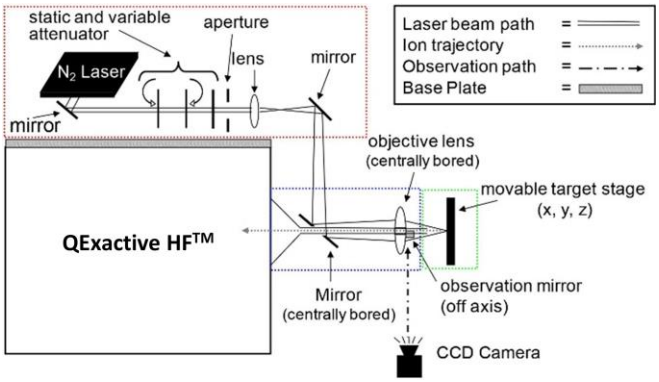

Figure 6. Schematic representation of the AP-SMALDI 10 source for MALDI MSI used in this dissertation.[62] For a schematic of the QExactive HF™ mass spectrometer visit www.planetorbitrap.com.

2.8 Tuberculosis and MSI

2.8.1 Tuberculosis

Tuberculosis (TB), also known as 'Consumption' or 'White Death', is a common infectious disease of the pulmonary system with *Mycobacterium tuberculosis* (Mtb) as the main causative agent in humans. TB occurs globally with high incidence rates in the developing world, especially Africa, Southeast Asia and the successor states of the former USSR. Statistically, one in three humans is latently infected with Mtb. For 2019, the World Health Organization (WHO) estimated 10 million new active TB cases and 1.2 million registered deaths in HIV negative people. TB is therefore 'the leading cause of death from a single infectious agent'[5] responsible for more deaths than other, much more prominent, infectious diseases such as HIV/AIDS. This is despite the fact that TB can be cured whereas HIV/AIDS cannot. Due to the economic fallout from the COVID-19 pandemic causing the disruption of essential services in high incidence countries coupled with the reallocation of research funding, the WHO estimates an increase of TB cases and related deaths in the coming years.[96, 97]

Most bacterial infections can be cured with short term antibiotic monotherapy. Treatment of TB is unique in that it relies on long term antibiotic combination therapies, at least 6 months for new active cases using specialized antibiotics that are often used exclusively against TB. These compounds include antibiotics such as pyrazinamide, isoniazid, rifampicin or ethambutol which are the current first line drugs recommended by the WHO for treatment of new active TB cases.[6, 7] The main reasons for the long duration of TB chemotherapy are the slow replication rate of Mtb as well as the specific pathology of the disease. In humans, the hallmark of an active TB infection is the formation of necrotic granuloma in the lung. Granuloma are inflammatory sites, which carry a high mycobacterial burden.[98-100] Granuloma formation begins with the phagocytosis of Mtb by macrophages. Mtb is able to survive and multiply inside the phagosome, eventually killing the macrophage and releasing more mycobacteria. Early stage 'cellular granuloma' contain a core region made up of Mtb infected macrophages surrounded by additional macrophages recruited to the site in an attempt to wall off the infection from the surrounding tissue. Cellular granuloma, while able to contain the infection, are still unable to eliminate it. In a small percentage of these latently infected individuals, the containment of the infection fails, prompting more immune cells to infiltrate the affected regions and causing the cellular granuloma to grow and change their internal structure. Eventually, the growing granuloma begins to necrotize from the inside out marking the transition from cellular to 'necrotic granuloma'. The central necrotic mass (caseum) contains a large number of extracellular Mtb, which can survive in the hypoxic

microenvironment.[101] The necrotic core is surrounded by multiple layers of macrophages followed by a fibrous cuff made up mostly of newly formed connective tissue, mainly collagen. If an expanding granuloma reaches an airway, the necrotic center fuses with the epithelium lining releasing the necrotic mass into the airway leaving behind a hollow space called a cavity. In this stage, Mtb can be detected within a person's sputum which facilitates the spread of Mtb, Figure 7.

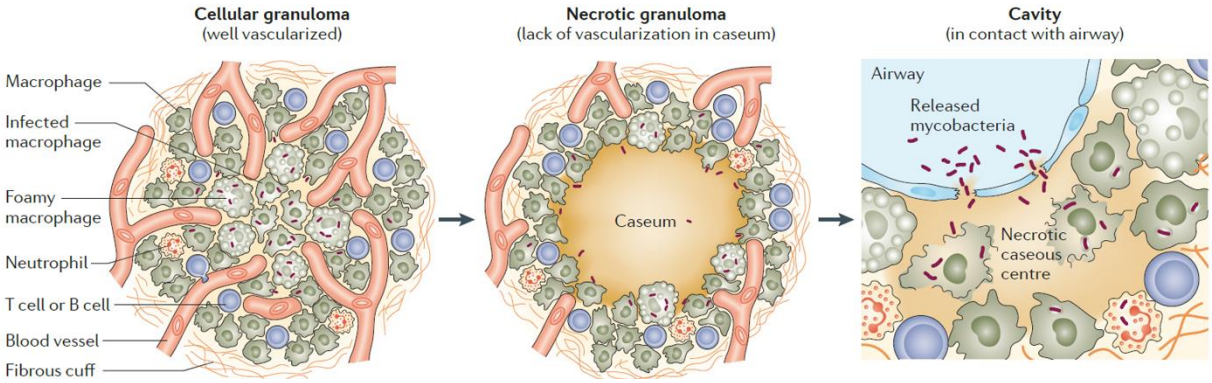

Figure 7. Schematic[98] showing the maturation of a pulmonary granuloma in humans from the cellular over the necrotic into the cavity stage.

Cellular granuloma are still vascularized and thus readily penetrated by anti-TB drugs. The lack of vascularization in later stage necrotic granuloma makes it very difficult for anti-TB drugs to penetrate into these structures. Necrotic granuloma thus provide a haven for Mtb. Eliminating Mtb only outside of granuloma is not sufficient to cure TB, as the bacteria can emerge from the granuloma after the antimicrobial therapy has passed and cause a relapse. Therefore, in order to cure TB, antibiotics must reach the necrotic core of TB granuloma in sufficient concentrations to locally eliminate the mycobacteria.[8] In conjunction with the slow replication rate of Mtb and compliance issues usually associated with long term drug regimens this fosters the development of drug resistant Mtb[102] strains which ultimately leads to a demand for novel anti-TB drugs. [103]

2.8.2 MALDI MSI in TB research

The efficacy of anti-TB drugs is directly dependent on their ability to penetrate into TB granuloma. Therefore, drugs that are effective against Mtb *in vitro* may be ineffective *in vivo* if they cannot penetrate into TB granuloma. Determining the drug penetration behavior, which is highly compound specific, is therefore a key concern during the development of novel anti-TB drugs. As discussed in Section 2.5.3, MALDI MSI is capable of imaging the distribution of intact organic molecules in small biological structures. Therefore, MALDI MSI can also be employed in anti-TB drug development by visualizing their distributions and providing direct information about a compounds ability to penetrate into TB granuloma. In 2011, Prideaux et al. were the first to use MALDI MSI for TB research by investigating the distribution and penetration behavior of the anti-TB drug moxifloxacin in sections of TB infected rabbit lung tissue.[8] In further studies on TB infected rabbit lung, the distributions of pyrazinamide[104], rifampicin[105, 106], rifapentin[106], levofloxacin[107, 108], gatifloxacin[108], moxifloxacin[105, 108] and ethambutol[109] were investigated using MALDI MSI. In two clinical studies the distribution of pyrazinamide, moxifloxacin, linezolid, rifampicin and clofazimine were investigated in resected lung tissue of TB patients[110, 111].In pre-clinical animal trials, inbred mice, e.g. BALB/c or SWISS, are the most commonly used animal models.[9, 10] This is mainly due to the lower space and upkeep requirements of mice in comparison to other rodent models. However, these mouse models fail to develop a human

like TB pathology as described in Section 2.8.1 and exclusively form non-necrotic cellular granuloma.[112] As the microenvironment in necrotic parts of a granuloma is different from that in cellular parts, predictions on the efficacy of anti-TB drugs in humans derived from pre-clinical studies that use these mouse models are unreliable. Humanized mouse models[113] produced through genetic engineering which develop a TB pathology similar that of humans offer a way to overcome the shortcomings of current mouse models and improve the predictive power of pre-clinical drug trials. Two MALDI MSI studies have been published that use the humanized TB mouse model C3HeB/FeJ (also known as 'Kramnik' mice) which forms human like necrotic granuloma.[114] Irwin et al.[115] have investigated the distribution of bedaquiline and pyrazinamide while DeMarco et al.[116] have reported the imaging of rifampicin. Bedaquiline and rifampicin were found unable to penetrate into the necrotic granuloma of these mice. Pyrazinamide was found able to penetrate into the granuloma. All of these studies, including those performed on mice were conducted with a spatial resolution ≥ 50 µm. The generally small size of anatomical structures in mice however requires a higher spatial resolution to distinguish the distribution of drug compounds in small biological compartments such as the different regions of TB granuloma.

In this work, MALDI MSI of anti-TB drugs was conducted with a spatial resolution down to 5 µm, to enable a visualization of differences in the drug distribution between small biological compartments. This also constitutes the so far the highest reported spatial resolution for imaging of drug compounds in lung tissue. Imaging measurements were performed on lung sections of an interleukin-13-overexpressing transgenic (IL-13^{tg}) mouse model.[11] Interleukin 13 is a protein which, among a number of other functions, is a mediator of the inflammatory response. The increased expression of the IL 13 protein in the IL-13^{tg} mice leads to an altered immune response to TB infection which is similar to human TB pathology. TB infected IL-13^{tg} mice form centrally necrotic pulmonary granuloma very similar to those found in humans.

2.9 Visualizing analyte penetration

For a good *in vivo* efficacy, drug compounds must reach their intended point of action, i.e. their target, for example a tumor or a TB granuloma. As mentioned in Section 2.8.2, the evaluation of a drugs *in vivo efficacy* requires the study of its penetration behavior. Usually the investigation of analyte penetration in MALDI MSI is based on the ion images.[8, 104-109, 117] In cases where a more in-depth investigation of the penetration behavior is required, ion images alone are not sufficient. Previous works have used MSI to visualize analyte penetration. In 2018, Bonnel et al. [118] have reported a method to visualize the penetration of drug compounds contained in ointments into human skin. Their approach assumes the movement of analytes only in one direction starting from a flat surface, with uneven surfaces turned into even surfaces. In 2019, Machálková et al. [119] reported a method including fluorescence microscopy to visualize the penetration of drug compound into circular shaped 3D spheroid cultures. This approach uses an algorithm to evaluate the signal intensity in equidistant layers from the spheroid boundary to its center. The 'penetration analysis tool' used in this work is based on MATLAB and was written by Dr. Alan Race as part of the DZIF project at our group. It represents an advancement of the work of Dr. Julia Kokesch-Himmelreich, who used the tool to visualize the penetration of superficially applied antifungal agents into cheese[120], which is a one-dimensional problem. Here it was expanded towards a two-dimensional approach. The tool uses co-detected lipid species to determine the edge of a region of interest, i.e. a TB granuloma, and calculates the mean intensity of an analyte based on the distance from the determined edge. The tool is capable of

visualizing the penetration of analytes into irregularly shaped two-dimensional structures while assuming a movement of analytes in x and y direction.

2.10 Previous works and status built upon

The results of this dissertation represent a continuation and expansion of previous works. At the beginning of my work, the MALDI MSI system had been set up and the basic workflow for imaging the distribution of lipids in section of murine brain with a spatial resolution down to 5 µm had been established. This workflow included the sectioning of unembedded whole mouse brains at -20°C, application of DHB, CHCA or pNA matrix using a pneumatic sprayer built in house, and the measurement of phospholipids with full scan acquisition. Conversion of proprietary RAW files into imzML was conducted using the 'raw to imzML converter' (Version 1.2.1i) developed at the University of Gießen under the supervision of Prof. Römpp. The MSiReader Software[42] (Version 0.9) was used for generation of ion mages and overlays. The DZIF project for the imaging of drug compounds in murine lung was already running at the time I started my work and preliminary work had been conducted by Dr. Katharina Huber at the University of Gießen and Dr. Amol Fatangare and Bastian Jahreis at the University of Bayreuth, all in the group of Prof. Römpp. This work included the sectioning of CMC embedded murine lung lobes for the imaging of lipids with up to 10 µm spatial resolution and first attempts to optimize matrix choice and application conditions for the detection of BTZ-043, using CHCA matrix. A successful imaging of BTZ-043 in lung sections was however not possible with these conditions. Furthermore, it was unknown if this sample preparation approach has an impact the on distribution of the other six drug compounds (PZA, CFZ, RIF or INH, EMB, MXF) investigated in this dissertation as no tissue samples of mice that had received these drugs had been shipped to our group. Published earlier works using the same MALDI imaging system included the imaging of lipids and peptides in mouse pituitary gland with 5 µm[75], and lipids in mouse choroid plexus with 3 μm^2 spatial resolution. Furthermore the drug imatinib was imaged with at 10 µm spatial resolution in mouse kidney medulla.[68] This publication is significant as the drug compound in this work was not only imaged with high spatial resolution but also HR-MS, which enabled an identification of the drug directly from the imaging data without additional identification steps such as multiple reaction monitoring MS/MS. As a continuation of this work, MALDI imaging and sample preparation in this dissertation were improved to achieve higher sensitivity required to detect drug compounds at therapeutic level concentrations as well as higher spatial resolution. Furthermore, sample preparation was adapted to produce viable sections of difficult to handle murine lung and to minimize the delocalization of water soluble compounds.

3 Results

3.1 Publications included in this work and author contributions

This thesis lead to the publication of three full papers in peer reviewed scientific journals. At the time this dissertation was submitted, the manuscript for a fourth publication was in in preparation.

The DZIF project on which the first, third and the manuscript for a fourth publication of this thesis are based was initiated and directed (for our part) by Prof. Dr. Andreas Römpp.

First publication

Axel Treu, Julia Kokesch-Himmelreich, Kerstin Walter, Christoph Hölscher, Andreas Römpp. Integrating High-Resolution MALDI Imaging into the Development Pipeline of Anti-Tuberculosis Drugs. *Journal of the American Society for Mass Spectrometry.* 2020, 31, 11, 2277–2286

Author contributions

Experiments for this publication were conceived and designed by A.T., J.K-H. and A.R.. A.T. performed the main MALDI imaging work, including sample preparation and data analysis. Data were interpreted by A.T., J.K-H. and A.R.. J.K-H. conducted initial experimental work and the experimental coordination with cooperation partners. Animal experiments were conducted by K.W. from the Infection Immunology group C.H. at the Research Center Borstel. The manuscript was prepared by A.T. and edited by J.K-H. and A.R.

Second publication

Axel Treu, Andreas Römpp. Matrix ions as internal standard for high mass accuracy matrix assisted laser desorption/ionization mass spectrometry imaging. *Rapid Communications in Mass Spectrometry*. 2021, 35 (16), e9110

*Author contribution*s

Experiments were conceived and designed by A.T and A.R. The experimental work, data analysis and interpretation was conducted by A.T. The manuscript was written by A.T. and edited by A.R..

Third publication

Julia Kokesch-Himmelreich, Axel Treu, Alan Mark Race, Kerstin Walter, Christoph Hölscher, Andreas Römpp. Do Anti-tuberculosis Drugs Reach Their Target? – High Resolution Matrix-Assisted Laser Desorption/Ionization Mass Spectrometry Imaging Provides Information on Drug Penetration into Necrotic Granulomas. *Analytical Chemistry.* 2022, 94, 14, 5483–5492.

Author contributions

The experimental design was conceived by J. K-H., A.T. and A.R.. The experimental work was carried out by A.T.. Data analysis and interpretation was shared between A.T., J. K-H and A.R.. The MATLAB data analysis tool was written and provided by A.M.R. Animal experimentation, sample preparation inside the BSL 3 laboratory and immunohistochemical stainings were conducted by K.W. from the Infection Immunology group of C.H. at the Research Center Borstel. The manuscript was prepared by

J. K-H supported by A.T., who provided several figures and certain parts of the manuscript. The final manuscript was edited by all co-authors.

Manuscript for a fourth publication

Axel Treu, Kerstin Walter, Julia Kokesch-Himmelreich, Franziska Waldow, Julia Dreisbach, Dominik Schwudke, Michael Hölscher, Christoph Hölscher, Andreas Römpp. The efficacy of the novel antitubercular agent BTZ-043 in preclinical Tuberculosis mouse models. *Manuscript in preparation*.

Author contributions

The experimental and study design (concerning MS imaging) was conceived by A.T., J. K-H. and A.R.. CFU reduction studies for dose ranging on TB infected BALB/c mice, CFU reduction studies on IL-13^{tg} mice and histological staining on IL-13^{tg} mice as well as all animal experimentation of mice used for MALDI MSI and LC-MS of tissue was conducted by K.W. from the Infection Immunology group of C.H. at the Research Center Borstel. Pharmacokinetic data was provided by J.D. from the Division of Infectious Diseases and Tropical Medicine of the LMU Munich headed by M.H.. LC-MS experiments of tissue sections were conducted by F.W. from the Bioanalytical Chemistry group of D.S. at the Research Center Borstel. MALDI MSI experiments, data analysis as well as post-measurement haematoxylin and eosin stainings were conducted by A.T. Data interpretation was conducted by A.T., J.K-H. and A.R.. The manuscript was prepared by A.T. and edited by A.R..

The full length versions of all papers as well as the manuscripts in preparation are contained in section 5.

3.2 First publication – Integrating High-Resolution MALDI MSI into the Development Pipeline of Anti-Tuberculosis Drugs

Successful MALDI MS imaging is not a single stage process. It rather comprises a number of consecutive steps which are each equally important for the success of the final step which is the actual MALDI MSI measurement. As such, the first publication included in this work reports on the development of the MALDI imaging workflow for the imaging of anti-TB drugs in sections of murine lung. Given in the following is an overview of all steps (Figure 8) of the workflow that was developed and optimized on TB uninfected BALB/c lung tissue as part of the first publication.

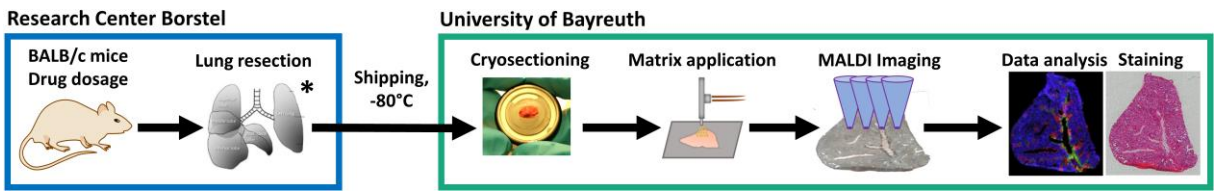

Figure 8. Schematic of the MALDI MSI workflow developed for the imaging of anti-TB drugs in uninfected BALB/c lung sections. * = Ref.[121]

Sample collection and cryosectioning

Obtaining viable sample material, i.e. thin tissue sections, is the essential first step for any MALDI MSI measurement. When imaging the distribution of drug compounds it is also of utmost importance to minimize the post mortal delocalization of these compounds, especially of easily delocalized water-soluble drug compounds such as pyrazinamide or isoniazid. Among the most important aspects in minimizing the delocalization of water-soluble compounds is an uninterrupted deep freeze chain, beginning immediately after organ harvest. Following euthanization of mice, resected organs were folded into aluminium foil, flash frozen in liquid nitrogen and then stored at -80°C. Whole lung lobes of uninfected BALB/c mice were shipped on dry ice from the Research Center Borstel to our laboratory for cryosectioning and MALDI MSI analysis.

Cryosectioning of murine lung lobes presented a significant challenge in this work. Murine lung lobes are small and possess a malleable quality which makes them easily deformed. A common approach to obtain intact cryosections from whole murine lung lobes is by inflating the lobes with inflation media such as acquaeous formalin[79], gelatin[80] or agarose[81] at room temperature and then refreezing the lobe. In addition, common embedding techniques such as CMC or gelatin embedding may be used to stabilize the sample during the sectioning process. In initial experiments, sections were cut from CMC embedded whole lung lobes at -20°C, which delivered sections with good tissue integrity. MALDI MSI on these sections showed a tissue matching distribution for the water insoluble drug CFZ[122] whereas the water-soluble drug PZA (150 mg/kg)[122] had leaked out of the section. Most likely, PZA was washed out of the tissue during the embedding process by the aqueous CMC medium. To prevent the delocalization of water-soluble drugs, sectioning was subsequently performed on unembedded lung lobes at -40°C cryostat and sample holder temperature. With this procedure, it was possible to obtain intact lung sections without inflation or embedding. MALDI MSI of these sections still showed a delocalization of the water soluble drug EMB[122], which could be identified as a result of mounting the sections on room temperature adhesive glass slides. Subsequently, sections were mounted on adhesive glass slides that were cooled down to the sectioning temperature inside the cryostat chamber. Slides were warmed briefly from the backside by finger contact to allow only the minimum heat required for a proper mounting to enter the section. Section thickness ranged between from 10 to 16 µm. With this procedure it was possible to minimize the delocalization of the (partly) water-soluble drugs[122] PZA, INH and EMB covered in this study.

Choice of matrix and application method

For imaging of drug compounds with low in tissue concentration choosing the right matrix, matrix application and measurement parameters determines the success or failure of the imaging experiment. For example, assuming a tissue section of a mouse dosed intravenously with 10 mg/kg of a drug compound. A MALDI MSI instrument with a 5 µm laser focus must be able to detect roughly 2 fg of this drug compound in a complex biological matrix (assuming a tissue density of 1 g/cm³). If the drug was administered orally these numbers drop even further due to a reduced bioavailability.[123]

The appropriate method of matrix application is determined by the experimental goals. High spatial resolution requires small homogenous crystal sizes which are achievable by solvent free matrix application methods such as sublimation. Solvent based ‘wet’ application methods provide superior analyte extraction which is required for imaging of drug compounds with low in tissue concentrations but also promote a delocalization of drug compounds in case of too wet application.[83] Balancing the need for both small matrix crystals and sufficient analyte extraction, matrix substances were applied

in this study via a pneumatic spray. The solvent systems used in this study for the pneumatic matrix application were able to readily dissolve both the matrix compound and the targeted analytes. The choice of matrix is determined by the chemical properties of the targeted analyte. Polar analytes require a polar matrix and vice versa. To determine the matrix substance best suited for detecting a drug compound, drug standard solutions in different concentrations were spotted onto blank porcine liver sections and measured with different matrices. The resulting drug signal intensities were compared for each matrix. The matrix delivering the highest drug intensities was chosen for imaging this particular drug. This procedure was performed for most of the six compounds covered in this study. The results are compiled in Table 1.

Table 1. Matrix substances suitable for imaging the drug compounds covered in the first publication.

Drug compound	**Suitable matrix**
Pyrazinamide	2DHB
Clofazimine	DHB, CHCA, 2,6-DHAP
Rifampicin	pNA
Isoniazid	CHCA
Ethambutol	DHB, CHCA, 2,6-DHAP
Moxifloxacin	2,6-DHAP

MALDI MSI measurement

To detect drug compounds at low in tissue concentrations, regular full scan acquisition may not provide the required sensitivity to detect these compounds. In LC-MS applications performed on quadrupole Orbitrap instruments similar to the instrument used in this study, selected ion monitoring (SIM) was able to achieve a distinct increase in sensitivity over regular full scan acquisition.[124] Therefore, SIM can also be used to boost the detection sensitivity of drug compounds with low concentration or poor ionization efficiency in MALDI MSI at the cost of losing the ability to correlate the measured drug distribution with biological structures via co-detected lipid species. To overcome this problem, MALDI MSI measurements were performed with alternating SIM and full scan acquisition windows to enable a sensitive detection of drug compounds and the co-detection of lipids in the same measurement. This approach also serves to minimize the consumption of scarce sample material. Accommodating two alternating acquisition modes in one measurement necessitated some adjustments to the measurement setup. The number of pixels in x direction (N_X) must be a positive multiple integer of the number of used acquisition modes (n_{Ac}) to ensure that pixels of the same modality are arranged in vertical lines which simplifies conversion of raw data into imzML. To avoid rectangular shaped pixels, the pixel size in x direction (S_X) was defined as the pixel size in y direction (S_Y) divided by n_{Ac}. Imaging was performed on drug compounds at therapeutically relevant doses. Mice received daily doses of either PZA 150 mg/kg, CFZ 25 mg/kg, RIF 10 mg/kg or INH 25 mg/kg, EMB 100 mg/kg, MXF 100 mg/kg. Theoretical masses were calculated using tabulated values from the Commission of Isotopic Abundances and Atomic Weights.[125]

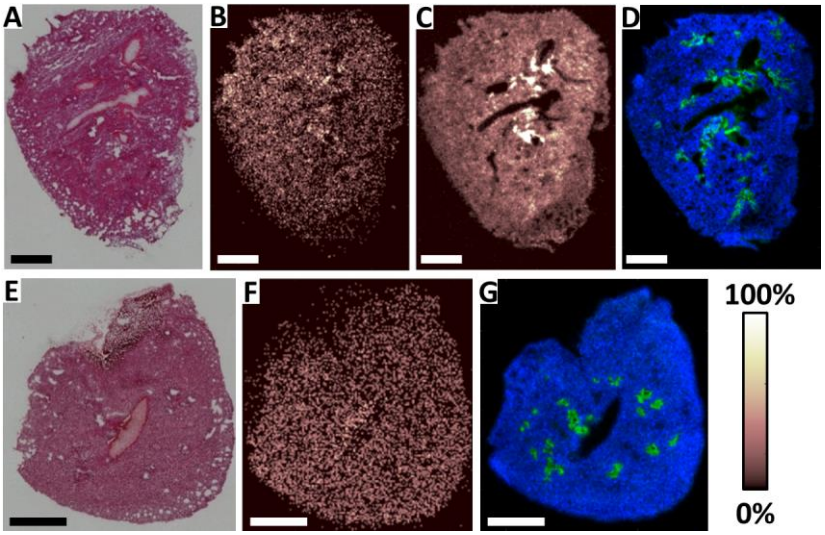

Figure 9. MALDI MS imaging of PZA, CFZ RIF, and lipids in uninfected BALB/c lung using alternating SIM and fullscan acquisition with a step size of 30 x 15 µm and an image pixel size of 30 x 30 µm. **A)** Post-measurement HE staining. **B)** Distribution of PZA $[M+2H]^{+\cdot}$,$C_5H_7N_3O^{+\cdot}$, *m/z* 125.05836, RMSE 0.61 ppm (9781 spectra). **C)** Distribution of CFZ $[M+H]^+$, $C_{27}H_{23}Cl_2N_4^+$, *m/z* 473.12942, RMSE 0.51 ppm (23839 spectra). **D)** Overlay of PC(36:4) $[M+K]^+$, $C_{44}H_{80}NO_8PK^+$, *m/z* 820.52531 in green and PC(30:0) $[M+K]^+$, $C_{38}H_{76}NO_8PK^+$, *m/z* 744.49401 in blue; Raster size for B-C: 330 x 220 pixel. **E)** Post measurement HE stain. **F)** Distribution RIF detected with SIM (*m/z* 810 - 830) $[M-H]^-$, $C_{43}H_{57}N_4O_{12}^-$, *m/z* 821.39784, RMSE 1.43 ppm (7394 spectra). **G)** Overlay of PI(38:4), $[M-H]^-$, $C_{47}H_{82}O_{13}P^-$, *m/z* 885.54985 in green and PS(38:4), $[M-H]^-$, $C_{44}H_{77}NO_{10}P^-$, *m/z* 810.52905; Raster size for F-G: 290 x 160 pixels. Scale bars = 1 mm.

The drug compounds PZA and CFZ as well as lipid species were detected in positive ion mode in one measurement with alternating SIM and full scan acquisition using DHB as matrix. As a polar, water soluble compound, PZA has a low ionization efficiency in MALDI. It was detected with SIM acquisition from *m/z* 120 to 140 as the double protonated radical cation $[M+2H]^{+\cdot}$ (*m/z* 125.05836) using the matrix ion $[DHB+H-H_2O]^+$ (*m/z* 137.02332) for internal mass calibration, Figure 9 B. CFZ $[M+H]^+$ (*m/z* 473.12942) (Figure 9 C) and lipids were detected in the full scan window from *m/z* 450 to 900 using the matrix ion $[5DHB+NH_4-4H_2O]^+$ (*m/z* 716.12461) for internal mass calibration. Co detected lipid species can be used to correlate the drug distribution with the sample histology. The overlay in Figure 9 D shows the distribution of PC(36:4) in green highlighting blood vessels and PC(30:0) in blue showing the lung parenchyma. In addition to the single protonated molecule, CFZ was also detected as the double protonated radical cation $[M+2H]^{+\cdot}$, see full length publication in Section 5.1. RIF $[M-H]^-$ (*m/z* 821.39784)was detected in negative ion mode using pNA as matrix with SIM (*m/z* 810 to 830) (Figure 9 F) and full scan acquisition (*m/z* 400 to 900) for the co-detection of lipids, Figure 9 G. A direct comparison of SIM and full scan acquisition showed that SIM gives an eight fold increase in signal coverage over full scan acquisition. As pNA does not produce ions in the concerning mass range, the measurement was conducted without internal mass calibration. Another polar and water soluble compound, INH $[M+H]^+$ (*m/z* 138.06618), was detected in SIM from *m/z* 120 to 180 to include the CHCA matrix ion $[CHCA+H-CO_2]^+$ (*m/z* 146.06004) for internal mass calibration, Figure 10 B. Lipids were detected in the full scan window from *m/z* 400 – 900 using the CHCA ion $[3CHCA+Na+2K-2H]^+$ (*m/z* 666.02876) for internal mass calibration. EMB $[M+H]^+$ (*m/z* 205.19105) and MXF $[M+H]^+$ (*m/z* 402.18236) were imaged in positive ion mode with full scan acquisition from *m/z* 205 to 405 using the 2,6-DHAP matrix ion $[2,6-DHAP+2K-H]^+$ (*m/z* 228.96638) for internal mass calibration, Figure 10 D, E.

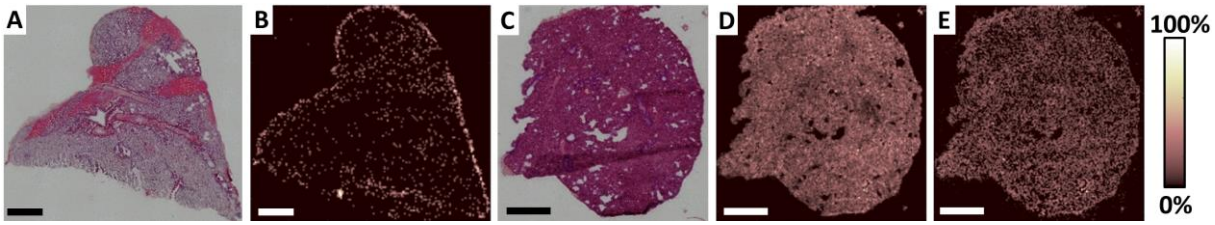

Figure 10. MALDI MS imaging of INH, EMB and MXF in uninfected BALB/c lung using alternating SIM and full scan acquisition. **A)** Post-measurement HE staining. **B)** Distribution of INH $[M+H]^+$, $C_6H_8N_3O^+$, *m/z* 138.06618, RMSE 0.49 ppm (1330 spectra); step size 20 x 40 µm, image pixel size 40 x 40 µm, raster size 155 x 140 pixel. **C)** Post-measurement HE staining. **D)** Distribution EMB $[M+H]^+$, $C_{10}H_{25}N_2O_2^+$, *m/z* 205.19105, RMSE 0.26 ppm (24912 spectra). **E)** Distribution MXF $[M+H]^+$, $C_{21}H_{25}FN_3O_4^+$, *m/z* 402.18236, RMSE 0.75 ppm (17462 spectra); For D-E: Pixel size 30 x 30 µm, raster size 150 x 155 pixel. Scale bars = 1 mm.

As expected for orally administered drugs, PZA, RIF, INH, EMB and MXF are distributed homogenously throughout the lung parenchyma, including blood vessels. The distribution of CFZ however showed a higher abundance around airways, which was investigated further using a higher spatial resolution.

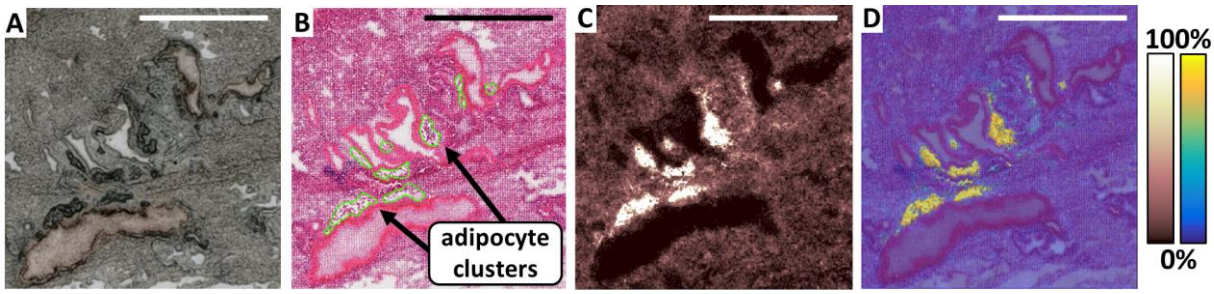

Figure 11. Imaging of CFZ with a pixel size of 10 x 10 µm. **A)** Pre-measurement optical image. **B)** Post-measurement HE staining with adipocyte clusters framed in green. **C)** Distribution of CFZ $[M+H]^+$, $C_{27}H_{23}Cl_2N_4^+$, *m/z* 473.12942, RMSE 0.66 ppm (42168 spectra), raster size 220 x 225 pixel. **D)** Optical overlay of the CFZ distribution with the post measurement HE stain showing the accumulation of CFZ in adipocyte clusters around airways. Scale bars = 1 mm.

Imaging measurements with 10 x 10 µm step size were performed in positive ion mode using DHB matrix with full scan acquisition from *m/z* 450 to 900 for CFZ and *m/z* 130 to 900 for EMB. This constituted the smallest pixel size with which anti-drugs have been investigated in MS imaging. With these measurements, it was possible to co-localize the higher CFZ abundance around airways mentioned above with adipocyte clusters[126], Figure 11. This accumulation is likely a result of the high lipophilicity of CFZ and its long biological half life of 70 days[127].

On tissue, drug compounds were identified based on accurate mass identification and the comparison of the on tissue MS/MS with that of a standard substance. Apart from identifying the molecular ions of drug compounds, the high mass resolution and mass accuracy used for the imaging measurements also enabled the distinction of the isotopic fine structure of the protonated molecular ion CFZ $[M+H]^+$ from the isotopic pattern of the neighboring double protonated molecular ion $[M+2H]^{+\cdot}$ of CFZ. Fragmentation pathways were formulated for the molecular ions PZA, EMB, CFZ and RIF. Furthermore, a structural proposal for the previously reported[104, 110, 115] but unconfirmed double protonated molecular ion $[M+2H]^{+\cdot}$ of PZA that explains the recorded MS/MS spectrum was given. Structural formulas of the drug compounds investigated in the first, second and third publication are given in Figure 12.

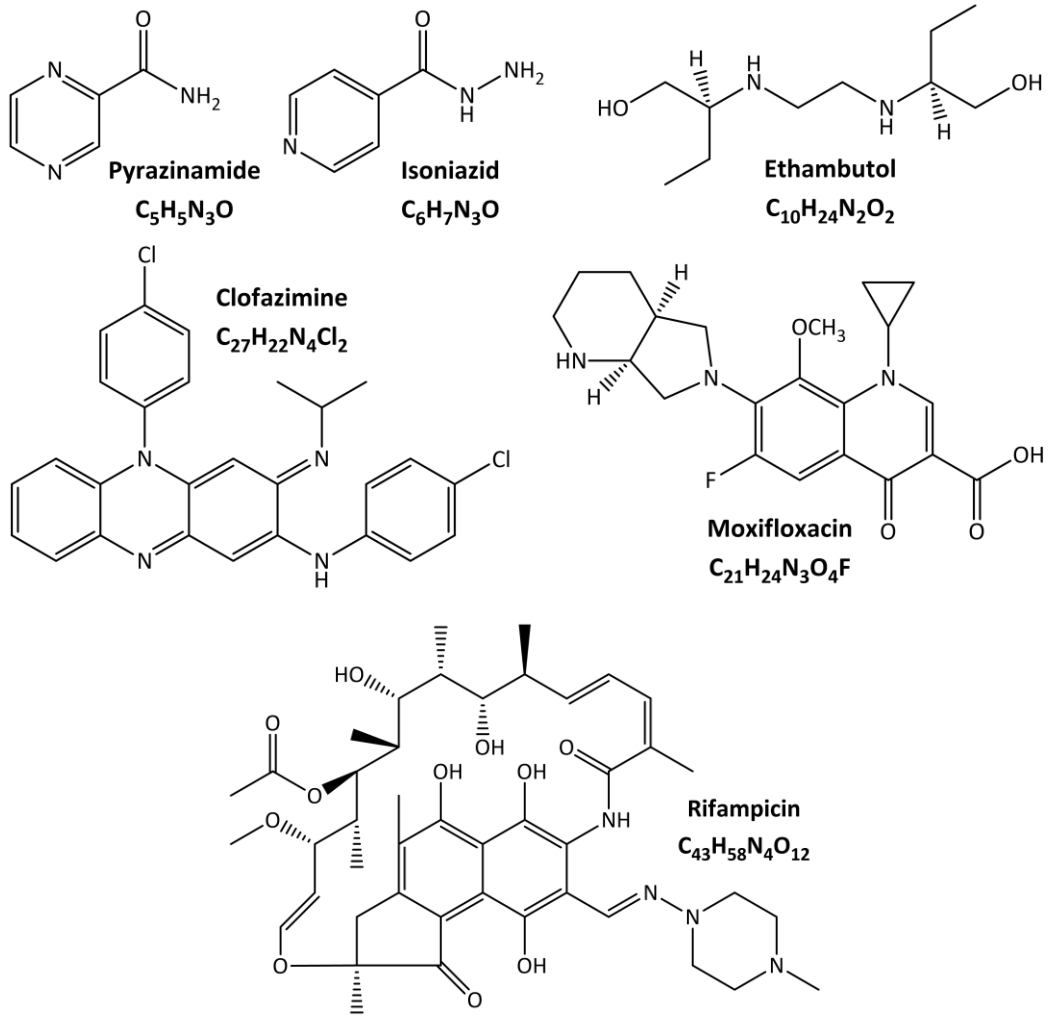

Figure 12. Structural formulas of the drug compounds investigated in the first and third publication.

Summary and conclusion

All six drug compounds, including all current first-line anti-TB drugs, could be successfully imaged at therapeutic concentrations in murine lung tissue. Of these six compounds, CFZ, EMB, INH and MXF were imaged for the first time in murine lung tissue while PZA and RIF were imaged with a higher spatial resolution than previously reported in murine lung. In addition, measurements with 10 µm pixel size, which is the highest reported spatial resolution (at the time of publication) for imaging of drug compounds in mouse lung, revealed an accumulation of CFZ in lipid deposits located around airways. These results demonstrate that the developed workflow is not only capable to image the distribution of anti-TB drugs at therapeutic concentrations in lung tissue but can also visualize these drugs in small histological structures. As part of the development pipeline of novel anti-TB drugs, these abilities make the developed workflow a powerful analytical tool to visualize the distribution of compounds in the substructures of TB granuloma. Therefore, the developed workflow will be used in further studies on TB infected murine lung tissue within the framework of the DZIF.

3.3 Second publication – Matrix ions as internal standard for high mass accuracy MALDI mass spectrometry imaging

The first publication reported on MALDI MSI of drug compounds on complex biological samples and their identification directly from the imaging data. This is one of the major challenges of MALDI MSI and is only possible with high resolution mass spectrometry (HR MS)[85] which entails both high mass resolution, which is necessary to separate the multitude of isobaric ions generated from biological samples, and high mass accuracy to enable a comparison of the imaging data with mass spectral data repositories (see Section 2.7). While the achievable mass resolution in a given mass range is an instrumental parameter which depends on the type of the mass analyzer, the mass accuracy depends greatly on the quality of the mass calibration. In mass calibration, a number of well-known *m/z* values or 'reference masses' that are distributed over wide mass range are detected and the measured *m/z* values subsequently correlated against the theoretical *m/z* values. If the deviation between the measured and theoretical *m/z* values exceeds a certain threshold, the calibration data can be applied to future measurements or retroactively to past measurements to achieve/restore mass accuracy.[88] If the measurement of reference masses and the actual sample takes place at different time points, the procedure is referred to as external mass calibration. In internal mass calibration, the sample and the reference masses are measured at the same time, which enables a real time mass calibration and generally yields better results than external calibration. The reference masses required for mass calibration can be supplied by a number of different commercially available reference compounds[89, 90], monoisotopic elements[91] or salts[92], ubiquitous impurities[93] or endogenous compounds such as lipids when investigating biological samples[76, 94, 128]. Matrix ions may also be used as references for internal mass calibration, if their elemental composition is known[2, 62, 94]. At lower *m/z* range, most MALDI matrices form a large number of easily identifiable ions. In the past, the abundance of matrix ions at lower *m/z* range presented a problem for measurements of small molecules with low mass resolving power instruments. With high mass resolving power instruments, an abundance of matrix ions can actually be turned into an advantage as these ions can be used for internal mass calibration. At higher mass range, matrix ions are scarcer, especially on tissue sections due to ion suppression effects exerted by the sample. At these higher mass ranges, matrix ions usually belong to ascending series of homologues clusters such as, for example, $[a\text{DHB}+\text{NH}_4\text{-}b\text{H}_2\text{O}]^+$ with $a = 0,1,2,3\ldots$ and $b \leq a$. To be usable for internal mass calibration in MALDI MSI, a matrix ion is ideally detectable in the entire field of view of the measurement with sufficient abundance and should not be superimposed by neighboring peaks.

The goal of this second publication was to compile lists of reference masses generated on tissue by common MALDI matrices, which can be used for either internal or external mass calibration in MALDI MSI. To this end, eleven common MALDI matrices (Table 2) suitable for positive, negative and dual polarity mode were applied onto coronal mouse brain sections and the identity of the ions generated on tissue by these matrices was investigated.

Matrices were applied onto coronal mouse brain sections via pneumatic spraying using a pneumatic sprayer built in house. Measurements for matrix cluster investigation were conducted with a pixel size of 30 x 30 µm covering a 20 x 20 pixel grid and internal mass calibration using already known matrix clusters. Sum formulas were assigned to matrix ions based on accurate mass data and MS/MS for ions of DHB.

Table 2. List of the matrix substances covered in the second publication.

Matrix (abbreviation)	CAS number	Sum Formula	Ion mode(s)
9-aminoacridine (**9AA**)	90-45-9	$C_{13}H_{10}N_2$	Neg
2[(2E)-3-(4-tert-butylphenyl)-2-methylprop-2-enylidene]malononitrile (**DCTB**)	300364-84-5	$C_{17}H_{18}N_2$	Pos
Caffeic acid (**CA**)	331-39-5	$C_9H_8O_4$	Pos
alpha-cyano-4-hydroxycinnamic acid (**CHCA**)	28166-41-8	$C_{10}H_7NO_3$	Pos
1,5-diaminonaphthalene (**1,5 DAN**)	2243-62-1	$C_{10}H_{10}N_2$	Neg / Pos
2,5-dihydroxybenzoic acid (**DHB**)	490-79-9	$C_7H_6O_4$	Pos / Neg
4-nitronaniline (**pNA**)	100-01-6	$C_6H_6N_2O_2$	Neg / Pos
Norharmane	244-63-3	$C_{11}H_8N_2$	Neg / Pos
Sinapic acid (**SA**)	530-59-6	$C_{11}H_{12}O_5$	Pos
2,4,6-trihydroxyacetophenone (**THAP**)	480-66-0	$C_8H_8O_4$	Neg
2,6-dihydroxyacetophenone (**2,6 DHAP**)	699-83-2	$C_8H_8O_3$	Pos / Neg

Results

The measured *m/z* values of matrix clusters, the corresponding matched sum formulas, theoretical mass and cluster composition were compiled into tables for each matrix and polarity. In these tables, the matrix clusters used for internal mass calibration are highlighted with an asterisk '*****'.

Among the eleven matrices investigated in this study, DHB delivered by far the most numerous clusters in positive and negative ion mode. In the positive ion mode, most of the identified DHB clusters belong to four ascending homologues cluster series, which contain H^+, NH_4^+, Na^+, or K^+ as single charge carriers and show a multiple dehydration. The clusters of these series which are summarized in this work with the general cluster composition of $[a\text{DHB+X-}b\text{H}_2\text{O}]^+$ (a = 1,2,3,…; $b \leq a$) are highly periodic and cover a wide mass range from *m/z* 100 to about 1500 and can contain up to ten basis molecules. In addition, DHB forms a number of clusters based on a multiple hydrogen / alkali metal cation exchange followed by the loss of water with a general cluster composition of $[a\text{M+}b\text{Alkali-}(b\text{-}1)\text{H-}c\text{H2O}]^+$ (a = 1,2,3…; b = 1,2,3…; c = 0,1,2,3…). Similar compositions were observed for DHB ions in the negative ion mode between *m/z* 100 and 850, $[a\text{M-}b\text{H+}(b\text{-}1)\text{Alkali-}c\text{H2O}]^-$, $[a\text{M-}b\text{H-H+}(b\text{-}1)\text{Alkali}]^{\cdot-}$ (a = 1,2,3…; b = 1,2,3…; c = 1,2,3…). As DHB delivers a large number of ions in both polarities distributed over a wide mass range, the matrix is also well suited for use in external mass calibration and may be considered as a lower mass analogue or accompanying substance to Ultramark 1621™. The general cluster compositions generated by the matrices investigated in in this work are presented in Table 3. Full lists of the clusters generated by the investigated matrices are given in the full length version of the manuscript in Section 5.2.

Derivatives of cinnamic acid are a major class of matrices, represented in this work by *alpha*-cyano-4-hydroxycinnamic acid (CHCA) , sinapinic acid (SA) and caffeic acid (CA). They generate a large number of matrix clusters in the positive ion mode based mainly around a multiple hydrogen / alkali metal cation exchange often in conjunction with the additional loss of CO_2 or H_2O. These ions cover a similar mass range as the DHB clusters and can be summarized with the general cluster composition $[a\text{M+}b\text{Alkali-}(b\text{-}1)\text{H}]^+$ (a = 1,2,3…; b = 1,2,3…). Clusters of this composition containing predominantly K^+ as charge carriers showed a higher abundance than clusters containing predominantly Na^+ as charge carrier. Similar to DHB, derivatives of cinnamic acid are also ideally suited for use in external mass calibration.

Table 3. Overview of the general clusters compositions generated by the matrices investigates in this work

Matrix	General cluster composition in positive ion mode	General cluster composition in negative ion mode
DHB	$[aM+X-bH_2O]^+$ *(X = H^+, NH_4^+, Na^+, K^+; a = 1,2,3…; b ≤ a)* $[aM+bAlkali-(b-1)H-cH_2O]^+$ *(a = 1,2,3…; b = 1,2,3…; c = 0,1,2,3…)*	$[aM-bH+(b-1)Alkali-cH_2O]^-$ $[aM-bH-H+(b-1)Alkali]^{\cdot-}$ *(a = 1,2,3…; b = 1,2,3…; c = 1,2,3…)*
CHCA, SA, CA	$[aM+bAlkali-(b-1)H]^+$ $[aM+bAlkali-(b-1)H-CO_2]^+$ $[aM+bAlkali-(b-1)H-CO_2]^+$ *(a = 1,2,3…; b = 1,2,3…)*	-
DCTB	$[aM+X-Alkyl]^{+/+\cdot}$ *a = 1,2,3…; X = H^+, Na^+, K^+; Alkyl = CH_4, CH_3, CH_2, C_2H_4, C_2H_6, C_4H_8*	-
pNA	$[aM+X-bNO]^{+/+\cdot}$ *(X = H^+, Na^+, K^+; a = 1,2,3…; b ≤ a)*	$[aM-H-bH_2]^-$ *(a = 1,2,3…; b = 1,2,3…)*
1,5 DAN	No general cluster composition applicable	$[aM-H-bH_2]^-$ *(a = 1,2,3…; b = 1,2,3…)*
2,6 DHAP	$[aM+bAlkali-(b-1)H]^+$ *(a = 1,2,3…; b = 1,2,3…)*	$[aM-H-bH_2]^-$ $[aM-bH+(b-1)Alkali]^-$ *(a = 1,2,3…; b = 1,2,3…)*
Norharmane	$[aM+X]^+$ *(a = 1,2,3…; X = H^+, Na^+, K^+)*	$[aM-H-bH_2]^-$ *(a = 1,2,3…; b = 1,2,3…)*
THAP	-	$[aM-H-bH_2]^-$ $[aM-bH+(b-1)Alkali]^-$ *(a = 1,2,3…; b = 1,2,3…)*
9AA	-	$[aM-H-bH_2]^-$ *(a = 1,2,3…; b = 1,2,3…)*

Cluster composition comparable to those of CHCA, SA and CA were observed for the other matrices intended for use in positive ion mode that are included in this work. Apart from DHB, matrices intended for negative ion mode show less variation in the cluster composition, which is centered on the consecutive loss of H_2 from the deprotonated cluster body. These ions, which generally do not exceed *m/z* 600 can be summarized with the general cluster composition $[aM-H-bH_2]^-$ (*a* = 1,2,3…; *b* = 1,2,3…). In total, around 450 individual matrix ions could be identified. In addition, an example for using matrix ions for internal mass calibration in MALDI MSI of drug compounds and lipids is presented. In this example, the anti-tuberculosis drug ethambutol and phospholipids were imaged in a section of murine lung using matrix clusters for internal mass calibration to achieve sub ppm mass accuracy for the imaged compounds.

Summary and Conclusion

Matrix ions are ubiquitous in all MALDI MS spectra. Using these ions for mass calibration negates the need for additional standard substances and sample preparation steps and is both an effective and elegant way to achieve high mass accuracy. For a robust identification of compounds in complex sample matrices such as biological tissues, high mass accuracy is indispensable. As such, the cluster lists compiled in this publication are of interest to the entire field of MALDI MS, especially to all users of MALDI MSI. These results will be incorporated into the developed MALDI MSI workflow for the imaging of drug compounds and used for future experiments.

3.4 Do Anti-tuberculosis Drugs Reach Their Target? – High Resolution Matrix-Assisted Laser Desorption/Ionization Mass Spectrometry Imaging Provides Information on Drug Penetration into Necrotic Granulomas

Following the development of the MALDI MSI workflow reported upon in detail in the first publication and the use of matrix clusters for mass calibration to achieve high mass accuracy reported in the second publication, the next step of this work was to apply the workflow on lung sections of TB infected IL-13^{tg} mice. These mice received the same PZA, CFZ and RIF cocktail doses used on the uninfected BALB/c mice from the first publication. The goal of this was first to determine if the developed workflow is actually capable of visualizing these drugs in sections of inactivated TB infected tissue. To evaluate the suitability of the IL-13^{tg} model for pre-clinical testing of anti-TB drugs, the distribution of the already established anti-TB drugs PZA, CFZ and RIF was to be investigated to determine if their penetration behavior in IL-13^{tg} mice is comparable to what is reported in the literature. An overview of the MALDI MSI workflow adapted for TB infected IL-13^{tg} samples is given in Figure 13. The handling of TB infected samples requires a laboratory with the biological safety level 3. As a result, all sample preparation steps including sectioning according to the sectioning method described in the first publication were conducted in the BSL 3 laboratory of the Research Center Borstel by our cooperation partner Dr. Kerstin Walter. For MALDI MSI, sections were inactivated via γ irradiation. Of every inactivated sample batch a sample was sent to the on-site National Reference Center for mycobacteria to confirm the deactivation. Following clearance, sections were sent to our laboratory on dry ice for MALDI MSI analysis.

Sectioning and measurement of irradiated / non-irradiated sections

Cryosectioning of TB infected IL-13^{tg} lung was conducted inside BSL 3 conditions according to the procedure described in Section 3.2. For safe use in a regular laboratory sections had to be inactivated. As opposed to simple and well-known inactivation techniques, such as boiling or immersion in organic solvents, mounted sections were inactivated via γ irradiation to maintain the integrity of the tissue and reduce the delocalization of analytes. Glass slides with the mounted sections were placed on dry ice in a ^{137}Cs gamma ray source and a dose of 5854 Gy. After microbiological testing and clearance from the National Reference Center for Mycobacteria based on the mycobacteria growth indicator tube (MGIT) system, sections were shipped to our laboratory on dry ice. Before measurements could be conducted on inactivated IL-13^{tg} sections, a possible influence of the irradiation procedure on the drug distribution had to be ruled out. To this end, pairs of directly neighboring irradiated / non-irradiated sections of uninfected BALB/c mouse lung, which received the same drug treatment as the infected IL-13^{tg} mice, were produced. These section pairs were imaged simultaneously in one measurement to directly visualize any influence of the irradiation on the drug distribution without batch effects. It was found, that the irradiation has no discernible influence on the distribution of PZA, CFZ, RIF and the lipid pattern.

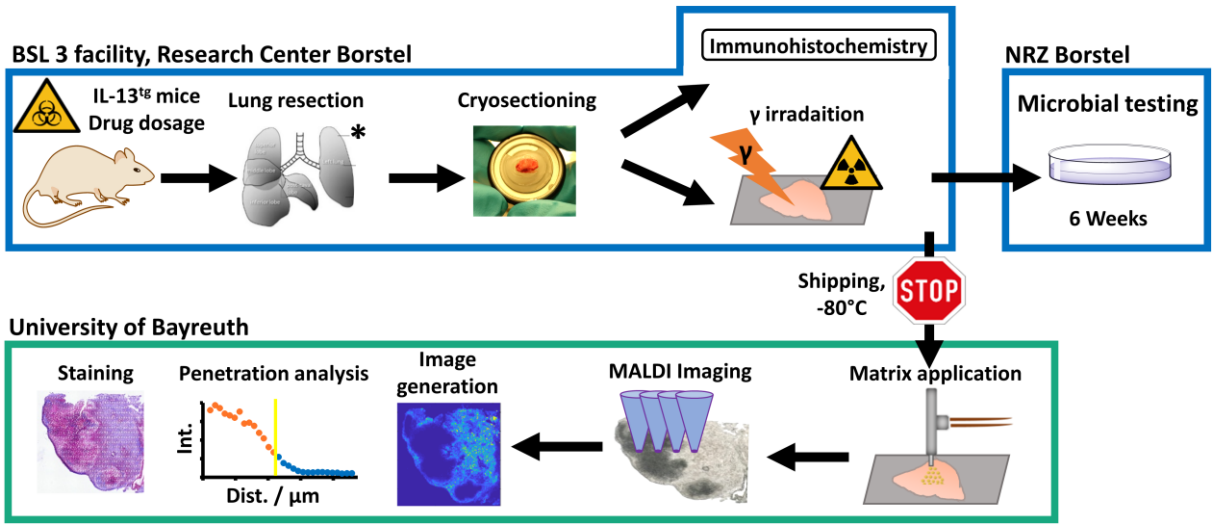

Figure 13. Schematic of the MALDI MSI workflow developed for the imaging of anti-TB drugs in infected IL-13^{tg} lung tissue. * = Ref.[121]

Measurement of infected IL-13^{tg} lung sections with 30 µm pixel size

Using the measurement setups described in the first publication (mass ranges, lock masses, alternating SIM and full scan acquisition), imaging measurements were performed on inactivated IL-13^{tg} sections containing centrally necrotic granuloma. As a deviation from Section 3.2, imaging measurements of RIF were conducted with 2,6-DHAP matrix which in further matrix optimization steps was found to be better suited for the imaging of RIF than pNA.

Lipid species characteristic for the granuloma area and the surrounding tissue were detected in positive ion mode and were identified via accurate mass based databank search and MS/MS. Lipids were imaged in conjunction with PZA and CFZ using the alternating SIM / full scan acquisition described in Section 3.2. Representing the granuloma area is PC(O-34:2). PC(36:4) was chosen to represent the surrounding area of the granuloma. The same lipids were used in the penetration tool to distinguish granuloma and surrounding area.

PZA and its active metabolite pyrazinoic acid (see Section 5) as well as CFZ and RIF could be successfully imaged in the IL-13^{tg} lung tissue Figure 14. PZA is detected in the entire section including the granuloma area, Figure 14 E-F. POA is detected mainly in the granuloma areas. CFZ shows a high intensity outside of the granuloma which rapidly declines towards the centers of the granuloma areas Figure 14 G-H.

A similar behavior can be observed for RIF, albeit with a much lower intensity in the areas surrounding the granuloma (see Section 5.3), indicating that PZA is able penetrate the entire granuloma including the necrotic core while CFZ and RIF do not. The distribution of PZA and RIF has been investigated with MALDI MSI in previous studies on TB infected C3HeB/FeJ ('Kramnik') mice[115, 116], rabbits[104-106] and in a clinical investigation[110]. The behavior of PZA in our study matches that reported in the literature in mice, rabbits and humans.

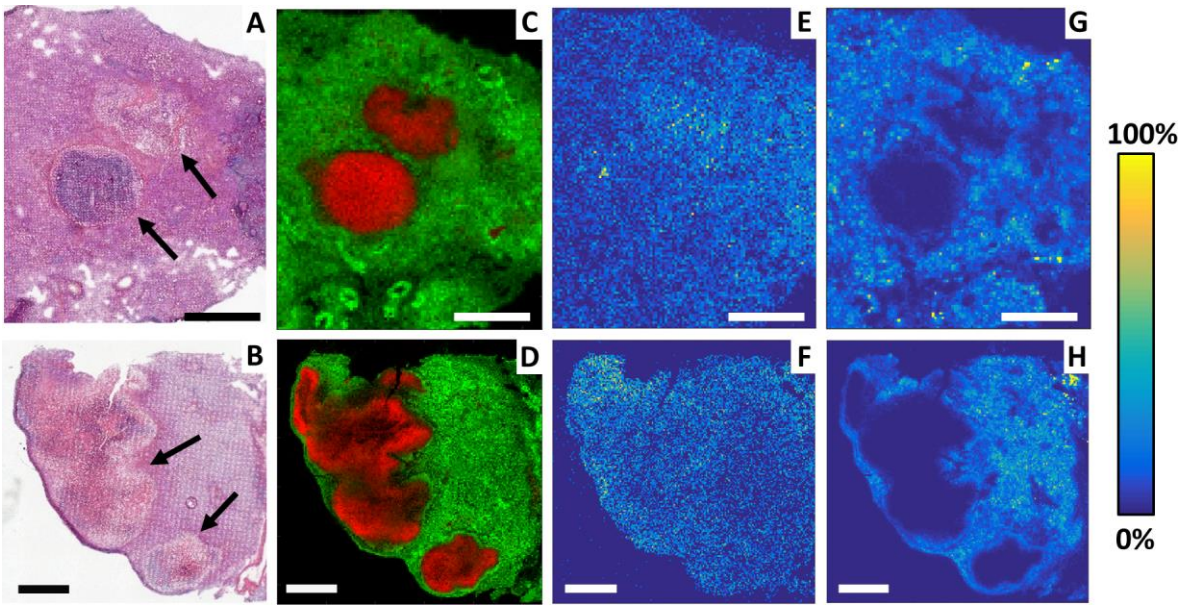

Figure 14. MALDI MSI of lipids and the drug compounds PZA and CFZ in TB infected, inactivated IL-13^{tg} lung sections. **A-B)** Post-measurement HE stains. Granuloma are indicated with black arrows. **C-D)** Overlay of PC(O-34:2) $[M+Na]^+$, $C_{42}H_{82}NO_7PNa^+$, *m/z* 766.57211 in red showing the granuloma area and PC(36:4) $[M+K]^+$, $C_{44}H_{80}PNO_8K^+$, *m/z* 820.52531 in green showing the surrounding area. **E-F)** Distribution of PZA $[M+2H]^{+\cdot}$, $C_5H_7N_3O^{+\cdot}$, *m/z* 125.05836. E) RMSE 0.87 ppm (10633 spectra). F) RMSE 0.36 ppm (11985 spectra). **G-H)** Distribution of CFZ $[M+H]^+$, $C_{27}H_{23}Cl_2N_4^+$, *m/z* 473.12942. G) RMSE 0.30 ppm (13933 spectra). H) RMSE 0.81 ppm (25891 spectra). Scale bars = 1 mm.

In studies on mice and rabbits, RIF was found unable to penetrate into TB granuloma, whereas in a clinical study the drug was found to accumulate inside the necrotic core of the granuloma after it had attained a steady state concentration 26 h following a 180 day therapy with a dose comparable to the 10 mg/kg dose used in our work. Apparently, RIF did not reach a steady state concentration in our case as well as in the previous mice and rabbit studies. CFZ was imaged here for the first time in a mouse model that mimics human TB pathology and our findings concur with results from clinical studies[110, 111]. These results show that the IL-13^{tg} model delivers results comparable to rabbit models and human studies and is thus suitable for use in pre-clinical drug trials.

Penetration analysis of drug compounds

To gain more insight into the penetration behavior of drugs at the transition zone between the granuloma and surrounding area and especially at the border between necrotic core and cellular layer, a dedicated penetration analysis tool written in MATLAB by Dr. Alan Race in our group was employed to generate 'penetration plots' of anti-TB drug compounds. As mentioned above, the lipid chosen to represent the granuloma area is PC(O-34:2), Figure 14 C-D. As the first step, the tool uses the distribution of PC(O-34:2) to create a 'granuloma mask'. This can be done for multiple granuloma in the same measurement. After filtering, the remaining holes in the mask are filled up and the 'edge' of the granuloma area(s) can be calculated. For each granuloma mask, a corresponding distance image is generated by grouping all pixels inside the calculated edge according to their distance from the edge. For the inclusion of the surrounding tissue, the distribution of the lipid PC(36:4) was employed using the same filtering and filling steps as used for the granuloma masks. This 'outside distance map' is created by grouping all pixels on tissue according to their distance towards the calculated granuloma edge. From both distance maps, the mean intensity of any analyte can be extracted for each distance

relative to the granuloma edge. The penetration plot is then generated by plotting the extracted mean intensities against their distance. A visualization of these steps, including the penetration plots of PZA and CFZ in the measurements shown in Figure 14 A-G, is shown in Figure 15. A more in depth description of the involved data analysis steps is included in the full length version of the manuscript in Section 5.3. As already visible from the ion images, the penetration plot of PZA (Figure 15 B) shows similar abundances in the inside and outside regions. The penetration plot of CFZ (Figure 15 C) and RIF (see Section 5.3) show that their intensity decline towards the necrotic core is not immediate but rather a gradual process, which already begins outside of the determined edge and also shows that both drugs are able to penetrate into the granuloma to some extent. This behavior can be explained by the structure of the surrounding tissue area. As explained in Section 2.8.1, TB granuloma are encapsulated by a fibrotic cuff made up of connective tissue, mainly collagen.[98] Depending on its thickness, which is individual for every granuloma, this layer may be hindering the penetration of CFZ towards the granuloma. In additional granuloma investigated as part of this publication, the penetration plots of CFZ showed an abundance maximum just inside the determined granuloma edge. It is known that several anti-TB drugs belonging to the fluoroquinolone class, accumulate in the macrophage layers surrounding the necrotic core, especially in regions with lipid rich foamy macrophages.[108] An accumulation of CFZ in macrophages could be shown in *ex situ* studies.[129, 130] *In situ* evidence for the accumulation of CFZ in macrophages however has not been reported to date.

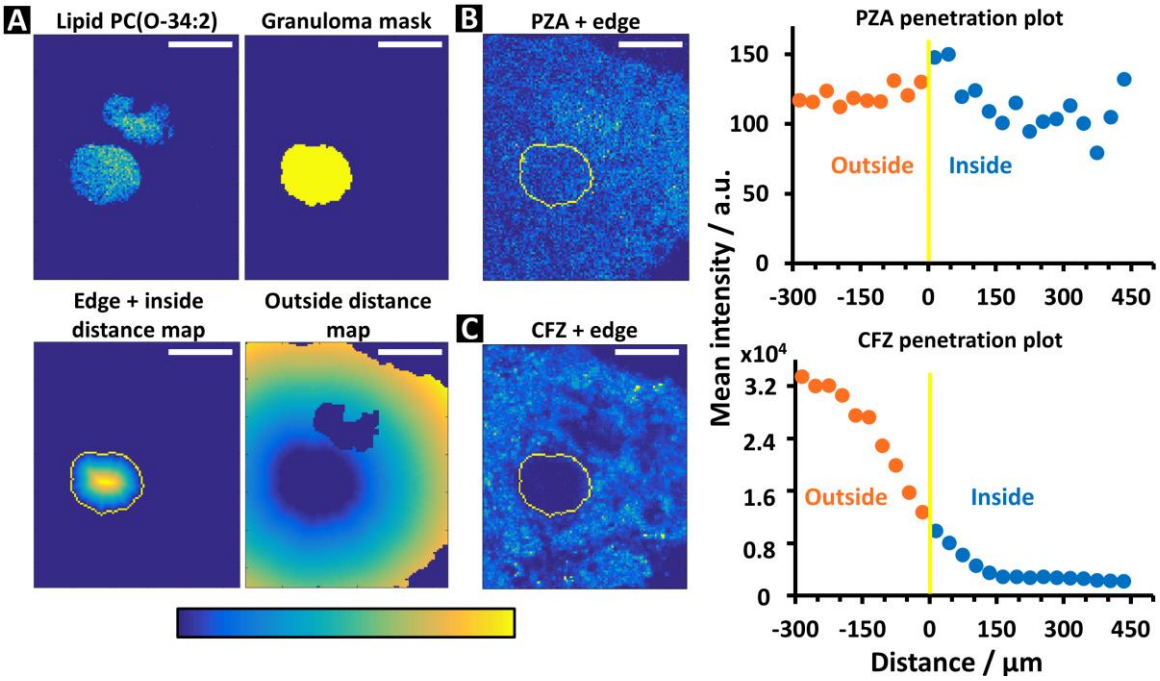

Figure 15. A) Visualization of the general steps involved in the generation of penetration plots of drug compounds. **B)** Ion image of PZA from Figure 14 E overlayed the granuloma edge generated by the penetration tool and the resulting penetration plot. **C)** Ion image of CFZ from Figure 14 G overlayed the granuloma edge generated by the penetration tool and the resulting penetration plot. Scale bars = 1 mm.

5 µm pixel size MALDI MSI of CFZ

To determine if the abundance maximum of CFZ on the edge between the inside and the outside region correlates with the presence of the macrophage layer, measurements were conducted on well structured granuloma containing a central necrotic core surrounded by a layer of macrophages with 10 and 5 µm pixel size, Figure 16. At the time this dissertation was submitted it was the highest

reported spatial resolution MALDI MSI of drug compounds in lung tissue. To visualize the macrophage layer surrounding the necrotic core, a macrophage specific staining (macrosialin, CD68) was performed on directly neighboring sections by Dr. Kerstin Walter at the Research Center Borstel. The CD68 staining colors CD68 expressing macrophages in yellow, Figure 16 B. Granuloma masks for these measurements were generated manually in Spectral Analysis[131] and imported into the penetration tool. In contrast to the measurements with 30 µm pixel size, the 5 and 10 µm pixel sizes used here enabled a more detailed insight into the internal structure of the granuloma. This is represented by the co-detected lipid species now showing the central necrotic are of the granuloma PC(O-36:3) in red, the macrophage layer PC(O-36:4) in blue and the surrounding tissue PC(36:4) in green, Figure 16 C. Correlation of the penetration plots of with the CD68 stains and the lipid pattern shows that the abundance maxima coincide with the layer of CD68 expressing macrophages surrounding the necrotic core. In the 5 µm measurement shown in Figure 16, the penetration shows a second CFZ abundance maximum outside the granuloma edge which coincides with the macrophage clusters outside of the granuloma edge visible in the CD68 stain in Figure 16 B. This means CFZ does accumulate in the macrophage rich regions of TB granuloma and is the first *in situ* evidence of CFZ accumulation in macrophages.

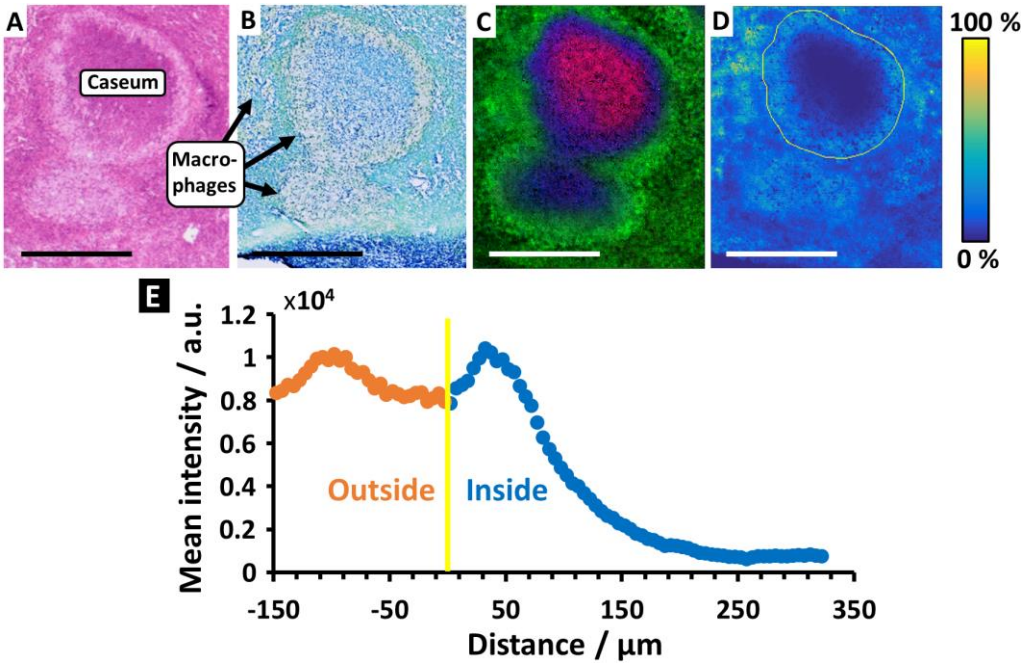

Figure 16. MALDI MSI of CFZ with a pixel size of 5 x 5 µm and penetration analysis. **A)** HE stain of a neighboring section. The necrotic core located in the upper part of the granuloma is annotated. **B)** CD68 stain performed on a neighboring section. CD68 positive macrophages appear in yellow and are highlighted by arrows. **C)** RGB overlay of PC(O-36:3) $[M+K]^+$, $C_{44}H_{84}NO_7PK^+$, m/z 808.56170 in red showing the central necrotic core; PC(O-36:4)$^+$, $[M+K]^+$ $C_{44}H_{82}PNO_7K^+$, m/z 806.54604 in blue showing the macrophage layer surrounding the necrotic core; PC(36:4)$^+$, $C_{44}H_{80}PNO_8K^+$, m/z 820.52531 in green showing the surrounding tissue. **D)** Distribution of CFZ $[M+H]^+$, $C_{27}H_{23}Cl_2N_4^+$, m/z 473.12942 RMSE 0.35 ppm (65096 spectra). Given in yellow is the granuloma edge imported from Spectral Analysis. **E)** Penetration plot of CFZ inside the area demarcated by the imported edge in (D). Scale bars = 500 µm.

Impact of granuloma pathology on the drug distribution

The impact of granuloma pathology and the suitability of the IL-13^{tg} model for pre-clinical testing of drug compounds and how it compares to the regular BALB/c mice is investigated in more detail in a

publication by our cooperation partner Dr. Kerstin Walter from the Research Center Borstel. The paper has been published in Antimicrobial Agents and Chemotherapy (AAC) with the DOI: https://doi.org/10.1128/AAC.01588-21. The main focus of this work is the investigation of granuloma specific pathology in IL-13^{tg} and BALB/c mice and its influence on the drug distribution. For this publication, I performed the MALDI MSI work, data analysis and prepared the relevant figures. BALB/c mice which are the most commonly used animal model for pre-clinical drug testing do not form a human like TB pathology. TB granuloma of BALB/c mice are strictly cellular, i.e. made up mostly of macrophages, and lack a central necrotic core whereas IL-13^{tg} mice form human like granuloma with a central necrotic core. To investigate the distribution of PZA, CFZ and RIF, MALDI MS imaging with a step size of 35 µm was performed on sections of TB infected BALB/c and IL-13^{tg} mice. In contrast to the IL-13^{tg} mice, in which only PZA was able to penetrate the entirety of the granuloma, all three drug compounds were able to penetrate into the granuloma of BALB/c mice. Furthermore, the accumulation of CFZ which in the IL-13^{tg} mice is limited to the macrophage layer surrounding the necrotic core encompasses the entire granuloma in BALB/c mice. These results very clearly show the impact of granuloma pathology on the penetration behavior of drugs and highlight the need for specialized mouse models for pre-clinical screening and testing of anti-TB drugs and the ability of the IL-13^{tg} model to fill this role.

Summary and Conclusion

The high resolution MALDI MSI workflow described in the first publication, was applied on γ ray inactvated IL-13^{tg} lung tissue. It could be verified, that the irradiation procedure has no influence on the drug distribution. The anti-TB drug compounds PZA, CFZ and RIF were imaged with higher spatial resolution than reported in previous publications.[8, 104-111, 115, 116, 132, 133] CFZ was imaged for the first time in a specialized animal model that mimics human TB pathology. PZA was found able to penetrate the entire granuloma, whereas CFZ and RIF showed a declining intensity towards the granuloma center. These findings are generally in accordance with results from previous pre-clinical and clinical studies. Characteristic lipid species for the granuloma and surrounding areas could be identified and were used in a newly developed penetration analysis tool to visualize the penetration of PZA, CFZ and RIF. These plots showed that the intensity decline of CFZ and RIF inside the granuloma already begins outside of determined granuloma areas, likely due to the fibrotic cuff, and that both drugs are still, to a certain degree, able to penetrate into the granuloma. Furthermore, measurements with 10 and 5 µm pixel size, the highest reported spatial resolution for MALDI MSI of drugs in lung tissue, in combination with matching CD68 stainings confirmed an accumulation of CFZ in the macrophage layers surrounding the necrotic core. These results show that the developed workflow is capable of imaging anti-TB drugs in TB infected lung tissue and compare the penetration behavior of multiple drug compound into TB granuloma and that the IL-13^{tg} mouse model is suitable for pre-clinical studies of anti-TB drug compounds. The results obtained by the penetration analysis tool show that the workflow can further the understanding of the *in vivo* drug efficacy. In all, the combination of the MALDI MSI workflow with the IL-13^{tg} mouse model is suitable for the pre-clinical study anti-TB drugs and will be used in further studies on novel drug compounds within the framework of the DZIF.

3.5 Manuscript for a fourth publication – The efficacy of the novel antitubercular agent BTZ-043 in preclinical Tuberculosis mouse models

As presented in the third publication, the developed workflow is capable of imaging anti-TB drugs at relevant concentrations and investigate their penetration behavior in infected murine lung tissue with high mass accuracy and spatial resolution. Furthermore, the utilized IL-13^{tg} mouse model is suitable for the pre-clinical testing and evaluation of anti-TB drugs. The logical next step is to use the MALDI MSI / IL-13^{tg} workflow as an analytical platform to evaluate the efficacy of novel anti-TB drugs. This is the goal of the fourth publication included in this dissertation. It utilizes the groundwork of the previous three publications and applies it to investigate the efficacy of the novel anti-TB drug benzothiazinone-043 (BTZ-043). Furthermore, this publication is not limited to MALDI MSI alone and includes work from three other groups to supplement the MALDI MSI data and put them into a broader context. For that purpose, the workflow described in Figure 13 in the third publication is expanded to include LC-MS of γ ray inactivated sections to gain quantitative information on the amount of BTZ-043 present in tissue sections neighboring those used for MALDI MSI and to determine the impact of the irradiation on the drug concentration.

BTZ-043 is a novel anti-TB drug belonging to the benzothiazinone class, Figure 17. Benzothiazinones are sulfur containing nitroaromatic spiro compounds which were found capable of killing Mtb *in vivo*, *ex vivo* and in animal models.[134]

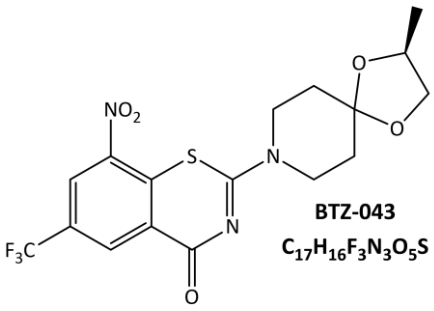

Figure 17. Structural formula of BTZ-043.

BTZ-043 interferes with the cell wall formation by inhibiting the enzyme decaprenylphosphoryl-β-D-ribofuranose-2'-epimerase.[135] This prevents the formation of decaprenylphosphoryl arabinose, which is an arabinose donor for the synthesis of arabinogalactan and lipoarabinomannan. The lack of these polysaccharides in the cell wall subsequently promotes cell wall lysis and cell death.BTZ-043 is the most advanced candidate of the benzothiazinone class of antibiotics. It is currently undergoing Phase 1 and 2 clinical trials (NCT03590600) and is set to be used in combination therapies with other compounds against drug-sensitive and extensively drug-resistant TB.

Dose ranging experiments

Initial CFU reduction studies were conducted by Dr. Kerstin Walter on TB infected BALB/c mice to determine a suitable dose for treatment of mice with BTZ-043. 22 days post infection, BTZ-043 treatment was started with single daily oral doses of 50, 100, 250, 500 and 1000 mg/kg BTZ-043. CFU reduction was determined after 47, 615 and 75 days of treatment. After 5 weeks of treatment, the 250, 500 and 1000 mg/kg doses showed a higher efficacy than the control group which received a daily dose of 25 mg/kg INH, which is an established first line anti-TB drug. After seven weeks, the efficacy of

the 250, 500 and 1000 mg/kg doses has increased further in comparison to INH. However, the efficacy of the 500 and 1000 mg/kg doses is not significantly higher than that of the 250 mg/kg dose. Accordingly, the 250 mg/kg dose was chosen for further experiments on TB infected IL-13^{tg} mice.

Pharmacokinetic study

PK curves of different BTZ-043 doses in BALB/c mice were recorded between 0.5 and 8 h post dose (0.5, 1, 2, 4, 8 h).The data shows that from 50 mg/kg/day upwards, an increase of the BTZ-043 dose does not lead to an increase in the plasma C_{max}. After passing C_{max}, BTZ-043 is eliminated in a biphasic manner. The first rapid elimination phase begins after C_{max} has passed and lasts until 2 h post dose. At this point the second slower elimination phase begins. At the onset of the second elimination phase the concentration in animals that received 250 mg/kg/day BTZ-043 is much higher than in animals that received only 50 mg/kg/day. Considering that dose ranging showed that the 250 mg/kg/day dose is much more effective than the 50 mg/kg/day dose, this indicates that a major driving factor for the efficacy of BTZ-043 is the area under the curve (AUC), i.e. the exposure, and not the C_{max}.

CFU reduction in IL-13^{tg} mice and granuloma histology

CFU reduction in IL-13^{tg} mice was investigated on animals, which received 250 mg/kg/day BTZ-043 for ten days, 60 days post infection. As these animals were mainly intended for MALDI MSI, only one time point was investigated. After treatment, CFU reduction in BTZ-043 monotherapy mice was aprrox. 1 log unit in comparison to untreated control mice and around 0.7 log units less than mice treated with a combination of PZA (150 mg/kg/day), CFZ (25 mg/kg/day) and RIF (10 mg/kg/day), which are established anti-TB drugs. This data shows that, even in monotherapy, the efficacy of BTZ-043 is comparable to established first and second line drugs in IL-13^{tg} mice, which have a human like TB pathology.[11] Ziehl-Neelsen (ZN) stains of IL-13^{tg} mice and those treated with PZA/CFZ/RIF at the same dose used in the first and second publication show a large number of acid-fast rods, i.e. Mtb, especially in the cellular parts of the granuloma. In comparison, ZN stains of BTZ-043 treated mice show almost no acid-fast rods. The waxy layer of mycolic acids on the outside of Mtb cell is responsible for the staining with carbol fuchsin used in the ZN stain. BTZ-043 interferes with the formation of the arabinogalactan layer located under the mycolic acid layer.[135] Accordingly, BTZ-043 causes a loss of acid fastness in Mtb, making them invisible to the ZN staining. This also means that BTZ-043 is able to reach at least the cellular layers of the granuloma.

LC-MS

To determine the influence of the γ ray inactivation on the BTZ-043 concentration and to quantify BTZ-043 in IL-13^{tg} lung sections from the same animals used in MALDI MSI, LC-MS/MS was conducted by Dr. Franziska Waldow from the Research Center Borstel. Measurements of irradiated / non-irradiated sections from uninfected BALB/c mice showed that the irradiation has no significant impact on the BTZ-043 concentration. In infected IL-13^{tg} mice, BTZ-043 reaches the highest in tissue concentration 0.5 h post dose at 6.71 ng/mg (tissue), which drops to 0.27 ng/mg after 8 h. Despite the overall decrease of the BTZ-043 concentration it is still, at least 200 times the MIC (plasma) of 1 ng/mL at any investigated timepoint.

MALDI MSI

MALDI MSI was performed with a pixel size of 10 x 10 µm on granuloma with a well defined internal structure from an IL-13^{tg} mice sacrificed 2 h post dose, Figure 18. As a sulfur containing nitroaromatic

compound, BTZ-043 suffers from poor ionization efficiency. It was not possible to detect BTZ-043 on tissue sections with regularly used MALDI matrices such as DHB or CHCA. Following a lengthy matrix optimization process as described in the first publication, DCTB, a matrix originally intended for the analysis of polymers and large macromolecules, was determined as suitable matrix for BTZ-043. To ensure a sufficient analyte extraction, the matrix was sprayed from 1:1 ethanol/chloroform solution acidified with 0.1 Vol. % of trifluoroacetic acid. BTZ-043 was detected as the protonated molecule $[M+H]^+$ (*m/z* 432.08355) in full scan acquisition (*m/z* 420 - 550) to include the DCTB matrix ions $[2M+K]^+$ (*m/z* 539.25715) and $[2M+Na]^+$ (*m/z* 523.28322) for internal mass calibration and allow a co-detection of lipid species needed for the penetration analysis as described in the second publication. Neighboring sections were used for HE (Figure 18 A), AZAN trichrome (Figure 18 B), CD68 (Figure 18 C) and oil red staining (Figure 18 D) conducted by Dr. Kerstin Walter. The CD68 stain is specific for CD68 expressing macrophages which are present in the cellular rim of the granuloma. AZAN trichrome stains collagen fibers in blue thus visualizing the fibrous cuff of the granuloma. Oil red staining stains areas with high lipophilicity in red. Comparison of the CD68 and oil red stains shows areas with a high macrophage density coincide with areas of high lipophilicity which indicated the presence of lipid rich foamy macrophages[136]. Outside of the granuloma areas, BTZ-043 shows a homogenous distribution (Figure 18 E). In the two granuloma areas, BTZ-043 shows a heterogeneous distribution with an abundance maximum which, according to the corresponding stainings, is located within the fibrotic cuff in the cellular layer of the granuloma. It is likely that due to its high lipophilicity[137], BTZ-043 is accumulating in foamy macrophages similar to the accumulation of CFZ reported in the second publication. For the generation of penetration plots, the lipid *m/z* 482.36050 assigned as lysophosphatidylcholine(O-16:0) was used to demarcate the granuloma area, *m/z* 488.44620 assigned as *N*-acylethanolamine(30:4) was used to demarcate the surrounding area respectively, Figure 18 F. The width of the BTZ-043 abundance maxima in the penetration plots of both granuloma (Figure 18 G) corresponds to the thickness of the macrophage layer. The macrophage layer of the left granuloma is much thicker (Figure 18 C) resulting in the penetration plot showing an abundance plateau rather than a simple maximum. This is a good example for the biological variance associated with TB granuloma which show very different progression of the BTZ-043 penetration despite originating from the same animal and being contained in the same section.

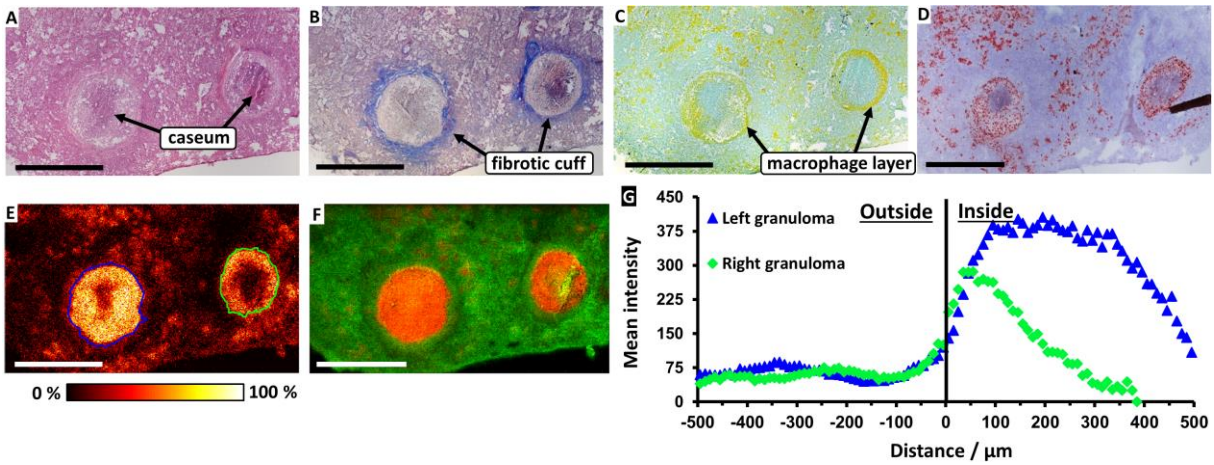

Figure 18. MALDI MSI of BTZ-043 2 h post-dose with a pixel size of 10 x 10 µm on granuloma with a well defined histology. Histological stainings were conducted on neighboring sections. **A)** HE stain. **B)** AZAN trichrome stain. **C)** CD68 stain. **D)** Oil red stain. **E)** Distribution of BTZ-043 $[M+H]^+$, $C_{17}H_{17}F_3N_3O_5S^+$, *m/z* 432.08355, RMSE 0.54 ppm (47525 spectra), m/z 420 – 550, raster size 410 x 235 pixel. The blue line demarcates the edge of the left granuloma. The green line demarcates the edge of the right granuloma. **F)** Overlay of lysophosphatidylcholine(O-

16:0) $[M+H]^+$, $C_{24}H_{53}NO_6P^+$, *m/z* 482.36050 in red and N acylethanolamine(30:4) $C_{32}H_{58}NO_2^+$, *m/z* 488.44620 in green. **G)** Penetration plots showing the penetration of BTZ-043 into both granuloma present in the section. The color schemes of the data points correspond to the color of the respective granuloma edges in panel E. Scale bars = 1 mm.

Towards the caseum however, both penetration plots show a steep decline in BTZ-043 abundance. This data shows that 2 h post-dose, BTZ-043 has not penetrated the caseum. It was however able to penetrate the fibrotic cuff of tuberculous granuloma and accumulate in the macrophage layer surrounding the caseum.

To further investigate the progress of the BTZ-043 penetration, MALDI MSI was performed on additional sections from IL-13^{tg} mice sacrificed 0.5, 2, 4 and 8 h post-dose with a pixel size of 30 x 30 µm. To account for the impact of biological variation, MALDI MSI was performed on sections that contained similar granuloma, i.e. granuloma with a clear internal structure, featuring a central caseum surrounded by a macrophage layer. In the post-measurement HE stains of each section given in Figure 19 A-D, the caseum of the granuloma is visible in a dark violet. The surrounding macrophage layer is visible in light pink.

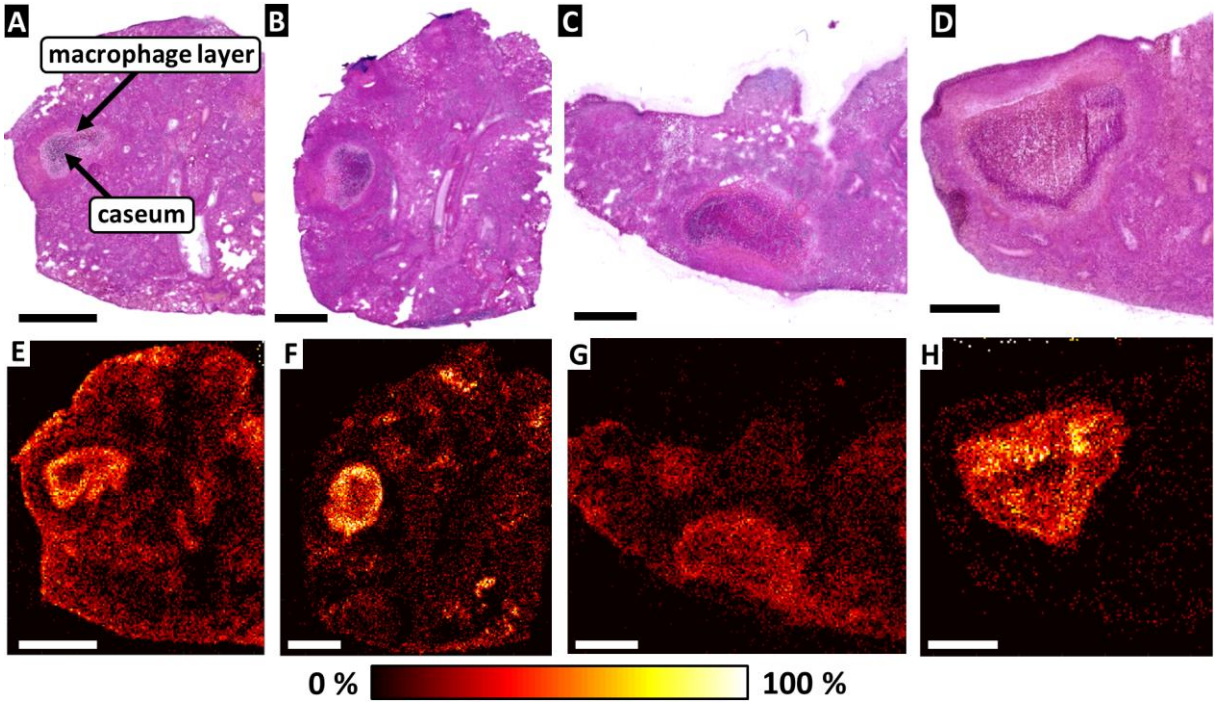

Figure 19. MALDI MSI of BTZ-043 0.5, 2, 4 and 8 h post dose with a pixel size of 30 x 30 µm and a mass range of m/z 420-550. **A-D)** Post-measurement HE stains of the imaged sections showing that all granuloma investigated in this timeline posess a central caseum surrounded by a layer of macrophages. Time points are A = 0.5 h, B = 2 h, C = 4 h and D = 8 h. **E-H)** Corresponding ion images of BTZ-043 $[M+H]^+$, $C_{17}H_{17}F_3N_3O_5S^+$, m/z 432.08355. **E)** 0.5 h post-dose, RMSE 0.55 ppm (11014 spectra), raster size 175 x 160 pixel **F)** 2 h post-dose, RMSE 0.49 ppm (11380 spectra), raster size 210 x 242 pixel. **G)** 4 h post-dose, RMSE 0.17 ppm (5690 spectra),raster size 160 x 175 pixel. H) 8 h post-dose, RMSE 0.63 ppm (4460 spectra), raster size 175 x 165 pixel. Scale bars = 1 mm

Half an hour after receiving the final dose, BTZ-043 has already accumulated in the macrophage layer surrounding the granuloma with a lower abundance in the caseum. Outside the granuloma, BTZ-043 shows a homogenous distribution as expected for orally administered drugs, Figure 19 E. After 2 h, the distribution of BTZ-043 has not changed substantially and still shows a high abundance in the macrophage layer followed by a low abundance in the caseum, Figure 19 F. Four hours post-dose,

BTZ-043 is still evenly distributed in the tissue surrounding granuloma but shows similar abundances in both the macrophage layer and the central caseum, Figure 19 G. Eight hours post-dose the abundance and signal coverage outside the granuloma has significantly dropped while in the granuloma area BTZ-043 is still detected with a similar abundance in both the caseum and the cellular layer, Figure 19 H. These findings indicate that BTZ-043 is able to penetrate into the caseum of tuberculous granuloma thus reaching the most important point of action of anti-TB drugs, despite the overall decreasing concentration in the tissue.

Summary and Conclusion

CFU reduction and dose ranging showed that BTZ-043 has a higher efficacy than INH in TB infected BALB/c mice. Pharmacokinetic data suggest that the AUC is mainly responsible for the efficacy of BTZ-043 and not the C_{max}. In IL-13^{tg} mice, the efficacy of BTZ-043 is comparable to that of current first and second line anti-TB drugs. ZN stainings of mice treated with BTZ-043 show that the drug causes a loss of acid fastness in Mtb likely due the loss of the mycolic acid layer. This may make Mtb more susceptible to other drug compounds and therapy approaches, when used in combination with other drug compounds which would otherwise struggle to reach past the mycolic acid layer. LC-MS/MS of sections showed the irradiation has no influence on the drug concentration and that 8 h post dose the BTZ-043 concentration is still several hundred times above the plasma MIC. High resolution MALDI MSI in conjunction with histochemical methods shows an accumulation of BTZ-043 in the macrophage layers of the granuloma. Investigation of further post-dose time points reveals that BTZ-043 is able to penetrate into the caseum of tuberculous granuloma thus reaching the main point of action for anti-TB drugs. Considering that the BTZ-043 efficacy likely depends on the AUC, the fact that BTZ-043 remains detectable inside the granuloma longer than in the surrounding area may also mean an increased efficacy inside the granuloma. By showing that novel BTZ-043 is able to penetrate into tuberculous granuloma, the developed MALDI MSI workflow has shown its capability to assist in the development of novel anti-TB drugs and integrate into the drug development pipeline and operate in conjunction with established complementary analytical techniques.

4 Conclusion and Outlook

The main scientific advancement of this work was the development of a high resolution MALDI MSI workflow and its establishment as a versatile analytical platform to investigate the *in vivo* distribution of pharmaceutical compounds. The developed workflow was then to be used to investigate the penetration behavior of anti-TB drug compounds into pulmonary granuloma of IL-13^{tg} mice which mimic human TB pathology. The ultimate goal was to integrate MALDI MSI into the development pipeline of anti-TB drugs to accelerate drug screening and development and to improve the predictive power of pre-clinical trials. The publications included in this work form a common theme leading towards this very goal.

The first publication of this work reports upon the development of the MALDI MS imaging workflow and shows its capability to image the distribution of current anti-TB drugs at therapeutic concentration in small histological structures in uninfected BALB/c murine lung with high spatial resolution and mass accuracy. The second publication continues with the importance of mass accuracy in MALDI MS imaging on complex biological samples and reports lists of matrix clusters generated on tissue by eleven common MALDI matrices which can be used as references for mass calibration. In the third publication, the techniques and procedures reported in the first and second publication are applied on TB infected lung tissue of IL-13^{tg} mice to investigate the penetration of current anti-TB drugs into necrotic pulmonary granuloma using the highest reported spatial resolution reported so far for MS imaging of anti-TB drugs and a newly developed data analysis tool to visualize the drug penetration. Apart from confirming the abilities of the workflow on real infected samples, this publications demonstrates the suitability of the IL-13^{tg} mouse model for pre-clinical drug testing. This point is explored further in a publication by our cooperation partner Dr. Kerstin Walter using MALDI MSI data from our laboratory. The manuscript for a fourth publication of this dissertation uses the groundwork laid by the first three publications to combine techniques commonly used in drug development such as CFU reduction, PK studies and LC-MS of tissue with MALDI MSI to facilitate the integration of the developed workflow into the development pipeline of the novel anti-Tuberculosis drug BTZ-043.

The results of this dissertation show that the developed MALDI MS imaging workflow, by using it within the framework of the German Center for Infection research to investigate the penetration behavior of current and novel anti-TB drugs, is indeed capable to evaluate the *in vivo* efficacy of anti-TB drugs. In order to support efforts towards ending the TB pandemic, the developed workflow must now be used routinely as part of the regular drug screening and the development process.

In this regard, possible avenues for further using the developed workflow are using it to investigate the penetration behavior of additional new anti-TB drug compounds currently under development such as sutezolid, delamanid or bedaquiline. Other possibilities would be to investigate the penetration behavior of anti-TB drugs in combination with compounds that alter the inflammatory response to TB infection, i.e. compounds that can alter the histology of the formed granuloma, such as kinase inhibitors like doramapimod. Lastly, it is also possible to employ the developed methods to investigate drug penetration in other granulatomous infections such as leprosy, histoplamosis; or in cancer therapy to investigate the penetration of anti-cancer drugs into tumors.

5 Scientific publications and manuscripts

5.1 First publication - Integrating High-Resolution MALDI MSI into the Development Pipeline of Anti-Tuberculosis Drugs

Integrating High-Resolution MALDI Imaging into the Development Pipeline of Anti-Tuberculosis Drugs

Axel Treu,[‖] Julia Kokesch-Himmelreich,[‖] Kerstin Walter, Christoph Hölscher, and Andreas Römpp*

Cite This: *J. Am. Soc. Mass Spectrom.* 2020, 31, 2277−2286 Read Online

ACCESS | Metrics & More | Article Recommendations | Supporting Information

ABSTRACT: Successful treatment of tuberculosis (TB) requires antibiotics to reach their intended point of action, i.e., necrotizing granulomas in the lung. MALDI mass spectrometry imaging (MSI) is able to visualize the distribution of antibiotics in tissue, but resolving the small histological structures in mice, which are most commonly used in preclinical trials, requires high spatial resolution. We developed a MALDI MSI method to image antibiotics in the mouse lung with high mass resolution (240k @ m/z 200 fwhm) and high spatial resolution (10 μm pixel size). A crucial step was to develop a cryosectioning protocol that retains the distribution of water-soluble drugs in small and fragile murine lung lobes without inflation or embedding. Choice and application of matrices were optimized to detect human-equivalent drug concentrations in tissue, and measurement parameters were optimized to detect multiple drugs in a single tissue section. We succeeded in visualizing the distribution of all current first-line anti-TB drugs (pyrazinamide, rifampicin, ethambutol, isoniazid) and the second-line drugs moxifloxacin and clofazimine. Four of these compounds were imaged for the first time in the mouse lung. Accurate mass identification was confirmed by on-tissue MS/MS. Evaluation of fragmentation pathways revealed the structure of the double-protonated molecular ion of pyrazinamide. Clofazimine was imaged for the first time with 10 μm pixel size revealing clofazimine accumulation in lipid deposits around airways. In summary, we developed a platform to resolve the detailed histology in the murine lung and to reliably detect a range of anti-TB drugs at human-equivalent doses. Our workflow is currently being employed in preclinical mouse studies to evaluate the efficacy of novel anti-TB drugs.

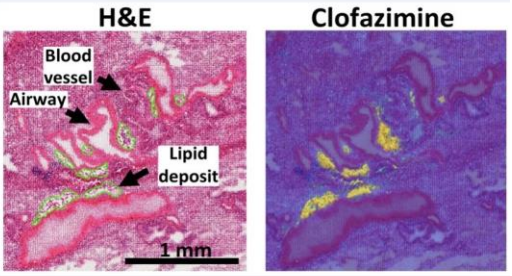

KEYWORDS: *MALDI imaging, tuberculosis, drugs, sample preparation, high-resolution*

INTRODUCTION

Mass spectrometry imaging (MSI) has evolved in the past two decades into a versatile and highly specific tool for studying the spatial distribution of analytes in biological samples. It has gained widespread acceptance as an imaging application that links molecular with histological information.[1−3] Apart from numerous applications, e.g., in pathology,[4] plant research,[5] and microbiology,[6] MALDI MSI has been extensively used to analyze the distribution of drug compounds.[7,8] In comparison to classic autoradiography, MALDI MSI does not require radioactive labeling, as analytes are identified based on their m/z ratio, which allows the simultaneous detection and identification of multiple drug compounds and their metabolites in a single measurement. MALDI imaging has been used to evaluate the drug distribution in studies on HIV,[9] malaria,[10] and cancer.[11] The reliable detection of drugs in the complex background of tissue samples requires the application of either tandem mass spectrometry approaches or high-mass-resolution techniques. On the other hand, resolving the small histological structures in mice, the most prominent animal model for drug development, requires high spatial resolution. In a previous study we have demonstrated the first combination of these approaches for drug compound imaging on the example of imatinib imaged at a pixel size of 10 μm in the mouse kidney.[12] More recent examples of drug compound imaging with high spatial resolution include salmeterol with a pixel size of 10 μm in rat lung tissue[13] and ezogabine with 5 μm pixel size in rat tissue.[14]

In order to perform this high-spatial-resolution imaging of drugs, the *in vivo* drug distribution must be retained throughout the whole sample preparation process to enable a meaningful correlation of the measured drug distribution with histological features. This presents a challenge, especially for water-soluble drug compounds, which are easily delocalized during sample sectioning or mounting steps. Retaining the distribution of water-soluble compounds during sectioning of less rigid, malleable tissue such as the murine lung is very demanding. Previous MALDI imaging studies on the mouse and macaque lung obtained cryosections from lung lobes

Received: June 17, 2020
Revised: September 15, 2020
Accepted: September 23, 2020
Published: September 23, 2020

Journal of the American Society for Mass Spectrometry pubs.acs.org/jasms Research Article

inflated with inflation media based on aqueous formalin,[15] gelatin,[16] or agarose.[17] However, lung inflation may be unsuitable for imaging of water-soluble compounds as the aqueous media employed in this technique could potentially dissolve the targeted compounds from the tissue. Therefore, sectioning of lung tissue for imaging of water-soluble compounds should be performed without lung inflation. This approach has already been used for the murine lung.[18]

The choice and application procedure of the matrix has a major effect on the successful detection of drug compounds at low, i.e., therapeutic, tissue concentrations. The matrix best suited for an imaging experiment is determined by the chemical properties of the targeted analyte(s). In general, polar analytes require polar matrices. Faced with the vast number of available matrix substances, choosing the right matrix can be a very tedious process. Several studies concerning the detection of small molecules with different matrices, which can be used as an orientation, have been published so far.[7,19−21] The matrix application method must balance the need for analyte extraction and small matrix crystal size.[22] Sufficient analyte extraction is required to detect drugs at low tissue concentrations while small matrix crystal sizes are required for high-spatial-resolution MALDI imaging. In summary, sample preparation for imaging of (water-soluble) drug compounds is challenging, especially for easily malleable lung tissue, which is of particular importance in tuberculosis (TB) research.

Tuberculosis is a common infectious disease caused by *Mycobacterium tuberculosis* (*Mtb*) which affects the respiratory tract. It is listed by the WHO as the most likely cause of death from an infectious disease before HIV/AIDS, malaria, or leprosy.[23] TB treatment relies on antibiotic combination therapies, which can last for more than a year.[24] The long duration of TB drug regimens, in combination with the overall robustness of *Mtb*, fosters the development of drug-resistant Mtb strains ultimately creating a demand for novel anti-TB drugs. The pathology of TB is characterized by the formation of centrally necrotizing granulomas in the lung. These granulomas carry a high bacterial burden and represent the main structural point of action for drugs. These anti-TB drugs must penetrate the necrotic core of TB granulomas in sufficient concentrations to eliminate local mycobacteria in order to treat the disease.

As part of the preclinical evaluation of novel TB antibiotics, MALDI MSI can visualize this penetration of drug compounds into TB granulomas. It allows the assessment of this important aspect of a drug's *in vivo* effectiveness against *Mtb* infection, and therefore, this technology has the potential to accelerate drug development in TB research. Accordingly, MALDI MSI has already been used in this capacity to visualize the distribution of antibiotics in the lung tissue of TB patients.[25] The majority of MALDI imaging studies on the distribution of anti-TB drugs in the lung have been conducted using tissue of *Mtb*-infected rabbits.[26−32] However, the animal model most commonly used for the preclinical evaluation of novel TB antibiotics drug trials is (inbred) mice.[33,34] Mice offer the possibility of producing humanized models through genetic engineering[35] and overall low cost and maintenance requirements. Two studies have been published so far regarding the distribution of anti-TB drugs in the lung of infected mice.[18,36] In these and all other previous studies, MALDI imaging of anti-TB drugs was conducted with a pixel size ≥50 μm and a mass resolution well below 100k full width at half-maximum (fwhm) (60k @ m/z 400). A detailed investigation of biological structures in mice, however, requires high spatial resolution to enable a direct correlation between the measured drug distribution and small histological features, such as airways, blood vessels, or different regions of TB granulomas. Consequently, the integration of MALDI imaging into existing screening and development pipelines of anti-TB drugs requires the development of methods that are able to visualize these compounds in mouse lung tissue with higher spatial and mass resolution than previously reported.

In this study, we developed an AP-MALDI imaging method to map the distribution of anti-TB drugs in mouse lung tissue, with a pixel size down to 10 μm at human-equivalent drug doses. Cryosectioning of fragile and easily deformed murine lung lobes was optimized without any embedding or inflation media to minimize the delocalization of water-soluble drug compounds. Choice and application of the matrix were adapted to both minimize the delocalization of water-soluble compounds and to enable the imaging of drugs at the employed doses. Measurements feature a mass resolution of R = 240 k fwhm @ m/z 200 with a mass accuracy <1.5 ppm (root-mean-square deviation: RMSE) enabling accurate mass identification, which was verified by on-tissue MS/MS. In addition, a combination of selected ion monitoring (SIM) and full scan (FS) was used in the same measurement to boost detection sensitivity for low-dose drugs and detect additional drugs and other compound classes, such as lipids, simultaneously, which serves to reduce the consumption of scarce sample material in mouse model studies. Utilizing this workflow, we imaged the distribution of various anti-TB drugs, including all four current first line drugs (pyrazinamide, ethambutol, rifampicin, isoniazid) and the second line drugs moxifloxacin and clofazimine, in mouse lung tissue.

EXPERIMENTAL SECTION

Matrices and Consumables. Consumables and matrices were purchased from Sigma-Aldrich (Taufkirchen, Munich, Germany). Solvents (HPLC grade) were purchased from Carl Roth (Karlsruhe, Germany). Adhesive glass slides (Menzel Gläser, SuperFrost) were purchased from VWR (Darmstadt, Germany).

Animal Experiments. Animal experiments were conducted at the Research Center Borstel (Borstel, Germany). Female BALB/c mice received a daily combination of either pyrazinamide (PZA) 150 mg/kg, clofazimine (CFZ) 25 mg/kg, and rifampicin (RIF) 10 mg/kg or isoniazid (INH) 25 mg/kg, ethambutol (EMB) 100 mg/kg, and moxifloxacin (MXF) 100 mg/kg via oral gavage for 5 days. Mice were euthanized 1 h after the last administration; organs were harvested, flash frozen in liquid N_2, and stored at −80 °C. All animal experimentation was in accordance with the German Animal Protection Law and was approved by the Animal Research Ethics Board of the Ministry of Energy, Agriculture, the Environment, Nature, and Digitalization (reference number: 3-1/15).

Cryosectioning. Serial lung sections (12−14 μm) were cut from unembedded whole lung lobes at −40 °C (chamber and sample holder temperature) using a Leica CM3050 S cryostat (Leica Microsystems, Wetzlar, Germany). Lung lobes were solid frozen before sectioning started, and sections were mounted on adhesive glass slides (Menzel Gläser, SuperFrost) which were previously cooled down inside the cryostat chamber. A small area of the cooled slide was warmed from

https://dx.doi.org/10.1021/jasms.0c00235
J. Am. Soc. Mass Spectrom. 2020, 31, 2277−2286

Journal of the American Society for Mass Spectrometry pubs.acs.org/jasms Research Article

behind by finger contact to ensure proper sample mounting. Sections were stored at −80 °C prior to matrix application. Images were taken using a Keyence VHX-5000 digital microscope (Keyence Corporation, Osaka, Japan). See the Supporting Information for details on the hematoxylin and eosin (H&E) staining protocol and Figure S1, for premeasurement optical images.

Matrix Application. Sections were transferred directly from the −80 °C storage into a desiccator for 10 min prior to matrix application. Matrices were applied using a semiautomatic pneumatic sprayer system built in-house. Matrix solutions were prepared as follows: 9-aminoacridine (9AA) 5 mg/mL in MeOH/H_2O (3:1, (v/v)), α-cyano-4-hydroxycinnamic acid (CHCA) 10 mg/mL in acetone/H_2O (1:1, (v:v)), 2,6-dihydroxyacetophenone (DHAP) 10 mg/mL or 2,5-dihydroxybenzoic acid (DHB) 20 mg/mL in MeOH/H_2O (1:1, (v/v)), 4-nitroanilline (pNA) 5 mg/mL in acetone/H_2O (3:1 (v/v)). Matrix solutions used for the positive ion mode were acidified with 0.1% (v/v) trifluoroacetic acid.

MS Acquisition. MALDI MSI measurements were performed using the atmospheric pressure MALDI imaging source AP-SMALDI10 (TransMIT GmbH, Gießen, Germany) equipped with a λ = 337 nm N_2 laser operating at a repetition rate of 60 Hz, coupled to a hybrid orbital trapping mass spectrometer QExactive HF (Thermo Fisher Scientific GmbH, Bremen, Germany).[37,38] Measurements were carried out in positive and negative ion mode with one scanning event and 30 shots per pixel at a mass resolution of 240 k @ m/z 200 fwhm. Single pixel mass spectra indicating the actual mass resolution of the drug signals are included in the Supporting Information, Figure S2. Measurements featured either single or alternating acquisition modes. Pixel sizes ranged between 10 and 40 μm. Further information on the measurement setup for alternating acquisition modes can be found in the Supporting Information, Figure S3. All measurements were performed with a fixed C-trap injection time of 500 ms. Online mass calibration was performed using matrix clusters of a known sum formula for <1 ppm mass accuracy. A list of the matrix ions used for online mass calibration is given in the Supporting Information (Table S1). MS/MS was performed with an isolation window of ±0.2 m/z of the selected precursor ion using higher energy collision-induced dissociation (HCD). Negative controls for all drugs covered in this study are included in the Supporting Information, Figure S4.

Data Analysis. Conversion of proprietary Thermo "RAW" files to imzML was performed using the Java-based open access software "jimzMLConverter" (Version 2.0.4).[39] The RAW files containing alternating acquisition modes were converted into individual imzML files for each modality. Further information on data processing and imzML conversion is contained in the Supporting Information (Figure S3). Ion images, RGB composite images, and optical overlays were generated in MSiReader Version 1.0.[40] The image generation parameters were as follows: bin width ±2.5 ppm, smoothing function linear 2 without normalization if not specifically mentioned. Mass to charge ratios of known compounds are given as the calculated exact mass. Lipid species were tentatively identified by matching measured masses with the online data bank Lipid Maps using a search window of ±0.005 m/z. Mass deviations across imaging data sets are given as the RMSE of the Δm values in ppm of each individual spectrum containing the targeted ion within a ± 2.5 ppm window of the exact mass.

RESULTS AND DISCUSSION

Cryosectioning. Performing MALDI MSI of drugs in any kind of biological tissue puts an emphasis on sample preparation and handling to maintain the *in vivo* distribution present in the section. Measures must be taken to minimize the delocalization of these compounds, especially when investigating the distribution of water-soluble drugs, as is the case in this study. Analyte delocalization, if not controlled, will impede a meaningful correlation between the drug distribution measured and its point of action, for example, TB lesions, rendering the data useless.

Initial experiments in this study were performed with the standard sample preparation workflow, which has been used for many compounds in our lab. This included CMC embedding and cryosectioning at −20 °C. These conditions provided good tissue integrity, Figure 1A, and also provided a

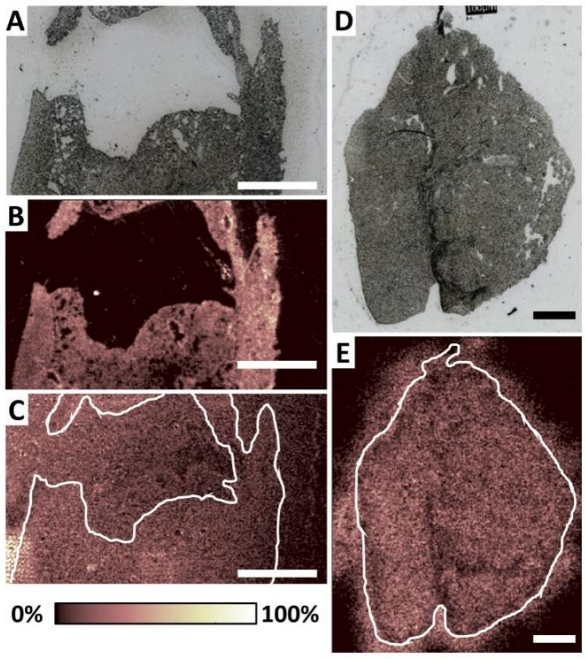

Figure 1. Distribution of clofazimine, pyrazinamide, and ethambutol in mouse lung tissue. Scale bar = 1 mm. (A) Optical image. (B) Distribution of CFZ $[M + H]^+$ m/z 473.129 42 detected in the same section as PZA, which retains a tissue-congruent distribution as a result of its water insolubility. (C) Distribution of PZA $[M + 2H]^{+\bullet}$ m/z 125.058 36 showing substantial out-of-tissue delocalization. The edge of the tissue is highlighted in white; pixel size 15 × 15 μm, 270 × 160 pixels m/z 110−800. (D) Optical image. (E) Distribution of EMB $[M + H]^+$ m/z 205.191 05. Out-of-tissue delocalization leading to a drug coffee stain around the section. The edge of the of the tissue is highlighted in white; pixel size 30 × 30 μm, 205 × 260 pixels, m/z 110−800.

tissue-matching distribution for CFZ, as shown in Figure 1B. However, PZA, which is contained in the same section as CFZ, was detected both on and off tissue in the entire measurement field of view (Figure 1C). These findings are most likely the result of the different water solubility of both drugs. CFZ, which is not water-soluble,[41] retains its distribution, while the water-soluble (150 mg/mL)[41] PZA is apparently washed out of the tissue. We believe that the aqueous CMC medium is partly

https://dx.doi.org/10.1021/jasms.0c00235
J. Am. Soc. Mass Spectrom. 2020, 31, 2277−2286

Journal of the American Society for Mass Spectrometry pubs.acs.org/jasms Research Article

responsible for this effect. The influence of the matrix application process can be excluded because the same procedure was successfully used in later experiments, see the Data Acquisition section (e.g., Figure 3F). In order to minimize the sample exposure to aqueous solutions and subsequent delocalization of water-soluble drugs, we performed cryosectioning on unembedded and uninflated lung lobes. The sectioning of mouse lung tissue samples without embedding proved very challenging due to their small size and easily deformed shape. In our experience, sectioning is best performed at the lowest possible temperature, i.e., above the temperature at which the sample turns too brittle for sectioning, to maintain the histology of the lung during sectioning and prevent any tissue shearing. In this study, we performed sectioning of mouse lung tissue at −40 °C (cryostat chamber and sample holder temperature). Using these conditions, we were able to obtain intact lung sections without CMC embedding (Figure 1D). Figure 1E shows the distribution of EMB measured in this section. The moderately water-soluble (7.58 mg/mL)[41] EMB is detected in a distinctive "halo" around the section, showing that the drug has leaked out of the tissue onto the glass slide. This is believed to be the result of the section thawing completely during thaw mounting, allowing the tissue fluid to leak out of the tissue edges like a "coffee stain". Therefore, we decided to mount sections on slides which were cooled down to the sectioning temperature inside the cryostat chamber to circumvent this problem. These precooled slides were briefly warmed up from the back by finger contact in the tissue mounting area to allow only the necessary minimum heat required for a proper section mounting. We found that this approach works best for section thicknesses of 10−16 μm. Thicker sections are too brittle and inflexible at the used sectioning temperature, resulting in cracks, creases, and irregular section surfaces. Thinner sections will thaw completely during mounting, leading to the artifacts discussed above.

Utilizing these optimized sample preparation conditions and sectioning protocol, we were able to detect various drug compounds in mouse lung tissue at high spatial resolution with minimized drug delocalization, as shown in the following.

Choice of Matrix and Application Method. Acquiring suitable tissue sections is the critical first step toward the MALDI imaging of drug compounds. Choosing a suitable matrix, however, is equally important. The detection of drugs administered at therapeutic concentrations requires high sensitivity. In the case of a 10 μm thick tissue section of an animal dosed intravenously with 10 mg/kg of a drug compound, a MALDI MSI instrument with a 5 μm laser focus diameter must therefore be able to detect roughly 2 fg of the drug in a very complex biological matrix (assuming a tissue density of 1 g/cm^3 and a homogeneous drug distribution). In the case of drugs administered via oral gavage in human-equivalent drug doses, as is the case in this study, the in-tissue drug concentration is even lower due to reduced bioavailability.[42] The ionization efficiency of the drug and the choice and application of the matrix are crucial in this concentration range for the measurement quality and detectability of the target drug. The appropriate method of matrix application is determined by the experimental goals. High spatial resolution requires small homogeneous crystals, while the detection of low-concentration drugs requires efficient analyte extraction. Solvent-free "dry" techniques, such as sublimation,[43] deliver homogeneous matrix layers with small crystal sizes, while "wet" solvent-based applications provide superior analyte extraction at the cost of larger crystal sizes and possible analyte diffusion in the case of an application that is too "wet."[22,44] Balancing the need for both small crystal sizes and analyte extraction, matrices were applied in this study using a pneumatic sprayer and carefully optimized spray parameters. Solvent systems required for a pneumatic spray matrix application must be able to dissolve the matrix substance and the target drug to ensure efficient analyte extraction. Determining the matrix best suited for the detection of a target drug can be a very tedious process when faced with the vast number of matrix substances available. Applying a calibration standard on blank tissue to compare analyte responses with different matrices (or solvent systems) yields quantitative information on the aptitude of matrix substances for the detection of the drug in question. An example of this approach is given in Figure 2. The RIF

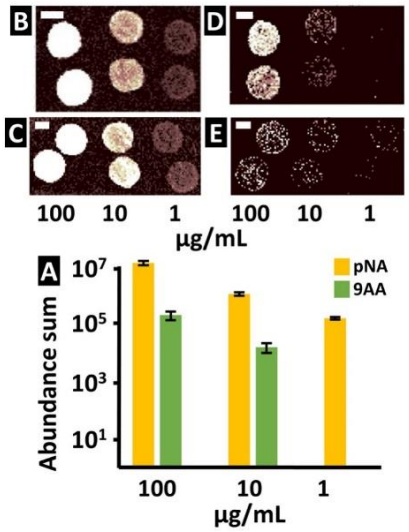

Figure 2. Detection of an RIF standard spotted onto pig liver control tissue using pNA and 9AA matrix. Scale bar = 1 mm. (A) Bar chart showing the signal abundance sum of RIF $[M - H]^-$ m/z 821.397 84 for each concentration achieved with pNA and 9AA matrix. Error bars indicate the standard deviation (n = 4). The pNA delivers a 100 times higher average intensity for RIF $[M - H]^-$. Ion images of RIF $[M - H]^-$ using (B, C) pNA and (D, E) 9AA.

solutions (0.5 μL of 100, 10, and 1 μg/mL) were applied on blank sections of the pig liver and measured using pNA and 9AA as matrices. The resulting signal intensity is a combination of the chosen matrix substance and the solvent system used to apply it. To achieve a homogeneous matrix coating, the 9AA and pNA matrix were sprayed using different solvent systems, as indicated in the Experimental Section. The 9AA matrix was sprayed from MeOH/H_2O (3:1(v:v)) while pNA was sprayed from acetone/H_2O (3:1(v:v)). The solvent system used for 9AA has a higher extraction efficiency, as RIF is more readily soluble in MeOH than in acetone. However, in comparison to 9AA, the pNA matrix delivers 100 times higher RIF signal abundances on average (Figure 2A) and enables the detection of all concentration levels applied (Figure 2B,C). Regarding 9AA, the 1 μg/mL RIF standard is not detectable (Figure 2D,E). In this study, imaging experiments on lung sections of RIF dosed animals were therefore conducted using pNA matrix. As shown in the Supporting Information (Figures S5−

https://dx.doi.org/10.1021/jasms.0c00235
J. Am. Soc. Mass Spectrom. 2020, 31, 2277−2286

Journal of the American Society for Mass Spectrometry pubs.acs.org/jasms Research Article

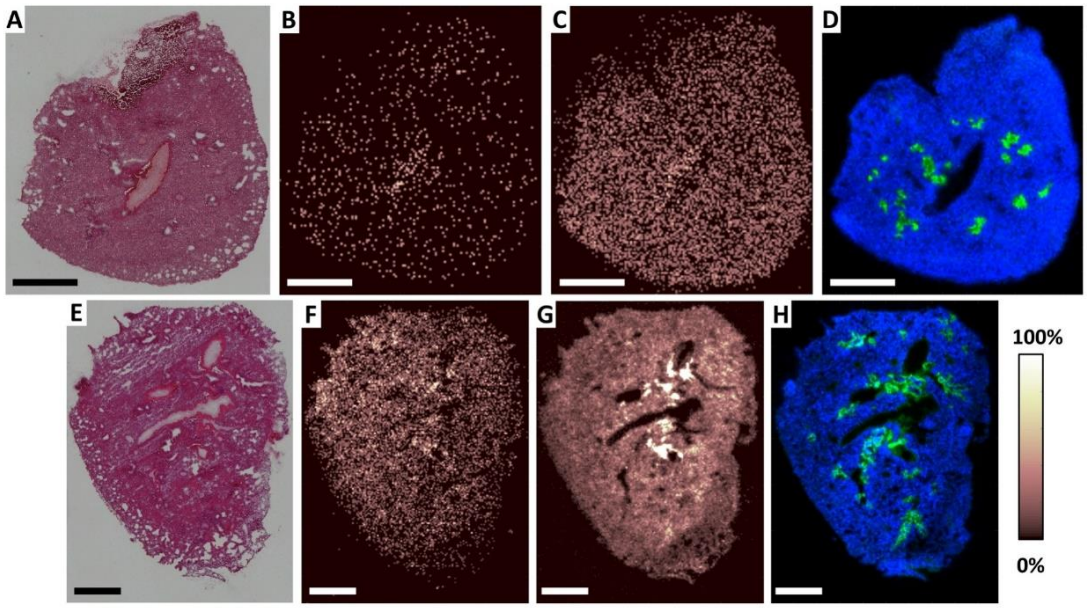

Figure 3. Detection of TB antibiotics in mouse lung sections from the same animal using alternating scan modes. Scale bar = 1 mm. (A) H & E stain. (B) RIF $[M - H]^-$ m/z 821.397 84 detected in FS m/z 400−900 with a tissue signal coverage of 6%. (C) RIF detected in SIM m/z 810−830 with a tissue signal coverage of 31%. (D) Overlay of PI(38:4) $[M - H]^-$ m/z 885.549 85 in green and PS(38:4) $[M - H]^-$ m/z 810.529 05 in blue; pixel size 30 × 30, 290 × 160 pixels, m/z 400−900 and 810−830. (E) H&E stain. (F) PZA $[M + 2H]^{+\bullet}$ m/z 125.058 36 detected in SIM m/z 120−140. (G) CFZ $[M + H]^+$ m/z 473.129 42 detected in FS m/z 450−900. (H) RGB overlay of PC(36:4) $[M + K]^+$ m/z 820.525 31 in green, and PC(30:0) $[M + K]^+$ m/z 744.494 01 in blue; pixel size 30 × 30 μm, 330 × 220 pixels; m/z 120−140 and 450−900. Both measurements were performed with two alternating acquisition modes with a raster step size of 15 × 30 μm resulting in an image pixel size of 30 × 30 μm; see the Supporting Information, Figure S3, for more details on measurement setup and data processing. Single pixel mass spectra displaying the actual mass resolution of the drug signals for the measurements shown in this figure are given in the Supporting Information, Figure S2.

S7), matrix optimization experiments were carried out for all drugs covered in this study. In summary, DHB was best suited to detect PZA; CHCA enabled the detection of INH, and 2,6-DHAP was best suited for the detection of MXF. The readily ionizable compounds CFZ and EMB could be detected with either DHB, 2,6-DHAP, or CHCA. Anti-TB drugs are always administered as a cocktail to avoid the development of resistances. To reduce the number of required measurements and sample material, the choice of matrix must balance the need for both sensitivity required to detect drugs at human-equivalent doses and versatility to enable the detection of multiple compounds in a single tissue section.

Data Acquisition. Adapting the choice and application of the matrix may not be sufficient to ensure a reliable detection of the target drug compound. MS imaging of RIF using pNA matrix in negative ion mode with a pixel size of 30 × 30 μm (145 × 160 pixels) is shown as an example in Figure 3B. In the employed full scan acquisition window from m/z 400 to 900, RIF $[M - H]^-$ is detected at m/z 821.397 84 with a pixel coverage of only 4%, and an average intensity of 1.62 E2 with an RMSE of 1.42 ppm (945 spectra). The FS acquisition evidently cannot enable a reliable detection of RIF. Low dosed drugs, such as RIF in this case, or drugs that exhibit poor ionization efficiency (see below) may require an additional degree of sensitivity for detection, which FS is not able to provide. In LC-ESI-MS applications performed on quadrupole Orbitrap instruments, selected ion monitoring (SIM) acquisition was reported to achieve a distinct increase in sensitivity in comparison to regular FS acquisition.[45] Accordingly, SIM acquisition can also be used to increase the sensitivity of drug detection in MALDI MSI at the cost of losing the ability to correlate the measured drug distribution with histological features through the codetection of lipids. The result of using SIM acquisition with a window of m/z 810−830 is shown in Figure 3C. RIF is detected with a significantly increased pixel coverage of 31%, and an average intensity of 1.2 E2 with an RMSE of 1.43 ppm (7394 spectra). Single pixel mass spectra displaying the actual mass resolution of the drug signals for the measurements shown in Figure 3 are given in the Supporting Information, Figure S2. Furthermore, RIF was detected here with a smaller pixel size (30 μm) than reported previously.[36] In this particular example, both data sets (Figure 3B,C) were acquired from the same tissue section in one measurement (alternating scan events, see the Supporting Information, Figure S3), allowing a direct comparison of the SIM and FS mode. The information about phospholipid distribution provided by the FS data set is given in Figure 3D. The distribution of the two deprotonated phospholipid species PI(38:4) in green and PS(38:4) in blue represent blood vessels and the lung parenchyma, respectively. Combining SIM and FS acquisition in one measurement, therefore, enables both a more sensitive detection of RIF and the codetection of phospholipids.

The advantage of the combined SIM/FS approach is even more evident in the following example on a lung section from the same animal, where mass ranges do not overlap (Figure 3F−H). PZA, which is a low-mass drug (123 u) exhibiting poor ionization efficiency, was imaged in positive ion mode (DHB matrix) using SIM acquisition (m/z 120−140), at a pixel size of 30 × 30 μm (Figure 3F). In combination with the

https://dx.doi.org/10.1021/jasms.0c00235
J. Am. Soc. Mass Spectrom. 2020, 31, 2277−2286

Journal of the American Society for Mass Spectrometry pubs.acs.org/jasms Research Article

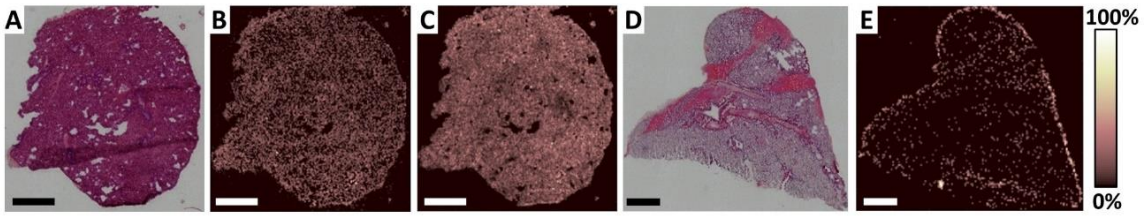

Figure 4. MALDI Imaging of moxifloxacin, ethambutol, and isoniazid in mouse lung sections from the same animal; scale bar = 1 mm, images normalized to the total ion current. (A) H&E stain. (B) Distribution of moxifloxacin $[M + H]^+$ m/z 402.182 36 and (C) ethambutol $[M + H]^+$ m/z 205.191 05, which is detected in the same measurement; pixel size 25 × 25 μm, 170 × 175 pixels, m/z 202−405. (D) H&E stain. (E) Distribution of isoniazid detected in SIM (m/z 120−180) $[M + H]^+$ m/z 138.066 18; pixel size 40 × 40 μm, 155 × 140 pixels, m/z 120−180 and 400−900. The measurement was performed with two alternating acquisition modes with a raster step size of 20 × 40 μm resulting in an image pixel size of 40 × 40 μm; see the Supporting Information, Figure S3, for more details on measurement setup and data processing. Single pixel mass spectra displaying the actual mass resolution of the drug signals for the measurements shown in this figure are given in the Supporting Information, Figure S2.

SIM window, a positive mode FS window (m/z 450−900, Figure 3G,H) was employed in the same measurement to detect CFZ and phospholipids to enable a correlation of the drug distribution with sample histology while minimizing sample consumption. Providing an overview of the sample histology, Figure 3H shows the distribution of the potassiated molecular ions of PC(36:4) in green highlighting blood vessel walls and PC(30:0) in blue showing the lung parenchyma. PZA, which was imaged with a smaller pixel size (30 μm) than previously reported (75 μm),[18,25] is detected solely as a double protonated, single charged ion species at m/z 125.058 36 with an RMSE of 0.61 ppm (9781 spectra; Figure 3F). This double protonated molecular ion of PZA was reported previously as the even electron ion "$[M + 2H]^{+}$".[18,25,32] However, the ion must be an odd electron ion to enable a double protonation while maintaining a single positive charge. Furthermore, an even electron "$[M + 2H]^{+}$" ion of PZA with a nominal mass of 125 u would violate the nitrogen rule. Therefore, the molecular ion of PZA should be correctly denoted as a radical cation $[M + 2H]^{+\bullet}$. PZA is distributed evenly throughout the section with no abundance hot spots or signs of the leaking out of tissue mentioned above. However, PZA is also detected in tissue-free areas, such as airway holes, which indicates that the drug has delocalized into these areas during sample preparation, which is a result of the compound's high water solubility (see the Cryosectioning section). CFZ, which was imaged here for the first time in mouse lung tissue, was detected at m/z 473.129 42 $[M + H]^+$ with an RMSE of 0.51 ppm (23 839 spectra; Figure 3G). In contrast to the other drug compounds covered in this study, CFZ is not evenly distributed throughout the tissue section and shows an accumulation around major airways. An exact assignment of these abundance hot spots to histological features is, however, not possible at the pixel size of 30 μm employed in this measurement and will be discussed below (see the Spatial Resolution section). Considering the molecular complexity of biological samples, using high mass resolution is required to differentiate between the multitudes of isobaric ion species, which can have vastly different distributions. The molecular ion of CFZ, for instance, is codetected with an accompanying DHB matrix-related peak at m/z 473.134 20 (Δm = 4.78 mu), which shows a high signal abundance around the tissue section. A mass resolution of at least 96 k fwhm is needed to separate both signals and prevent a superposition of the measured drug distribution (Supporting Information, Figure S8). Furthermore, CFZ is detected not only as the protonated molecular ion but also as the radical cation species $[M + 2H]^{+\bullet}$ at m/z 474.137 25 (RMSE 0.60 ppm, 20 960 spectra). A mass resolution of at least 100 k fwhm is required to distinguish the CFZ $[M + 2H]^{+\bullet}$ ion and its isotopic pattern from isobaric peaks of the CFZ $[M + H]^+$ isotopic pattern (Supporting Information, Figure S9). This additional ion species can be used to further confirm the identity of CFZ.

The examples discussed so far originated from a mouse study based on a drug cocktail consisting of PZA, CFZ, and RIF. In addition, we analyzed lung tissue of mice that were dosed with a mixture of INH, EMB, and MXF originating from a second study. In these samples, we could image all three of these drugs for the first time in mouse lung tissue. MXF and EMB were imaged in one measurement (mass range m/z 202−405, 30 × 30 μm pixel size) using 2,6-DHAP matrix in positive mode, which reduces the number of tissue sections and the measurement time required. Both drugs show a homogeneous distribution with no visible hot spots. MXF, which is a water-insoluble compound[41] and, thus, not affected by leaking out of the tissue, is detected at m/z 402.182 36 $[M + H]^+$ with an RMSE of 0.75 ppm (17 462 spectra; Figure 4B). EMB is detected at m/z 205.191 05 $[M + H]^+$ with an RMSE of 0.26 (24 912 spectra; Figure 4C). Although the drug is moderately water-soluble (see the Cryosectioning section), it has retained a distribution congruent to the tissue section and is not detected inside tissue-free areas, such as bronchiole holes. The edges of the EMB distribution at the borders between tissue and tissue-free areas appear sharp, which indicates that the drug has retained its native distribution and is unaffected by tissue leaking. The readily water-soluble (140 mg/mL)[41] INH was imaged in a different section to the one used for EMB and MXF with combined SIM/FS acquisition at a pixel size of 40 × 40 μm using CHCA matrix in positive ion mode. INH is detected in SIM (m/z 120−180) at m/z 138.066 18 $[M + H]^+$ with an RMSE of 0.49 (1330 spectra) in the lung parenchyma and shows a higher abundance around the tissue edges, which is a result of the compounds' high water solubility (see the Cryosectioning section). Single pixel mass spectra displaying the actual mass resolution of the drug signals for the measurements shown in Figure 4 are given in the Supporting Information, Figure S2.

MS/MS-Based Signal Identification. High mass resolution and accurate mass measurements are both necessary for a tentative identification of targeted drug compounds directly from imaging data. Taking into account the vast number of isobaric ion species found in biological samples, however, on-

https://dx.doi.org/10.1021/jasms.0c00235
J. Am. Soc. Mass Spectrom. 2020, 31, 2277−2286

Journal of the American Society for Mass Spectrometry pubs.acs.org/jasms Research Article

tissue MS/MS provides a tool to achieve more reliable signal identification than accurate mass identification alone. The comparison of MS/MS spectra performed on tissue with those of standard substances can often bring confirmation toward an unambiguous identification of the target drug(s). As an example, fragments and abundance ratios of the PZA $[M + 2H]^{+\bullet}$ MS/MS spectrum recorded from tissue (Figure 5A) match that of the calibration standard (Figure 5B), which

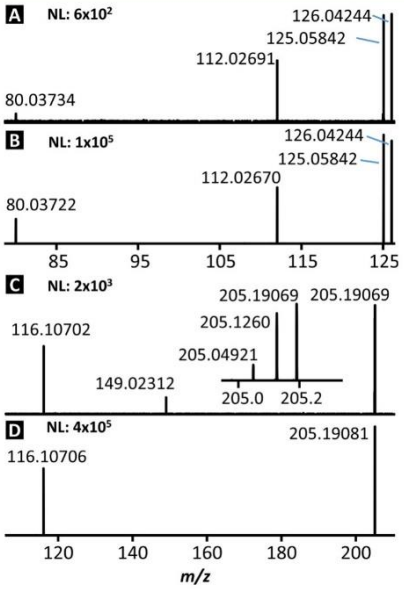

Figure 5. Comparison of MS/MS spectra recorded from tissue with standard substances; NL = normalized level. (A) PZA on tissue, (B) PZA standard, (C) EMB on tissue, and (D) EMB standard.

confirms the signal detected on the tissue as PZA. However, a structural proposal for the double protonated radical cation, which is able to explain the MS/MS spectrum, has not been reported to date. We propose that following the HCD activation, the main reaction of PZA $[M + 2H]^{+\bullet}$ is the conversion into pyrazinoic acid ($C_5H_4N_2O_2$) $[M + 2H]^{+\bullet}$ at m/z 126.042 via an NH_3/H_2O exchange. The loss of formic acid from pyrazinoic acid or formamide from the $[M + 2H]^{+\bullet}$ ions yields m/z 80.037. Subsequently, m/z 112.026 is formed via the attachment of molecular oxygen to m/z 80.037, which is a known reaction of radical cation species.[46] The presence of m/z 80.037 in the MS/MS spectrum indicates that the CO double bond of the formamide moiety is still intact in the $[M + 2H]^{+\bullet}$ ion of PZA. In comparison to neutral PZA, the degree of unsaturation of the PZA $[M + 2H]^{+\bullet}$ is reduced by one unit. Consequently, the ion contains one π bond less, most likely resulting in a dearomatized pyrazine ring (Figure 6). This proposed mechanism and structure can explain the observed fragmentation behavior and would confirm the structure of the postulated $[M + 2H]^{+\bullet}$ molecular ion of PZA.

In some cases, matching on-tissue MS/MS with that of a standard is more complex. Due to the large number of different compounds in biological samples, fragment spectra recorded from tissue often contain fragments of peaks coisolated with the molecular ion of the drug in the precursor selection window. This occurs even in the case of a narrow selection window of ±0.2 m/z, which was employed in this study. EMB

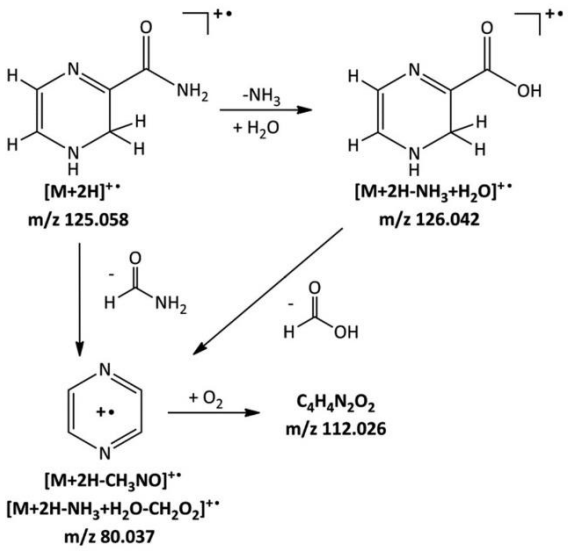

Figure 6. CID fragmentation path of PZA based on a structural proposal for the $[M + 2H]^{+\bullet}$ molecular ion.

serves as a good example to demonstrate the effect of isolating accompanying peaks in the precursor selection window due to the simplicity of its MS/MS spectrum. The on-tissue MS/MS spectrum of EMB (Figure 5C) shows an additional fragment at m/z 149.023 which is not present in the MS/MS spectrum of the standard substance (Figure 5D). Comparing the mass of the corresponding neutral loss to a plausible sum formula reveals that m/z 149.023 is not a fragment ion of EMB $[M + H]^+$ but rather of m/z 205.049, an accompanying peak of EMB coisolated in the precursor selection window, which is visible in the enlargement in Figure 5C.

The fragmentation mechanism of EMB is discussed in the Supporting Information (Figure S10). The comparison of on-tissue MS/MS of RIF and CFZ with the standard substance spectra and the fragmentation mechanism for both drugs is given in the Supporting Information (Figures S11 and S12). On-tissue MS/MS spectra could not be recorded for either MXF or INH due to very low precursor ion intensities. Negative controls for all drugs covered in this study are included in the Supporting Information, Figure S4.

Spatial Resolution. When studying the distribution of drugs in tissue, high spatial resolution allows a clear differentiation of tissue types or compartments reached by a drug. High spatial resolution is needed, especially when mapping the distribution of drugs whose efficacy depends on their ability to penetrate into small and highly stratified anatomical structures. In Figure 7, we visualized the distribution of CFZ and EMB in sections of the mouse lung with high mass resolution and a pixel size of 10 μm, which is the highest reported spatial resolution MALDI imaging of drug compounds in mouse lung tissue so far. The distributions of both drug compounds were measured in similar biological structures for comparison (H&E stain shown in Figure 7A,C; premeasurement optical images and monochrome ion images can be found in the Supporting Information, Figure S13). Apart from the lung parenchyma, both measured areas contain bronchioles that are lined by epithelial cells as well as blood vessels (structures highlighted in the H&E stain).

https://dx.doi.org/10.1021/jasms.0c00235
J. Am. Soc. Mass Spectrom. 2020, 31, 2277−2286

Journal of the American Society for Mass Spectrometry pubs.acs.org/jasms Research Article

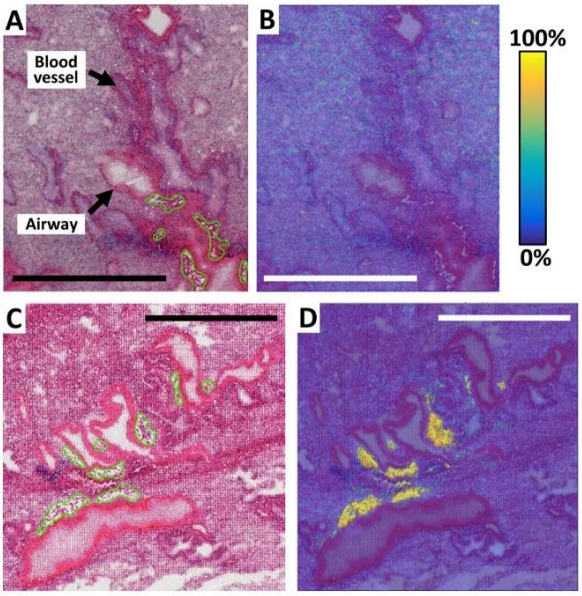

Figure 7. Distribution of EMB and CFZ measured at 10 μm pixel size. Scale bar = 1 mm. (A) H&E stain of the measurement field of view showing blood vessels and bronchioles. Adipocyte clusters are highlighted in green. (B) Overlay of the H&E stain with the ion signal of EMB $[M + H]^+$ m/z 205.191 05; 10 × 10 μm, 220 × 225 pixels, m/z 130−900. (C) H&E stain of the measurement field of view containing blood vessels and bronchioles. Adipocyte clusters are highlighted in green. (D) Overlay of the H&E stain with the ion signal of CFZ $[M + H]^+$ m/z 473.129 42; 10 × 10 μm, 150 × 180 pixels, m/z 120−480. Single pixel mass spectra displaying the actual mass resolution of the drug signals for the measurements shown in this figure are given in the Supporting Information, Figure S2.

Using DHB as a matrix, EMB was detected in positive ion mode at m/z 205.191 05 $[M + H]^+$ with an RMSE of 1.05 ppm (25 922 spectra; Figure 7B). EMB is distributed evenly in both lung parenchyma and blood vessels. While CFZ is detected in the same tissue areas as EMB, its distribution is heterogeneous.

The protonated molecular ion of CFZ (m/z 473.129 42, DHB matrix) was detected with an RMSE of 0.66 ppm (42 168 spectra) in the 10 μm pixels of this measurement. As has already been mentioned in the discussion of Figure 3G, the distribution of CFZ is not homogeneous across all histological structures present in the sample and shows abundance hot spots, which are located around airways. At the employed high spatial resolution, the overlay of the CFZ distribution with the H&E stain (Figure 7D) reveals that all detected abundance hot spots colocalize exactly with seemingly tissue-free areas (areas highlighted in green in the H&E stains). These tissue-free areas are adipocyte clusters,[47] i.e., lipid deposits which have been reported to form in mice lung following drug treatment. CFZ is a highly lipophilic drug with a long biological half-life of up to 70 days. As a result, CFZ can accumulate in organs with a high lipid content such as the lungs, liver, spleen, and kidney.[48] Accordingly, the observed abundance hot spots are most likely the result of CFZ accumulating in these particularly lipid-rich tissue regions and not an experimental artifact. Due to a lower lipophilicity, EMB does not accumulate in lipid deposits, as can be seen in Figure 7A,B. These results show that MALDI imaging of drug compounds with 10 μm pixel size and high mass resolution in mouse lung sections not only is feasible but also enables the colocalization of small histological features and drug distribution which would not be possible at a lower spatial resolution. Single pixel mass spectra displaying the actual mass resolution of the drug signals for the measurements shown in Figure 7 are given in the Supporting Information, Figure S2.

CONCLUSION

In this study, we present an AP MALDI MSI workflow, which can resolve the distribution of anti-TB drugs in substructures of mouse lung tissue. In order to integrate this workflow into the preclinical development and evaluation of novel anti-TB drugs, it was specifically designed to analyze the distribution of relevant drug compounds at concentrations used in current preclinical animal experiments. Our measurements are based on high mass resolution and mass accuracy, allowing a reliable identification of the imaged compounds. On-tissue MS/MS confirmed the identity of tentatively identified drug compounds. The suggestion of fragmentation pathways led to the first structural proposal for the previously unconfirmed double protonated molecular ion of PZA. Our workflow was established for all first-line anti-TB drugs, of which only PZA and RIF had been imaged previously in mouse lungs, albeit with both lower mass and spatial resolution. In addition, the distribution of the second-line antibiotics MXF and CFZ was imaged for the first time in the mouse lung. We showed that alternating full scan and selected ion monitoring acquisition in one measurement allows a more sensitive drug detection, while maintaining the ability to detect additional drugs and biomolecules, such as phospholipids, to correlate the drug distribution with sample histology. Furthermore, this approach serves to minimize the use of scarce TB sample material as more information can be obtained from a single tissue section. It was possible at 10 μm pixel size to assign CFZ accumulation to lipid deposits located around airways, demonstrating the ability of our workflow to locate drug compounds in small histological structures. Within the development of novel anti-TB drugs, the abilities of the presented workflow make it a powerful tool to localize compounds in substructures of TB granulomas. Accordingly, we currently apply our workflow within the framework of the German Center for Infection Research (DZIF) to advance drug studies using a preclinical TB animal model that develops a human-like pathology.

ASSOCIATED CONTENT

Supporting Information

The Supporting Information is available free of charge at https://pubs.acs.org/doi/10.1021/jasms.0c00235.

Additional figures including optical images, single pixel mass spectra, schematics, negative control measurements, INH standard detection, PZA standard detection, a comparison of the detection of MXF, CFZ, and EMB using DHB, CHCA, and DHAP matrix, spectra showing molecular ion peaks, high mass resolution differentiation, fragmentation pathways, on-tissue MS/MS spectra, and monochrome ion images (PDF)

AUTHOR INFORMATION

Corresponding Author

Andreas Römpp − *Chair of Bioanalytical Sciences and Food Analysis, University of Bayreuth, 95447 Bayreuth, Germany; German Center for Infection Research (DZIF), 38124*

https://dx.doi.org/10.1021/jasms.0c00235
J. Am. Soc. Mass Spectrom. 2020, 31, 2277−2286

Journal of the American Society for Mass Spectrometry pubs.acs.org/jasms Research Article

Braunschweig, Germany; orcid.org/0000-0001-8384-9250; Phone: +49 921 553662; Email: andreas.roempp@uni-bayreuth.de

Authors

Axel Treu − *Chair of Bioanalytical Sciences and Food Analysis, University of Bayreuth, 95447 Bayreuth, Germany; German Center for Infection Research (DZIF), 38124 Braunschweig, Germany*

Julia Kokesch-Himmelreich − *Chair of Bioanalytical Sciences and Food Analysis, University of Bayreuth, 95447 Bayreuth, Germany; German Center for Infection Research (DZIF), 38124 Braunschweig, Germany*

Kerstin Walter − *Infection Immunology, Leibniz Lung Center, Research Center Borstel, 23845 Borstel, Germany; German Center for Infection Research (DZIF), 38124 Braunschweig, Germany*

Christoph Hölscher − *Infection Immunology, Leibniz Lung Center, Research Center Borstel, 23845 Borstel, Germany; German Center for Infection Research (DZIF), 38124 Braunschweig, Germany*

Complete contact information is available at: https://pubs.acs.org/10.1021/jasms.0c00235

Author Contributions

‖A.T. and J.K.-H. contributed equally.

Notes

The authors declare no competing financial interest.

A.T. (axel.treu@uni-bayreuth.de), J.K.-H. (julia.kokesch-himmelreich@uni-bayreuth.de), K.W. (kwalter@fz-borstel.de), and C.H. (choelscher@fz-borstel.de)

■ ACKNOWLEDGMENTS

Financial support from the German Center for Infection Research (DZIF) TTU 02.806 and TTU 02.810, the Deutsche Forschungsgemeinschaft (DFG) INST 91/373-1-FUGG, and the TechnologieAllianzOberfranken (TAO) is gratefully acknowledged. Furthermore, the authors would like to thank Alan Race for his support in RAW file conversion and Janick Peter and Monique Geidies for their support in sample preparation.

■ REFERENCES

(1) McDonnell, L. A.; Heeren, R. M. A. Imaging mass spectrometry. *Mass Spectrom. Rev.* **2007**, *26* (4), 606−643.

(2) Spengler, B. Mass spectrometry imaging of biomolecular information. *Anal. Chem.* **2015**, *87* (1), 64−82.

(3) Römpp, A.; Spengler, B. Mass spectrometry imaging with high resolution in mass and space. *Histochem. Cell Biol.* **2013**, *139* (6), 759−783.

(4) Aichler, M.; Walch, A. MALDI Imaging mass spectrometry: current frontiers and perspectives in pathology research and practice. *Lab. Invest.* **2015**, *95* (4), 422−31.

(5) Bhandari, D.; Wang, Q.; Friedt, W.; Spengler, B.; Gottwald, S.; Römpp, A. High resolution mass spectrometry imaging of plant tissues: Towards a plant metabolome atlas. *Analyst* **2015**, *140* (22), 7696−7709.

(6) Dunham, S. J. B.; Ellis, J. F.; Li, B.; Sweedler, J. V. Mass Spectrometry Imaging of Complex Microbial Communities. *Acc. Chem. Res.* **2017**, *50* (1), 96−104.

(7) Prideaux, B.; Stoeckli, M. Mass spectrometry imaging for drug distribution studies. *J. Proteomics* **2012**, *75* (16), 4999−5013.

(8) Schulz, S.; Becker, M.; Groseclose, M. R.; Schadt, S.; Hopf, C. Advanced MALDI mass spectrometry imaging in pharmaceutical research and drug development. *Curr. Opin. Biotechnol.* **2019**, *55*, 51−59.

(9) Seneviratne, H. K.; Hendrix, C. W.; Fuchs, E. J.; Bumpus, N. N. MALDI Mass Spectrometry Imaging Reveals Heterogeneous Distribution of Tenofovir and Tenofovir Diphosphate in Colorectal Tissue of Subjects Receiving a Tenofovir-Containing Enema. *J. Pharmacol. Exp. Ther.* **2018**, *367* (1), 40−48.

(10) Grove, K. J.; Hoque, S.; Rudewicz, P. J. Investigation of amodiaquine localization in liver lobules using matrix-assisted laser desorption/ionization imaging mass spectrometry. *Rapid Commun. Mass Spectrom.* **2019**, *33* (3), 252−258.

(11) Giordano, S.; Zucchetti, M.; Decio, A.; Cesca, M.; Fuso Nerini, I.; Maiezza, M.; Ferrari, M.; Licandro, S. A.; Frapolli, R.; Giavazzi, R.; Maurizio, D.; Davoli, E.; Morosi, L. Heterogeneity of paclitaxel distribution in different tumor models assessed by MALDI mass spectrometry imaging. *Sci. Rep.* **2016**, *6*, 39284.

(12) Römpp, A.; Guenther, S.; Takats, Z.; Spengler, B. Mass spectrometry imaging with high resolution in mass and space (HR2MSI) for reliable investigation of drug compound distributions on the cellular level. *Anal. Bioanal. Chem.* **2011**, *401* (1), 65−73.

(13) Bäckström, E.; Hamm, G.; Nilsson, A.; Fihn, B.-M.; Strittmatter, N.; Andrén, P.; Goodwin, R. J. A.; Fridén, M. Uncovering the regional localization of inhaled salmeterol retention in the lung. *Drug Delivery* **2018**, *25* (1), 838−845.

(14) Groseclose, M. R.; Castellino, S. An Investigation into Retigabine (Ezogabine) Associated Dyspigmentation in Rat Eyes by MALDI Imaging Mass Spectrometry. *Chem. Res. Toxicol.* **2019**, *32* (2), 294−303.

(15) Carter, C. L.; Jones, J. W.; Farese, A. M.; MacVittie, T. J.; Kane, M. A. Inflation-Fixation Method for Lipidomic Mapping of Lung Biopsies by Matrix Assisted Laser Desorption/Ionization-Mass Spectrometry Imaging. *Anal. Chem.* **2016**, *88* (9), 4788−4794.

(16) Scott, A. J.; Chandler, C. E.; Ellis, S. R.; Heeren, R. M. A.; Ernst, R. K. Maintenance of Deep Lung Architecture and Automated Airway Segmentation for 3D Mass Spectrometry Imaging. *Sci. Rep.* **2019**, *9* (1), 20160.

(17) Berry, K. A. Z.; Li, B.; Reynolds, S. D.; Barkley, R. M.; Gijón, M. A.; Hankin, J. A.; Henson, P. M.; Murphy, R. C. MALDI imaging MS of phospholipids in the mouse lung. *J. Lipid Res.* **2011**, *52* (8), 1551−1560.

(18) Irwin, S. M.; Prideaux, B.; Lyon, E. R.; Zimmerman, M. D.; Brooks, E. J.; Schrupp, C. A.; Chen, C.; Reichlen, M. J.; Asay, B. C.; Voskuil, M. I.; Nuermberger, E. L.; Andries, K.; Lyons, M. A.; Dartois, V.; Lenaerts, A. J. Bedaquiline and Pyrazinamide Treatment Responses Are Affected by Pulmonary Lesion Heterogeneity in Mycobacterium tuberculosis Infected C3HeB/FeJ Mice. *ACS Infect. Dis.* **2016**, *2* (4), 251−267.

(19) Sun, N.; Walch, A. Qualitative and quantitative mass spectrometry imaging of drugs and metabolites in tissue at therapeutic levels. *Histochem. Cell Biol.* **2013**, *140* (2), 93−104.

(20) Sturtevant, D.; Lee, Y. J.; Chapman, K. D. Matrix assisted laser desorption/ionization-mass spectrometry imaging (MALDI-MSI) for direct visualization of plant metabolites in situ. *Curr. Opin. Biotechnol.* **2016**, *37*, 53−60.

(21) Goodwin, R. J. A. Sample preparation for mass spectrometry imaging: small mistakes can lead to big consequences. *J. Proteomics* **2012**, *75* (16), 4893−4911.

(22) Gemperline, E.; Rawson, S.; Li, L. Optimization and Comparison of Multiple MALDI Matrix Application Methods for Small Molecule Mass Spectrometric Imaging. *Anal. Chem.* **2014**, *86* (20), 10030−10035.

(23) WHO. *Tuberculosis global facts sheet*; WHO, 2019.

(24) WHO. *WHO treatment guidelines for drug resistant tuberculosis*; WHO, 2016.

(25) Prideaux, B.; Via, L. E.; Zimmerman, M. D.; Eum, S.; Sarathy, J.; O'Brien, P.; Chen, C.; Kaya, F.; Weiner, D. M.; Chen, P.-Y.; Song, T.; Lee, M.; Shim, T. S.; Cho, J. S.; Kim, W.; Cho, S. N.; Olivier, K. N.; Barry, C. E., III; Dartois, V. The association between sterilizing

activity and drug distribution into tuberculosis lesions. *Nat. Med.* **2015**, *21*, 1223.
(26) Blanc, L.; Daudelin, I. B.; Podell, B. K.; Chen, P.-Y.; Zimmerman, M.; Martinot, A. J.; Savic, R. M.; Prideaux, B.; Dartois, V. High-resolution mapping of fluoroquinolones in TB rabbit lesions reveals specific distribution in immune cell types. *eLife* **2018**, *7*, No. e41115.
(27) Manier, M. L.; Reyzer, M. L.; Goh, A.; Dartois, V.; Via, L. E.; Barry, C. E.; Caprioli, R. M. Reagent Precoated Targets for Rapid In-Tissue Derivatization of the Anti-Tuberculosis Drug Isoniazid Followed by MALDI Imaging Mass Spectrometry. *J. Am. Soc. Mass Spectrom.* **2011**, *22* (8), 1409−1419.
(28) Prideaux, B.; Dartois, V.; Staab, D.; Weiner, D. M.; Goh, A.; Via, L. E.; Barry, C. E.; Stoeckli, M. High-Sensitivity MALDI-MRM-MS Imaging of Moxifloxacin Distribution in Tuberculosis-Infected Rabbit Lungs and Granulomatous Lesions. *Anal. Chem.* **2011**, *83* (6), 2112−2118.
(29) Prideaux, B.; ElNaggar, M. S.; Zimmerman, M.; Wiseman, J. M.; Li, X.; Dartois, V. Mass spectrometry imaging of levofloxacin distribution in TB-infected pulmonary lesions by MALDI-MSI and continuous liquid microjunction surface sampling. *Int. J. Mass Spectrom.* **2015**, *377*, 699−708.
(30) Zimmerman, M.; Lestner, J.; Prideaux, B.; O'Brien, P.; Dias-Freedman, I.; Chen, C.; Dietzold, J.; Daudelin, I.; Kaya, F.; Blanc, L.; Chen, P.-Y.; Park, S.; Salgame, P.; Sarathy, J.; Dartois, V. Ethambutol Partitioning in Tuberculous Pulmonary Lesions Explains Its Clinical Efficacy. *Antimicrob. Agents Chemother.* **2017**, *61* (9), No. e00924-17.
(31) Blanc, L.; Lenaerts, A.; Dartois, V.; Prideaux, B. Visualization of Mycobacterial Biomarkers and Tuberculosis Drugs in Infected Tissue by MALDI-MS Imaging. *Anal. Chem.* **2018**, *90* (10), 6275−6282.
(32) Blanc, L.; Sarathy, J. P.; Alvarez Cabrera, N.; O'Brien, P.; Dias-Freedman, I.; Mina, M.; Sacchettini, J.; Savic, R. M.; Gengenbacher, M.; Podell, B. K.; Prideaux, B.; Ioerger, T.; Dick, T.; Dartois, V. Impact of immunopathology on the antituberculous activity of pyrazinamide. *J. Exp. Med.* **2018**, *215* (8), 1975−1986.
(33) Kim, W. Y.; Sharpless, N. E. Drug efficacy testing in mice. *Curr. Top. Microbiol. Immunol.* **2010**, *355*, 19−38.
(34) Ericsson, A. C.; Crim, M. J.; Franklin, C. L. A brief history of animal modeling. *Mo Med.* **2013**, *110* (3), 201−205.
(35) Zuberi, A.; Lutz, C. Mouse Models for Drug Discovery. Can. New Tools and Technology Improve Translational Power? *ILAR J.* **2016**, *57* (2), 178−185.
(36) DeMarco, V. P.; Ordonez, A. A.; Klunk, M.; Prideaux, B.; Wang, H.; Zhuo, Z.; Tonge, P. J.; Dannals, R. F.; Holt, D. P.; Lee, C. K.; Weinstein, E. A.; Dartois, V.; Dooley, K. E.; Jain, S. K. Determination of [11C]rifampin pharmacokinetics within Mycobacterium tuberculosis-infected mice by using dynamic positron emission tomography bioimaging. *Antimicrob. Agents Chemother.* **2015**, *59* (9), 5768−5774.
(37) Koestler, M.; Kirsch, D.; Hester, A.; Leisner, A.; Guenther, S.; Spengler, B. A high-resolution scanning microprobe matrix-assisted laser desorption/ionization ion source for imaging analysis on an ion trap/Fourier transform ion cyclotron resonance mass spectrometer. *Rapid Commun. Mass Spectrom.* **2008**, *22* (20), 3275−3285.
(38) Römpp, A.; Guenther, S.; Schober, Y.; Schulz, O.; Takats, Z.; Kummer, W.; Spengler, B. Histology by Mass Spectrometry: Label-Free Tissue Characterization Obtained from High-Accuracy Bioanalytical Imaging. *Angew. Chem., Int. Ed.* **2010**, *49* (22), 3834−3838.
(39) Race, A. M.; Styles, I. B.; Bunch, J. Inclusive sharing of mass spectrometry imaging data requires a converter for all. *J. Proteomics* **2012**, *75* (16), 5111−5112.
(40) Bokhart, M. T.; Nazari, M.; Garrard, K. P.; Muddiman, D. C. MSiReader v1.0: Evolving Open-Source Mass Spectrometry Imaging Software for Targeted and Untargeted Analyses. *J. Am. Soc. Mass Spectrom.* **2018**, *29* (1), 8−16.
(41) Wishart, D. S.; Feunang, Y. D.; Guo, A. C.; Lo, E. J.; Marcu, A.; Grant, J. R.; Sajed, T.; Johnson, D.; Li, C.; Sayeeda, Z.; Assempour, N.; Iynkkaran, I.; Liu, Y.; Maciejewski, A.; Gale, N.; Wilson, A.; Chin, L.; Cummings, R.; Le, D.; Pon, A.; Knox, C.; Wilson, M. DrugBank 5.0: a major update to the DrugBank database for 2018. *Nucleic Acids Res.* **2018**, *46* (D1), D1074−D1082.
(42) Lappin, G.; Rowland, M.; Garner, R. C. The use of isotopes in the determination of absolute bioavailability of drugs in humans. *Expert Opin. Drug Metab. Toxicol.* **2006**, *2* (3), 419−427.
(43) Hankin, J. A.; Barkley, R. M.; Murphy, R. C. Sublimation as a method of matrix application for mass spectrometric imaging. *J. Am. Soc. Mass Spectrom.* **2007**, *18* (9), 1646−1652.
(44) Buchberger, A. R.; DeLaney, K.; Johnson, J.; Li, L. Mass Spectrometry Imaging: A Review of Emerging Advancements and Future Insights. *Anal. Chem.* **2018**, *90* (1), 240−265.
(45) Kaufmann, A. Analytical performance of the various acquisition modes in Orbitrap MS and MS/MS. *J. Mass Spectrom.* **2018**, *53*, 725.
(46) Treu, A.; Rittner, M.; Kemken, D.; Schiebel, H.-M.; Spiteller, P.; Dülcks, T. Loss of atomic nitrogen from even-electron ions? A study on benzodiazepines. *J. Mass Spectrom.* **2015**, *50* (8), 978−986.
(47) Lam, A. P.; Gottardi, C. J. Fat in fibrosis. *Am. J. Respir. Crit. Care Med.* **2013**, *188* (10), 1268−1269.
(48) Bahuguna, A.; Rawat, D. S. An overview of new antitubercular drugs, drug candidates, and their targets. *Med. Res. Rev.* **2020**, *40* (1), 263−292.

https://dx.doi.org/10.1021/jasms.0c00235
J. Am. Soc. Mass Spectrom. 2020, 31, 2277−2286

Supporting Information

Integrating high resolution MALDI imaging into the development pipeline of anti-tuberculosis drugs

Axel Treu[a,c,x], Julia Kokesch-Himmelreich[a,c,x] , Kerstin Walter[b,c], Christoph Hölscher[b,c] and Andreas Römpp[a,c,*]

[a] Chair of Bioanalytical Sciences and Food Analysis, University of Bayreuth, Universitätsstraße 30, 95447 Bayreuth, Germany

[b] Infection Immunology, Leibniz Lung Center, Research Center Borstel, Parkallee 1-40, 23845 Borstel, Germany

[c] German Center for Infection Research (DZIF) , Inhoffenstraße 7, 38124 Braunschweig, Germany

[x] Authors contributed equally

[*] Correspondence to this author

Keywords: MALDI imaging, tuberculosis, drugs, sample preparation, high-resolution

E-Mail adresses:

axel.treu@uni-bayreuth.de

julia.kokesch-himmelreich@uni-bayreuth.de

andreas.roempp@uni-bayreuth.de

kwalter@fz-borstel.de

choelscher@fz-borstel.de

Address reprint requests to: Andreas Römpp, Universitaetsstrasse 30, 95447 Bayreuth, +49 921 553662, andreas.roempp@uni-bayreuth.de

Pre-measurement optical images

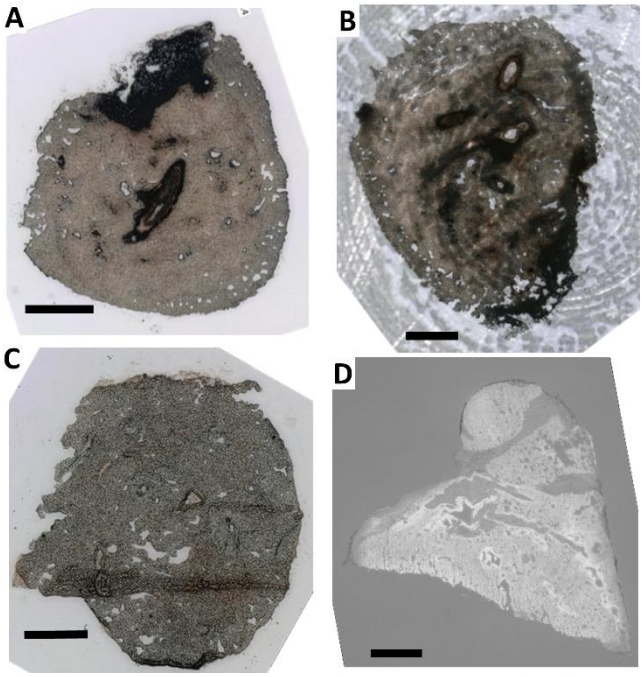

Figure S1. Pre-measurement optical images of mouse lung sections corresponding to: (A) Figure 3 A-D. (B) Figure 3 E-H. (C) Figure 4 A-C. (D) Figure 4 D-E. Scale bar = 1 mm.

H&E staining

Following MALDI MSI analysis, the matrix layer was washed off with MeOH. Rehydrated (2 min in 100 %, 70 %, 40 % EtOH then 100 % H_2O) samples were submerged in Mayers Hematoxylin Solution for 12 min followed by 10 min submersion in Na_2CO_3 (1 %) and rinsed with distilled water. Counterstaining was performed by 2-min submersion in 0.5 % acidified Eosin Y. Stained sections were conserved using Eukitt mounting medium and coverslips.

Single pixel mass spectra

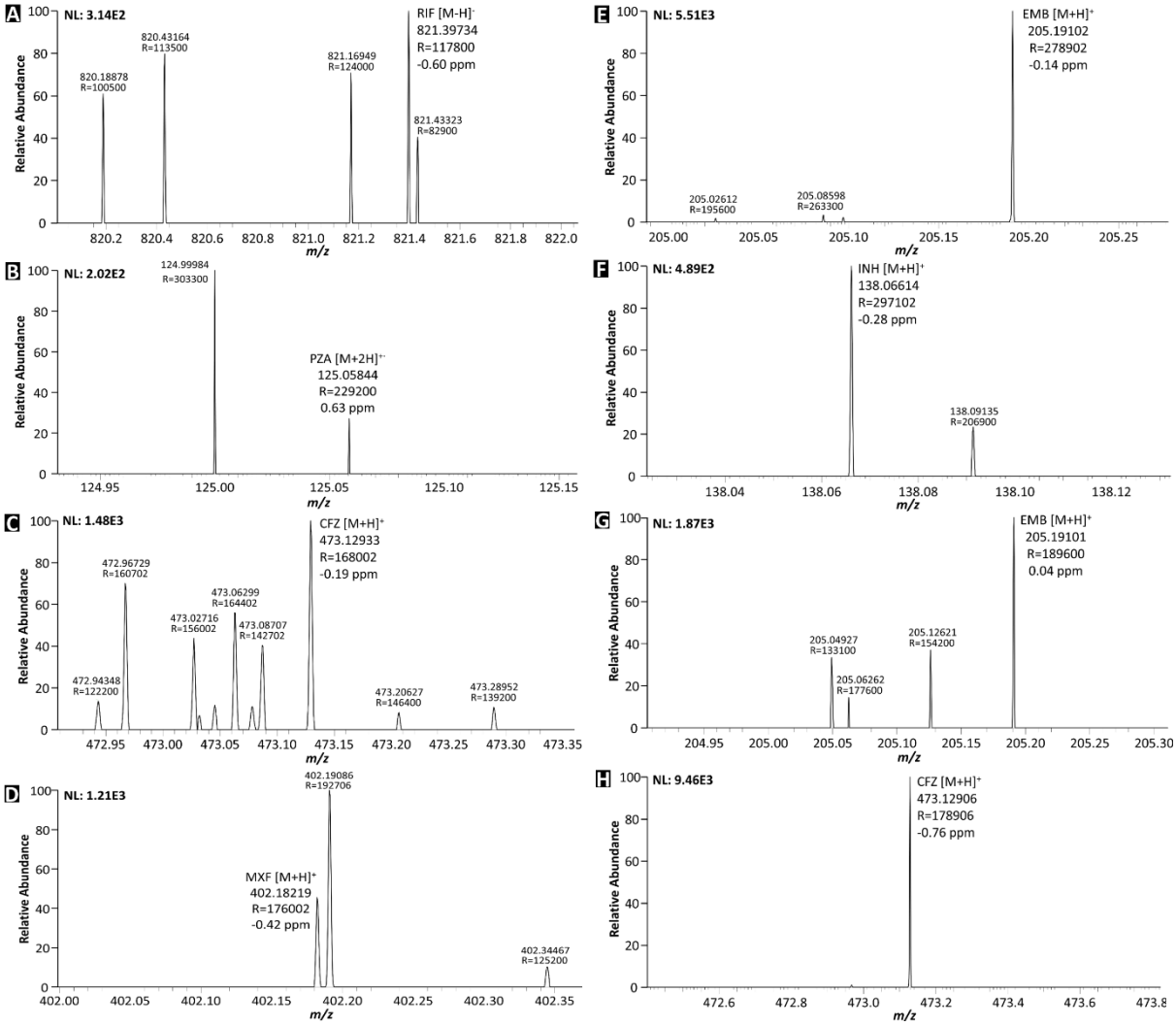

Figure S2. Single pixel mass spectra of the drugs shown in the Figure 3, 4 and 7. Included in the spectra is the achieved mass resolution (FWHM) as well as the mass deviation in ppm. A) RIF from Figure 3 B, C. B) PZA from Figure 3 F. C) CFZ from Figure 3 G. D) MXF from Figure 4 B. E) EMB from Figure 4 C. F) INH from Figure 4 D. G) EMB from Figure 7 B. H) CFZ from Figure 7 D.

Measurement setup and data processing

The measurements shown in Figures 2 and 3 were performed with alternating SIM/FS scan events. Ion images generated directly from such measurements will contain empty pixels. This can be prevented by converting "RAW" files into individual imzML files for each modality (see below). To enable this operation, the number of pixels in the *x* direction must be a common multiple of the number of employed acquisition modes (*n*) to ensure that pixels of the same modality are arranged in vertical lines (see below) and not in a chessboard pattern. To avoid rectangular shaped pixels in measurements with alternating SIM and FS acquisition, the pixel size in *x* direction is defined as *y/n*, with *y* as the pixel size in the *y* direction and *n* the number of acquisition modes employed.

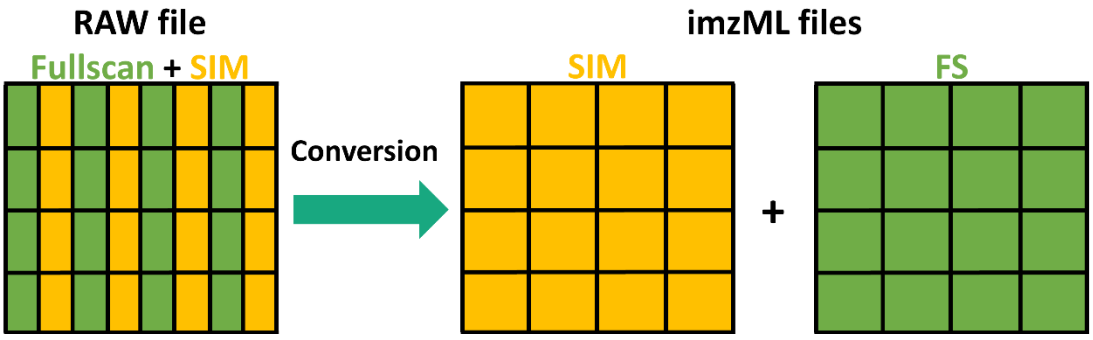

Figure S3. Schematic showing the conversion of a "RAW" file containing two alternating acquisition modes (SIM/FS) into two individual imzML files.

Matrix signals used for mass calibration

Online mass calibration was performed using the "lock mass" function of the QExactive HF™ orbital trapping mass spectrometer. Given below is an overview over the matrix ions used for online mass calibration in this study.

Table S1. Overview of the matrix ions used in online mass calibration.

Matrix	Exact mass	Composition	Sum formula
DHB	137.02332	M+H-H_2O	$C_7H_5O_3$
DHB	716.12461	5M+NH_4-4H_2O	$C_{35}H_{26}NO_{16}$
pNA (negative mode)	409.09020	3M-H-2H_2	$C_{18}H_{13}N_6O_6$
2,6-DHAP (positive mode)	228.96638	M+2K-H	$C_8H_7O_3K_2$
CHCA	146.06004	M+H-CO_2	C_9H_8NO
CHCA	666.02876	3M+Na+2K-2H	$C_{30}H_{19}N_3O_9NaK_2$

Negative controls

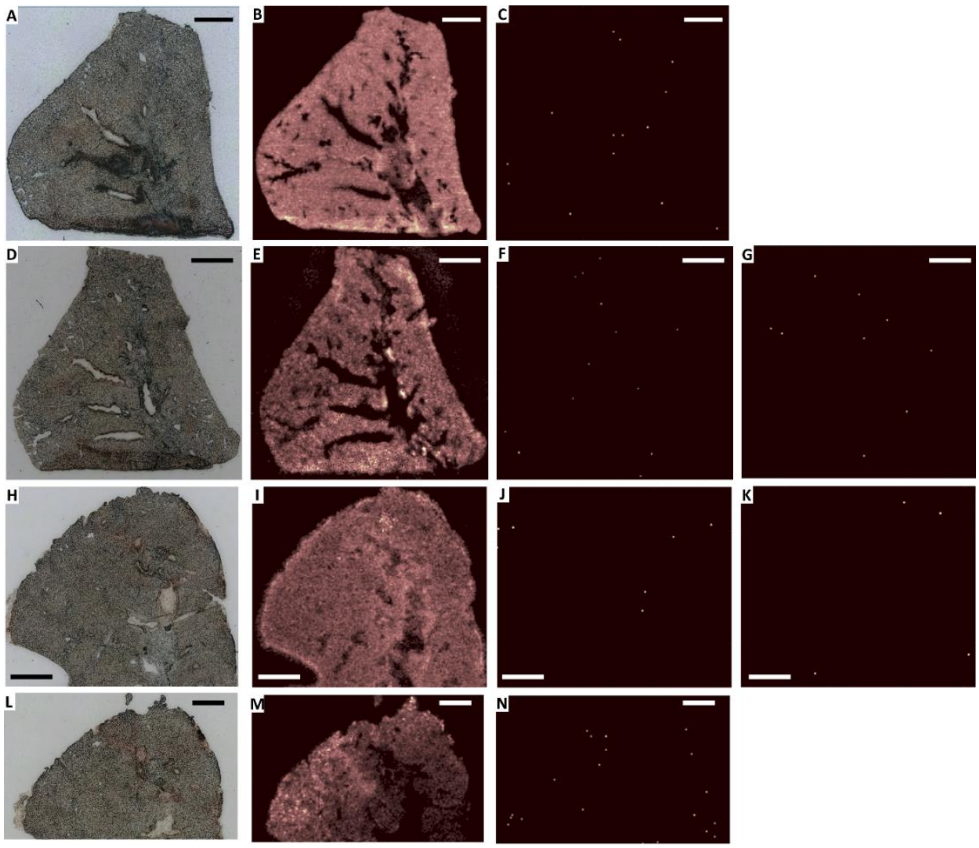

Figure S4. Negative control measurements for all drugs covered in this study. Negative controls for PZA, CFZ and RIF were conducted with sections from mice dosed with INH, EMB and MXF and vice versa. Measurements were conducted using the same matrices and measurement setup as was used in the main text. A) Optical image. B) Distribution of PS (38:4) $[M-H]^-$ *m/z* 810.52905. C) RIF $[M-H]^-$ *m/z* 821.39784; 30 x 30 µm, 180 x 180 Pixel, *m/z* 810 – 830. D) Optical image. E) Distribution of PC (30:0) $[M+K]^+$ *m/z* 772.52531. F) CFZ $[M+H]^+$ *m/z* 473.12942. G) PZA $[M+2H]^{+\cdot}$ *m/z* 125.05836; 30 x 30 µm, 194 x 191 Pixel, m/z 120 – 140 and 450 – 900, measurement was performed with two alternating acquisition modes with a raster step size of 15 x 30 µm resulting in an image pixel size of 30 x 30 µm. H) Optical image. I) Distribution of cholesterol $[M+H-H_2O]^+$ *m/z* 387.36214. J) MXF $[M+H]^+$ *m/z* 402.18236. K) EMB $[M+H]^+$ *m/z* 205.19105; 30 x 30 µm, 175 x 150 Pixel, *m/z* 202 – 405. L) Optical image. M) Distribution of PC (30:0) $[M+K]^+$ *m/z* 772.52531. N) INH $[M+H]^+$ *m/z* 138.06618, 40 x 40 µm, 173 x 110 Pixel, *m/z* 120 – 180 and 400 – 900, measurement was performed with two alternating acquisition modes with a raster step size of 20 x 40 µm resulting in an image pixel size of 40 x 40 µm. Scale bar = 1 mm.

Matrix optimization

As shown in Figure 2, a spotting approach was used to evaluate the efficacy of 9AA and pNA for the detection of RIF, which is low dosed at 10 mg/kg, orally. The same procedure was used to determine matrices suited to detect PZA and INH, Figure V and VI. Both of these drugs are water-soluble, polar molecules and thus not readily detected in MALDI, which necessitates a more thorough matrix optimization. The matrix optimization of the remaining three drug compounds covered in this study (MXF, CFZ and EMB) was conducted directly on dosed lung tissue, Figure VII. These compounds were more easily detected in MALDI due to their unpolar properties (MXF, CFZ) or higher dose (MXF, EMB; both 100 mg/kg).

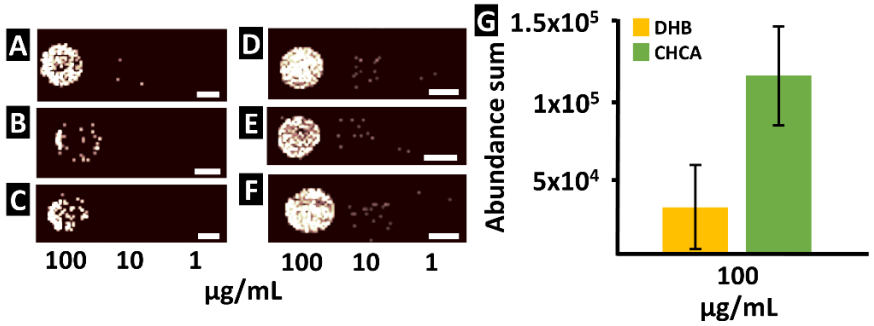

Figure S5. Detection of a INH standard spotted onto pig liver control tissue using DHB and CHCA matrix. Scale bar 1 mm. A-F) Ion images of INH $[M+H]^+$ using (A-C) DHB and (D-F) CHCA matrix. G) Bar chart showing the signal abundance sum of INH $[M+H]^+$ *m/z* 138.06618 for the 100 µg/mL concentration achieved with DHB and CHCA matrix. The 10 and 1 µg/mL were not detectable with either matrix. Error bars indicate the standard deviation (n = 3). Scale bar = 1 mm.

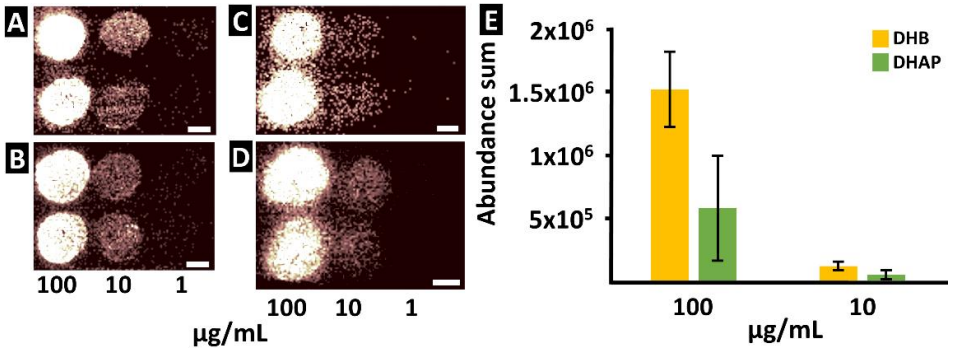

Figure S6. Detection of a PZA standard spotted onto pig liver control tissue using DHB and 2,6-DHAP matrix. Scale bar 1 mm. A-D) Ion images of PZA $[M+2H]^{+\cdot}$ using (A-B) DHB and (C-D) 2,6-DHAP matrix. E) Bar chart showing the signal abundance sum of PZA $[M+2H]^{+\cdot}$ *m/z* 125.05836 for the 100 µg/mL concentration achieved with DHB and 2,6-DHAP matrix. The 1 µg/mL concentration was not detectable with either matrix. Error bars indicate the standard deviation (n = 4). Scale bar = 1 mm.

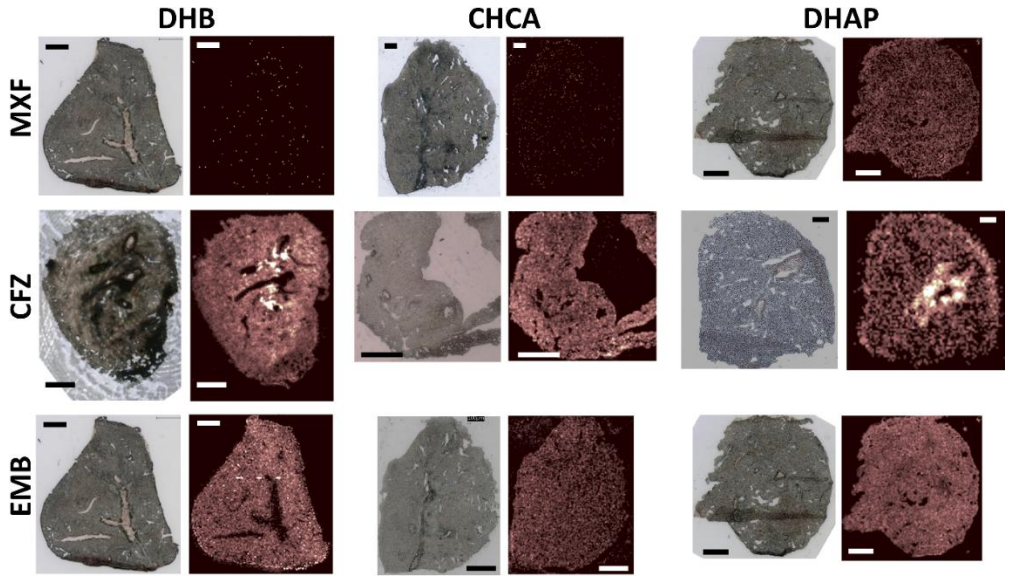

Figure S7. Comparison of the detection of MXF, CFZ and EMB using DHB, CHCA and 2,6-DHAP matrix. Scale bar = 1 mm.

High mass resolution

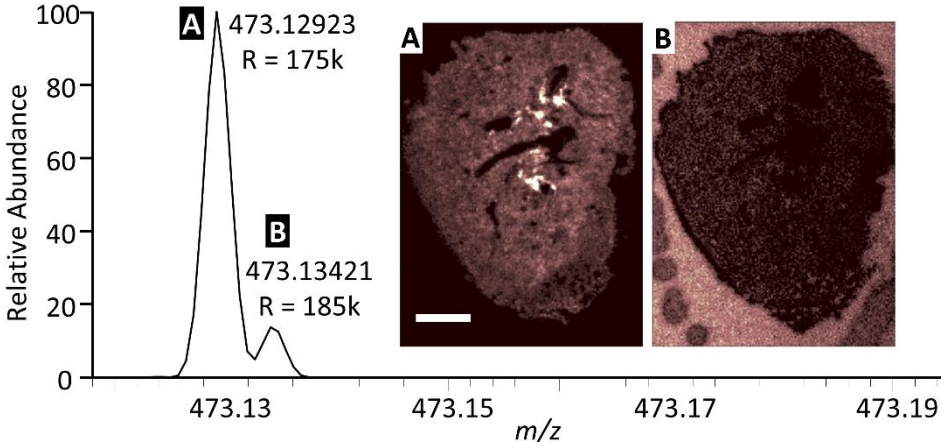

Figure S8. Molecular ion peak of CFZ (A) (*m/z* 473.12928) and a DHB-related matrix peak at *m/z* 473.13420 (B). Both signals show completely different spatial distributions and require a mass resolution of at least 96 k (FWHM) to be detected as two separate peaks. The data shown was recorded with a mass resolution of 240 k @ *m/z* 200, to prevent a superposition of the CFZ distribution. Scale bar = 1 mm.

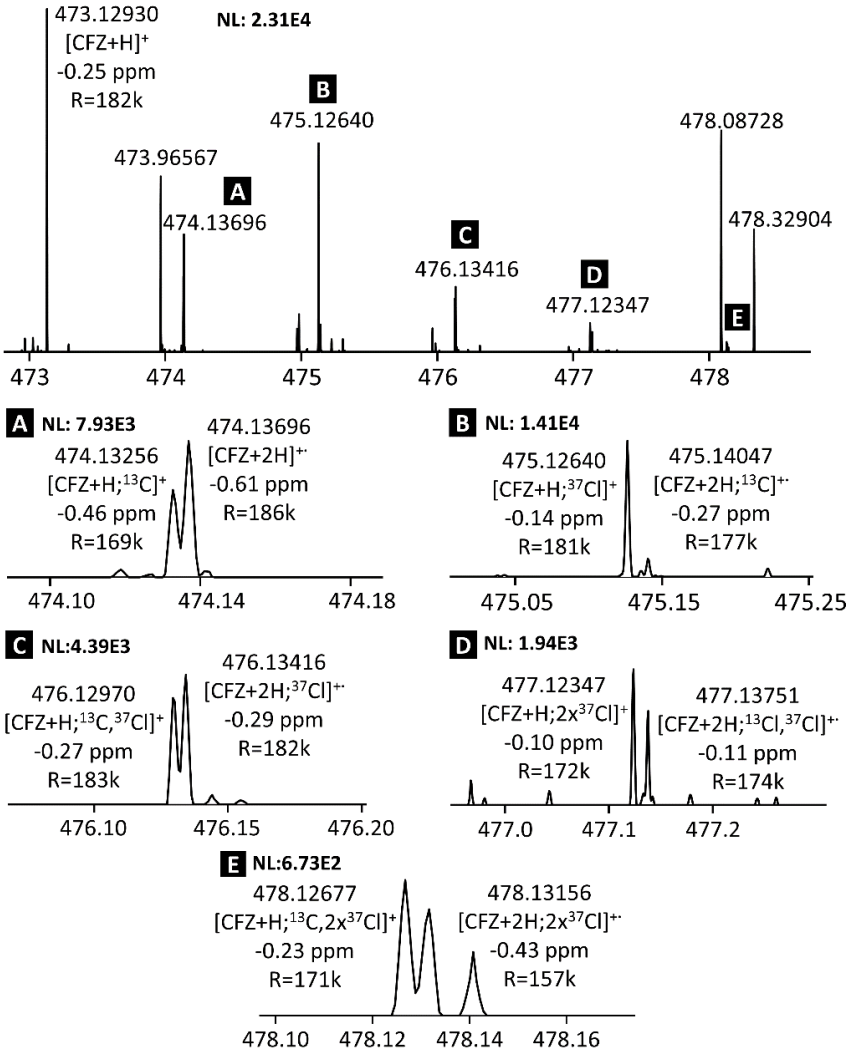

Figure S9. High mass resolution differentiation between the isotopic patterns of the CFZ $[M+H]^+$ and the CFZ $[M+2H]^{+\cdot}$. The data shown was recorded with a mass resolution of 240k @ *m/z* 200 to prevent a superposition of the isotopic patterns.

MSMS of EMB, RIF and CFZ

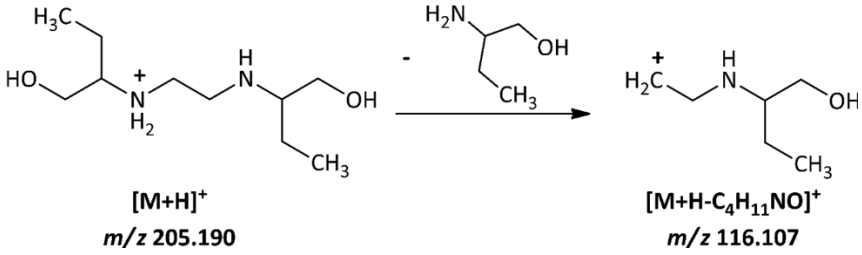

Figure S10. Fragmentation pathway of EMB. The only fragmentation of EMB in the MS/MS spectrum of a calibration standard (Figure 5 A) is the neutral loss of 2-Amino-butanol via an alpha cleavage resulting in *m/z* 116.107.

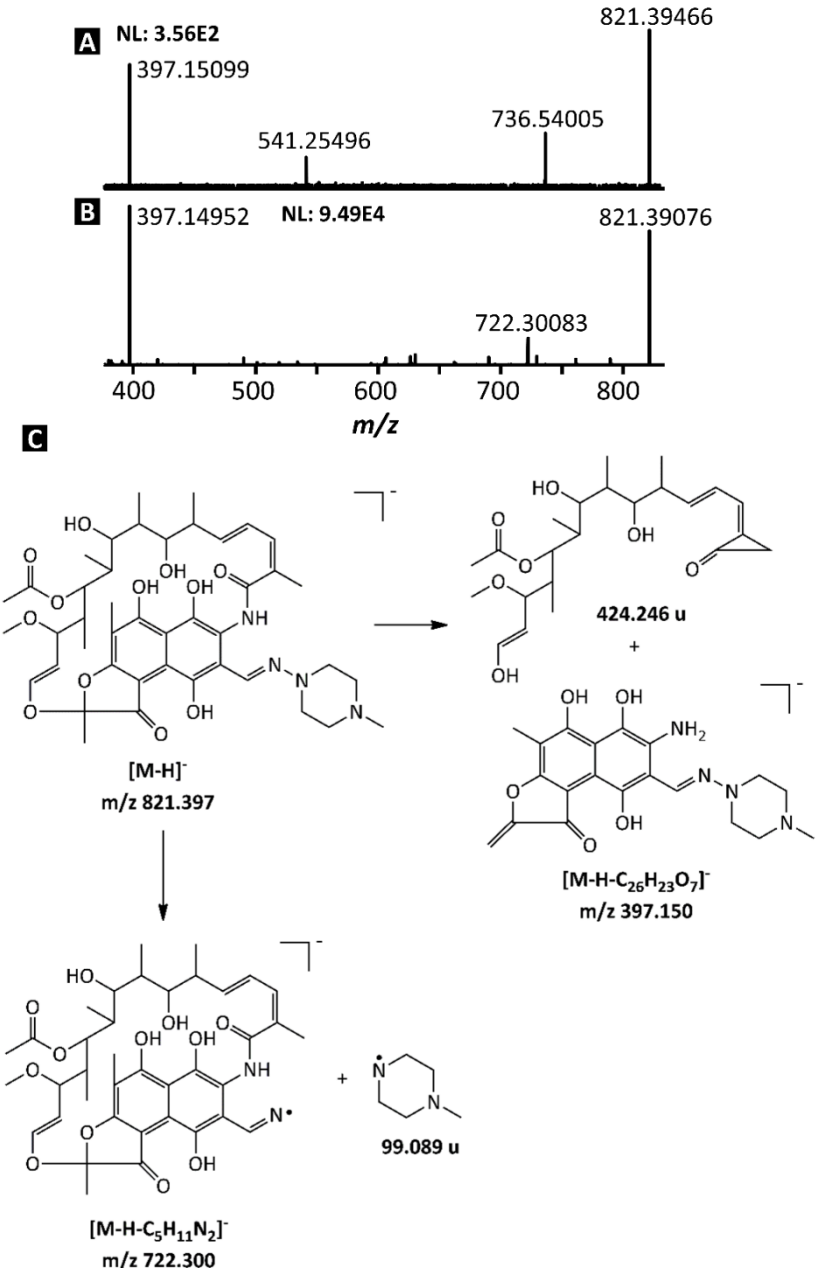

Figure S11. Comparison of the on-tissue MSMS spectrum of Rifampicin (A) with that of that of standard substance (B). The on-tissue MS/MS spectrum contains both the precursor ion and the main fragment ion of Rifampicin at *m/z* 397.150. The fragment found at *m/z* 722.300, which is visible in the spectrum of the standard substance, is

missing in the on-tissue MS/MS, which is probably a result of its low signal abundance. Furthermore, the two additional peaks in the on-tissue MS/MS at *m/z* 736.540 and 541.254 probably originate from co-isolated accompanying peaks of the RIF molecular ion. (C) As a heteroatomic cyclophane bearing a number of sidechains, the MS/MS spectrum of Rifampicin $[M-H]^-$ is naturally complex. Apart from the expected (low abundant) neutral losses of MeOH and acetic acid at *m/z* 798.365 and *m/z* 761.371 (not annotated in the MS/MS spectrum) and a number of additional fragments between *m/z* 450 and 700, the main fragment ions of RIF $[M-H]^-$ following the HCD activation are *m/z* 722.300 and 397.150. The cleavage of the 1-Methylpiperazine moiety ($C_5H_{11}N_2$) from the RIF molecular ion is the only plausible neutral loss leading to the formation of the *m/z* 722.300 fragment. The fragment *m/z* 722.300 still contains two nitrogen atoms and should, therefore, have an uneven mass, if it was an even electron ion. Therefore, the formation of *m/z* 722.300 is only possible through the homolytic cleavage of the N-N bond, even though this violates the even electron rule. The homolytic cleavage of the N-N bond yields *m/z* 722.300 as the radical anion $[M-H-C_5H_{11}N_2]^{\cdot-}$. The main fragment *m/z* 397.150 is formed by the loss of the bridging alkyl chain ($C_{23}H_{36}O_7$, 424.246 u) from the aromatic body by two onium-like rearrangements.

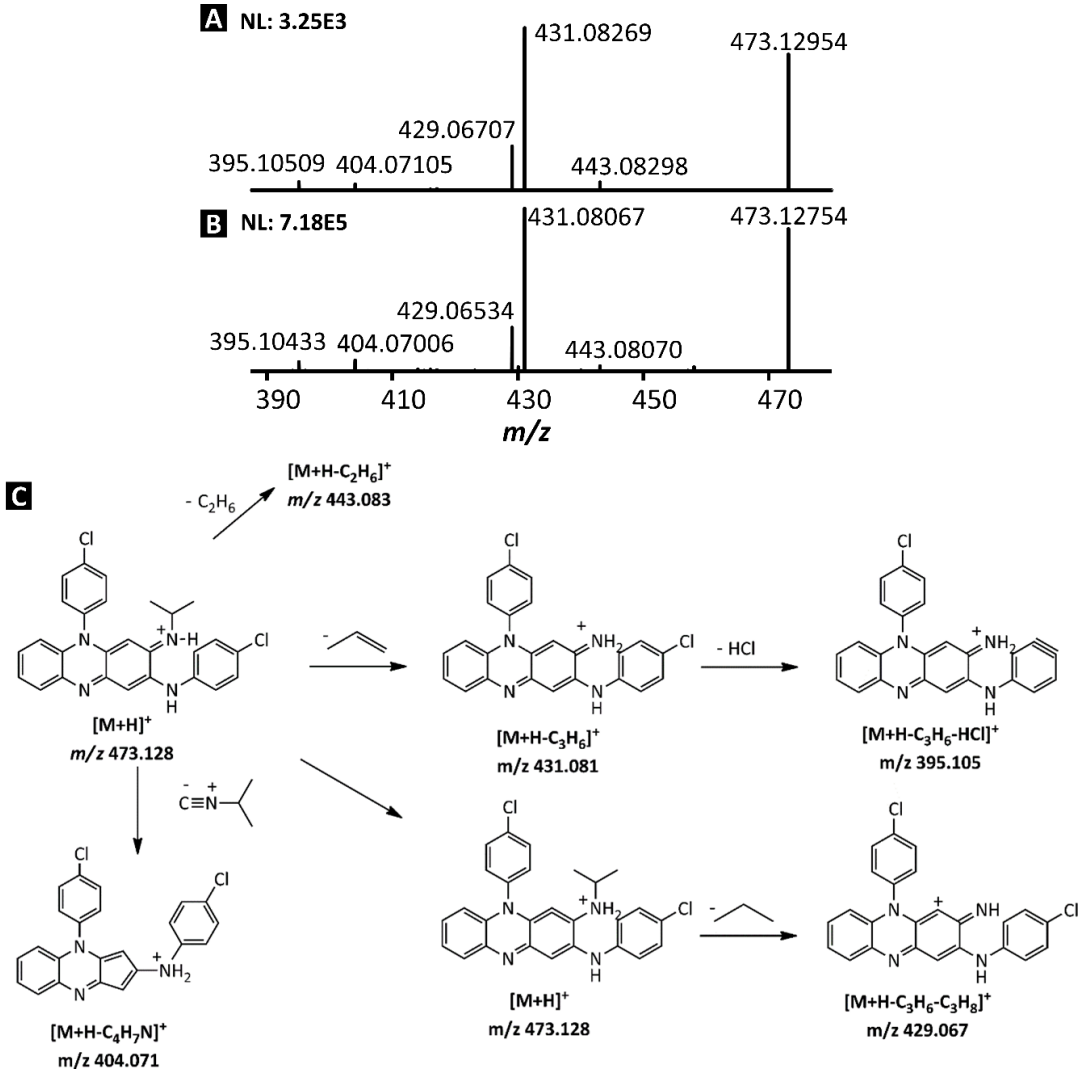

Figure S12. (A) Comparison of the on-tissue MSMS spectrum of Clofazimine with that of that of a standard substance (B). The on-tissue MS/MS matches that of the standard substance, which confirms the identity of the drug. (C) Fragmentation pathway of Clofazimine $[M+H]^+$. The main primary fragmentation pathway of Clofazimine following HCD activation is the neutral loss of propene (C_3H_6) from the imine moiety via an onium rearrangement yielding m/z 431.081 with a subsequent loss of hydrogen chloride at m/z 395.105. After

tautomerization of the protonated molecular ion into the enamine form, the second most abundant fragment ion at m/z 429.067 is formed via the neutral loss of propane (C_3H_6). Further fragmentation reactions are the losses of ethane and 2-isocyanopropane from the molecular ion at m/z 443.083 and 404.071, respectively.

Monochrome ion images and pre-measurement optical images of 10 µm measurements

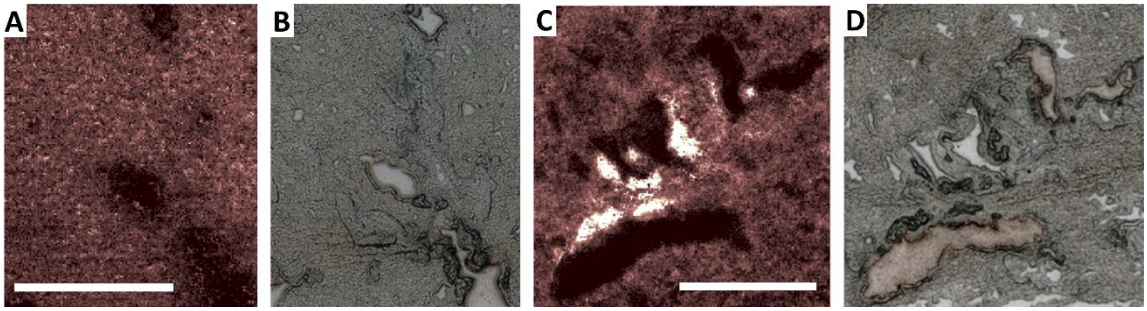

Figure S13. (A and B) Monochrome ion image and pre-measurement optical image of the EMB distribution shown in Figure 7 A – B. (C and D) Monochrome ion image and pre-measurement optical image of the CFZ distribution shown in Figure 7 C – D. Scale bar = 1 mm.

5.2 Second publication – Matrix ions as internal standard for high mass accuracy MALDI mass spectrometry imaging

RESEARCH ARTICLE

Rapid Communications in Mass Spectrometry WILEY

Matrix ions as internal standard for high mass accuracy matrix-assisted laser desorption/ionization mass spectrometry imaging

Axel Treu | Andreas Römpp

Bioanalytical Sciences and Food Analysis, University of Bayreuth, Bayreuth, Germany

Correspondence
A. Römpp, Bioanalytical Sciences and Food Analysis, University of Bayreuth, Bayreuth, Germany.
Email: andreas.roempp@uni-bayreuth.de

Funding information
Deutsche Forschungsgemeinschaft, Grant/Award Number: INST 91/373-1-FUGG and SFB 1357

Rationale: High mass accuracy is indispensable for reliable identification in matrix-assisted laser desorption/ionization mass spectrometry (MALDI MS) imaging. Ubiquitous matrix ions can serve as reference masses for mass calibration if their sum formula is known. Here we report an overview of ions generated on tissue by 11 common MALDI matrices for use in internal or external mass calibration.

Methods: Matrices covered in this study were applied onto coronal mouse brain sections using a pneumatic sprayer setup. MALDI imaging was performed on a Q Exactive HF orbital trapping mass spectrometer coupled to an AP-SMALDI 10 source. Measurements were conducted with high mass resolution (240 k full width at half maximum at *m/z* 200) and high mass accuracy with a root mean square mass error of better than 1.5 ppm achieved via internal mass calibration using matrix ions.

Results: MALDI MS imaging was used to investigate ions generated on tissue by 11 common MALDI matrices. An example of using matrix ions for internal mass calibration in MALDI imaging of drug substances and lipids in murine lung sections is presented. Tables containing the cluster composition, sum formulae, and the measured and theoretical *m/z* ratios of the identified ions were compiled for each matrix.

Conclusion: Using matrix ions as reference masses for internal and external mass calibration in MALDI MS imaging is an effective and elegant way to achieve sub-ppm mass accuracy as it makes use of ubiquitous signals present in every MALDI MS spectrum without the need for an additional calibration standard.

1 | INTRODUCTION

Mass spectrometry (MS) imaging has developed into a powerful tool for studying the distribution of analytes in tissue samples.[1,2] Apart from desorption electrospray ionization[3] and secondary ion mass spectrometry,[4] matrix-assisted laser desorption/ionization (MALDI)[1] is the most common ionization technique used in MS imaging.[5]

In MALDI MS imaging, the sample is covered with a thin matrix layer using a variety of techniques such as pneumatic spraying or sublimation. The matrix layer is subsequently ablated by a laser in a defined pattern.[1] This generates an array of mass spectra containing both molecular and spatial information.

The matrix used in a MALDI imaging experiment is usually a nonvolatile crystalline solid, which is able to absorb light radiation of the same wavelength as the employed laser. UV lasers are the most commonly used lasers in MALDI. For effective energy absorption and transfer onto the sample molecules, matrices used in UV-MALDI always contain a chromophore, typically electron-rich delocalized π

systems in the form of a central aromatic structure. Connected to this structure are substituents exerting +M or −M effects (e.g., −OH, $-NH_2$, $-CO_2H$, and $-NO_2$). Many common UV-MALDI matrices are derived from small aromatic organic acids such as nicotinic or phenolic acid to further assist in the formation of protonated molecules.[6,7]

One of the major challenges in performing MS imaging of complex biological samples such as tissue sections is the identification of an analyte directly from the sample under imaging conditions. In full-scan acquisition, this is possible only with high-resolution mass spectrometry, which entails both high mass resolution and high mass accuracy. High mass resolution is required to differentiate between the multitude of superimposing isobaric peaks, whereas high mass accuracy is required to allow reliable mass identification.

The mass accuracy can be significantly improved through mass calibration. Generally, mass calibration entails the measurement of a reference or calibration compound that generates a number of known *m/z* values "reference masses" or "lock masses" that are ideally evenly distributed over a wide mass range. The theoretical *m/z* values are then matched against the actual measured values. In external mass calibration the reference compound and the actual sample are measured at different time points, whereas in internal mass calibration, the reference compound and the sample are both measured at the same time, meaning they are contained in the same spectrum.

Widely used reference compounds for external mass calibration are per- or polyfluoroalkyl substances that generate numerous equidistant ions ($\Delta m = 50$, 100 u), such as perfluorokerosene[8] or Ultramark 1621.[9] Furthermore, clusters of monoisotopic elements[10] such as gold (Au_n^+, Au_n^-) or phosphorus (P_n^+, P_n^-) as well as clusters of monoisotopic inorganic salts[11] such as CsI or CsI_3 ($[Cs\ (CsI)_n]^+$, $[I\ (CsI)_n]^-$) are widely used for external mass calibration.

In internal mass calibration, reference masses can be supplied by adding reference compounds to the sample or by ubiquitous impurities[12] such as plasticizers (e.g., phthalates) and UV stabilizers (e.g., butylated hydroxytoluene). When investigating biological samples such as thin tissue sections, well-characterized endogenous compounds (e.g., lipids) can serve as references for internal mass calibration.[13–15] Matrix ions are abundant in every MALDI MS spectrum and are employed as references for internal mass calibration.[1,15,16] Commonly used MALDI matrices such as derivatives of cinnamic acid or 2,5-dihydroxybenzoic acid (DHB) are known to form a large number of highly abundant ions,[17,18] especially at lower mass-to-charge (*m/z*) ratios, including agglomerates with analyte ions.[19] It should be noted that, in the past, this has complicated the detection and identification of "small molecules" in MALDI. This is no longer the case if high mass resolution instruments are used. On the contrary, the high number of ions in the lower mass range can be an advantage if they are used as references for internal mass calibration.

At higher *m/z* ratios, matrix ions tend to be scarcer, especially on biological tissues due to ion suppression effects[20,21] exerted by the sample. Matrix ions found at these higher *m/z* ratios usually belong to an ascending homologous series of clusters, for example, $[a\mathrm{DHB} + \mathrm{NH_4}\text{-}b\mathrm{H_2O}]^+$.

To be usable as a lock mass in internal mass calibration, an ion is ideally detectable in the entire measurement field of view, that is on and off sample, with sufficient abundance and should not be superimposed by neighboring signals.

In this work, we systematically investigated the ions generated on tissue by 11 common MALDI matrices (Table 1) in MS imaging experiments. Cluster compositions and sum formulae were assigned to specific matrix ions based on accurate mass measurements, and selected 2,5-DHB cluster ions were confirmed by MS/MS data. With this, we aim to provide lists of reference masses for use in internal or external mass calibration.

2 | EXPERIMENTAL

2.1 | Materials

Solvents and matrix substances were purchased from Sigma-Aldrich (Taufkirchen, Germany). Adhesive glass slides (Menzel Gläser, Superfrost) were purchased from VWR (Darmstadt, Germany). Matrices were of the highest available purity. Brains of 6 week old male and female BALB/c mice were purchased from Charles River (L'Arbresle, France). Sections of murine lung tissue for drug imaging were obtained from the surplus material of another study[22] conducted in our laboratory.

2.2 | Sample preparation

Serial coronal mouse brain sections (10 µm) were cut at −25°C using a CM3050 S cryostat (Leica Microsystems, Wetzlar, Germany) and deposited onto adhesive glass slides (Menzel Gläser, Superfrost) and stored at −80°C. The sections were placed in a desiccator for 10 min before matrix application. The matrices were applied using a semiautomatic pneumatic sprayer system built in-house. The matrix solutions were prepared as follows: 1,5-diaminonaphthalene (1,5-DAN) 5 mg/mL in 50% acetone; 2,6-dihydroxyacetophenone (DHAP) and norharmane 10 mg/mL in 50% methanol; 2,5-dihydroxybenzoic acid (DHB) 30 mg/mL in 50% acetone; alpha-cyano-4-hydroxycinnamic acid (CHCA), sinapic acid (SA), and caffeic acid (CA) 10 mg/mL in 50% acetone; 9-aminoacridine (9AA) and 2[(2*E*)-3-(4-*tert*-butylphenyl)-2-methylprop-2-enylidene]malononitrile (DCTB) 10 mg/mL in 75% acetone; 4-nitroaniline (pNA) 5 mg/mL in 75% acetone; and 2,4,6-trihydroxyacetophenone (THAP) 15 mg/mL in 75% methanol. The matrices used in the positive ion mode were acidified with 0.1% (v/v) trifluoroacetic acid. A short overview of the matrix substances covered in this study is provided in Table 1. The structural formulae of all the matrices used in this work are given in Figure S1 (supporting information).

2.3 | MS acquisition and data analysis

MALDI MS imaging measurements were performed using a Q Exactive HF mass spectrometer (Thermo Fisher Scientific GmbH,

TABLE 1 Overview of the matrix substances covered in this study

Matrix (abbreviation)	CAS Registry Number	Sum formula	Ion mode(s)
9-Aminoacridine (**9AA**)	90-45-9	$C_{13}H_{10}N_2$	Negative
2[(2*E*)-3-(4-*tert*-Butylphenyl)-2-methylprop-2-enylidene]malononitrile (**DCTB**)	300364-84-5	$C_{17}H_{18}N_2$	Positive
Caffeic acid (**CA**)	331-39-5	$C_9H_8O_4$	Positive
Alpha-cyano-4-hydroxycinnamic acid (**CHCA**)	28166-41-8	$C_{10}H_7NO_3$	Positive
1,5-Diaminonaphthalene (**1,5 DAN**)	2243-62-1	$C_{10}H_{10}N_2$	Negative/Positive
2,5-Dihydroxybenzoic acid (**DHB**)	490-79-9	$C_7H_6O_4$	Positive/Negative
4-Nitronaniline (**pNA**)	100-01-6	$C_6H_6N_2O_2$	Negative/Positive
Norharmane	244-63-3	$C_{11}H_8N_2$	Negative/Positive
Sinapic acid (**SA**)	530-59-6	$C_{11}H_{12}O_5$	Positive
2,4,6-Trihydroxyacetophenone (**THAP**)	480-66-0	$C_8H_8O_4$	Negative
2,6-Dihydroxyacetophenone (**2,6 DHAP**)	699-83-2	$C_8H_8O_3$	Positive/Negative

Bremen, Germany) coupled to an atmospheric pressure MALDI imaging source AP-SMALDI10 (TransMIT GmbH, Gießen, Germany) equipped with a $\lambda = 337$ nm N_2 laser operating at a repetition rate of 60 Hz.[23] Measurements were carried out in positive and negative ion mode with 30 laser shots per pixel and a mass resolution of 240 k (full width at half maximum) at *m/z* 200. The measurements intended for cluster identification were conducted using a pixel size of 30 × 30 µm covering a 20 × 20 pixel grid. These measurements employed previously identified matrix clusters for internal mass calibration, which are highlighted with an "*." Measured *m/z* values given in Tables S1–S18 (supporting information) are averaged across all 400 spectra of the measurement to correct for signal fluctuation. The identification of matrix clusters was based on accurate mass identification. Theoretical masses and *m/z* values were calculated using tabulated values from the Commission on Isotopic Abundances and Atomic Weights[24] and were rounded to five decimal places. The murine lung was measured using two alternating full-scan acquisition windows from *m/z* 120 to 450 and *m/z* 700 to 900; the step size was set to 20 × 40 µm resulting in an image pixel size of 40 × 40 µm. Further information on this measurement setup can be found in our previously reported study.[22]

3 | RESULTS AND DISCUSSION

For the investigation of matrix clusters, matrices were applied onto coronal mouse brain sections and measured in MALDI MS imaging. Each investigated matrix compound or compound class is presented here, starting with matrices intended primarily for use in positive ion mode. Tables containing the respective cluster composition, sum formulae, and the theoretical and measured *m/z* of the identified matrix clusters are provided as a basis for internal or external mass calibration.

3.1 | 2,5-Dihydroxybenzoic acid (DHB)

2,5-Dihydroxybenzoic acid or gentisic acid (DHB, $C_7H_6O_4$, 154.02661 u) is one of the most common matrix substances used in positive mode MALDI MS imaging for a wide range of analytes, including small molecules,[25] lipids,[16] and peptides.[26] Furthermore, 2,5-DHB was shown to be suitable for the analysis of phospholipids in the negative ion mode.[27] In the positive ion mode, 2,5-DHB readily forms clusters based on the addition of H^+, NH_4^+, Na^+, or K^+ and subsequent dehydration. Four highly periodic cluster series of the general cluster composition $[aM + X\text{-}bH_2O]^+$ ($X = H^+$, NH_4^+, Na^+, K^+; $a = 1, 2, 3, \ldots$; $b \leq a$) were identified, with members of the NH_4^+ adduct $[aM + NH_4\text{-}bH_2O]^+$ series being the most abundant. An overview of this cluster series, including the cluster composition, sum formulae, and the theoretical and measured *m/z*, is provided in Table 2. Similar overviews of the three other DHB cluster series are provided in Tables S1–S3 (supporting information). An overview of the general composition of clusters from all matrices covered in this work is provided in Table 3. An overview of the mass spectra of DHB on mouse brain tissue is shown in Figures S2 and S3 (supporting information). In addition to these four cluster series, DHB forms a number of clusters based on hydrogen/alkali metal cation exchange followed by the loss of water. These ions share the general cluster composition $[aM + b\text{Alkali-}(b\text{-}1)H\text{-}cH_2O]^+$ ($a = 1, 2, 3, \ldots$; $b = 1, 2, 3, \ldots$; $c = 0, 1, 2, 3, \ldots$) (Table S4 [supporting information]). A similar composition is observed for the 2,5-DHB clusters in the negative ion mode detected between *m/z* 150 and 850. These ions are formed based on a hydrogen/alkali metal cation exchange followed by the loss of water and share the general cluster composition $[aM\text{-}bH + (b\text{-}1)\text{Alkali-}cH_2O]^-$ ($a = 1, 2, 3, \ldots$; $b = 1, 2, 3, \ldots$; $c = 0, 1, 2, 3, \ldots$). A number of these ions are preceded by intensive M-1 peaks caused by the loss of a hydrogen radical that has general cluster composition of $[aM\text{-}bH\text{-}H + (b\text{-}1)\text{Alkali-}cH_2O]^{\cdot-}$ ($a = 1, 2, 3, \ldots$; $b = 1, 2, 3, \ldots$; $c = 0, 1, 2, 3, \ldots$) (Table S5 and

TABLE 2 Overview of all identified **DHB** ions belonging to the $[aM + NH_4\text{-}bH_2O]^+$ ($a = 1, 2, 3, \ldots; b \leq a$) series detected on tissue in **positive** ion mode

Cluster composition	Sum formula	Theoretical *m/z*	Measured *m/z*	RMSE (ppm)
$M + NH_4\text{-}H_2O^+$	$C_7H_8NO_3^+$	154.04987	154.04974	1.01
$2M + NH_4\text{-}H_2O^+$	$C_{14}H_{14}NO_7^+$	308.07648	308.07651	0.19
$2M + NH_4\text{-}2H_2O^+$	$C_{14}H_{12}NO_6^+$	290.06591	290.06586	0.18
***3M + NH_4-2H_2O^+**	**$C_{21}H_{18}NO_{10}^+$**	**444.09252**	**444.09252**	–
$3M + NH_4\text{-}3H_2O^+$	$C_{21}H_{16}NO_9^+$	426.08196	426.08200	0.42
4M + NH_4-3H_2O^+	**$C_{28}H_{22}NO_{13}^+$**	**580.10857**	**580.10840**	0.40
$4M + NH_4\text{-}4H_2O^+$	$C_{28}H_{20}NO_{12}^+$	562.09800	562.09808	0.59
$5M + NH_4\text{-}3H_2O^+$	$C_{35}H_{28}NO_{17}^+$	734.13517	734.13525	0.95
***5M + NH_4-4H_2O^+**	**$C_{35}H_{26}NO_{16}^+$**	**716.12461**	**716.12461**	–
$5M + NH_4\text{-}5H_2O^+$	$C_{35}H_{24}NO_{15}^+$	698.11405	698.11426	0.46
6M + NH_4-5H_2O^+	**$C_{42}H_{30}NO_{19}^+$**	**852.14065**	**852.14093**	**0.53**
$6M + NH_4\text{-}6H_2O^+$	$C_{42}H_{28}NO_{18}^+$	834.13009	834.12994	0.51
7M + NH_4-6H_2O^+	**$C_{49}H_{34}NO_{22}^+$**	**988.15670**	**988.15729**	0.54
$7M + NH_4\text{-}7H_2O^+$	$C_{49}H_{32}NO_{21}^+$	970.14613	970.14697	0.71
***8M + NH_4-7H_2O^+**	**$C_{56}H_{38}NO_{25}^+$**	**1124.17274**	**1124.17274**	–
$8M + NH_4\text{-}8H_2O^+$	$C_{56}H_{36}NO_{24}^+$	1106.16222	1106.16187	0.51
$9M + NH_4\text{-}7H_2O^+$	$C_{63}H_{44}NO_{29}^+$	1278.19940	1278.19873	1.02
9M + NH_4-8H_2O^+	**$C_{63}H_{42}NO_{28}^+$**	**1260.18879**	**1260.18896**	**0.25**
$9M + NH_4\text{-}9H_2O^+$	$C_{63}H_{40}NO_{27}^+$	1242.17822	1242.17822	0.69
10M + NH_4-9H_2O^+	**$C_{70}H_{46}NO_{31}^+$**	**1396.20483**	**1396.20557**	**0.40**
$10M + NH_4\text{-}10H_2O^+$	$C_{70}H_{44}NO_{30}^+$	1378.19427	1378.19531	0.88

Note. Bold letters indicate abundant ion species. Clusters marked with * were used for internal calibration. RMSE, root mean square mass error.

Figure S3 [supporting information]). MS/MS data of selected 2,5-DHB clusters from each cluster series are included in Figures S18–S23 (supporting information).

Among the matrices covered in this work, DHB delivers the highest number of matrix ions in both polarities. Furthermore, these ions are periodically distributed over a wide mass range from *m/z* 100 to around *m/z* 1400, making DHB ideal for internal and external mass calibration. In this regard, DHB may even be considered as a lower mass analogue of Ultramark 1621.

3.2 | Alpha-cyano-4-hydroxycinnamic acid, sinapic acid, and caffeic acid (CHCA)

The derivatives of cinnamic acid, represented in this study by alpha-cyano-4-hydroxycinnamic acid (CHCA, $C_{10}H_7NO_3$, 189.04260 u), sinapic acid (SA, $C_{11}H_{12}O_5$, 224.06847 u), and caffeic acid (CA, $C_9H_8O_4$, 180.04226 u), are a major class of matrix substances used in the positive ion mode for the analysis of small molecules,[28] peptides, and proteins.[29] All three matrices exhibited a high affinity toward alkali metal cations and formed a large number of cluster ions. Clusters of CA are detected between *m/z* 100 and 800 and CHCA clusters between *m/z* 100 and 900. SA delivers the heaviest clusters, which are detected between *m/z* 100 and 1500. The majority of the observed ions are formed based on a hydrogen/alkali metal cation exchange leading to a general sum formula of $[aM + b\text{Alkali-}(b\text{-}1)H]^+$ ($a = 1, 2, 3, \ldots; b = 1, 2, 3, \ldots$). Often these ions are accompanied by additional ions formed by the loss of water or CO_2 from the cluster body leading to a general sum formula of $[aM + b\text{Alkali-}(b\text{-}1)H\text{-}H_2O]^+$ and $[aM + b\text{Alkali-}(b\text{-}1)H\text{-}CO_2]^+$. In general, CHCA, SA, and CA clusters containing predominantly K^+ as charge carriers show a higher abundance than clusters containing predominantly Na^+ as charge carriers. See Tables S6–S8 (supporting information) for the cluster lists of CHCA, SA, and CA and Figures S4–S6 (supporting information) for single pixel mass spectra on mouse brain tissue.

Similar to DHB, the derivatives of cinnamic acid deliver a large number of abundant signals at high and low mass ranges, making them also ideal for use in internal and external mass calibration in the positive mode.

3.3 | 2[(2*E*)-3-(4-*tert*-Butylphenyl)-2-methylprop-2-enylidene]malononitrile (DCTB)

Although primarily used for the positive mode analysis of polymers[30] and large unpolar macromolecules[31] in regular MALDI, 2[(2*E*)-3-(4-*tert*-butylphenyl)-2-methylprop-2-enylidene]malononitrile (DCTB, $C_{17}H_{18}N_2$, 250.14699 u) was shown to be suitable for MALDI MS imaging, particularly for detecting small organic molecules.[32,33] Characteristically, DCTB ions exhibit the loss of alkyl moieties from

TABLE 3 Overview of the general composition of clusters generated by the matrices investigated in this work

Matrix	General cluster composition in positive ion mode	General cluster composition in negative ion mode
DHB	$[aM + X\text{-}bH_2O]^+$ ($X = H^+, NH_4^+, Na^+, K^+$; $a = 1, 2, 3, \ldots$; $b \le a$) $[aM + b\text{Alkali-}(b\text{-}1)H\text{-}cH_2O]^+$ ($a = 1, 2, 3, \ldots$; $b = 1, 2, 3, \ldots$; $c = 0, 1, 2, 3, \ldots$)	$[aM\text{-}bH + (b\text{-}1)\text{Alkali-}cH_2O]^-$ $[aM\text{-}bH\text{-}H + (b\text{-}1)\text{Alkali}]^{-\cdot}$ ($a = 1, 2, 3, \ldots$; $b = 1, 2, 3, \ldots$; $c = 1, 2, 3, \ldots$)
CHCA, SA, CA	$[aM + b\text{Alkali-}(b\text{-}1)H]^+$ $[aM + b\text{Alkali-}(b\text{-}1)H\text{-}CO_2]^+$ $[aM + b\text{Alkali-}(b\text{-}1)H\text{-}CO_2]^+$ ($a = 1, 2, 3, \ldots$; $b = 1, 2, 3, \ldots$)	–
DCTB	$[aM + X\text{-Alkyl}]^{+/+\cdot}$ $a = 1, 2, 3, \ldots$; $X = H^+, Na^+, K^+$; alkyl = CH_4, CH_3, CH_2, C_2H_4, C_2H_6, C_4H_8	–
pNA	$[aM + X\text{-}bNO]^{+/+\cdot}$ ($X = H^+, Na^+, K^+$; $a = 1, 2, 3, \ldots$; $b \le a$)	$[aM\text{-H-}bH_2]^-$ ($a = 1, 2, 3, \ldots$; $b = 1, 2, 3, \ldots$)
1,5-DAN	No general cluster composition applicable	$[aM\text{-H-}bH_2]^-$ ($a = 1, 2, 3, \ldots$; $b = 1, 2, 3, \ldots$)
2,6-DHAP	$[aM + b\text{Alkali-}(b\text{-}1)H]^+$ ($a = 1, 2, 3, \ldots$; $b = 1, 2, 3, \ldots$)	$[aM\text{-H-}bH_2]^-$ $[aM\text{-}bH + (b\text{-}1)\text{Alkali}]^-$ ($a = 1, 2, 3, \ldots$; $b = 1, 2, 3, \ldots$)
Norharmane	$[aM + X]^+$ ($a = 1, 2, 3, \ldots$; $X = H^+, Na^+, K^+$)	$[aM\text{-H-}bH_2]^-$ ($a = 1, 2, 3, \ldots$; $b = 1, 2, 3, \ldots$)
THAP	–	$[aM\text{-H-}bH_2]^-$ $[aM\text{-}bH + (b\text{-}1)\text{Alkali}]^-$ ($a = 1, 2, 3, \ldots$; $b = 1, 2, 3, \ldots$)
9AA	–	$[aM\text{-H-}bH_2]^-$ ($a = 1, 2, 3, \ldots$; $b = 1, 2, 3, \ldots$)

Note. CA, caffeic acid; CHCA, alpha-cyano-4-hydroxycinnamic acid; 1,5-DAN, 1,5-diaminonaphthalene; DCTB, 2[(2*E*)-3-(4-*tert*-butylphenyl)-2-methylprop-2-enylidene]malononitrile; DHAP, 2,6-dihydroxyacetophenone; DHB, 2,5-dihydroxybenzoic acid; 9AA, 9-aminoacridine; pNA, 4-nitroaniline; SA, sinapic acid; THAP, 2,4,6-trihydroxyacetophenone.

the *tert*-butyl group and contain no more than two DCTB base molecules with a single charge carrier that can be H^+, Na^+, or K^+. As a result, DCTB ions were not detected above *m/z* 550. This leads to a general cluster composition of $[aM + X\text{-Alkyl}]^{+/+\cdot}$ ($a = 1, 2, 3, \ldots$; $X = H^+, Na^+, K^+$; Alkyl = CH_4, CH_3, CH_2, C_2H_4, C_2H_6, C_4H_8) (Table S9 and Figure S7 [supporting information]).

3.4 | 4-nitroaniline (pNA)

A number of matrix substances are usable in positive and negative ion mode, which significantly increases their utility as general-purpose matrices and makes them suitable for dual polarity measurements. 4-Nitroaniline (pNA, $C_6H_6N_2O_2$, 138.04293 u) is suited for lipid analysis in both ion modes.[14,34] However, pNA is not vacuum stable and therefore limited to use in intermediate and atmospheric pressure ion sources. As with most matrices usable in the negative ion mode, the clusters of pNA show the loss of molecular hydrogen leading to a general cluster composition of $[aM\text{-H-}bH_2]^-$ ($a = 1, 2, 3, \ldots$; $b = 1, 2, 3, \ldots$). However, emanating from its nitro-group, pNA forms a number of clusters with unusual cluster compositions that show the loss of single oxygen atoms, the formal loss of atomic nitrogen via an NO_2/O_2 exchange,[35] and the release of nitric oxide (NO). Similar to DCTB, identified clusters of pNA did not exceed the *m/z* 550 threshold in positive and negative ion mode (Tables S10 and S11 and Figures S8 and S9 [supporting information]). In comparison to other matrices used exclusively in the positive ion mode, pNA generates only a small number of identifiable ions in the positive ion mode, which show a loss of NO. These ions can be described as $[aM + X\text{-}bNO]^{+/+\cdot}$ ($X = H^+, Na^+, K^+$; $a = 1, 2, 3, \ldots$; $b \le a$) (Table S11 and Figure S9 [supporting information]).

3.5 | 1,5-Diaminonaphthalene (1,5-DAN)

In the negative ion mode spectrum of 1,5-diaminonaphthalene (1,5-DAN, $C_{10}H_{10}N_2$, 158.08440 u), which is suitable for the analysis of small molecules and lipids,[36,37] only a small number of matrix clusters can be assigned unambiguously. All of these clusters are of the $[aM\text{-H-}bH_2]^-$ ($a = 1, 2, 3, \ldots$; $b = 1, 2, 3, \ldots$) cluster composition

and do not exceed *m/z* 400 (Table S12 and Figure S10 [supporting information]). Similarly, all 1,5-DAN ions identified in the positive ion mode are found below *m/z* 400 and do not contain more than two base molecules. In comparison to other positive mode matrices however, 1,5-DAN does not form a protonated molecule. Instead, it forms a highly abundant $M^{+\cdot}$ molecular ion (Table S13 and Figure S11 [supporting information]).

3.6 | 2,6-Dihydroxyacetophenone (2,6-DHAP)

2,6-Dihydroxyacetophenone (2,6-DHAP, $C_8H_8O_3$, 152.04734 u), which has been used for the analysis of phospholipids in mouse lung sections,[38] forms a small number of cluster ions in negative ion mode of the $[aM\text{-}H\text{-}bH_2]^-$ ($a = 1, 2, 3, \ldots$; $b = 1, 2, 3, \ldots$) and $[aM\text{-}bH + (b\text{-}1)\,Alkali]^-$ cluster composition which are detected up to *m/z* 600. In the positive ion mode, a number of $[aM + b\text{Alkali-}(b\text{-}1)H]^+$ ions are detected up to *m/z* 400 (Tables S14 and S15 and Figures S12 and S13 [supporting information]).

3.7 | Norharmane

Beta-carboline, commonly referred to as norharmane ($C_{11}H_8N_2$, 168.06875 u), is a nitrogen-containing heterocycle used for the analysis of lipids in both polarities[39] as well as bile acids in the negative ion mode.[40] In the negative ion mode, identified clusters do not exceed *m/z* 670 and are mainly of the $[aM\text{-}H\text{-}bH_2]^-$ ($a = 1, 2, 3, \ldots$; $b = 1, 2, 3, \ldots$) cluster composition (Table S16 and Figure S14 [supporting information]). In the positive mode, norharmane forms only a small number of clusters, which are detected up to *m/z* 540 (Table S17 and Figure S15 [supporting information]). In comparison to other dual polarity mode and positive mode matrices, the ions of norharmane do not show a hydrogen alkali metal cation exchange. These ions contain only a single charge carrier and share the cluster composition $[aM + X]^+$ ($a = 1, 2, 3, \ldots$; $X = H^+, Na^+, K^+$).

3.8 | 2,4,6-Trihydroxyacetophenone (THAP)

2,4,6-Trihydroxyacetophenone (THAP, $C_8H_8O_4$, 168.04225 u) is suited for the negative mode analysis of lipids and small molecules.[41] It mainly forms clusters of the $[aM\text{-}H\text{-}bH_2]^-$ and $[aM\text{-}bH + (b\text{-}1)\,Alkali]^-$ ($a = 1, 2, 3, \ldots$; $b = 1, 2, 3, \ldots$) cluster composition up to *m/z* 540 (Table S18 and Figure S16 [supporting information]).

3.9 | 9-Aminoacridine (9AA)

Similar to norhramane, 9-aminoacridine (9AA, $C_{13}N_{10}N_2$, 194.08440 u) is a nitrogen-containing heterocycle ideal for negative mode analysis of lipids.[42] 9AA forms only a small number of the clusters of the $[aM\text{-}H\text{-}bH_2]^-$ ($a = 1, 2, 3, \ldots$; $b = 1, 2, 3, \ldots$) cluster composition, which are detected up to *m/z* 580 (Table S19 and Figure S17 [supporting information]).

4 | MATRIX IONS FOR INTERNAL MASS CALIBRATION IN DRUG AND LIPID IMAGING

A section of murine lung dosed orally with the anti-tuberculosis drug ethambutol (EMB, 100 mg/kg) was imaged using DHB matrix. Highlighted in the hematoxylin and eosin staining of the measured section, which is given in Figure 1A, are the airways and blood vessels present in the section. The measurement was conducted using alternating high mass (*m/z* 700–900) and low mass (*m/z* 120–450) full-scan mass windows.[22] For internal mass calibration, $[DHB + H\text{-}H2O]^+$ ($C_7H_5O_3^+$) *m/z* 137.02332 was used in the low mass window and $[5DHB + NH_4\text{-}H_2O]^+$ ($C_{35}H_{26}NO_{16}^+$) *m/z* 716.12461 was used in the high mass window. Figure 1B shows the distribution of the matrix cluster $[2DHB + H\text{-}2H_2O]^+$ ($C_{14}H_9O_6^+$) detected at *m/z* 273.03936 with a root mean square mass error (RMSE) of 0.34 ppm across 23 198 spectra. Due to ion suppression effects, the cluster shows a lower intensity on the tissue. It is known that the mass accuracy of the orbital trapping

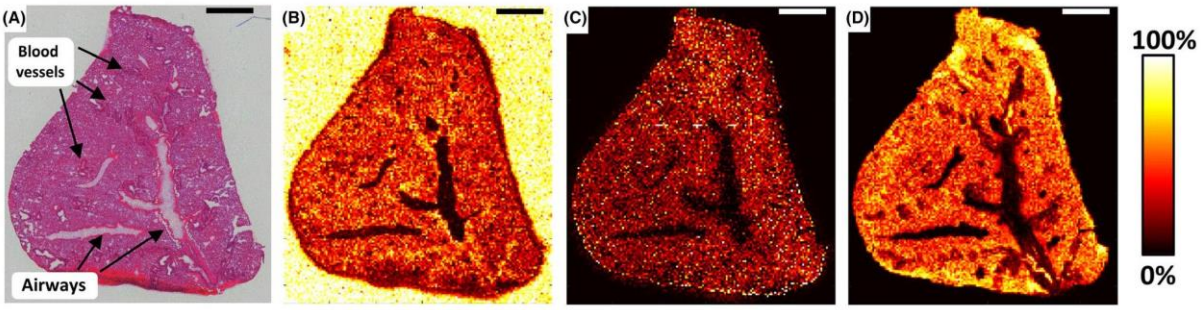

FIGURE 1 MALDI imaging of murine lung section using DHB matrix clusters for internal mass calibration. A) Post measurement haematoxylin and eosin stain. B) Distribution of the DHB cluster $[2DHB + H - 2H_2O]^+$ ($C_{14}H_9O_6^+$) m/z 273.03936. C) Distribution of ethambutol $[M + H]^+$ ($C_{10}H_{25}N_2O_2^+$) m/z 205.19105. D) Distribution of PC 32:0 $[M + K]^+$ ($C_{40}H_{80}NO_8PK^+$) m/z 772.52531. The measurement was carried out in positive ion mode with a raster size of 290 × 160 pixels and step size of 20 × 40 µm resulting in an image pixel size of 40 × 40 µm

mass analyzers decreases at the edges of the dynamic range.[43] Therefore, when choosing a matrix cluster for use in internal mass calibration with this type of instrument, one must consider not only the sample coverage and overall intensity of the cluster but also the intensity ratio between the cluster and the analyte. As expected for orally and intravenously administered drugs, EMB is distributed homogenously in the lung parenchyma and blood vessels but not inside the airway areas (Figure 1C). The protonated molecule of EMB ($C_{10}H_{25}N_2O_2^+$) is detected at *m/z* 205.19105 with an RMSE of 0.62 ppm across 14 215 spectra. Figure 1D shows the distribution of the potassiated molecule of phosphatidylcholine (PC) 32:0 ($C_{40}H_{80}NO_8PK^+$, *m/z* 772.52531) detected in the high mass window from *m/z* 700 to 900. In comparison to EMB, PC32:0 is detected only in the lung parenchyma with an RMSE of 0.66 ppm over 15 638 spectra.

5 | CONCLUSION

Matrix ions are ubiquitous in all MALDI MS spectra, therefore providing the ideal internal standard for mass calibration "free of charge" without the need for additional standard substances and sample preparation steps. In many cases, cluster series span a wide mass range. Using the matrix ions identified in this study for mass calibration in combination with high mass resolution can therefore bring about sub-ppm mass accuracy, enabling the identification of targeted compounds, for example, drug compounds directly from an imaging data set, as shown earlier and in our recent work.[14,22] Matrices used primarily in the positive ion mode tend to generate more matrix ions with higher abundances than matrices designated for use in the negative ion mode. Furthermore, ions generated by positive mode matrices, that is, DHB or cinnamic acid derivatives, tend to cover a wider mass range and are capable of forming heavy clusters with excess of *m/z* 1500 containing more than 10 base molecules, whereas ions of basic negative mode matrices are typically not detected above *m/z* 600. The commonality of negative mode matrices is the formation of clusters based on deprotonation followed by the additional loss of hydrogen. This results in little variation in cluster composition between different matrix substances, which simplifies the adaption of a new matrix substance. Positive mode matrices can be quite different in terms of cluster composition, as can be observed when comparing DHB and CHCA. Whereas DHB clusters are dehydrated and contain a single charge carrier, clusters of cinnamic acid derivatives are usually not dehydrated and show a hydrogen/alkali metal cation exchange, thus containing multiple charge carriers.

ACKNOWLEDGMENTS

The authors thank Kerstin Walter and Christoph Hölscher (FZ Borstel) for providing mouse lung tissue. This work was supported by the Deutsche Forschungsgemeinschaft (INST 91/373-1-FUGG and SFB 1357). Open Access funding enabled and organized by Projekt DEAL.

PEER REVIEW

The peer review history for this article is available at https://publons.com/publon/10.1002/rcm.9110.

DATA AVAILABILITY STATEMENT

Data available in article supplementary material.

ORCID

Axel Treu https://orcid.org/0000-0002-0999-6241

Andreas Römpp https://orcid.org/0000-0001-8384-9250

REFERENCES

1. Römpp A, Spengler B. Mass spectrometry imaging with high resolution in mass and space. *Histochem Cell Biol*. 2013;139(6):759-783.
2. Spengler B. Mass spectrometry imaging of biomolecular information. *Anal Chem*. 2015;87(1):64-82.
3. Claude E, Jones EA, Pringle SD. DESI Mass Spectrometry Imaging (MSI). In: Cole LM, ed. *Imaging Mass Spectrometry: Methods and Protocols*. New York, NY: Springer New York; 2017:65-75.
4. Agüi-Gonzalez P, Jähne S, Phan NTN. SIMS imaging in neurobiology and cell biology. *J Anal at Spectrom*. 2019;34(7):1355-1368.
5. Nilsson A, Goodwin RJA, Shariatgorji M, Vallianatou T, Webborn PJH, Andrén PE. Mass spectrometry imaging in drug development. *Anal Chem*. 2015;87(3):1437-1455.
6. Gross JH. MALDI Matrices. In: *Mass Spectrometry A Textbook*. 2nd ed. Heidelberg: Springer; 2011:516-527.
7. Zenobi R, Knochenmuss R. Ion formation in MALDI mass spectrometry. *Mass Spectrom Rev*. 1999;17(5):337-366.
8. Mohan KR, Bartlett MG, Busch KL, Schoen AE, Gore N. Calibration point for electron ionization MS/MS spectra measured with multiquadrupole mass spectrometers. *J Am Soc Mass Spectrom*. 1994;5(6):576-582.
9. Jiang L, Moini M. Ultramark 1621 as a reference compound for positive and negative ion fast-atom bombardment high-resolution mass spectrometry. *J Am Soc Mass Spectrom*. 1992;3(8):842-846.
10. Kolarova L, Prokes L, Kucera L, et al. Clusters of monoisotopic elements for calibration in (TOF) mass spectrometry. *J Am Soc Mass Spectrom*. 2017;28(3):419-427.
11. Lou X, van Dongen JL, Meijer EW. Generation of CsI cluster ions for mass calibration in matrix-assisted laser desorption/ionization mass spectrometry. *J Am Soc Mass Spectrom*. 2010;21(7):1223-1226.
12. Kim JW, Ramaswamy BR, Chang KH, Isobe T, Tanabe S. Multiresidue analytical method for the determination of antimicrobials, preservatives, benzotriazole UV stabilizers, flame retardants and plasticizers in fish using ultra high performance liquid chromatography coupled with tandem mass spectrometry. *J Chromatogr a*. 2011;1218(22):3511-3520.
13. Guenther S, Römpp A, Kummer W, Spengler B. AP-MALDI imaging of neuropeptides in mouse pituitary gland with 5μm spatial resolution and high mass accuracy. *Int J Mass Spectrom*. 2011;305(2):228-237.
14. Desbenoit N, Walch A, Spengler B, Brunelle A, Römpp A. Correlative mass spectrometry imaging, applying time-of-flight secondary ion mass spectrometry and atmospheric pressure matrix-assisted laser desorption/ionization to a single tissue section. *Rapid Commun Mass Spectrom*. 2017;32(2):159-166.
15. Heiles S, Kompauer M, Muller MA, Spengler B. Atmospheric-pressure MALDI mass spectrometry imaging at 213 nm laser wavelength. *J Am Soc Mass Spectrom*. 2020;31(2):326-335.
16. Römpp A, Guenther S, Schober Y, et al. Histology by mass spectrometry: Label-free tissue characterization obtained from high-

accuracy bioanalytical imaging. *Angew Chem Int Ed*. 2010;49(22):3834-3838.
17. Guo Z, He L. A binary matrix for background suppression in MALDI-MS of small molecules. *Anal Bioanal Chem*. 2007;387(5):1939-1944.
18. Smirnov IP, Zhu X, Taylor T, et al. Suppression of α-Cyano-4-hydroxycinnamic acid matrix clusters and reduction of chemical noise in MALDI-TOF mass spectrometry. *Anal Chem*. 2004;76(10):2958-2965.
19. Marijana Petkovic JS, Müller M, Süß R, Arnold K, Arnhold J. Detection of adducts with matrix clusters in the positive and negative ion mode MALDI-TOF mass spectra of phospholipids. *Z Naturforsch*. 2009;64b:331-334.
20. Moench PA, Catoire A, Glick J, Flarakos J. Determination of tissue-specific ion suppression by liquid extraction surface analysis mass spectrometry. *Rapid Commun Mass Spectrom*. 2015;30(2):340-342.
21. Taylor AJ, Dexter A, Bunch J. Exploring ion suppression in mass spectrometry imaging of a heterogeneous tissue. *Anal Chem*. 2018;90(9):5637-5645.
22. Treu A, Kokesch-Himmelreich J, Walter K, Holscher C, Rompp A. Integrating high-resolution MALDI imaging into the development pipeline of anti-tuberculosis drugs. *J Am Soc Mass Spectrom*. 2020;31(11):2277-2286.
23. Koestler M, Kirsch D, Hester A, Leisner A, Guenther S, Spengler B. A high-resolution scanning microprobe matrix-assisted laser desorption/ionization ion source for imaging analysis on an ion trap/Fourier transform ion cyclotron resonance mass spectrometer. *Rapid Commun Mass Spectrom*. 2008;22(20):3275-3285.
24. CIAAW. *Current Atomic Masses* 2017; http://www.ciaaw.org/atomic-masses.htm. Accessed 10.02, 2019.
25. Römpp A, Guenther S, Takats Z, Spengler B. Mass spectrometry imaging with high resolution in mass and space (HR2 MSI) for reliable investigation of drug compound distributions on the cellular level. *Anal Bioanal Chem*. 2011;401(1):65-73.
26. Huber K, Khamehgir-Silz P, Schramm T, Gorshkov V, Spengler B, Rompp A. Approaching cellular resolution and reliable identification in mass spectrometry imaging of tryptic peptides. *Anal Bioanal Chem*. 2018;410(23):5825-5837.
27. Schiller J, Suss R, Fuchs B, et al. The suitability of different DHB isomers as matrices for the MALDI-TOF MS analysis of phospholipids: Which isomer for what purpose? *Eur Biophys J*. 2007;36(4–5):517-527.
28. Calvano CD, Monopoli A, Cataldi TRI, Palmisano F. MALDI matrices for low molecular weight compounds: An endless story? *Anal Bioanal Chem*. 2018;410(17):4015-4038.
29. Angel PM, Caprioli RM. Matrix-assisted laser desorption ionization imaging mass spectrometry: In situ molecular mapping. *Biochemistry*. 2013;52(22):3818-3828. https://doi.org/10.1021/bi301519p
30. Winter JD, Deshayes G, Boon F, Coulembier O, Dubois P, Gerbaux P. MALDI-ToF analysis of polythiophene: Use of trans-2-[3-(4-t-butyl-phenyl)-2-methyl- 2-propenylidene]malononitrile—DCTB—As matrix. *J Mass Spectrom*. 2011;46(3):237-246.
31. Wyatt MF, Stein BK, Brenton AG. Characterization of various Analytes using matrix-assisted laser desorption/ionization time-of-flight mass spectrometry and 2-[(2E)-3-(4-tert-Butylphenyl)-2-methylprop-2- enylidene]malononitrile matrix. *Anal Chem*. 2006;78(1):199-206.
32. Peukert M, Matros A, Lattanzio G, Kaspar S, Abadía J, Mock H-P. Spatially resolved analysis of small molecules by matrix-assisted laser desorption/ionization mass spectrometric imaging (MALDI-MSI). *New Phytol*. 2011;193(3):806-815.
33. Rzagalinski I, Kovačević B, Hainz N, Meier C, Tschernig T, Volmer DA. Toward higher sensitivity in quantitative MALDI imaging mass spectrometry of CNS drugs using a nonpolar matrix. *Anal Chem*. 2018;90(21):12592-12600.
34. Steven RT, Race AM, Bunch J. Para-Nitroaniline is a promising matrix for MALDI-MS imaging on intermediate pressure MS systems. *J Am Soc Mass Spectrom*. 2013;24(5):801-804.
35. Treu A, Rittner M, Kemken D, Schiebel H-M, Spiteller P, Dülcks T. Loss of atomic nitrogen from even-electron ions? A study on benzodiazepines. *J Mass Spectrom*. 2015;50(8):978-986.
36. Korte AR, Lee YJ. MALDI-MS analysis and imaging of small molecule metabolites with 1,5-diaminonaphthalene (DAN). *J Mass Spectrom*. 2014;49(8):737-741.
37. Dueñas ME, Carlucci L, Lee YJ. Matrix recrystallization for MALDI-MS imaging of maize lipids at high-spatial resolution. *J Am Soc Mass Spectrom*. 2016;27(9):1575-1578.
38. Berry KAZ, Li B, Reynolds SD, et al. MALDI imaging MS of phospholipids in the mouse lung. *J Lipid Res*. 2011;52(8):1551-1560.
39. Scott AJ, Flinders B, Cappell J, et al. Norharmane matrix enhances detection of endotoxin by MALDI-MS for simultaneous profiling of pathogen, host, and vector systems. *Pathog Dis*. 2016;74(8). https://doi.org/10.1093/femspd/ftw097
40. Genangeli M, Heijens AMM, Rustichelli A, et al. MALDI-mass spectrometry imaging to investigate lipid and bile acid modifications caused by lentil extract used as a potential Hypocholesterolemic treatment. *J Am Soc Mass Spectrom*. 2019;30(10):2041-2050.
41. Prentice BM, Chumbley CW, Caprioli RM. High-speed MALDI MS/MS imaging mass spectrometry using continuous raster sampling. *Journal of Mass Spectrometry: JMS*. 2015;50(4):703-710.
42. Cerruti CD, Benabdellah F, Laprévote O, Touboul D, Brunelle A. MALDI imaging and structural analysis of rat brain lipid negative ions with 9-Aminoacridine matrix. *Anal Chem*. 2012;84(5):2164-2171.
43. Makarov A, Denisov E, Lange O, Horning S. Dynamic range of mass accuracy in LTQ Orbitrap hybrid mass spectrometer. *J Am Soc Mass Spectrom*. 2006;17(7):977-982.

SUPPORTING INFORMATION

Additional supporting information may be found online in the Supporting Information section at the end of this article.

How to cite this article: Treu A, Römpp A. Matrix ions as internal standard for high mass accuracy matrix-assisted laser desorption/ionization mass spectrometry imaging. *Rapid Commun Mass Spectrom*. 2021;35(16):e9110. https://doi.org/10.1002/rcm.9110

Supporting information

Matrix ions as internal standard for high mass accuracy MALDI mass spectrometry imaging

Axel Treu[a] and Andreas Römpp[a,*]

Affiliations

[a] Chair of Bioanalytical Sciences and Food Analysis, University of Bayreuth, Bayreuth, Germany

[*] Correspondence to this author

Tables of matrix clusters

Table S1. Overview of all identified **DHB** clusters of the general composition $[aM+H-bH_2O]^+$ (a = 1,2,3…; b ≤ a) series detected on tissue in **positive** ion mode. Bold letters indicate abundant ion species.

Cluster composition	Sum formula	Theoretical *m/z*	Measured *m/z*	RMSE [ppm]
$M+H^+$	$C_7H_7O_4^+$	155.03389	155.03381	0.58
***M+H-H_2O^+**	**$C_7H_5O_3^+$**	**137.02332**	**137.02332**	**-**
$2M+H-H_2O^+$	$C_{14}H_{11}O_7^+$	291.04993	291.04977	0.27
$2M+H-2H_2O^+$	**$C_{14}H_9O_6^+$**	**273.03936**	**273.03925**	**0.29**
$3M+H-2H_2O^+$	$C_{21}H_{15}O_{10}^+$	427.06597	427.06619	0.53
$3M+H-3H_2O^+$	**$C_{21}H_{13}O_9^+$**	**409.05541**	**409.05554**	**0.25**
$4M+H-4H_2O^+$	$C_{28}H_{17}O_{12}^+$	545.07145	545.07147	0.19
$5M+H-4H_2O^+$	$C_{35}H_{23}O_{16}^+$	699.09806	699.09869	1.11
$5M+H-5H_2O^+$	**$C_{35}H_{21}O_{15}^+$**	**681.08750**	**681.08789**	**0.45**
$6M+H-6H_2O^+$	$C_{42}H_{25}O_{18}^+$	817.10354	817.10382	0.51
$7M+H-6H_2O^+$	$C_{49}H_{31}O_{22}^+$	971.13015	971.13062	0.54
$7M+H-7H_2O^+$	$C_{49}H_{29}O_{21}^+$	953.11958	953.12036	0.81
$8M+H-7H_2O^+$	**$C_{56}H_{35}O_{25}^+$**	**1107.14620**	**1107.14648**	**0.31**
$8M+H-8H_2O^+$	**$C_{56}H_{33}O_{24}^+$**	**1089.13563**	**1089.13599**	**0.34**
$9M+H-8H_2O^+$	$C_{63}H_{39}O_{28}^+$	1243.16224	1243.16284	0.41
$9M+H-9H_2O^+$	$C_{63}H_{37}O_{27}^+$	1225.15167	1225.15222	0.43
$10M+H-9H_2O^+$	$C_{70}H_{43}O_{31}^+$	1379.17828	1379.17786	0.59
$10M+H-10H_2O^+$	$C_{70}H_{41}O_{30}^+$	1361.16772	1361.16809	0.60

Table S2. Overview of all identified **DHB** ions belonging to the $[aM+Na-bH_2O]^+$ (a = 1,2,3…; b ≤ a) series detected on tissue in **positive** ion mode. Bold letters indicate abundant ion species.

Cluster composition	Sum formula	Theoretical *m/z*	Measured *m/z*	RMSE [ppm]
$M+Na^+$	$C_7H_6O_4Na^+$	177.01583	177.01578	0.63
$M+Na-H_2O^+$	$C_7H_4O_3Na^+$	159.00526	159.00522	0.67
$2M+Na-H_2O^+$	$C_{14}H_{10}O_7Na^+$	313.03187	313.03162	0.89
$2M+Na-2H_2O^+$	$C_{14}H_8O_6Na^+$	295.02131	295.02127	0.17
$3M+Na-2H_2O^+$	$C_{21}H_{14}O_{10}Na^+$	449.04792	449.04745	1.20
$3M+Na-3H_2O^+$	**$C_{21}H_{12}O_9Na^+$**	**431.03735**	**431.03745**	**0.34**

4M+Na-2H_2O^+	$C_{28}H_{20}O_{14}Na^+$	603.07453	603.07452	0.35
***4M+Na-3H_2O^+**	**$C_{28}H_{18}O_{13}Na^+$**	**585.06396**	**585.06396**	**-**
4M+Na-4H_2O^+	$C_{28}H_{16}O_{12}Na^+$	567.05340	567.05377	0.69
5M+Na-3H_2O^+	$C_{35}H_{24}O_{17}Na^+$	739.09057	739.09106	0.51
5M+Na-4H_2O^+	$C_{35}H_{22}O_{16}Na^+$	721.08001	721.08020	0.31
5M+Na-5H_2O^+	$C_{35}H_{20}O_{15}Na^+$	703.06944	703.06964	0.63
6M+Na-4H_2O^+	$C_{42}H_{28}O_{20}Na^+$	875.10661	875.10602	0.87
6M+Na-5H_2O^+	$C_{42}H_{26}O_{19}Na^+$	857.09605	857.09601	0.45
7M+Na-6H_2O^+	$C_{49}H_{30}O_{22}Na^+$	993.11209	993.11285	0.66
9M+Na-8H_2O^+	$C_{63}H_{38}O_{28}Na^+$	1265.14418	1265.14465	0.75
9M+Na-9H_2O^+	$C_{63}H_{36}O_{27}Na^+$	1247.13362	1247.58753	1.15

Table S3. Overview of all identified **DHB** ions belonging to the [*a*M+K-*b*H_2O]$^+$ (a = 1,2,3…; b ≤ a) series detected on tissue in **positive** ion mode. Bold letters indicate abundant ion species.

Cluster composition	Sum formula	Theoretical *m/z*	Measured *m/z*	RMSE [ppm]
M+K^+	$C_7H_6O_4K^+$	192.98977	192.98972	0.40
M+K-H_2O^+	$C_7H_4O_3K^+$	174.97920	174.97920	0.49
2M+K^+	$C_{14}H_{12}O_8K^+$	347.01637	347.01611	1.18
2M+K-H_2O^+	**$C_{14}H_{10}O_7K^+$**	**329.00581**	**329.00552**	**0.92**
2M+K-2H_2O^+	**$C_{14}H_8O_6K^+$**	**310.99525**	**310.99509**	**0.59**
3M+K-2H_2O^+	**$C_{21}H_{14}O_{10}K^+$**	**465.02185**	**465.02158**	**0.55**
3M+K-3H_2O^+	**$C_{21}H_{12}O_9K^+$**	**447.01129**	**447.01108**	**0.49**
4M+K-2H_2O^+	$C_{28}H_{20}O_{14}K^+$	619.04846	619.04865	0.54
4M+K-3H_2O^+	**$C_{28}H_{18}O_{13}K^+$**	**601.03790**	**601.03766**	**0.41**
4M+K-4H_2O^+	$C_{28}H_{16}O_{12}K^+$	583.02734	583.02747	0.30
5M+K-3H_2O^+	$C_{35}H_{24}O_{17}K^+$	755.06451	755.06488	0.70
5M+K-4H_2O^+	$C_{35}H_{22}O_{16}K^+$	737.05394	737.05432	0.41
5M+K-5H_2O^+	$C_{35}H_{20}O_{15}K^+$	719.04338	719.04321	0.41
6M+K-4H_2O^+	$C_{42}H_{28}O_{20}K^+$	891.08055	891.08057	0.55
6M+K-5H_2O^+	$C_{42}H_{26}O_{19}K^+$	873.06999	873.06982	0.40
6M+K-6H_2O^+	$C_{42}H_{24}O_{18}K^+$	855.05942	855.06071	0.69
7M+K-5H_2O^+	$C_{49}H_{32}O_{23}K^+$	1027.09660	1027.09802	1.23
7M+K-6H_2O^+	$C_{49}H_{30}O_{22}K^+$	1009.08603	1009.08661	0.57
7M+K-7H_2O^+	$C_{49}H_{28}O_{21}K^+$	991.07546	991.07581	0.53
8M+K-6H_2O^+	$C_{56}H_{36}O_{26}K^+$	1163.11264	1163.11353	0.76
8M+K-7H_2O^+	$C_{56}H_{34}O_{25}K^+$	1145.10207	1145.10242	0.24
8M+K-8H_2O^+	$C_{56}H_{32}O_{24}K^+$	1127.09151	1127.09131	0.69
9M+K-8H_2O^+	$C_{63}H_{38}O_{28}K^+$	1281.11812	1281.11853	0.35
9M+K-9H_2O^+	$C_{63}H_{36}O_{27}K^+$	1263.10755	1263.10779	0.80
10M+K-9H_2O^+	$C_{70}H_{42}O_{31}K^+$	1417.13416	1417.13513	0.39

Table S4. Overview of all identified **DHB** ions belonging to the [*a*M+*b*Alkali-(*b*-1)H-*c*H_2O]$^+$ (*a* = 1,2,3…; *b* = 1,2,3…; *c* = 0,1,2,3…) series detected in **positive** ion mode.

Cluster composition	Sum formula	Theoretical *m/z*	Measured *m/z*	RMSE [ppm]
M+2Na-H^+	$C_7H_5O_4Na_2^+$	198.99777	198.99760	0.86

M+Na+K-H$^+$	$C_7H_5O_4NaK^+$	214.97171	214.97163	0.45
M+2K-H$^+$	$C_7H_5O_4K_2^+$	230.94565	230.94563	0.21
2M+Na+K-H-H_2O^+	$C_{14}H_9O_7NaK^+$	350.98775	350.98752	0.68
2M+2K-H-H_2O^+	**$C_{14}H_9O_7K_2^+$**	**366.96169**	**366.96152**	**0.59**
3M+2Na-H-2H_2O^+	$C_{21}H_{13}O_{10}Na_2^+$	471.02986	471.03000	0.39
3M+Na+K-H-2H_2O^+	$C_{21}H_{13}O_{10}NaK^+$	487.00380	487.00397	0.36
3M+Na+K-H-3H_2O^+	$C_{21}H_{11}O_{19}NaK^+$	468.99323	468.99326	0.42
3M+2K-H-2H_2O^+	**$C_{21}H_{13}O_{10}K_2^+$**	**502.97774**	**502.97766**	**0.37**
3M+2K-H-3H_2O^+	$C_{21}H_{11}O_{19}K_2^+$	484.96717	484.96738	0.76
3M+3Na-2H-H_2O^+	$C_{21}H_{14}O_{11}Na_3^+$	526.99631	526.99652	0.81
3M+Na+K_2-2H-H_2O^+	$C_{21}H_{14}O_{11}NaK_2^+$	542.97025	542.97083	0.76
3M+K_3-2H-H_2O^+	$C_{21}H_{14}O_{11}K_3^+$	558.94418	558.94464	0.78
4M+2Na-H-2H_2O^+	$C_{28}H_{19}O_{14}Na_2^+$	625.05647	625.05664	0.61
4M+2Na-H-3H_2O^+	$C_{28}H_{17}O_{13}Na_2^+$	607.04591	607.04639	0.77
4M+Na+K-H-2H_2O^+	$C_{28}H_{19}O_{14}NaK^+$	641.03041	641.03058	0.45
4M+Na+K-H-3H_2O^+	**$C_{28}H_{17}O_{13}NaK^+$**	**623.01984**	**623.02014**	**0.51**
4M+2K-H-2H_2O^+	**$C_{28}H_{19}O_{14}K_2^+$**	**657.00434**	**657.00488**	**0.56**
4M+2K-H-3H_2O^+	**$C_{28}H_{17}O_{13}K_2^+$**	**638.99378**	**638.99408**	**0.44**
4M+Na+2K-2H-2H_2O^+	$C_{28}H_{18}O_{14}NaK_2^+$	678.986290	678.98688	0.57
4M+3K-2H-2H_2O^+	**$C_{28}H_{18}O_{14}K_3^+$**	**694.96023**	**694.96069**	**0.49**
5M+Na+K-H-3H_2O^+	$C_{35}H_{23}O_{17}NaK^+$	777.04645	777.04639	0.45
5M+2K-H-3H_2O^+	**$C_{35}H_{23}O_{17}K_2^+$**	**793.02038**	**793.02081**	**0.63**
5M+2K-H-4H_2O^+	$C_{35}H_{21}O_{16}K_2^+$	775.00982	775.00989	0.44
5M+3K-2H-3H_2O^+	$C_{35}H_{22}O_{17}K_3^+$	830.97627	830.97662	0.73

Table S5. Overview of all identified **DHB** ions detected on tissue in **negative** ion mode. Bold letters indicate abundant ion species.

Cluster composition	Sum formula	Theoretical *m/z*	Measured *m/z*	RMSE [ppm]
***M-H$^-$**	**$C_7H_5O_4^-$**	**153.01933**	**153.01933**	**-**
M-2H$^{\cdot-}$	**$C_7H_4O_4^{\cdot-}$**	**152.01151**	**152.01136**	**0.92**
2M-H$^-$	$C_{14}H_{11}O_8^-$	307.04594	307.04602	0.30
2M-2H$^{\cdot-}$	$C_{14}H_{10}O_8^{\cdot-}$	306.03812	306.03807	0.85
***2M-H-H_2O^-**	**$C_{14}H_9O_7^-$**	**289.03538**	**289.03537**	**-**
2M-2H-$H_2O^{\cdot-}$	**$C_{14}H_8O_7^{\cdot-}$**	**288.02755**	**288.02759**	**-**
2M-H-2H_2O^-	$C_{14}H_7O_6^-$	271.02481	271.02481	0.12
2M-2H+Na$^-$	**$C_{14}H_{10}O_8Na^-$**	**329.02789**	**329.02773**	**0.48**
2M-3H+Na$^{\cdot-}$	**$C_{14}H_9O_8Na^{\cdot-}$**	**328.02006**	**328.02030**	**0.75**
2M-2H+Na-H_2O^-	$C_{14}H_8O_7Na^-$	311.01732	311.01728	0.86
2M-3H+Na-$H_2O^{\cdot-}$	$C_{14}H_7O_7Na^{\cdot-}$	310.00950	310.00946	0.59
2M-2H+K$^-$	**$C_{14}H_{10}O_8K^-$**	**345.00182**	**345.00170**	**0.34**
2M-3H+K$^{\cdot-}$	**$C_{14}H_{19}O_8K^{\cdot-}$**	**343.99400**	**343.99416**	**0.51**
2M-2H+K-H_2O^-	$C_{14}H_8O_7K^-$	326.99126	326.99146	0.84
2M-3H+K-$H_2O^{\cdot-}$	$C_{14}H_7O_7K^{\cdot-}$	325.98343	325.98372	1.45
3M-H-H_2O^-	**$C_{21}H_{15}O_{11}^-$**	**443.06198**	**443.06227**	**0.66**
3M-2H-$H_2O^{\cdot-}$	$C_{21}H_{14}O_{11}^{\cdot-}$	442.05416	442.05441	0.79
3M-H-2H_2O^-	**$C_{21}H_{13}O_{10}^-$**	**425.05142**	**425.05150**	**0.26**
3M-2H-2$H_2O^{\cdot-}$	$C_{21}H_{13}O_{10}^{\cdot-}$	424.04360	424.04397	0.90

3M-H-3H_2O^-	$C_{21}H_{11}O_9^-$	407.04086	407.04085	0.81
3M-2H+Na-H_2O^-	**$C_{21}H_{14}O_{11}Na^-$**	**465.04393**	**465.04367**	**0.57**
3M-3H+Na-$H_2O^{-\cdot}$	**$C_{21}H_{13}O_{11}Na^{-\cdot}$**	**464.03610**	**464.03638**	**0.63**
3M-2H+Na-2H_2O^-	$C_{21}H_{12}O_{10}Na^-$	447.03336	447.03355	0.46
3M-3H+Na-2$H_2O^{-\cdot}$	$C_{21}H_{11}O_{10}Na^{-\cdot}$	446.02554	446.02578	0.57
3M-2H+K-H_2O^-	**$C_{21}H_{14}O_{11}K^-$**	**481.01787**	**481.01770**	**0.38**
3M-3H+K-$H_2O^{-\cdot}$	**$C_{21}H_{13}O_{11}K^{-\cdot}$**	**480.01004**	**480.01034**	**0.65**
3M-2H+K-2H_2O^-	$C_{21}H_{12}O_{10}K^-$	463.00730	463.00784	1.20
3M-3H+K-2$H_2O^{-\cdot}$	**$C_{21}H_{11}O_{10}K^{-\cdot}$**	**461.99948**	**462.00004**	**1.25**
3M-3H+2Na$^-$	**$C_{21}H_{15}O_{12}Na_2^-$**	**505.03644**	**505.03647**	**0.16**
3M-4H+2Na$^{-\cdot}$	$C_{21}H_{14}O_{12}Na_2^{-\cdot}$	504.0286	504.02874	0.31
3M-3H+Na+K$^-$	**$C_{21}H_{15}O_{12}NaK^-$**	**521.01038**	**521.01031**	**0.26**
3M-4H+Na+K$^{-\cdot}$	**$C_{21}H_{14}O_{12}NaK^{-\cdot}$**	**520.00255**	**520.00263**	**0.23**
3M-3H+2K$^-$	**$C_{21}H_{15}O_{12}K_2^-$**	**536.98431**	**536.98440**	**0.23**
3M-4H+2K$^{-\cdot}$	**$C_{21}H_{14}O_{12}K_2^{-\cdot}$**	**535.97649**	**535.97653**	**0.22**
***4M-H-2H_2O^-**	**$C_{28}H_{19}O_{14}^-$**	**579.07803**	**579.07803**	**-**
4M-2H-2$H_2O^{-\cdot}$	**$C_{28}H_{18}O_{14}^{-\cdot}$**	**578.07020**	**578.07020**	**-**
4M-H-3H_2O^-	**$C_{28}H_{17}O_{13}^-$**	**561.06746**	**561.06771**	**0.46**
4M-2H-3$H_2O^{-\cdot}$	$C_{28}H_{16}O_{13}^{-\cdot}$	560.05964	560.06003	0.73
4M-H-4H_2O^-	$C_{28}H_{15}O_{12}^-$	543.05690	543.05688	0.43
4M-2H+Na-2H_2O^-	**$C_{28}H_{18}O_{14}Na^-$**	**601.06000**	**601.05987**	**0.22**
4M-3H+Na-2$H_2O^{-\cdot}$	$C_{28}H_{17}O_{14}Na^{-\cdot}$	600.0521	600.05257	0.72
4M-2H+Na-3H_2O^-	$C_{28}H_{16}O_{13}Na^-$	583.04941	583.04985	0.80
4M-2H+K-2H_2O^-	**$C_{28}H_{18}O_{14}K^-$**	**617.03391**	**617.03427**	**0.60**
4M-3H+K-2$H_2O^{-\cdot}$	$C_{28}H_{17}O_{14}K^{-\cdot}$	616.02609	616.02683	1.23
4M-3H+2Na-H_2O^-	$C_{28}H_{19}O_{15}Na_2^-$	641.05248	641.05296	0.76
4M-4H+2Na-$H_2O^{-\cdot}$	$C_{28}H_{18}O_{15}Na_2^{-\cdot}$	640.04466	640.04523	0.92
4M-3H+Na+K-H_2O^-	**$C_{28}H_{19}O_{15}NaK^-$**	**657.02642**	**657.02672**	**0.52**
4M-4H+Na+K-$H_2O^{-\cdot}$	$C_{28}H_{18}O_{15}NaK^{-\cdot}$	656.01859	656.01920	0.94
4M-3H+2K-H_2O^-	**$C_{28}H_{19}O_{15}NaK^-$**	**673.00036**	673.00081	0.70
5M-H-3H_2O^-	**$C_{35}H_{23}O_{17}^-$**	**715.09407**	**715.09443**	**0.51**
5M-2H-3$H_2O^{-\cdot}$	$C_{35}H_{22}O_{17}^{-\cdot}$	714.08625	714.08692	0.97
5M-H-4H_2O^-	$C_{35}H_{21}O_{16}^-$	697.08351	697.08409	0.86
5M-2H+Na-2H_2O^-	**$C_{35}H_{24}O_{18}Na^-$**	**755.08658**	**755.08703**	**0.62**
5M-2H+Na-3H_2O^-	**$C_{35}H_{22}O_{17}Na^-$**	**737.07602**	**737.07622**	**0.31**
5M-3H+Na-3$H_2O^{-\cdot}$	$C_{35}H_{21}O_{17}Na^{-\cdot}$	736.06819	736.06866	0.67
5M-2H+K-2H_2O^-	**$C_{35}H_{24}O_{18}K^-$**	**771.06052**	**771.06107**	**0.73**
5M-2H+K-3H_2O^-	**$C_{35}H_{22}O_{17}K^-$**	**753.04995**	**753.05058**	**0.85**
5M-3H+K-3$H_2O^{-\cdot}$	$C_{35}H_{21}O_{17}K^{-\cdot}$	752.04213	752.04297	1.14
5M-2H+K-4H_2O^-	$C_{35}H_{20}O_{16}K^-$	735.03939	735.03991	0.89
5M-3H+2Na-2H_2O^-	$C_{35}H_{23}O_{18}Na_2^-$	777.06853	777.06897	0.61
5M-3H+Na+K-2H_2O^-	**$C_{35}H_{23}O_{18}NaK^-$**	**793.04246**	**793.04275**	**0.40**
5M-4H+Na+K-2$H_2O^{-\cdot}$	$C_{35}H_{22}O_{18}NaK^{-\cdot}$	792.03464	792.03520	0.75
5M-3H+Na+K-3H_2O^-	$C_{35}H_{20}O_{17}NaK^-$	774.02407	774.02456	0.72
5M-3H+2K-2H_2O^-	**$C_{35}H_{23}O_{18}K_2^-$**	**808.00858**	**808.00902**	**0.63**
5M-4H+2Na+K-H_2O^-	$C_{35}H_{21}O_{19}Na_2K^-$	833.03497	833.03495	0.21
5M-4H+Na+K_2-H_2O^-	$C_{35}H_{21}O_{19}NaK_2^-$	849.00891	849.00885	0.21

Table S6. Overview of all identified **CHCA** ions detected on tissue in **positive** ion mode. Bold letters indicate abundant ion species.

Cluster composition	Sum formula	Theoretical *m/z*	Measured *m/z*	RMSE [ppm]
$M+H^+$	$C_{10}H_8NO_3^+$	190.04987	190.04982	1.15
*$M+H-CO_2^+$	$C_9H_8NO^+$	146.06004	146.06004	-
$M+Na^+$	$C_{10}H_7NO_3Na^+$	212.03181	212.03175	0.27
$M+Na-CO_2^+$	$C_9H_7NONa^+$	168.04198	168.04185	0.85
$M+K^+$	**$C_{10}H_7NO_3K^+$**	**228.00575**	**228.00563**	
$M+K-H_2O^+$	$C_{10}H_5NO_2K^+$	209.99519	209.99516	0.87
$M+K-CO_2^+$	$C_9H_7NOK^+$	184.01592	184.01582	0.38
$M+2Na-H^+$	$C_{10}H_6NO_3Na_2^+$	234.01376	234.01369	0.45
$M+Na+K-H^+$	**$C_{10}H_6NO_3NaK^+$**	**249.98770**	**249.98764**	**0.38**
$M+Na+K-H-CO_2^+$	$C_9H_6NONaK^+$	205.99787	205.99785	0.34
$M+2K-H^+$	**$C_{10}H_6NO_3K_2^+$**	**265.96163**	**265.96152**	**0.19**
$M+2K-H-CO_2^+$	$C_9H_6NOK_2^+$	221.97180	221.97182	0.82
$2M+Na^+$	$C_{20}H_{14}N_2O_6Na^+$	401.07441	401.07426	1.47
$2M+K^+$	$C_{20}H_{14}N_2O_6K^+$	417.04834	417.04825	1.21
$2M+K-CO_2^+$	$C_{19}H_{14}N_2O_4K^+$	373.05851	373.05826	1.65
$2M+2Na-H^+$	$C_{20}H_{13}N_2O_6Na_2^+$	423.05635	423.05624	1.26
$2M+Na+K-H^+$	**$C_{20}H_{13}N_2O_6NaK^+$**	**439.03029**	**439.03018**	**0.30**
***$2M+2K^+$**	**$C_{20}H_{13}N_2O_6K_2^+$**	**455.00423**	**455.00423**	**-**
$2M+K-H_2O^+$	$C_{20}H_{11}N_2O_5K_2^+$	436.99366	436.99365	1.28
$2M+2K-CO_2^+$	$C_{19}H_{13}N_2O_4K_2^+$	411.01440	411.01437	1.25
$2M+2Na+K-2H^+$	$C_{20}H_{12}N_2O_6Na_2K^+$	461.01223	461.01193	1.22
$2M+Na+2K-2H^+$	**$C_{20}H_{12}N_2O_6NaK_2^+$**	**476.98617**	**476.98593**	**0.51**
$2M+Na+2K-2H-CO_2^+$	$C_{19}H_{12}N_2O_4NaK_2^+$	432.99634	432.99609	1.1
$3M+Na+K-H^+$	$C_{30}H_{20}N_3O_9NaK^+$	628.07288	628.07245	1.01
$3M+Na+K-H-CO_2^+$	$C_{29}H_{20}N_3O_7NaK^+$	584.08305	584.08313	1.04
$3M+2K-H-CO_2^+$	$C_{30}H_{20}N_3O_9K_2^+$	600.05699	600.05701	1.1
$3M+2Na+K-2H^+$	$C_{30}H_{19}N_3O_9Na_2K^+$	650.05483	650.05469	1.18
$3M+Na+2K-2H^+$	**$C_{30}H_{19}N_3O_9NaK_2^+$**	**666.02876**	**666.02844**	**0.82**
$3M+Na+2K-2H-CO_2^+$	$C_{29}H_{19}N_3O_7NaK_2^+$	622.03893	622.03857	0.90
$3M+3K-2H^+$	**$C_{30}H_{19}N_3O_9K_3^+$**	**682.00270**	**682.00238**	**0.98**
$3M+3K-2H-CO_2^+$	$C_{29}H_{19}N_3O_7K_3^+$	638.01287	638.01263	1.05
$3M+3Na+K-3H^+$	$C_{30}H_{18}N_3O_9Na_3K^+$	672.03677	672.03644	0.92
$3M+2Na+2K-3H^+$	$C_{30}H_{18}N_3O_9Na_2K_2^+$	688.01071	688.01038	1.16
$3M+Na+3K-3H^+$	**$C_{30}H_{18}N_3O_9NaK_3^+$**	**703.98464**	**703.98444**	**1.1**
***$3M+4K-3H^+$**	**$C_{30}H_{18}N_3O_9K_4^+$**	**719.95858**	**719.95858**	**-**
$4M+3K-2H^+$	**$C_{40}H_{26}N_4O_{12}K_3^+$**	**871.04529**	**871.04468**	**1.08**
$4M+4K-3H^+$	$C_{40}H_{25}N_4O_{12}K_4^+$	909.00117	909.00140	0.93
$4M+2Na+3K-4H^+$	$C_{40}H_{24}N_4O_{12}Na_2K_3^+$	915.00918	915.00861	1.50
$4M+Na+4K-4H^+$	$C_{40}H_{24}N_4O_{12}NaK_4^+$	930.98312	930.98224	1.44

Table S7. Overview of all identified **SA** ions detected on tissue in **positive** ion mode. Bold letters indicate abundant ion species.

Cluster composition	Sum formula	Theoretical *m/z*	Measured *m/z*	RMSE [ppm]

$M+H^+$	**$C_{11}H_{13}O_5^+$**	**225.07575**	**225.07567**	0.49
$M+H-H_2O^+$	$C_{11}H_{13}O_5^+$	207.06519	207.06516	0.28
$M+H-CO_2^+$	$C_{10}H_{13}O_3^+$	181.08592	181.08591	0.72
$M+NH_4^+$	$C_{11}H_{16}NO_5^+$	242.10230	242.10228	0.49
$M+Na^+$	$C_{11}H_{12}O_5Na^+$	247.05769	247.05763	0.28
***M+K^+**	**$C_{11}H_{12}O_5K^+$**	**263.03163**	**263.03162**	**-**
$M+K-H_2O^+$	$C_{11}H_{10}O_4K^+$	245.02107	245.02095	0.28
$M+K-CO_2^+$	$C_{10}H_{12}O_3K^+$	219.04180	219.04176	0.29
$M+2Na-H^+$	$C_{11}H_{11}O_5Na_2^+$	269.03964	269.03970	0.72
$M+Na+K-H^+$	$C_{11}H_{11}O_5NaK^+$	285.01358	285.01355	0.29
$M+2K-H^+$	**$C_{11}H_{11}O_5K_2^+$**	**300.98751**	**300.98743**	**0.26**
$M+2K-H-H_2O^+$	$C_{11}H_9O_4K_2^+$	282.97695	282.97681	0.62
$M+2K-H-CH_3^+$	$C_{10}H_8O_5K_2^+$	285.96404	285.96396	0.37
$2M+H^+$	$C_{22}H_{25}O_{10}^+$	449.14422	449.14447	0.49
$2M+H-H_2O^+$	$C_{22}H_{23}O_9^+$	431.13366	431.13370	0.67
$2M+NH_4^+$	$C_{22}H_{28}NO_{10}^+$	466.17077	466.17123	0.89
$2M+Na^+$	$C_{22}H_{24}O_{10}Na^+$	471.12617	471.12650	0.80
$2M+K^+$	**$C_{22}H_{24}O_{10}K^+$**	**487.10011**	**487.10013**	**0.27**
$2M+K-H_2O^+$	$C_{22}H_{22}O_9K^+$	469.08954	469.08978	0.84
$2M+K-CO_2^+$	$C_{21}H_{24}O_8K^+$	443.11028	443.11053	0.68
$2M+2Na-H^+$	$C_{22}H_{23}O_{10}Na_2^+$	493.10811	493.10855	0.57
$2M+Na+K-H^+$	**$C_{22}H_{23}O_{10}NaK^+$**	**509.08205**	**509.08243**	**0.81**
***2M+2K-H^+**	**$C_{22}H_{23}O_{10}K_2^+$**	**525.05599**	**525.05597**	**-**
$2M+3K-2H^+$	$C_{22}H_{22}O_{10}K_3^+$	563.01187	563.01233	0.98
$3M+NH_4^+$	$C_{33}H_{40}NO_{15}^+$	690.23925	690.23999	1.02
$3M+Na^+$	$C_{33}H_{36}O_{15}Na^+$	695.19464	695.19543	0.87
$3M+K^+$	**$C_{33}H_{36}O_{15}K^+$**	**711.16858**	**711.16895**	**0.57**
$3M+K-H_2O^+$	$C_{33}H_{34}O_{14}K^+$	693.15801	693.15851	0.86
$3M+K-CO_2^+$	$C_{32}H_{36}O_{13}K^+$	667.17875	667.17859	1.13
$3M+Na+K-H^+$	**$C_{33}H_{35}O_{15}NaK^+$**	**733.15052**	**733.15027**	**0.76**
$3M+2K-H^+$	**$C_{33}H_{35}O_{15}K_2^+$**	**749.12446**	**749.12421**	**0.91**
$3M+2K-H-H_2O^+$	$C_{33}H_{35}O_{15}K_2^+$	731.11389	731.11359	0.84
$3M+2Na+K-2H^+$	$C_{33}H_{34}O_{15}Na_2K^+$	755.13247	755.13220	0.95
$3M+Na+2K-2H^+$	$C_{33}H_{34}O_{15}NaK_2^+$	771.10640	771.10614	0.97
$3M+3K-2H^+$	$C_{33}H_{34}O_{15}K_3^+$	787.08034	787.08002	0.98
$4M+Na^+$	$C_{44}H_{48}O_{20}Na^+$	919.26311	919.26255	0.39
***4M+K^+**	**$C_{44}H_{48}O_{20}K^+$**	**935.23705**	**935.23705**	**-**
$4M+K-H_2O^+$	$C_{44}H_{46}O_{19}K^+$	917.22649	917.22595	0.67
$4M+Na+K-H^+$	$C_{44}H_{47}O_{20}NaK^+$	957.21900	957.21865	0.14
$4M+2K-H^+$	**$C_{44}H_{47}O_{20}K_2^+$**	**973.19293**	**973.19220**	**0.30**
$4M+2K-H-H_2O^+$	$C_{44}H_{45}O_{19}K_2^+$	955.18237	955.18204	0.42
$4M+Na+2K-2H^+$	$C_{44}H_{46}O_{20}NaK_2^+$	995.17488	995.17453	0.19
$4M+3K-2H^+$	$C_{44}H_{46}O_{20}K_3^+$	1011.14881	1011.14819	0.19
$5M+Na^+$	$C_{55}H_{60}O_{25}Na^+$	1143.33159	1143.33130	0.57
$5M+K^+$	**$C_{55}H_{60}O_{25}K^+$**	**1159.30553**	**1159.30518**	**0.38**
$5M+Na+K-H^+$	$C_{55}H_{59}O_{25}NaK^+$	1181.28747	1181.28735	0.41
$5M+2K-H^+$	**$C_{55}H_{59}O_{25}K_2^+$**	**1197.26147**	**1197.26086**	**0.57**
$5M+2K-H-H_2O^+$	$C_{55}H_{57}O_{24}K_2^+$	1179.25084	1179.25085	0.52
$5M+Na+2K-2H^+$	$C_{55}H_{58}O_{25}NaK_2^+$	1219.24335	1219.24341	0.38
$5M+3K-2H^+$	$C_{55}H_{58}O_{25}K_3^+$	1235.21729	1235.21680	0.77

6M+K$^+$	**$C_{66}H_{72}O_{30}K^+$**	**1383.37310**	**1383.37329**	**0.19**
6M+Na+K-H$^+$	$C_{66}H_{71}O_{30}NaK^+$	1405.35594	1405.35522	1.11
6M+2K-H$^+$	**$C_{66}H_{71}O_{30}K_2^+$**	**1421.32988**	**1421.32849**	**1.19**
6M+2K-H-H_2O^+	$C_{66}H_{69}O_{29}K_2^+$	1403.31931	1403.31860	1.19
6M+3K-2H$^+$	$C_{66}H_{70}O_{30}K_3^+$	1459.28576	1459.28430	1.13

Table S8. Overview of all identified **CA** ions detected on tissue in **positive** ion mode. Bold letters indicate abundant ion species.

Cluster composition	**Sum formula**	**Theoretical *m/z***	**Measured *m/z***	**RMSE [ppm]**
***M+H$^+$**	$C_9H_9O_4^+$	181.04953	181.04953	-
M+H-H_2O^+	$C_9H_7O_3^+$	163.03897	163.03896	0.14
M+H-CO_2^+	$C_8H_9O_2^+$	137.05971	137.05972	0.37
M+Na$^+$	$C_9H_8O_4Na^+$	203.03148	203.03143	0.25
M+Na-H_2O^+	$C_9H_6O_3Na^+$	185.02091	185.02094	0.53
M+K$^+$	**$C_9H_8O_4K^+$**	**219.00542**	**219.00542**	**0.11**
M+K-H_2O^+	$C_9H_6O_3K^+$	200.99485	200.99485	0.17
M+Na+K-H$^+$	$C_9H_7O_4NaK^+$	240.98736	240.98730	0.26
M+Na+K-H-H_2O^+	$C_9H_5O_3NaK^+$	222.97680	222.97675	0.46
M+2K-H$^+$	**$C_9H_7O_4K_2^+$**	**256.96130**	**256.96123**	**0.25**
M+2K-H-H_2O^+	$C_9H_5O_3K_2^+$	238.95073	238.95071	0.32
M+2K-H-CO_2^+	$C_8H_7O_2K_2^+$	212.97147	212.97143	0.49
M+Na+2K-H$^+$	$C_9H_6O_4NaK_2^+$	278.94324	278.94313	0.66
M+3K-H$^+$	$C_9H_6O_4K_3^+$	294.91718	294.91706	0.62
2M+H$^+$	$C_{18}H_{17}O_8^+$	361.09179	361.09155	0.84
2M+H-H_2O^+	$C_{18}H_{15}O_7^+$	343.08123	343.08102	0.71
2M+Na$^+$	$C_{18}H_{16}O_8Na^+$	383.07374	383.07347	0.74
***2M+K$^+$**	**$C_{18}H_{16}O_8K^+$**	**399.04768**	**399.04746**	-
2M+K-H_2O^+	$C_{18}H_{14}O_7K^+$	381.03711	381.03685	0.66
2M+K-CO_2^+	$C_{17}H_{16}O_6K^+$	355.05785	355.05758	0.85
2M+2Na-H$^+$	$C_{18}H_{15}O_8Na_2^+$	405.05568	405.05558	0.30
2M+Na+K-H$^+$	**$C_{18}H_{15}O_8NaK^+$**	**421.02962**	**421.02957**	**0.14**
2M+Na+K-H-H_2O^+	$C_{18}H_{13}O_7NaK^+$	403.01905	403.01897	0.40
2M+2K-H$^+$	**$C_{18}H_{15}O_8K_2^+$**	**437.00356**	**437.00353**	**0.08**
2M+2K-H-H_2O^+	$C_{18}H_{13}O_7K_2^+$	418.99299	418.99302	0.22
2M+3Na-2H$^+$	$C_{18}H_{15}O_8Na_3^+$	427.03763	427.03758	0.40
2M+2Na+K-2H$^+$	$C_{18}H_{15}O_8Na_2K^+$	443.01156	443.01147	0.25
2M+Na+2K-2H$^+$	**$C_{18}H_{15}O_8NaK_2^+$**	**458.98550**	**458.98593**	**0.15**
2M+Na+2K-2H-H_2O^+	$C_{18}H_{12}O_7NaK_2^+$	440.97494	440.97489	0.42
2M+3K-2H$^+$	**$C_{18}H_{14}O_8K_3^+$**	**474.95944**	**474.95953**	**0.35**
2M+3K-2H-H_2O^+	$C_{18}H_{12}O_7K_3^+$	456.94887	456.94895	0.36
2M+2Na+2K-3H$^+$	$C_{18}H_{13}O_8Na_2K_2^+$	480.96745	480.96748	0.41
2M+Na+3K-3H$^+$	$C_{18}H_{13}O_8NaK_3^+$	496.94139	496.94155	0.55
2M+4K-3H$^+$	$C_{18}H_{13}O_8K_4^+$	512.91532	512.91573	0.93
3M+Na$^+$	$C_{27}H_{24}O_{12}Na^+$	563.11600	563.11606	0.41
3M+Na-H_2O^+	$C_{27}H_{22}O_{11}Na^+$	545.10543	545.10589	0.90
3M+K$^+$	**$C_{27}H_{24}O_{12}K^+$**	**579.08993**	**579.09004**	**0.37**

3M+K-H_2O^+	$C_{27}H_{22}O_{11}K^+$	561.07937	561.07949	0.35
3M+K-CO_2^+	$C_{26}H_{24}O_{10}K^+$	535.10010	535.10054	0.93
3M+2Na-H^+	$C_{27}H_{23}O_{12}Na_2^+$	585.09794	585.09802	0.45
3M+2Na-H-H_2O^+	$C_{27}H_{21}O_{11}Na_2^+$	567.08738	567.08747	0.60
3M+Na+K-H^+	**$C_{27}H_{23}O_{12}NaK^+$**	**601.07188**	**601.07198**	**0.45**
3M+Na+K-H-H_2O^+	$C_{27}H_{21}O_{11}NaK^+$	583.06132	583.06143	0.44
3M+Na+K-H-CO_2^+	$C_{26}H_{23}O_{10}NaK^+$	557.08205	557.08210	0.45
3M+2K-H^+	**$C_{27}H_{23}O_{12}K_2^+$**	**617.04582**	**617.04577**	**0.22**
3M+2K-H-H_2O^+	$C_{27}H_{21}O_{11}K_2^+$	599.03525	599.03553	0.54
3M+2K-H-CO_2^+	$C_{27}H_{21}O_{11}K_2^+$	573.05599	573.05613	0.52
3M+3Na-$2H^+$	$C_{27}H_{22}O_{12}Na_3^+$	607.07989	607.08012	0.60
3M+2Na+K-$2H^+$	$C_{27}H_{22}O_{12}Na_2K^+$	623.05383	623.05376	0.41
3M+Na+2K-$2H^+$	**$C_{27}H_{22}O_{12}NaK_2^+$**	**639.02776**	**639.02763**	**0.30**
3M+Na+2K-2H-H_2O^+	$C_{27}H_{20}O_{11}NaK_2^+$	621.01720	621.01714	0.74
***3M+3K-$2H^+$**	**$C_{27}H_{22}O_{12}K_2^+$**	**655.00170**	**655.00170**	**-**
3M+3K-2H-H_2O^+	$C_{27}H_{20}O_{11}K_2^+$	636.99113	636.99133	0.86
3M+3Na+K-$3H^+$	$C_{27}H_{21}O_{12}Na_3K^+$	645.03577	645.03577	0.41
3M+2Na+2K-$3H^+$	$C_{27}H_{21}O_{12}Na_2K_2^+$	661.00970	661.00972	0.46
3M+Na+3K-$3H^+$	**$C_{27}H_{21}O_{12}NaK_3^+$**	**676.98364**	**676.98346**	**0.34**
3M+4K-$3H^+$	$C_{27}H_{21}O_{12}K_4^+$	692.95758	692.95739	0.37
4M+Na^+	$C_{36}H_{32}O_{16}Na^+$	743.15826	743.15814	0.42
4M+K^+	$C_{36}H_{32}O_{16}K^+$	759.13219	759.13231	0.52
4M+2Na^+	$C_{36}H_{31}O_{16}Na_2^+$	765.14020	765.14024	0.54
4M+Na+K-H^+	$C_{36}H_{31}O_{16}NaK^+$	781.11414	781.11431	0.48
4M+2K-H^+	$C_{36}H_{31}O_{16}K_2^+$	797.08807	979.08834	0.47
4M+2K-H-H_2O^+	$C_{36}H_{29}O_{15}K_2^+$	779.07751	779.07774	0.49
4M+2Na+K-$2H^+$	$C_{36}H_{30}O_{16}Na_2K^+$	803.09608	803.09624	0.50
4M+Na+2K-$2H^+$	$C_{36}H_{30}O_{16}NaK_2^+$	819.07002	819.07025	0.47
4M+3K-$2H^+$	$C_{36}H_{30}O_{16}K_3^+$	835.04396	835.04439	0.72
4M+3Na+K-$3H^+$	$C_{36}H_{29}O_{16}Na_3K^+$	825.07803	825.07811	0.52
4M+2Na+2K-$3H^+$	$C_{36}H_{29}O_{16}Na_2K_2^+$	841.05196	841.05222	0.58
4M+Na+3K-$3H^+$	$C_{36}H_{29}O_{16}NaK_3^+$	857.02590	857.02625	0.66
4M+4K-$3H^+$	$C_{36}H_{29}O_{16}K_4^+$	872.99984	873.00089	1.23

Table S9. Overview of all identified **DCTB** ions detected on tissue in **positive** ion mode. Bold letters indicate abundant ion species.

Cluster composition	**Sum formula**	**Theoretical *m/z***	**Measured *m/z***	**RMSE [ppm]**
M-H^+	$C_{17}H_{17}N_2^+$	249.13862	249.13864	0.29
$M^{+\cdot}$	$C_{17}H_{18}N_2^+$	250.14645	250.14639	0.96
***M+H^+**	**$C_{17}H_{19}N_2^+$**	**251.15428**	**251.15428**	**-**
M+H+H_2O^+	$C_{17}H_{21}N_2O^+$	269.16484	269.16456	1.50
M+H-CH_2^+	**$C_{16}H_{17}N_2^+$**	**237.13863**	**237.13849**	**0.59**
M+H-CH_3+$H_2O^{+\cdot}$	$C_{16}H_{18}N_2O^{+\cdot}$	254.14136	254.14122	0.99
M-H-$CH_3^{+\cdot}$	$C_{16}H_{14}N_2^{+\cdot}$	234.11515	234.11507	0.75
M-H-CH_4^+	$C_{16}H_{13}N_2^+$	233.10732	233.10735	0.30
M+H-CH_4^+	**$C_{16}H_{15}N_2^+$**	**235.12297**	**235.12305**	**0.10**
M+H-$C_2H_4^+$	$C_{15}H_{15}N_2^+$	223.12297	223.12302	1.01
M+H-2CH_4^+	$C_{15}H_{11}N_2^+$	219.09167	219.09181	0.46

M+H-$C_4H_8^+$	**$C_{13}H_{11}N_2^+$**	**195.09167**	**195.09183**	**0.22**
M+Na^+	$C_{17}H_{18}N_2Na^+$	273.13622	273.13614	1.24
M+Na-CH_2^+	$C_{16}H_{16}N_2Na^+$	259.12057	259.12048	1.02
M+Na-$C_4H_8^+$	$C_{13}H_{10}N_2Na^+$	217.07362	217.07346	1.22
M+K^+	$C_{17}H_{18}N_2K^+$	289.11016	289.11001	0.49
M+K+H_2O^+	$C_{17}H_{20}N_2OK^+$	307.12072	307.12042	1.92
M+K-CH_2^+	**$C_{16}H_{16}N_2K^+$**	**275.09451**	**275.09439**	**0.65**
M+K-$CH_3^{+\cdot}$	$C_{16}H_{15}N_2K^{+\cdot}$	274.08668	274.08643	1.46
M+K-CH_4^+	**$C_{16}H_{14}N_2K^+$**	**273.07886**	**273.07889**	**0.14**
M+K-$C_2H_4^+$	$C_{15}H_{14}N_2K^+$	261.07886	261.07880	0.74
M+K-$C_2H_6^+$	$C_{15}H_{12}N_2K^+$	259.06321	259.06317	0.13
M+K-2CH_4^+	$C_{15}H_{10}N_2K^+$	257.04756	257.04733	0.17
M+K-$C_4H_8^+$	$C_{13}H_{10}N_2K^+$	233.04756	233.04764	0.22
2M+H^+	$C_{34}H_{37}N_4^+$	501.30127	501.30127	0.41
2M-H^+	$C_{34}H_{35}N_4^+$	499.28562	499.28534	0.79
2M+H-CH_4^+	$C_{33}H_{33}N_4^+$	485.26997	485.27005	0.68
2M+NH_4^+	$C_{34}H_{40}N_5^+$	518.32782	518.32776	0.49
2M+Na^+	**$C_{34}H_{36}N_4Na^+$**	**523.28322**	**523.28296**	**0.71**
2M+Na-CH_2^+	$C_{33}H_{34}N_4Na^+$	509.26757	509.26712	1.33
***2M+K^+**	**$C_{34}H_{36}N_4K^+$**	**539.25715**	**539.25715**	**-**
2M+K-CH_2^+	$C_{33}H_{34}N_4K^+$	525.24150	525.24127	0.43

Table S10. Overview of all identified **pNA** ions detected on tissue in **negative** ion mode. Bold letters indicate abundant ion species.

Cluster composition	**Sum formula**	**Theoretical *m/z***	**Measured *m/z***	**RMSE [ppm]**
***M-H^-**	**$C_6H_5N_2O_2^-$**	**137.03565**	**137.03565**	**-**
M-H-O^-	$C_6H_5N_2O^-$	121.04074	121.04062	1.02
M-H-H_2^-	**$C_6H_3N_2O_2^-$**	**135.02000**	**135.02007**	**0.37**
M-H-H_2-O^-	$C_6H_3N_2O^-$	119.02509	119.02496	1.14
M-H-H_2-$NO^{-\cdot}$	$C_6H_3NO^{-\cdot}$	105.02201	105.02187	1.42
M-H-NH_3+H_2O^-	**$C_6H_4NO_3^-$**	**138.01967**	**138.01965**	**0.10**
2M-H-H_2O^-	$C_{12}H_9N_4O_3^-$	257.06801	257.06819	0.68
2M-H-H_2-$NO^{-\cdot}$	$C_{12}H_9N_3O_3^{-\cdot}$	243.06494	243.06464	1.18
2M-H-H_2-NH_3+H_2O^-	$C_{12}H_8N_3O_5^-$	274.04694	274.04703	0.34
2M-2$H_2^{-\cdot}$	**$C_{12}H_8N_4O_4^{-\cdot}$**	**272.05510**	**272.05521**	**0.29**
2M-2H_2-$O^{-\cdot}$	$C_{12}H_8N_4O_3^{-\cdot}$	256.06019	256.06033	0.51
2M-2H_2-NO^-	**$C_{12}H_8N_3O_3^-$**	**242.05711**	**242.05735**	**0.96**
2M-2H_2-NO_2+O_2^-	**$C_{12}H_8N_3O_4^-$**	**258.05203**	**258.05215**	**0.51**
2M-2H_2-NH_3+$H_2O^{-\cdot}$	$C_{12}H_7N_3O_5^{-\cdot}$	273.03912	273.03958	1.67
2M-H-2H_2^-	**$C_{12}H_7N_4O_4^-$**	**271.04728**	**271.04752**	**0.86**
2M-H-2H_2-O^-	$C_{12}H_7N_4O_3^-$	255.05236	255.05259	0.85
2M-H-2H_2-$NO^{-\cdot}$	$C_{12}H_7N_3O_3^{-\cdot}$	241.04929	241.04932	0.83
2M-H-2H_2-NO_2+$O_2^{-\cdot}$	$C_{12}H_7N_3O_4^-$	257.04420	257.04419	1.00
3M-H-H_2-NH_3+H_2O^-	$C_{18}H_{14}N_5O_7^-$	412.08987	412.08993	1.07

***3M-H-2H$_2^-$**	**$C_{18}H_{13}N_6O_6^-$**	**409.09021**	**409.09021**	**-**
3M-3H$_2^{-\cdot}$	**$C_{18}H_{12}N_6O_6^{-\cdot}$**	**408.08238**	**408.08242**	**0.21**
3M-H-3H$_2^-$	**$C_{18}H_{11}N_6O_6^-$**	**407.07456**	**407.07498**	**1.05**
4M-H-2H$_2^-$	$C_{24}H_{19}N_8O_8^-$	547.13313	547.13312	0.34
4M-H-3H$_2^-$	$C_{24}H_{17}N_8O_8^-$	545.11750	545.11755	0.27
4M-H-4H$_2^-$	$C_{24}H_{15}N_8O_8^-$	543.10183	543.10175	0.32

Table S11. Overview of all identified **pNA** ions detected on tissue in **positive** ion mode. Bold letters indicate abundant ion species.

Cluster composition	Sum formula	Theoretical *m/z*	Measured *m/z*	RMSE [ppm]
*****M+H$^+$	$C_6H_7N_2O_2^+$	139.05020	139.05020	-
M+H-NO$_2$+O$_2^{+\cdot}$	$C_6H_7NO_2^+$	125.04713	125.04725	1.05
M+H-O$^+$	$C_6H_6N_2O^+$	123.05529	123.05544	1.30
M+Na$^+$	$C_6H_6N_2O_2Na^+$	161.03215	161.03210	0.26
M+Na-O$^+$	$C_6H_6N_2ONa^+$	145.03723	145.03705	0.60
M+Na-NO$^{+\cdot}$	$C_6H_6NONa^+$	131.03416	131.03424	0.61
M+K$^+$	**$C_6H_6N_2O_2K^+$**	**177.00609**	**177.00606**	**0.27**
M+K-O$^+$	$C_6H_6N_2OK^+$	161.01117	161.01109	0.30
M+K-NO$^{+\cdot}$	**$C_6H_6NOK^{+\cdot}$**	**147.00810**	**147.00807**	**0.12**
2M+H-2NO$^+$	$C_{12}H_{13}N_2O_2^+$	217.09715	217.09708	0.64
2M+Na-2NO$^+$	$C_{12}H_{12}N_2O_2Na^+$	239.07910	239.07895	0.86
2M+K-2NO$^+$	$C_{12}H_{12}N_2O_2K^+$	255.05304	255.05334	0.30

Table S12. Overview of all identified **1,5-DAN** ions detected on tissue in **negative** ion mode. Bold letters indicate abundant ion species.

Cluster composition	Sum formula	Theoretical *m/z*	Measured *m/z*	RMSE [ppm]
M-H$^-$	**$C_{10}H_9N_2^-$**	**157.07712**	**157.07712**	**-**
***M-H$_2^{-\cdot}$**	**$C_{10}H_8N_2^{-\cdot}$**	**156.06930**	**156.06930**	**-**
M-H-H$_2^-$	**$C_{10}H_7N_2^-$**	**155.06147**	**155.06154**	**-**
M-2H$_2^{-\cdot}$	$C_{10}H_6N_2^{-\cdot}$	154.05365	154.05371	0.36
M-H-2H$_2^-$	$C_{10}H_5N_2^-$	153.04582	154.04585	0.50
2M-H-H$_2^-$	$C_{20}H_{17}N_4^-$	313.14587	313.14590	1.11
2M-H-2H$_2^-$	$C_{20}H_{15}N_4^-$	311.13022	311.13043	1.27
2M-H-3H$_2^-$	$C_{20}H_{13}N_4^-$	309.11457	309.11472	0.83
2M-H-4H$_2^-$	$C_{20}H_{11}N_4^-$	307.09892	307.09897	0.90
2M-H-5H$_2^-$	$C_{20}H_9N_4^-$	305.08327	305.08326	0.90

Table S13. Overview of all identified **1,5-DAN** ions detected on tissue in **positive** ion mode. Bold letters indicate abundant ion species.

Cluster composition	Sum formula	Theoretical *m/z*	Measured *m/z*	RMSE [ppm]
M-H$^+$	$C_{10}H_9N_2^+$	157.07602	157.07642	2.45
***M$^{+\cdot}$**	**$C_{10}H_{10}N_2^{+\cdot}$**	**158.08385**	**158.08385**	**-**

$M+Na^+$	$C_{10}H_{10}N_2Na^+$	181.07362	181.07355	0.49
$M+K^+$	$C_{10}H_{10}N_2K^+$	197.04756	197.04760	0.18
$2M-H^+$	$C_{20}H_{19}N_2^+$	315.16042	315.15962	0.85

Table S14. Overview of all identified **2,6-DHAP** ions detected on tissue in **negative** ion mode. Bold letters indicate abundant ion species.

Cluster composition	Sum formula	Theoretical *m/z*	Measured *m/z*	RMSE [ppm]
***M-H⁻**	**$C_8H_7O_3^-$**	**151.04007**	**151.04007**	**-**
M-2H+K⁻	$C_8H_6O_3K^-$	188.99595	188.99582	1.04
***2M-H⁻**	**$C_{16}H_{15}O_6^-$**	**303.08741**	**303.08741**	**-**
2M-H-H_2⁻	**$C_{16}H_{13}O_6^-$**	**301.07176**	**301.07198**	**0.72**
2M-2H+Na⁻	**$C_{16}H_{14}O_6Na^-$**	**325.06935**	**325.06954**	**0.58**
2M-2H+K⁻	**$C_{16}H_{14}O_6K^-$**	**341.04329**	**341.04346**	**0.48**
3M-H⁻	$C_{24}H_{23}O_9^-$	455.13476	455.13457	0.81
3M-H-H_2⁻	$C_{24}H_{21}O_9^-$	453.11911	453.11895	0.68
3M-H-2H_2⁻	**$C_{24}H_{19}O_9^-$**	**451.10346**	**451.10338**	**0.30**
3M-H-3H_2⁻	$C_{24}H_{17}O_9^-$	449.08781	449.08766	0.45
3M-H-H_2+2K⁻	$C_{24}H_{21}O_9K_2^-$	531.04652	531.04645	0.60
4M-H-3H_2⁻	$C_{32}H_{25}O_{12}^-$	601.13515	601.13449	1.19

Table S15. Overview of all identified **2,6-DHAP** ions detected on tissue in **positive** ion mode. Bold letters indicate abundant ion species.

Cluster composition	Sum formula	Theoretical *m/z*	Measured *m/z*	RMSE [ppm]
***M+H⁺**	**$C_8H_9O_3^+$**	**153.05462**	**153.05462**	**-**
M+H-H_2O⁺	$C_8H_7O_2^+$	135.04406	135.04410	0.32
M+Na⁺	$C_8H_8O_3Na^+$	175.03657	175.03658	0.15
M+K⁺	$C_8H_8O_3K^+$	191.01050	191.01050	0.37
M+2Na-H⁺	$C_8H_7O_3Na_2^+$	197.01851	197.01843	0.34
M+Na+K-H⁺	$C_8H_7O_3NaK^+$	212.99245	212.99245	0.25
***M+2K-H⁺**	**$C_8H_7O_3K_2^+$**	**228.96638**	**228.96638**	**-**
M+3K-2H⁺	$C_8H_6O_3K_3^+$	266.92226	266.92227	0.59
2M+H⁺	$C_{16}H_{17}O_6^+$	305.10196	305.10186	0.79
2M+K+2Na-2H⁺	$C_{16}H_{14}O_6Na_2K^+$	387.02173	387.02166	0.90
2M+2K+Na-2H⁺	$C_{16}H_{14}O_6NaK_2^+$	402.99567	402.99555	0.55
2M+3K-2H⁺	$C_{16}H_{14}O_6K_3^+$	418.96961	418.96952	0.59

Table S16. Overview of all identified **norharmane** ions detected on tissue in **negative** ion mode. Bold letters indicate abundant ion species.

Cluster composition	Sum formula	Theoretical *m/z*	Measured *m/z*	RMSE [ppm]
***M-H⁻**	**$C_{11}H_7N_2^-$**	**167.06147**	**167.06147**	**-**
M-H-H_2⁻	**$C_{11}H_5N_2^-$**	**165.04582**	**165.04608**	**1.36**
2M-H⁻	$C_{22}H_{15}N_4^-$	335.13022	335.13014	0.31
***2M-H-H_2⁻**	**$C_{22}H_{13}N_4^-$**	**333.11457**	**333.11457**	**-**

2M-H-2H_2^-	$C_{22}H_{11}N_4^-$	331.09892	331.09907	0.45
2M-2H+Na^-	$C_{22}H_{14}N_4Na^-$	357.11216	357.11185	0.90
2M-2H+K^-	$C_{22}H_{14}N_4K^-$	373.08610	373.08591	0.51
3M-H^-	$C_{33}H_{23}N_6^-$	503.19897	503.19913	0.53
3M-H-H_2^-	$C_{33}H_{21}N_6^-$	501.18332	501.18344	0.38
3M-H-2H_2^-	$C_{33}H_{19}N_6^-$	499.16767	499.16785	0.33
3M-H-3H_2^-	$C_{33}H_{17}N_6^-$	497.15202	497.15218	0.39
4M-H-H_2^-	$C_{44}H_{29}N_8^-$	669.25207	669.25257	0.99
4M-H-2H_2^-	$C_{44}H_{27}N_8^-$	667.23642	667.23711	1.10

Table S17. Overview of all identified **norharmane** ions detected on tissue in **positive** ion mode. Bold letters indicate abundant ion species.

Cluster composition	Sum formula	Theoretical *m/z*	Measured *m/z*	RMSE [ppm]
***M+H^+**	**$C_{11}H_9N_2^+$**	**169.07602**	**169.07602**	**-**
M+Na^+	$C_{11}H_8N_2Na^+$	191.05797	191.05801	0.22
M+K^+	$C_{11}H_8N_2Na^+$	207.03191	207.03196	0.29
2M-H^+	**$C_{22}H_{15}N_4^+$**	**335.12912**	**335.12904**	**0.40**
***2M+H^+**	**$C_{22}H_{17}N_4^+$**	**337.14477**	**337.14477**	**-**
2M+Na^+	$C_{22}H_{16}N_4Na^+$	359.12672	359.12648	0.87
2M+K^+	$C_{22}H_{16}N_4K^+$	375.10065	375.10038	0.81
3M+H^+	$C_{33}H_{25}N_6^+$	505.21352	505.21410	0.81
3M+H^+	$C_{33}H_{25}N_6^+$	505.21352	505.21410	1.17
3M+Na^+	$C_{33}H_{25}N_6Na^+$	527.19547	527.19619	1.20
3M+K^+	$C_{33}H_{25}N_6K^+$	543.16940	543.16985	0.99

Table S18. Overview of all identified **THAP** ions detected on tissue in **negative** ion mode. Bold letters indicate abundant ion species.

Cluster composition	Sum formula	Theoretical *m/z*	Measured *m/z*	RMSE [ppm]
***M-H^-**	**$C_8H_7O_4^-$**	**167.03498**	**167.03498**	**-**
2M-H^-	$C_{16}H_{15}O_8^-$	335.07724	335.07718	-
***2M-H-H_2^-**	**$C_{16}H_{13}O_8^-$**	**333.06159**	**333.06159**	**-**
2M-H-2H_2^-	$C_{16}H_{11}O_8^-$	331.04594	331.04602	0.52
2M-H-3H_2^-	$C_{16}H_9O_8^-$	329.03029	329.03033	0.60
2M-2H+Na^-	**$C_{16}H_{14}O_8Na^-$**	**357.05919**	**357.05908**	**1.11**
2M-2H+K^-	**$C_{16}H_{14}O_8K^-$**	**373.03312**	**373.03287**	**0.76**
3M-H-2H_2^-	$C_{24}H_{19}O_{12}^-$	499.08820	499.08810	1.34
3M-H-3H_2^-	**$C_{24}H_{17}O_{12}^-$**	**497.07255**	**497.07254**	**1.28**
3M-2H+Na-H_2^-	**$C_{24}H_{20}O_{12}Na^-$**	**523.08579**	**523.08594**	**0.85**
3M-2H+K-H_2^-	**$C_{24}H_{20}O_{12}K^-$**	**539.05973**	**539.05975**	**0.64**
3M-2H+K-2H_2^-	$C_{24}H_{18}O_{12}K^-$	537.04408	537.04425	1.07

Table S19. Overview of all identified **9AA** ions detected on tissue in **negative** ion mode. Bold letters indicate abundant ion species.

Cluster composition	Sum formula	Theoretical *m/z*	Measured *m/z*	RMSE [ppm]
***M-H$^-$**	**$C_{13}H_9N_2^-$**	**193.07712**	**193.07705**	**-**
M-H-H_2^-	$C_{13}H_7N_2^-$	191.06147	191.06166	0.79
M-H-2H_2^-	$C_{13}H_5N_2^-$	189.04582	189.04602	0.79
***2M-H-H_2^-**	**$C_{26}H_{17}N_4^-$**	**385.14587**	**385.14587**	**-**
2M-H-2H_2^-	**$C_{26}H_{15}N_4^-$**	**383.13022**	**383.13028**	**0.62**
2M-H-3H_2^-	$C_{26}H_{13}N_4^-$	381.11457	381.11440	0.79
2M-H-4H_2^-	$C_{26}H_{11}N_4^-$	379.09892	379.09860	0.98
3M-H-2H_2^-	$C_{39}H_{25}N_6^-$	577.21462	577.21497	1.91
3M-H-3H_2^-	$C_{39}H_{23}N_6^-$	575.19897	575.19965	1.87

Structural formulas of matrices covered in this work

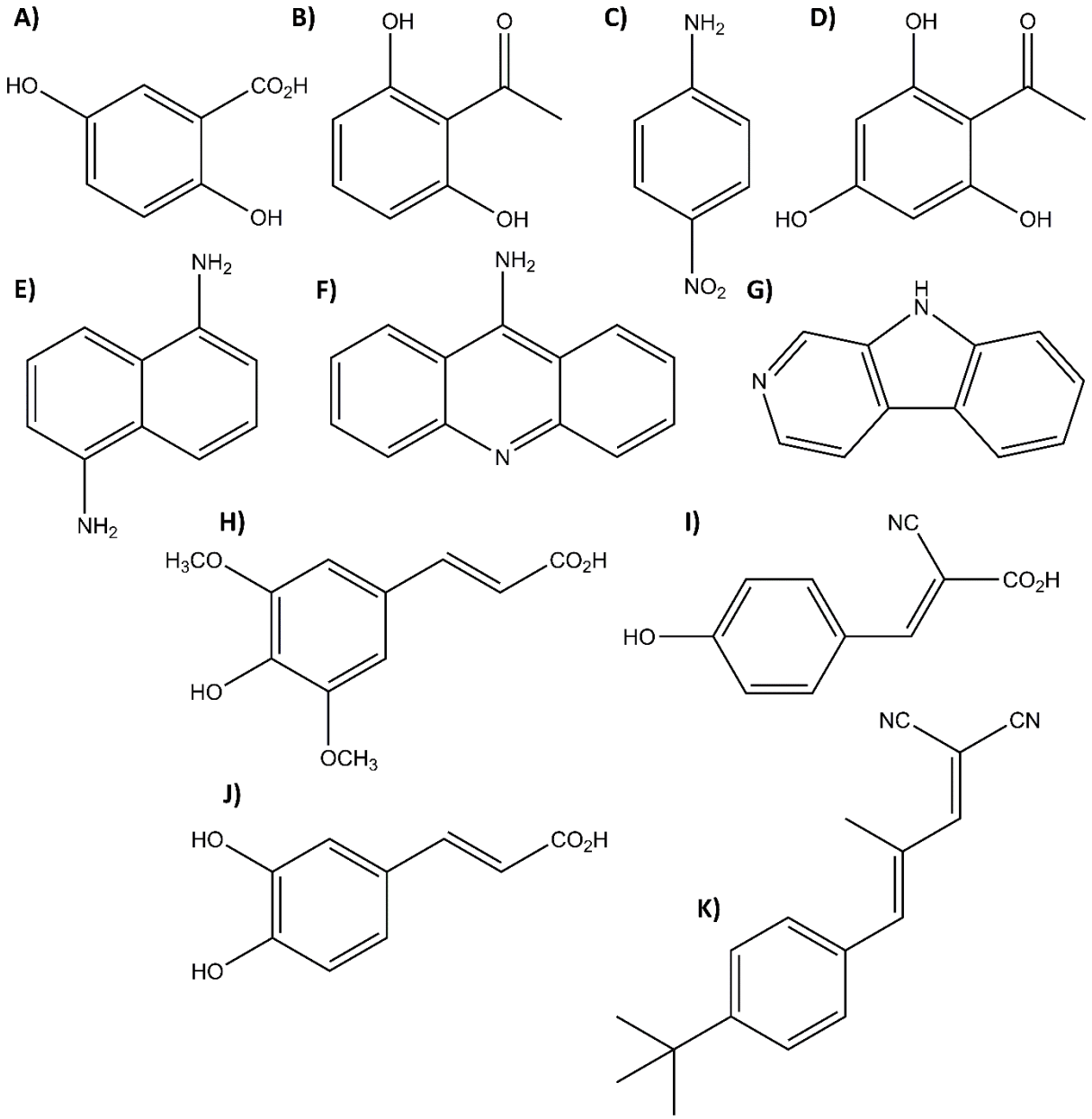

Figure S1. Structural formulas of the matrix substances covered in this study. A) 2,5-dihydroxybenzoic acid B) 2,6-dihydroxyacetophenone C) 4-nitroaniline D) 2,4,6-trihydroxyacetophenone E) 1,5-diaminonaphthalene F) 9-aminoacridine G) Norharmane H) Sinapic acid I) CHCA J) Caffeic acid K) DCTB

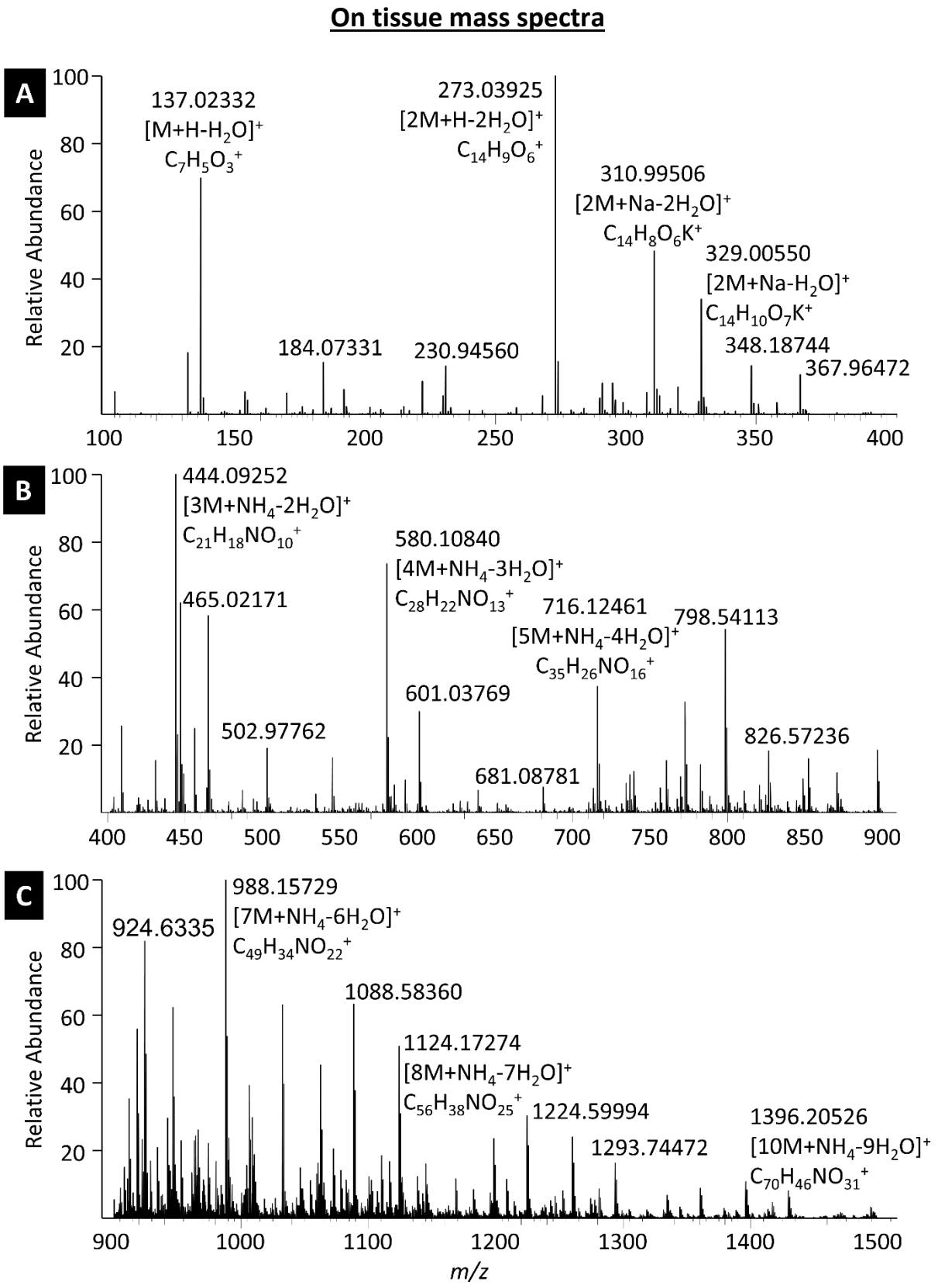

Figure S2. On tissue spectra of **DHB** in **positive ion mode** from A) *m/z* 100 – 400, B) *m/z* 400 – 900 and C) *m/z* 900 – 1500.

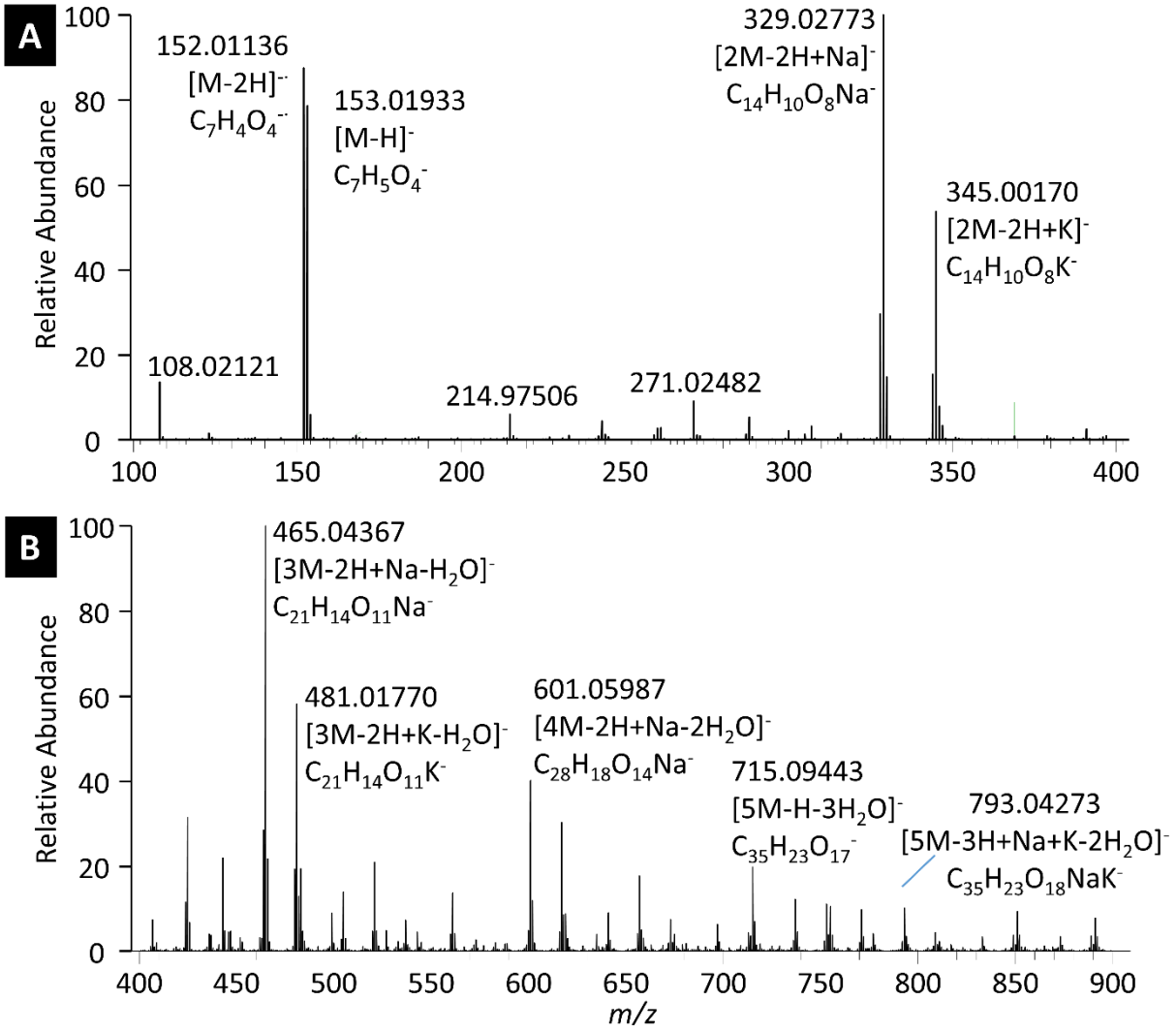

Figure S3. On tissue spectra of **DHB** in **negative ion mode** from A) *m/z* 100 – 400, B) *m/z* 400 – 900.

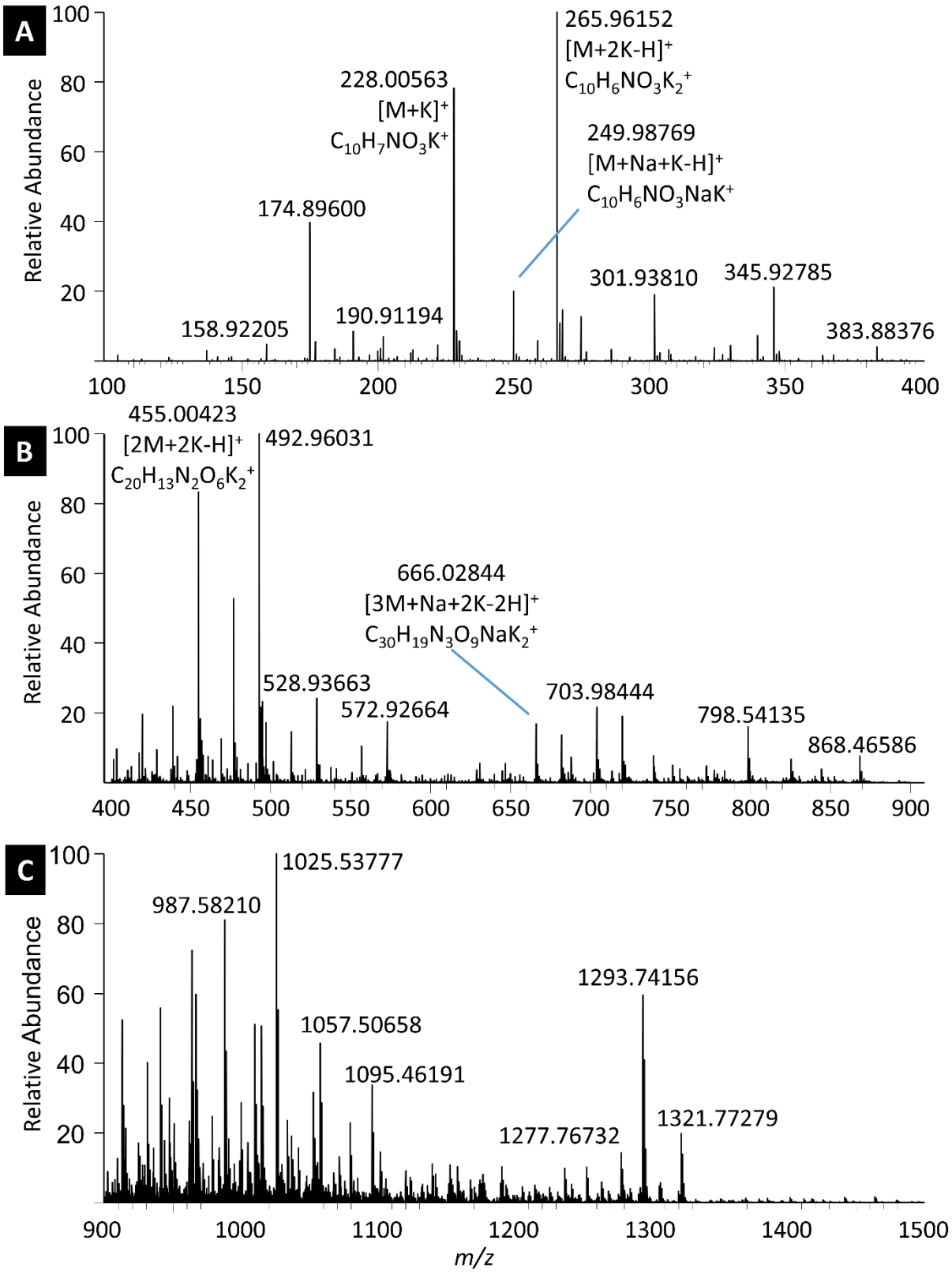

Figure S4. On tissue spectra of **CHCA** in **positive ion mode** from A) *m/z* 100 – 400, B) *m/z* 400 – 900 and C) *m/z* 900 – 1500.

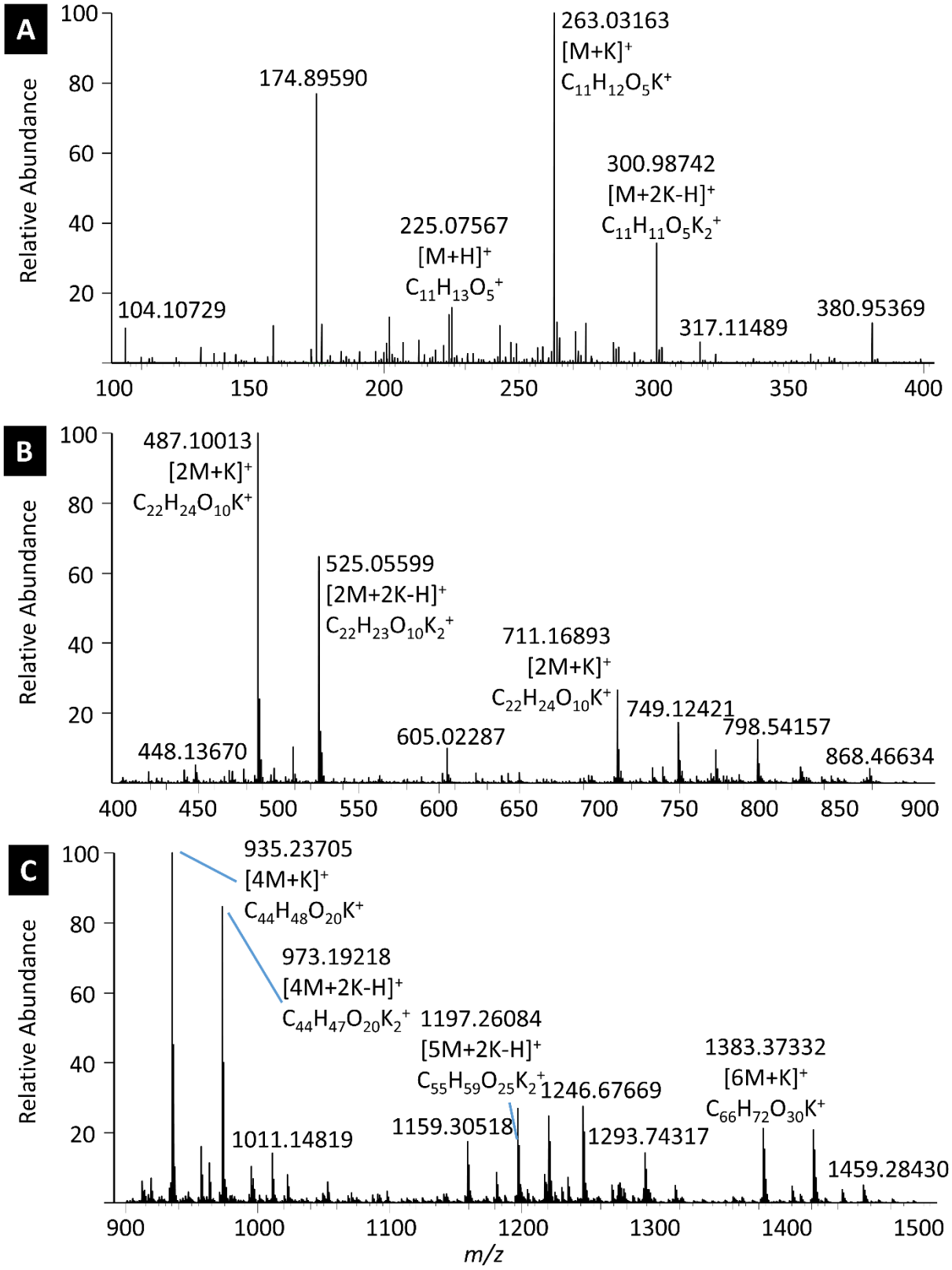

Figure S5. On tissue spectra of **SA** in **positive ion mode** from A) *m/z* 100 – 400, B) *m/z* 400 – 900 and C) *m/z* 900 – 1500.

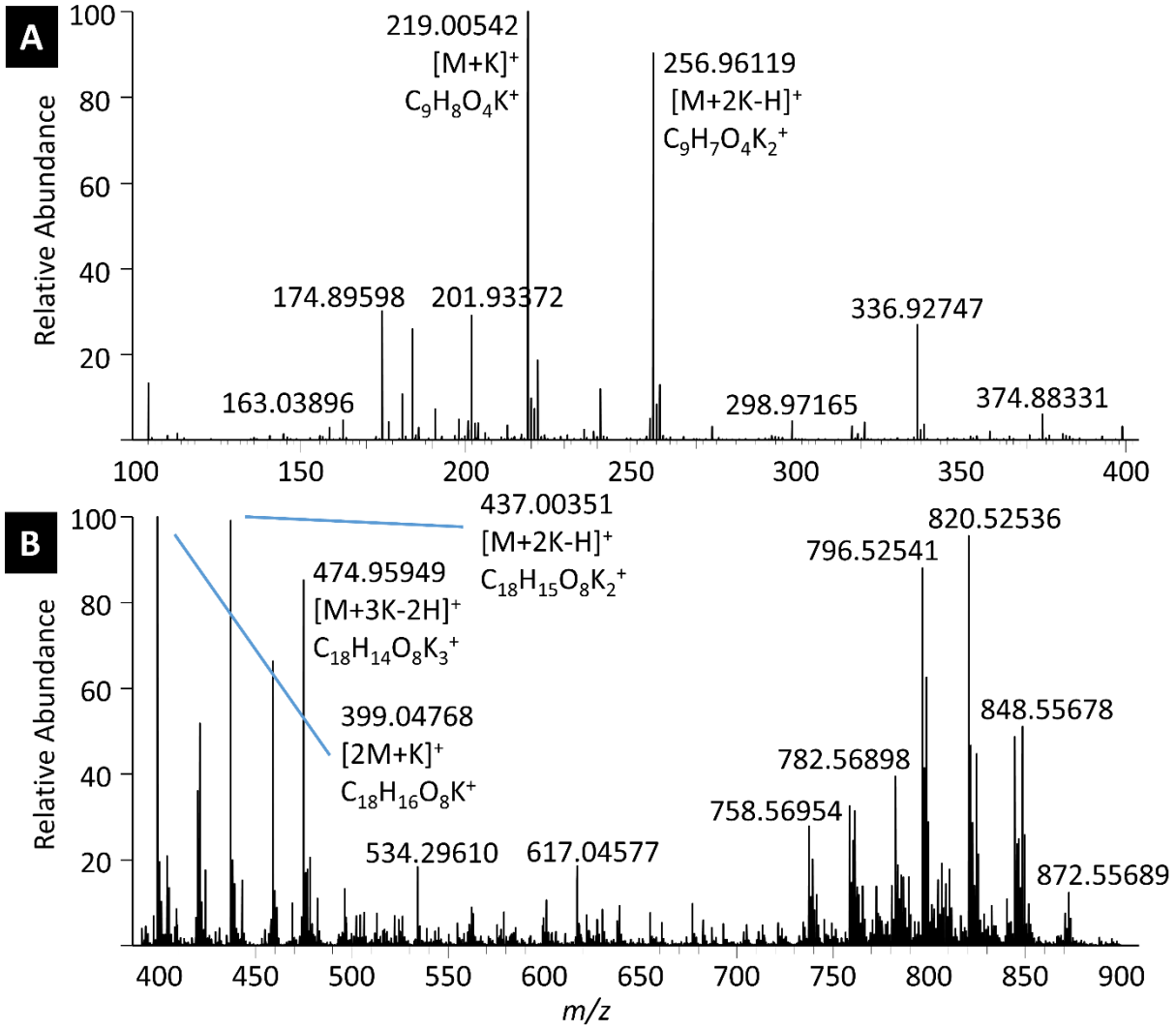

Figure S6. On tissue spectra of **CA** in positive **ion mode** from A) *m/z* 100 – 400 and B) *m/z* 400 – 900.

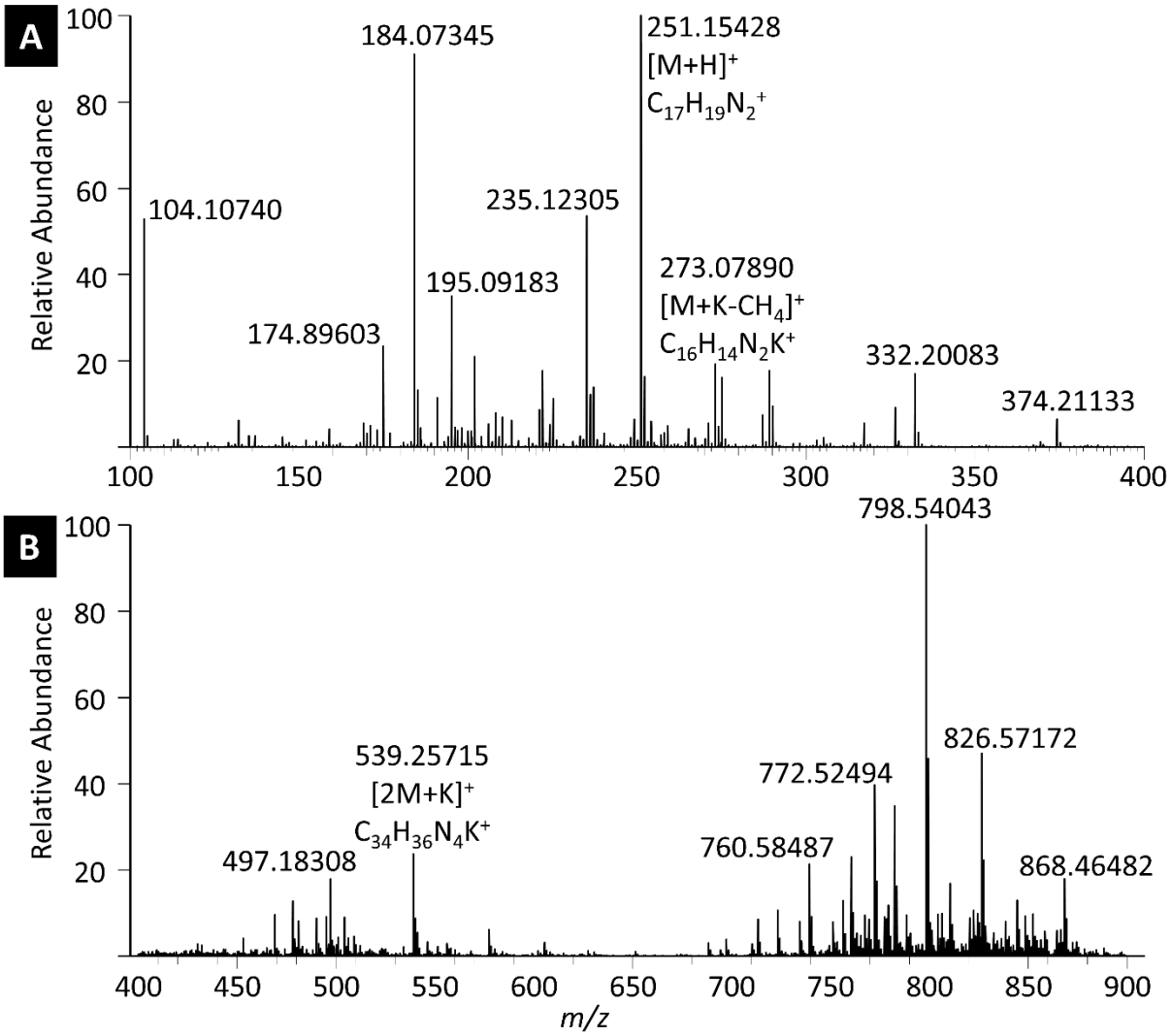

Figure S7. On tissue spectra of **DCTB** in **positive ion mode** A) m/z 100 – 400 and B) m/z 400 – 900.

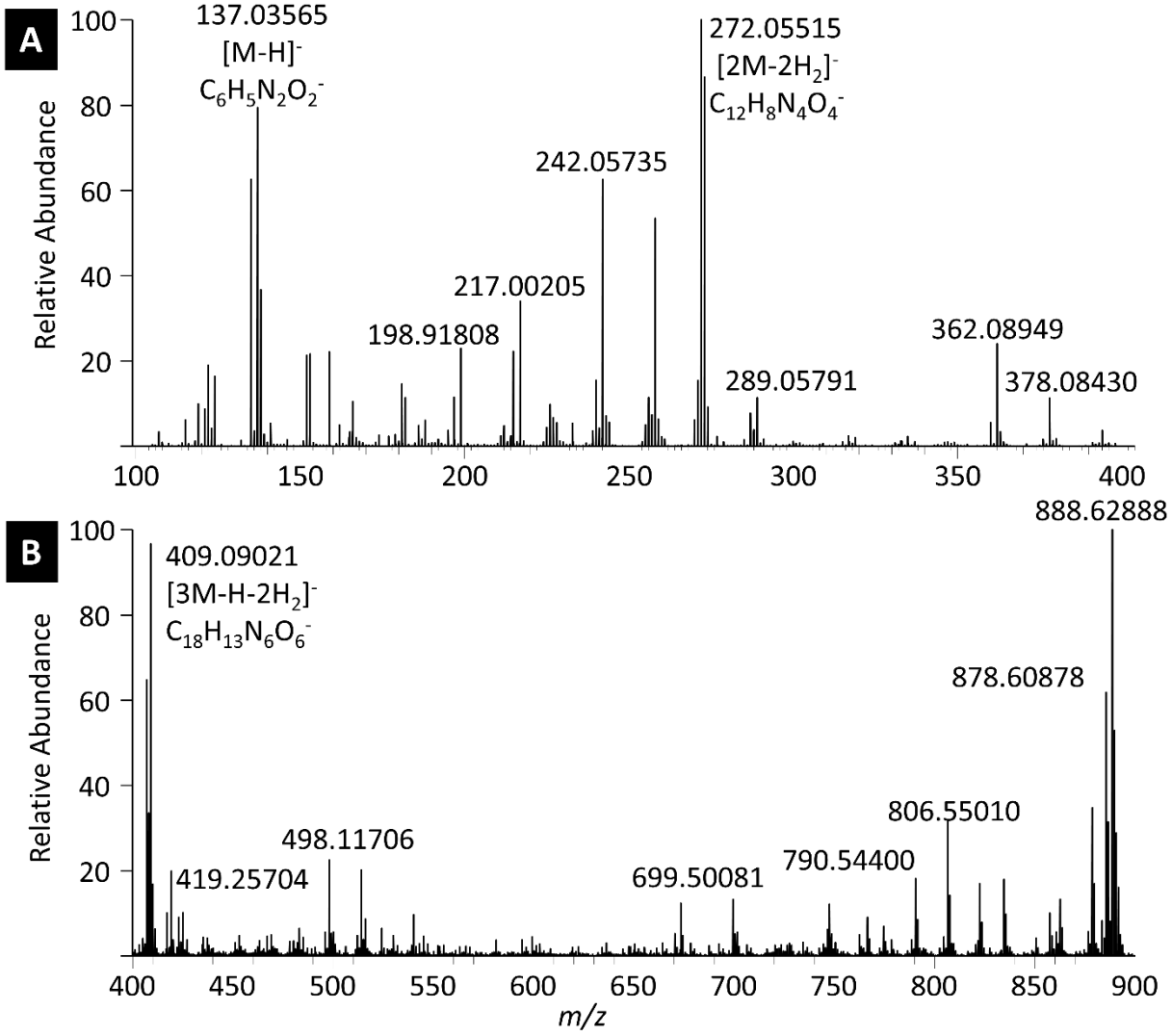

Figure S8. On tissue spectra of **pNA** in **negative ion mode** A) m/z 100 – 400 and B) m/z 400 – 900.

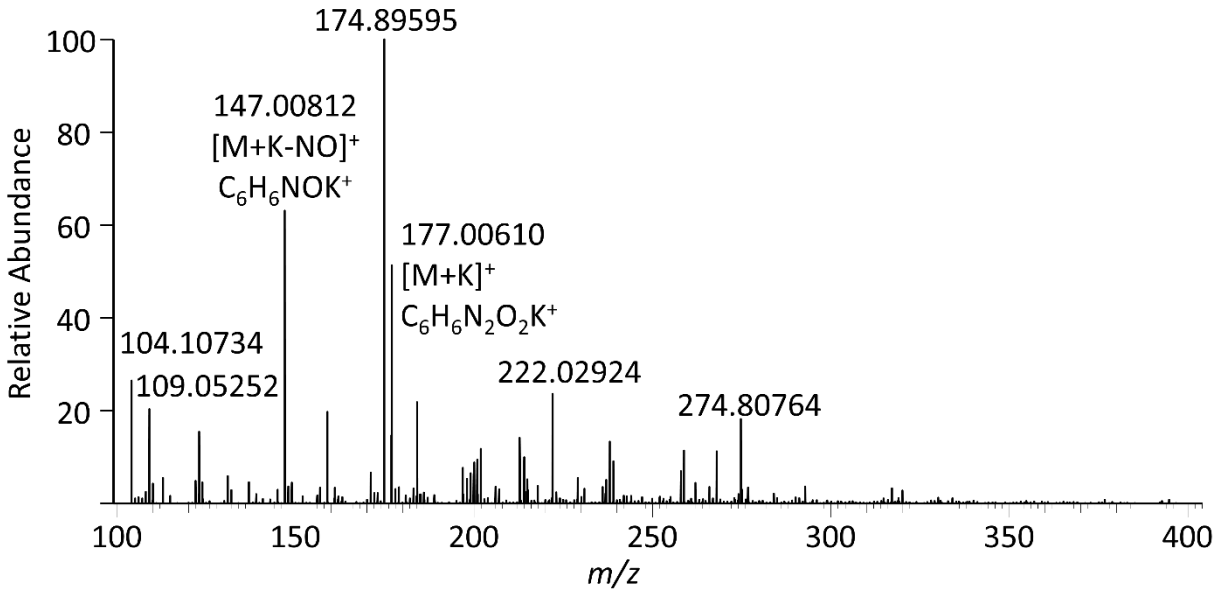

Figure S9. On tissue spectrum of **pNA** in **positive ion mode** from *m/z* 100 to 400.

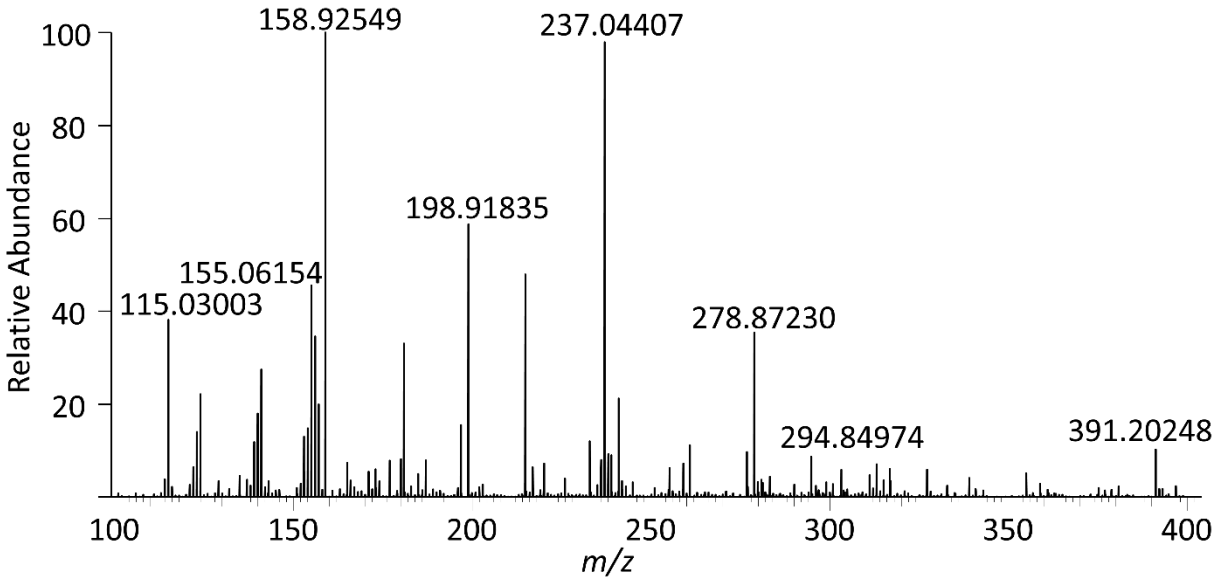

Figure S10. On tissue spectrum of **1,5-DAN** in **negative ion mode** from *m/z* 100 to 400.

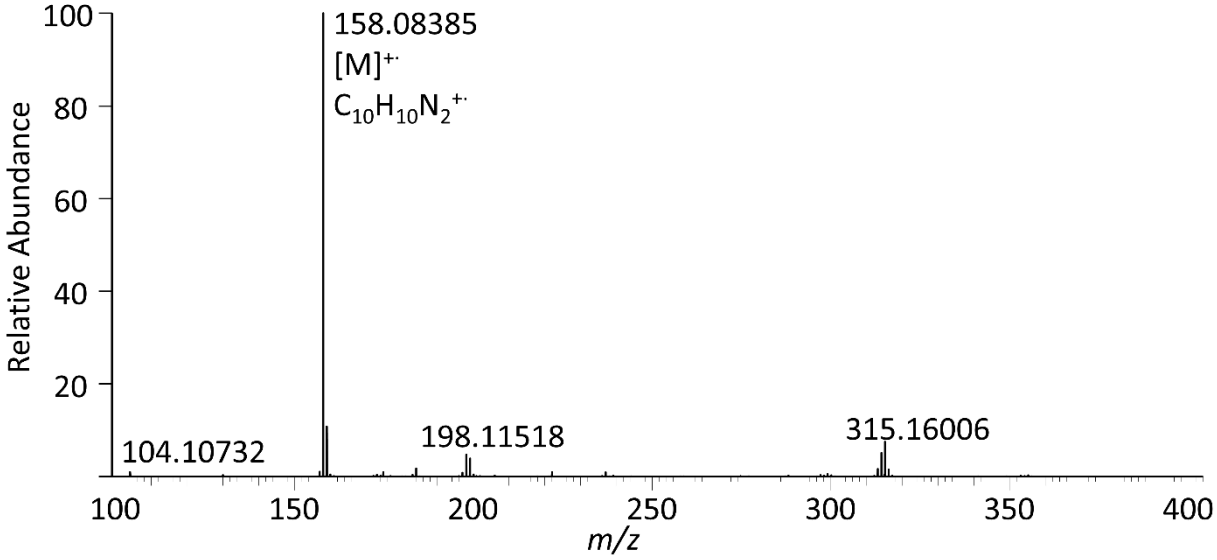

Figure S11. On tissue spectrum of **1,5-DAN** in **positive ion mode** from *m/z* 100 to 400.

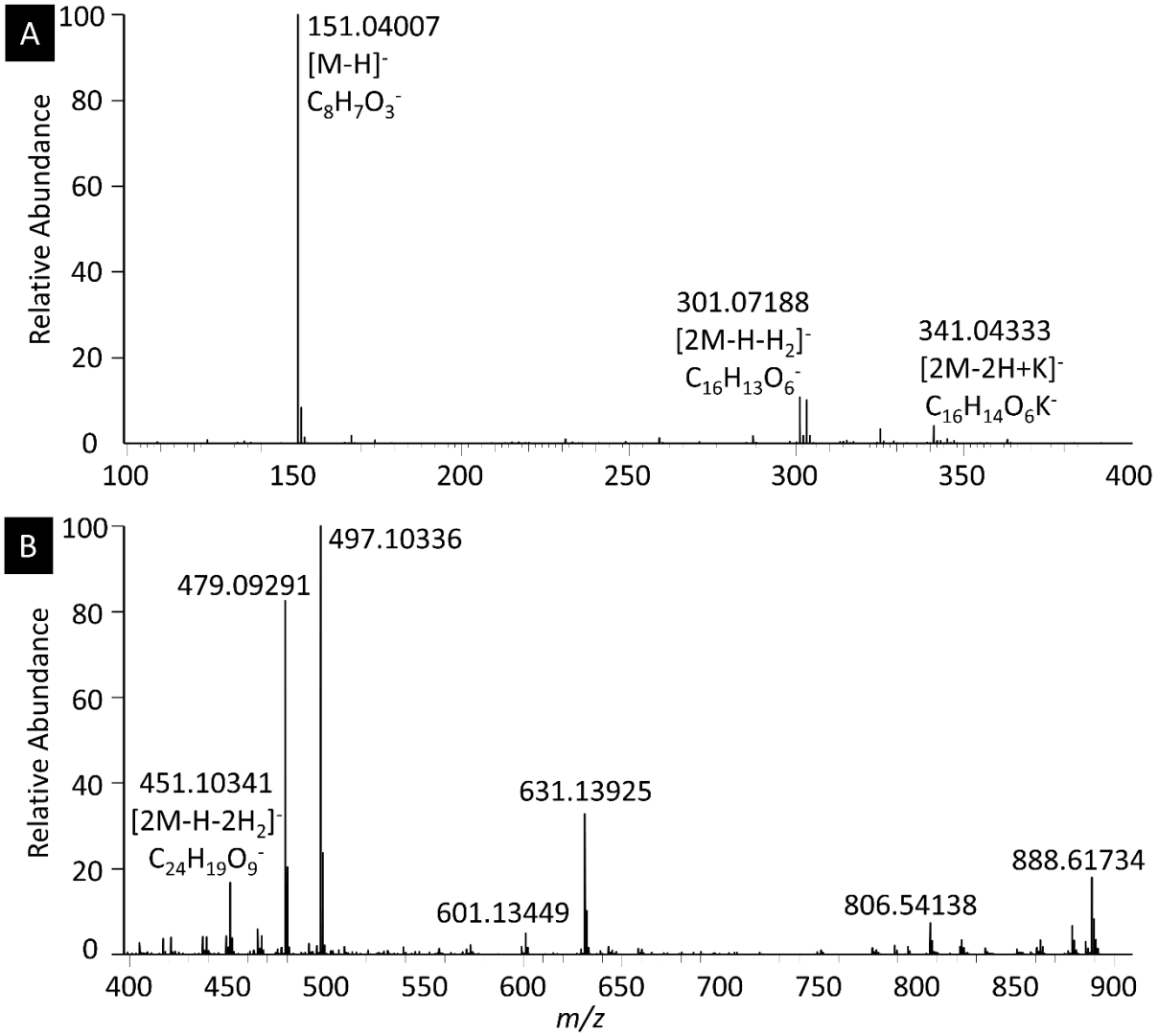

Figure S12. On tissue spectra of **2,6-DHAP** in **negative ion mode** A) m/z 100 – 400 and B) m/z 400 – 900.

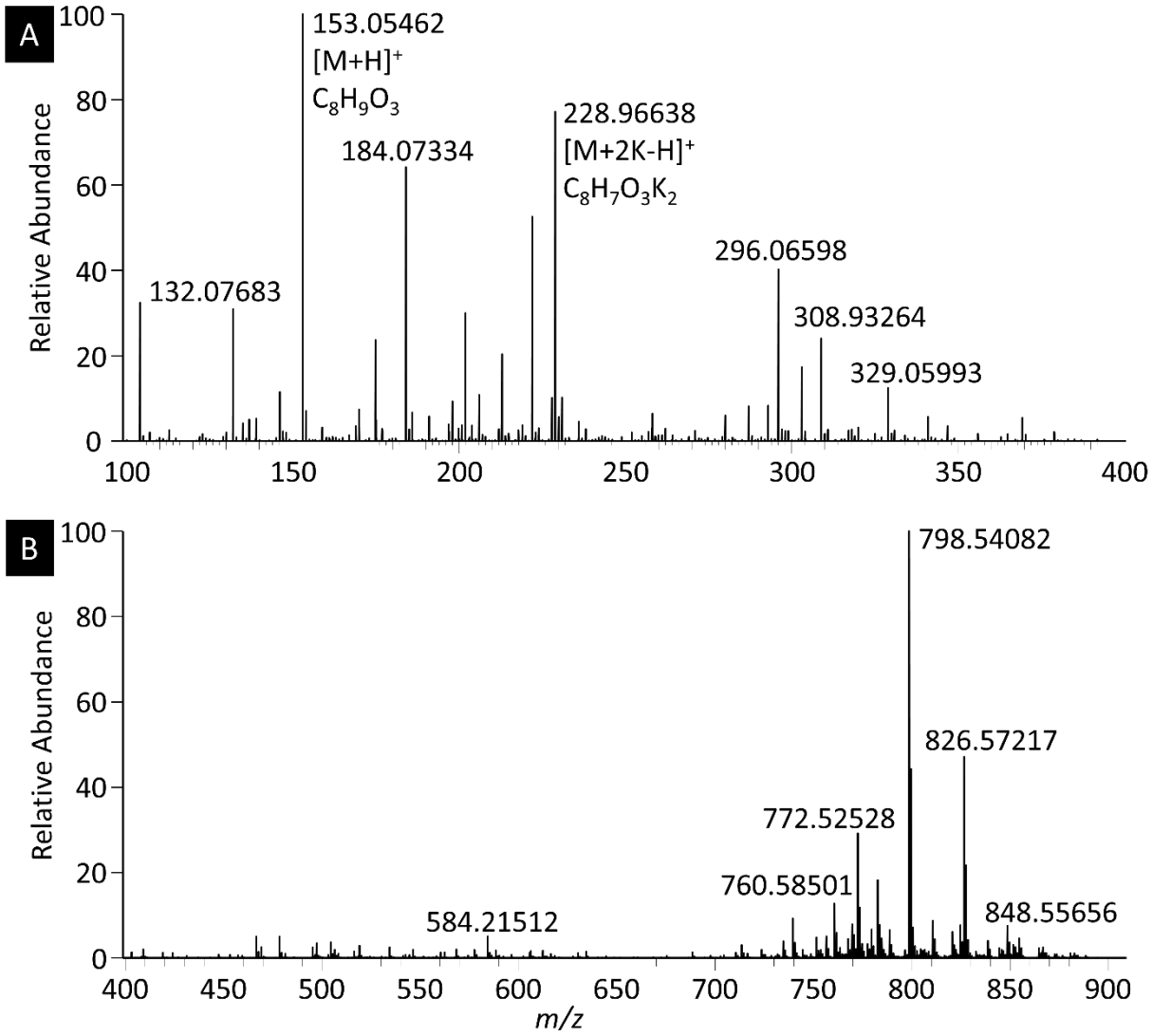

Figure S13. On tissue spectra of **2,6-DHAP** in **positive ion mode** A) m/z 100 – 400 and B) m/z 400 – 900.

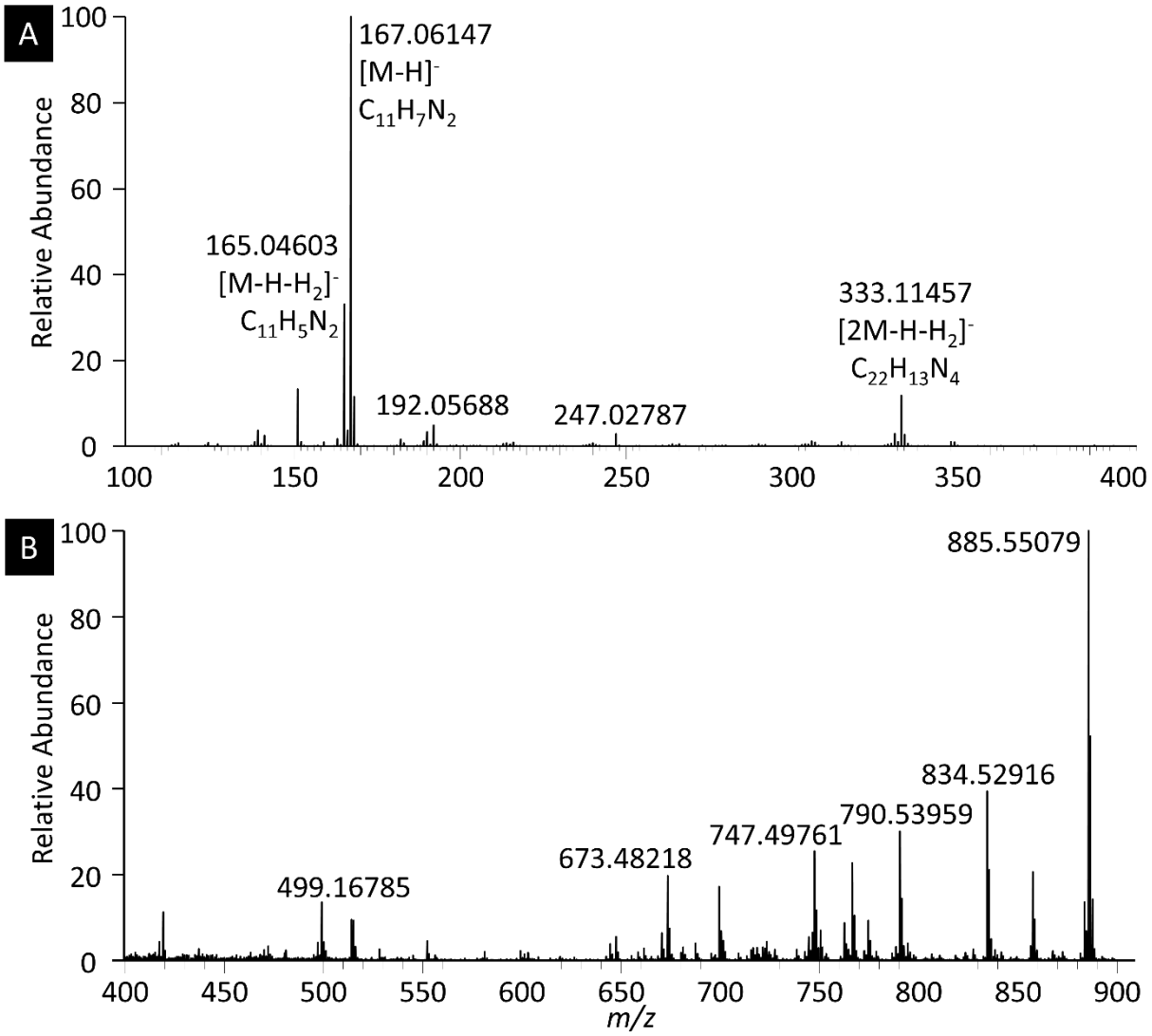

Figure S14. On tissue spectra of **norharmane** in **negative ion mode** A) m/z 100 – 400 and B) m/z 400 – 900.

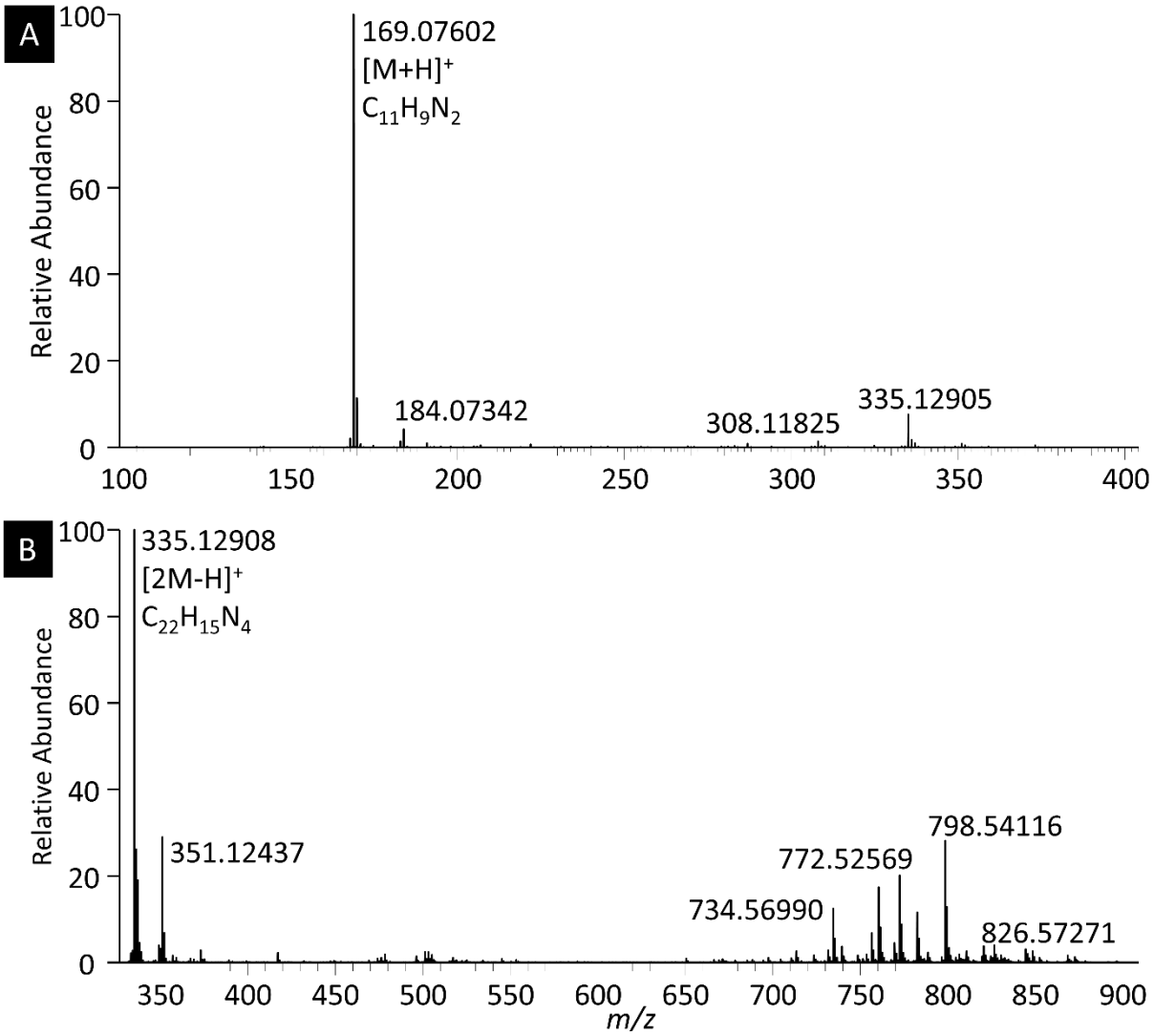

Figure S15. On tissue spectra of **norharmane** in **positive ion mode** A) m/z 100 – 400 and B) m/z 400 – 900.

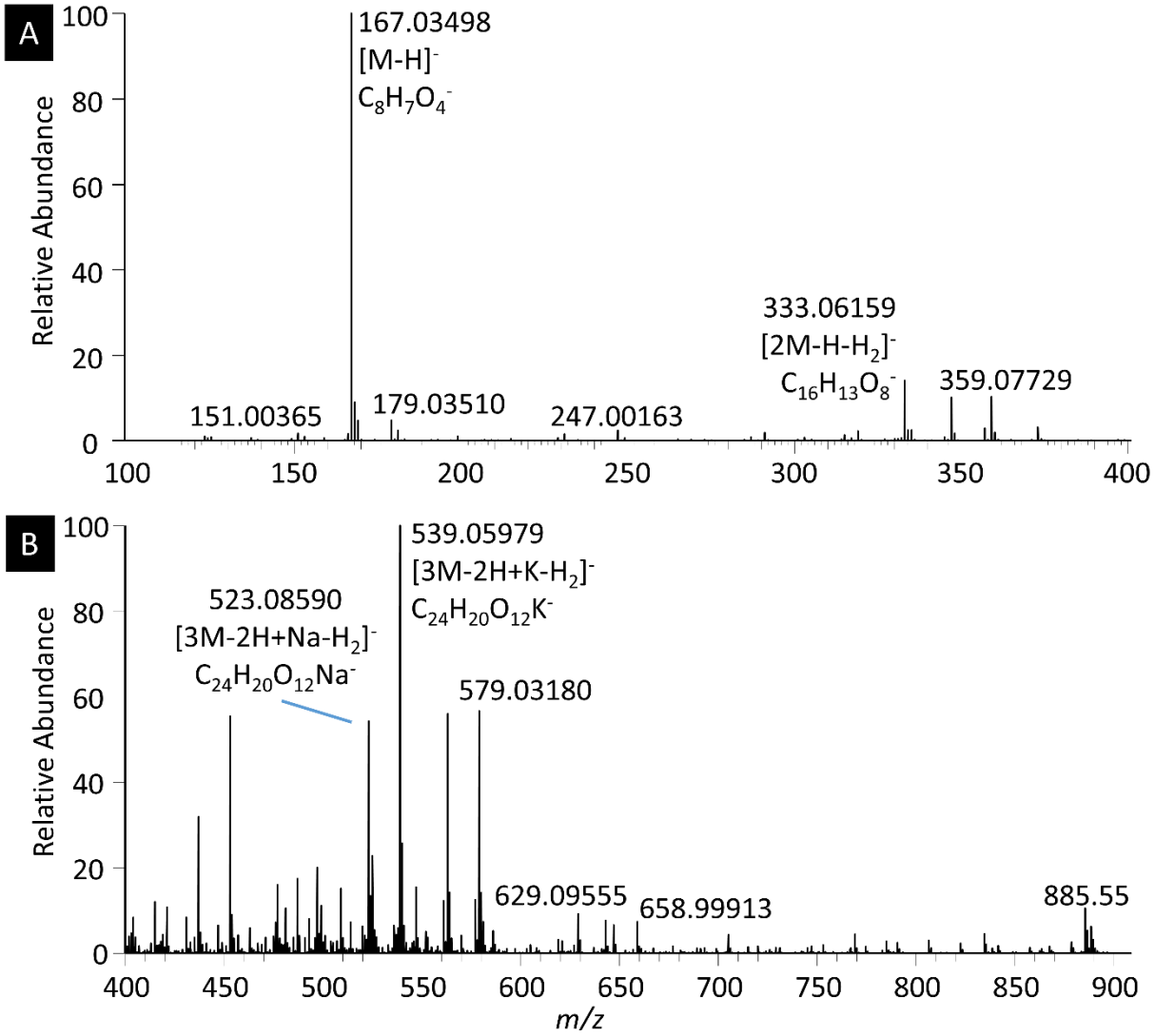

Figure S16. On tissue spectra of **THAP** in **negative ion mode** A) m/z 100 – 400 and B) m/z 400 – 900.

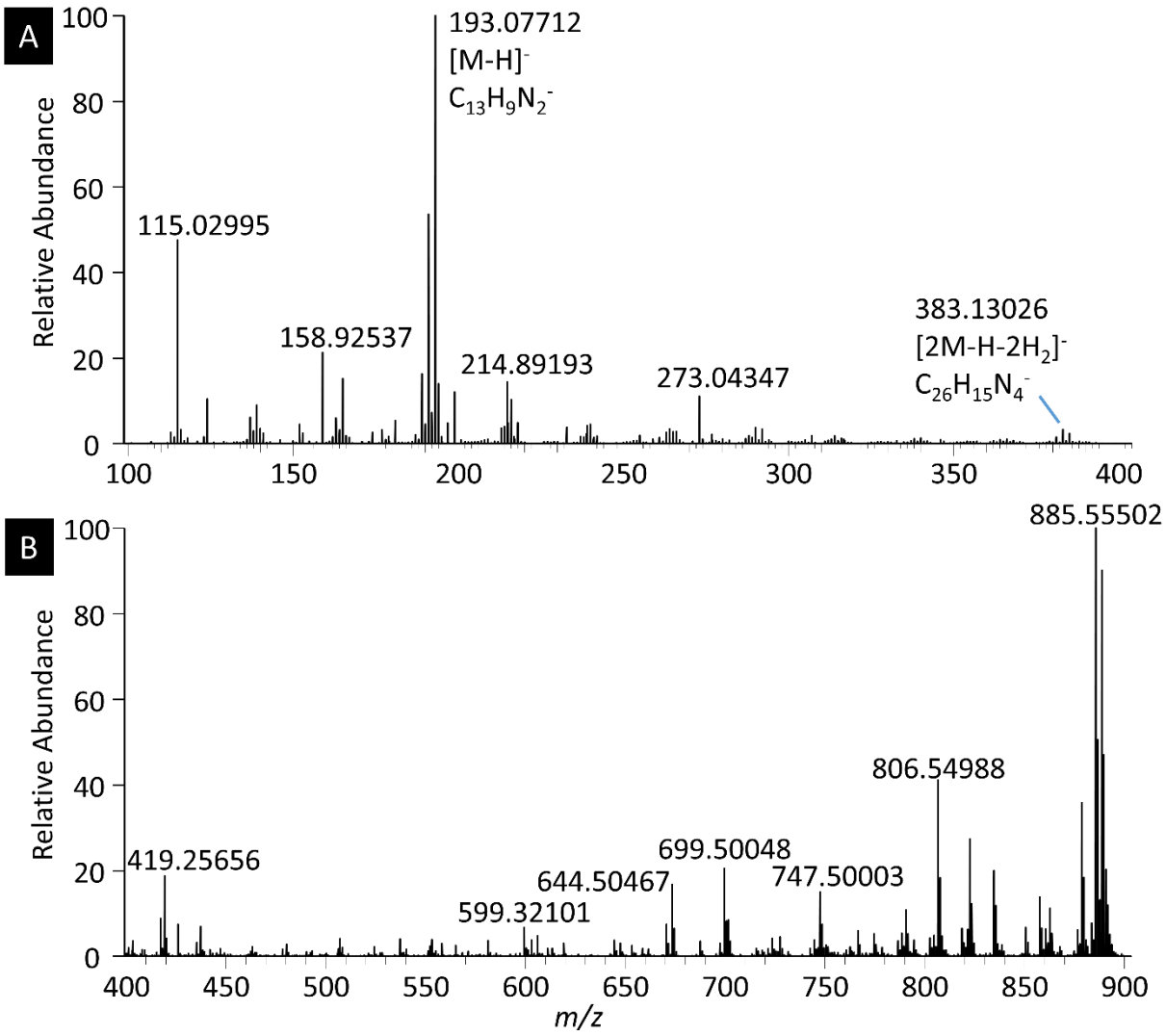

Figure S17. On tissue spectra of **9AA** in **negative ion mode** A) m/z 100 – 400 and B) m/z 400 – 900.

MS/MS spectra of DHB clusters

MS/MS of selected clusters from all identified DHB cluster series were recorded. In general, DHB clusters in both polarities fragment into lighter homologues of the same series with the exception of the $[aM+NH_4\text{-}bH_2O]^+$ (a = 1,2,3…; $b \leq a$) series. Upon activation, clusters of this series release ammonia causing all observed fragment ions of these clusters to have the general sum formula $[aM+H\text{-}bH_2O]^+$ (a = 1,2,3…; b ≤ a), identical to the DHB cluster series presented Table S1. See Figure S18 A for an annotated mass spectrum of the NH_4^+ containing DHB cluster $[3DHB+NH_4\text{-}2H_2O]^+$.

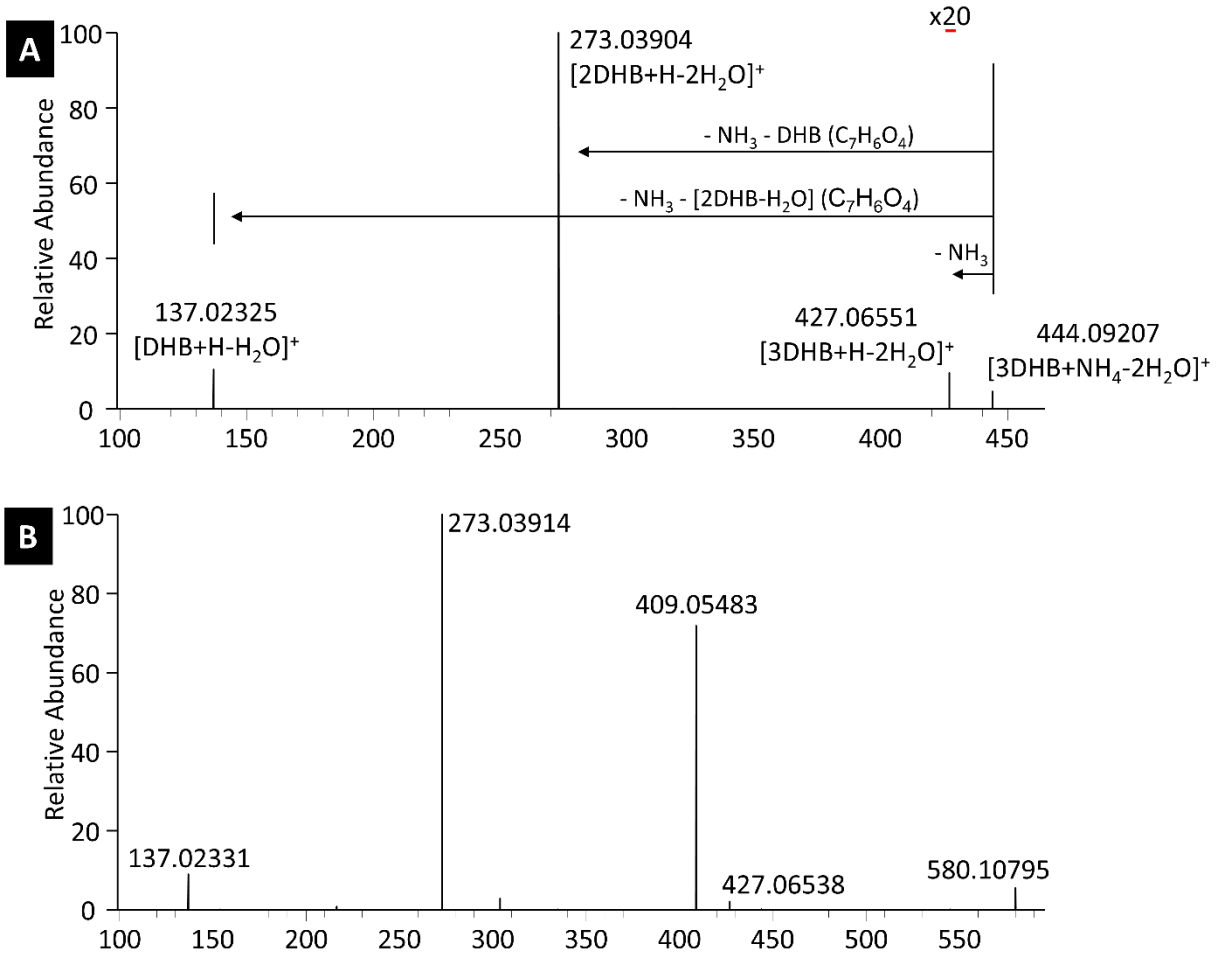

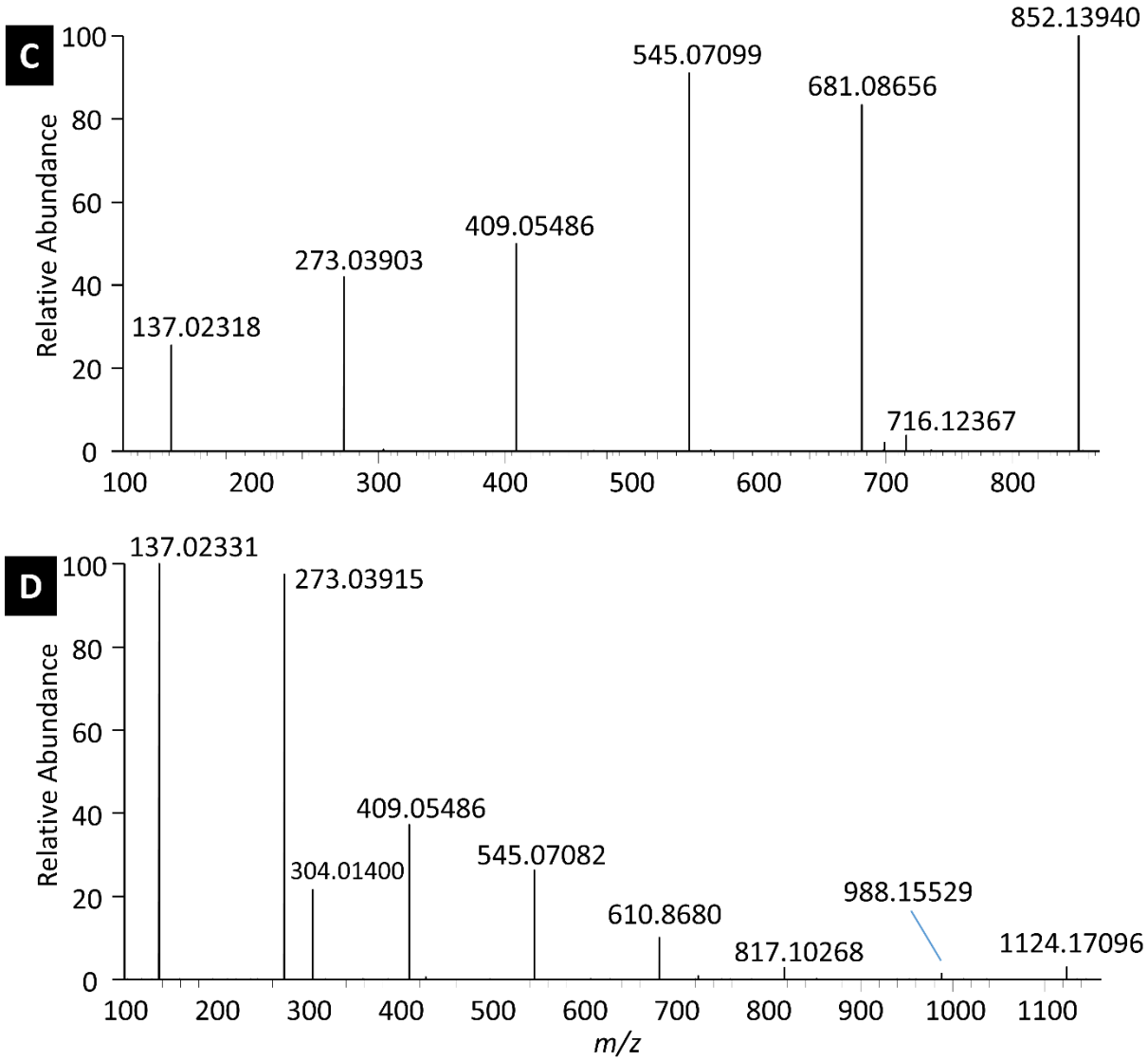

Figure S18. MS/MS spectra of DHB clusters belonging to the $[aM+NH_4-bH_2O]^+$ (a = 1,2,3…; $b \leq a$) series. A) MS/MS of $[3M+NH_4-2H_2O]^+$ ($C_{21}H_{18}NO_{10}^+$) *m/z* 444.09252. B) MS/MS of $[4M+NH_4-3H_2O]^+$ ($C_{28}H_{22}NO_{13}^+$) *m/z* 580.10857. C) MS/MS of $[6M+NH_4-5H_2O]^+$ ($C_{42}H_{30}NO_{19}^+$) *m/z* 852.14065. D) MS/MS of $[8M+NH_4-7H_2O]^+$ ($C_{56}H_{38}NO_{25}^+$) *m/z* 1124.17274.

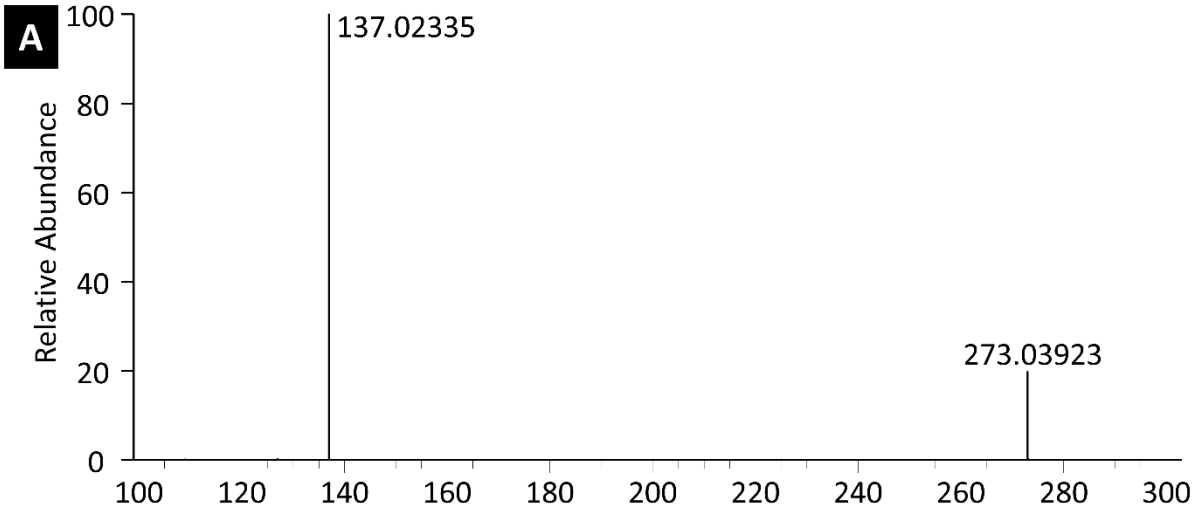
A
Relative Abundance
100
80
60
40
20
0
137.02335
273.03923
100
120
140
160
180
200
220
240
260
280
300

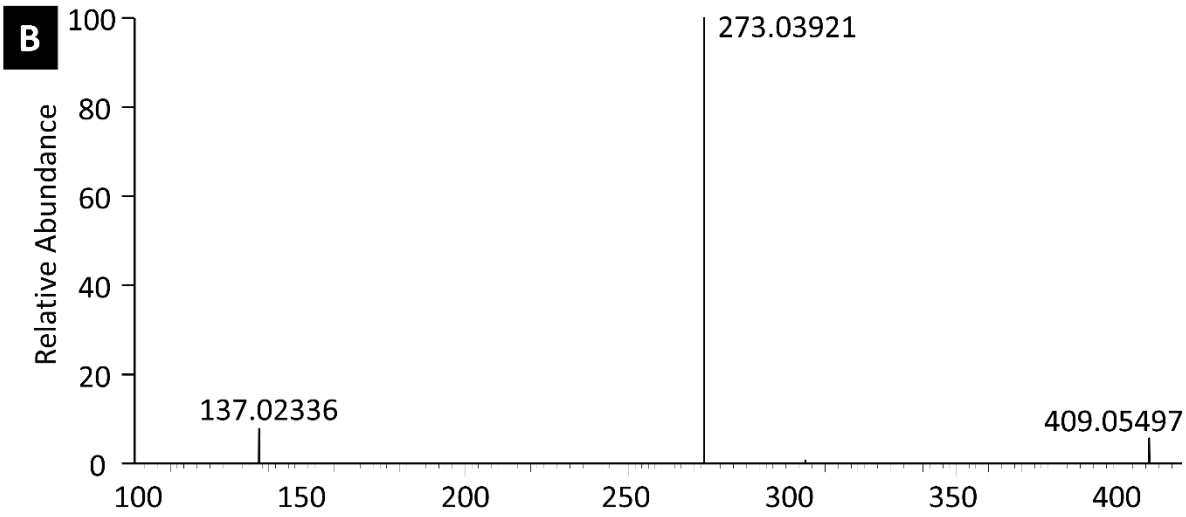
B
Relative Abundance
100
80
60
40
20
0
273.03921
137.02336
409.05497
100
150
200
250
300
350
400

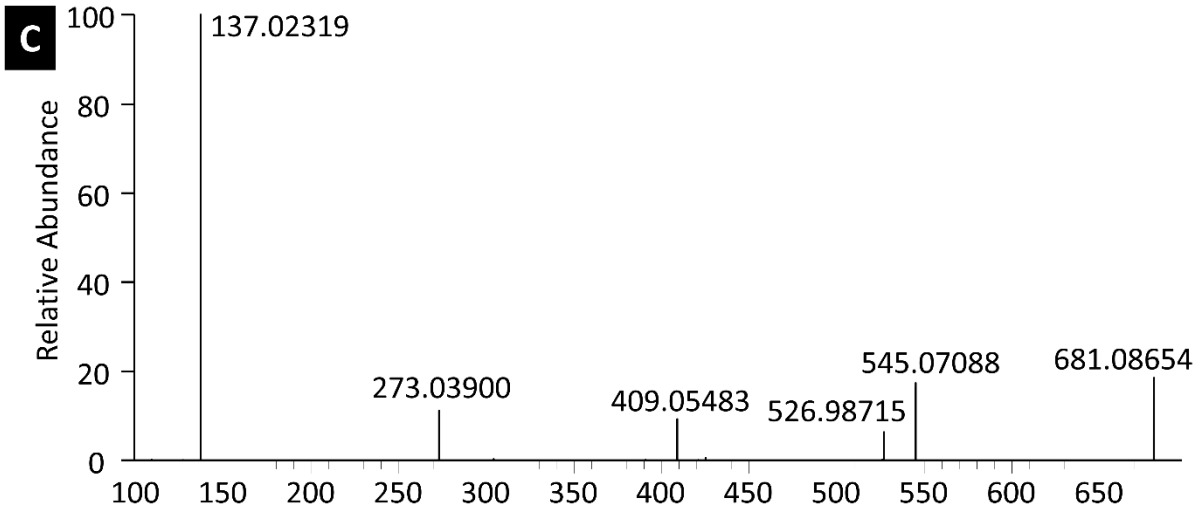
C
Relative Abundance
100
80
60
40
20
0
137.02319
273.03900
409.05483
526.98715
545.07088
681.08654
100
150
200
250
300
350
400
450
500
550
600
650

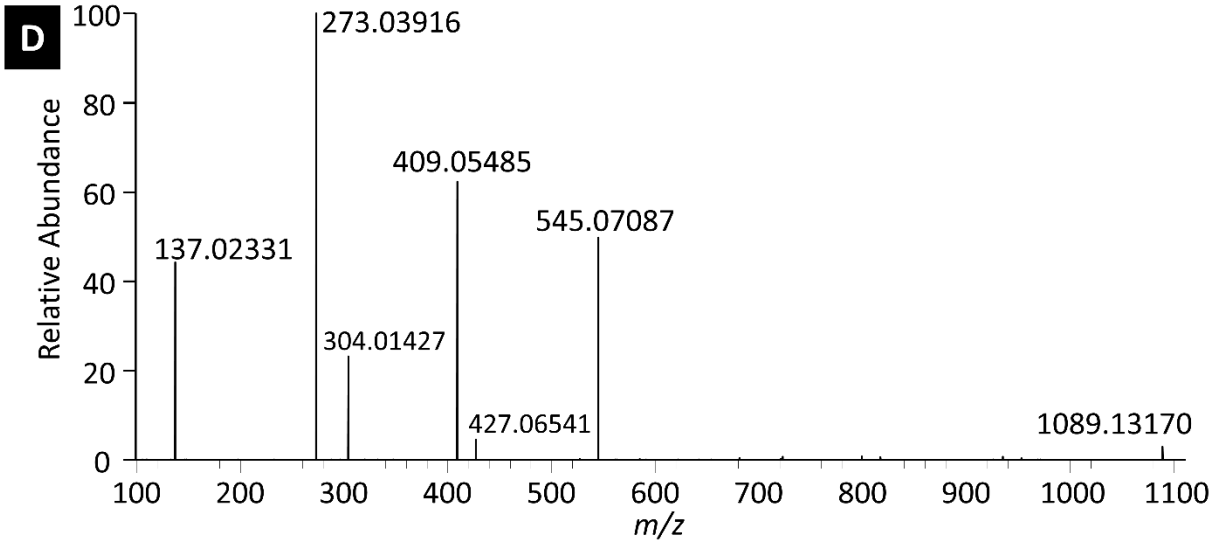

Figure S19. MS/MS spectra of DHB clusters belonging to the $[aM+H-bH_2O]^+$ (a = 1,2,3…; $b \leq a$) series. A) MS/MS of $[2M+H-2H_2O]^+$ ($C_{14}H_9O_6^+$) *m/z* 273.03936. B) MS/MS of $[3M+H-3H_2O]^+$ ($C_{14}H_9O_6^+$) *m/z* 409.05541. C) MS/MS of $[5M+H-5H_2O]^+$ ($C_{35}H_{21}O_{15}^+$) *m/z* 681.08750. D) MS/MS of $[8M+H-8H_2O]^+$ ($C_{56}H_{33}O_{24}^+$) *m/z* 1089.13563.

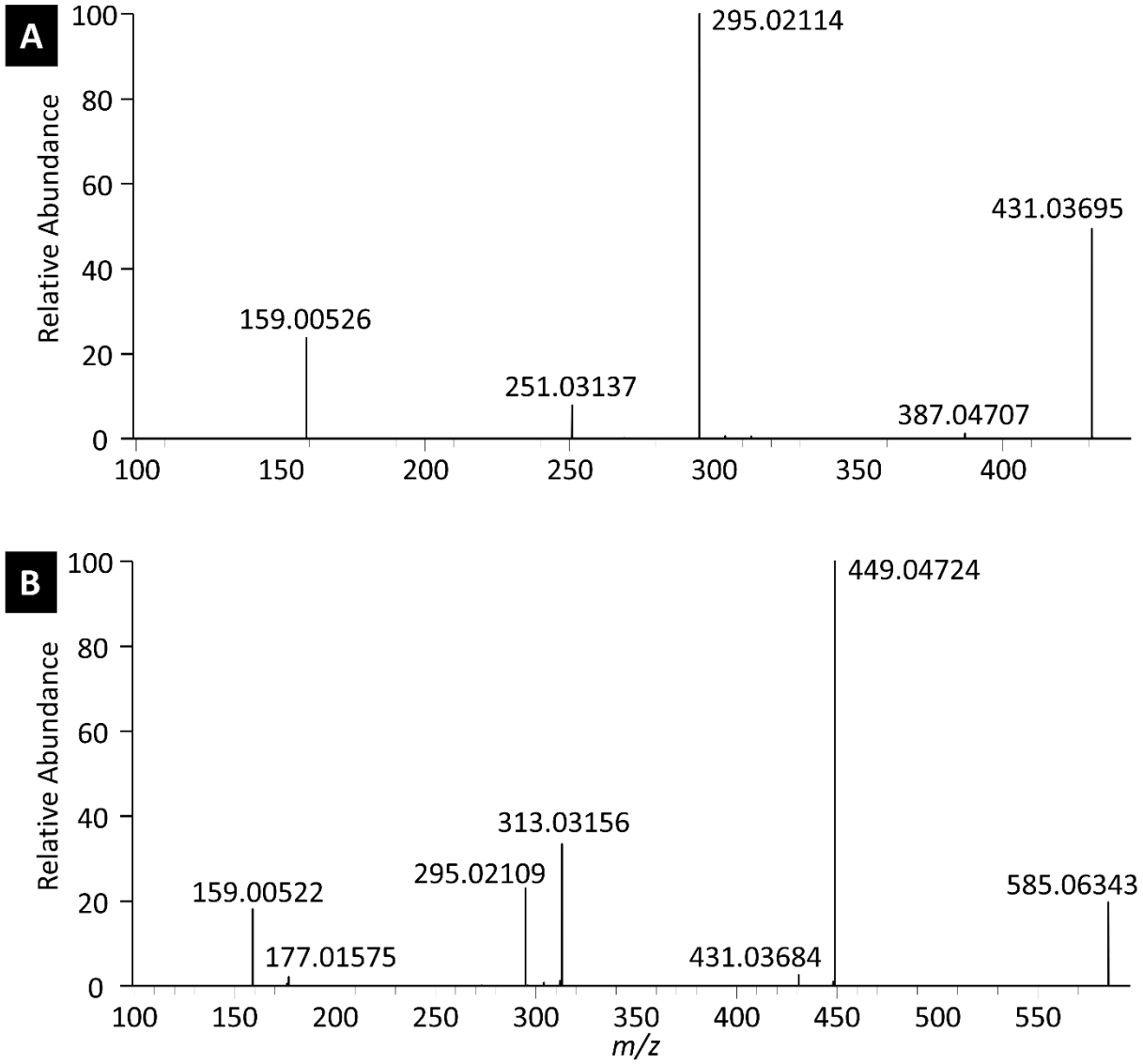

Figure S20. MS/MS spectra of DHB clusters belonging to the $[aM+Na-bH_2O]^+$ (a = 1,2,3…; b ≤ a) series. A) MS/MS of $[3M+Na-3H_2O]^+$ ($C_{21}H_{12}O_9Na^+$) *m/z* 431.03735. B) MS/MS of $[4M+Na-3H_2O]^+$ ($C_{28}H_{18}O_{13}Na^+$) *m/z* 585.06396

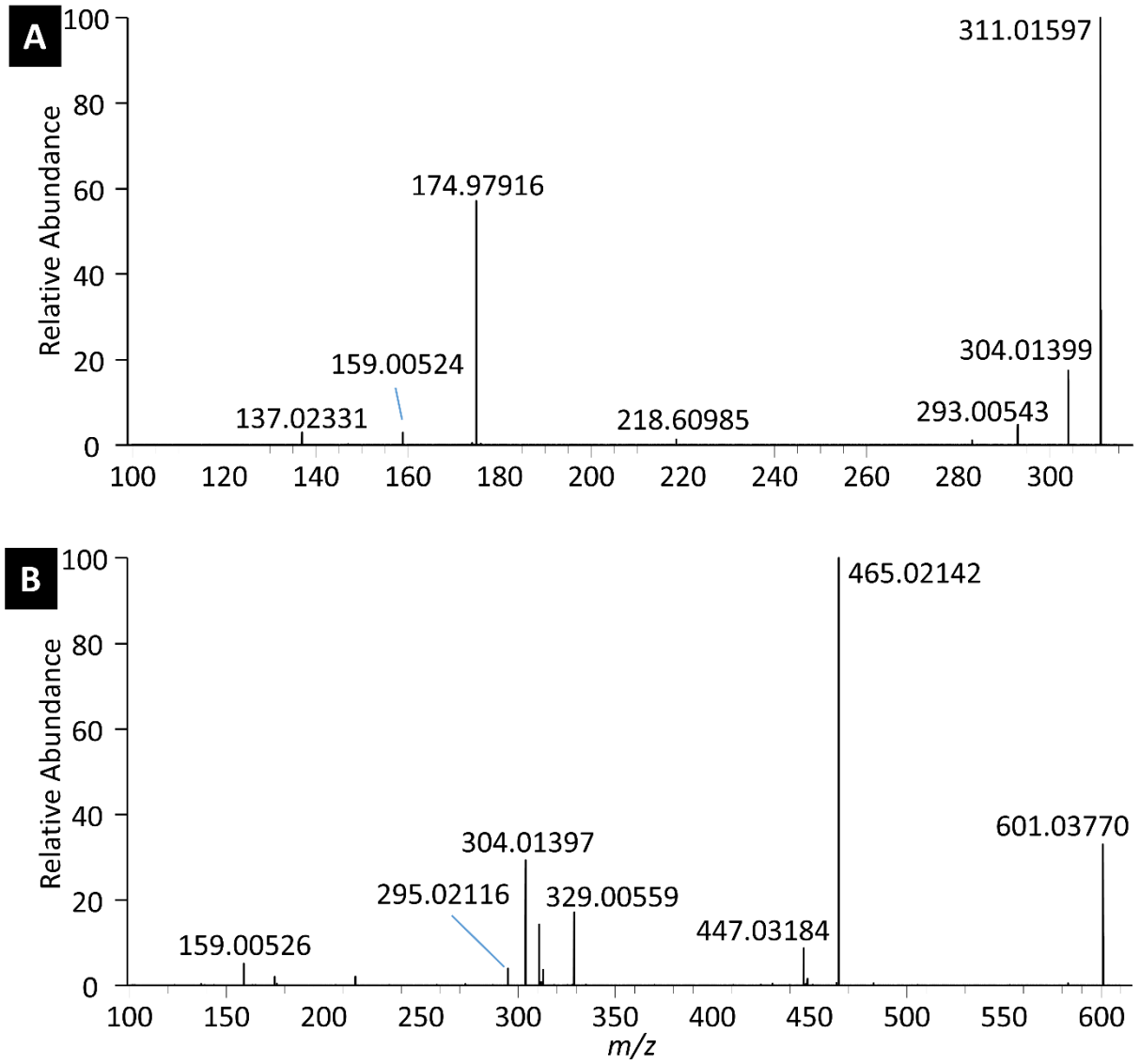

Figure S21. MS/MS spectra of DHB clusters belonging to the $[aM+K-bH_2O]^+$ (a = 1,2,3…; b ≤ a) series. A) MS/MS of $[2M+K-2H_2O]^+$ ($C_{14}H_8O_6K^+$) *m/z* 310.99525. B) MS/MS of $[4M+K-3H_2O]^+$ ($C_{28}H_{18}O_{13}K^+$) *m/z* 601.03790.

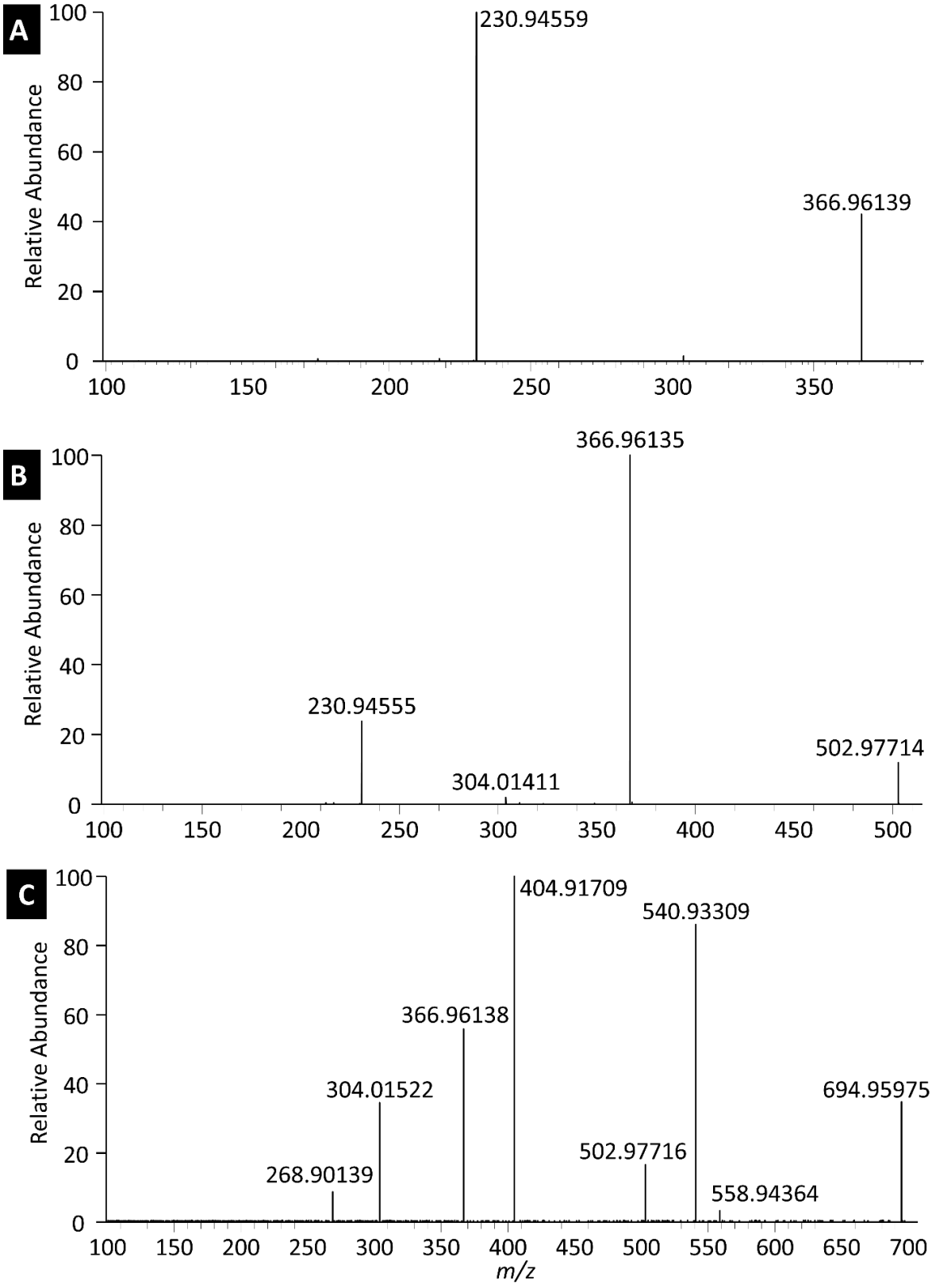

Figure S22. MS/MS spectra of DHB clusters belonging to the $[a\text{M}+b\text{Alkali}-(b\text{-}1)\text{H}-c\text{H}_2\text{O}]^+$ (a = 1,2,3…; b = 1,2,3…; c = 0,1,2,3…) series. A) MS/MS of $[2\text{M}+2\text{K}-\text{H}-\text{H}_2\text{O}]^+$ ($C_{14}H_9O_7K_2^+$) *m/z* 366.96169. B) MS/MS of $[3\text{M}+2\text{K}-\text{H}-2\text{H}_2\text{O}]^+$ ($C_{21}H_{13}O_{10}K_2^+$) *m/z* 502.97774. C) MS/MS of $[4\text{M}+3\text{K}-2\text{H}-2\text{H}_2\text{O}]^+$ ($C_{28}H_{18}O_{14}K_3^+$) *m/z* 694.96023.

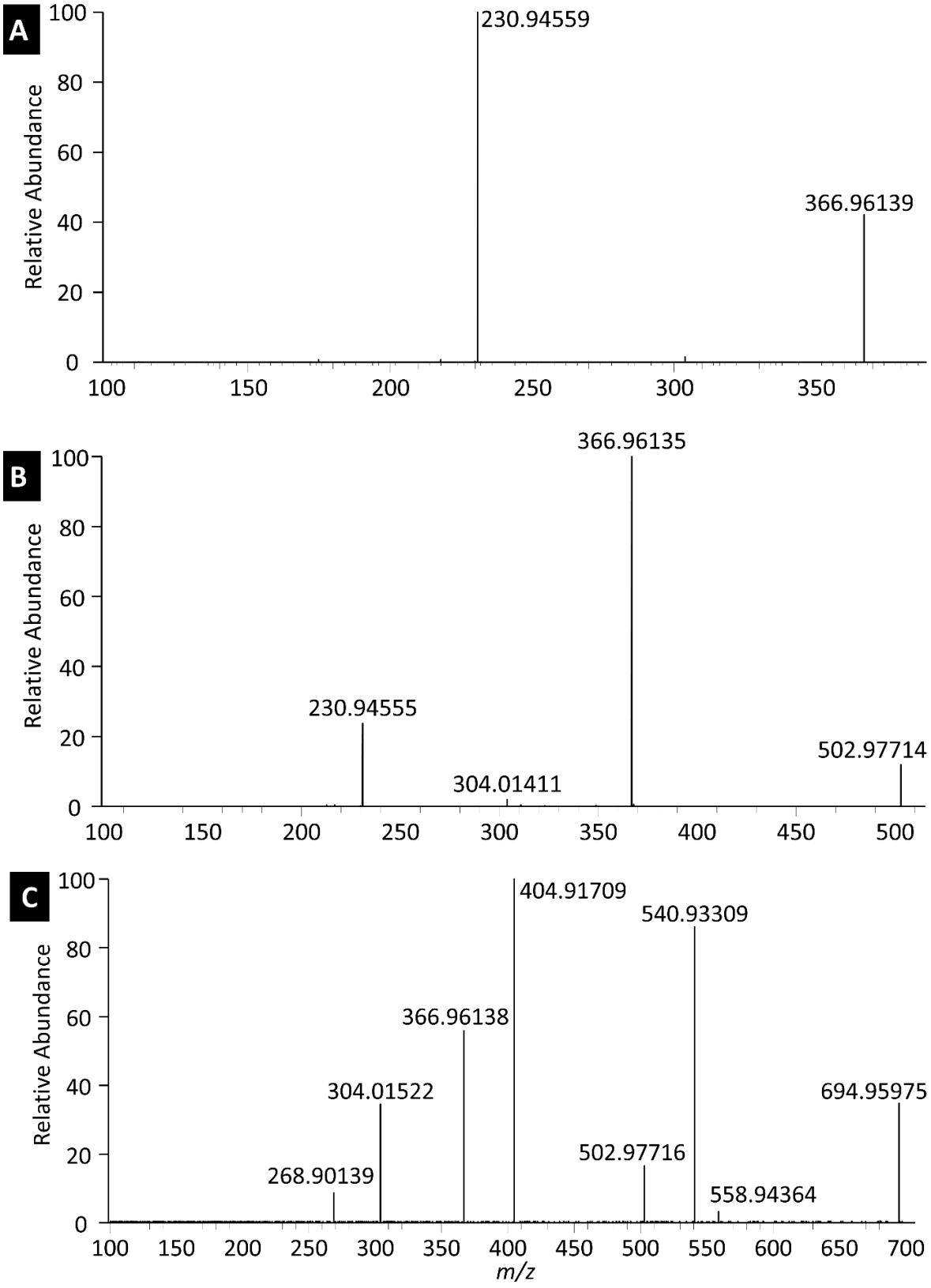

Figure S23. MS/MS spectra of DHB clusters belonging to the [*a*M-*b*H+*(b-1)*Alkali-*c*H_2O]$^-$ (*a* = 1,2,3…; *b* = 1,2,3…; *c* = 1,2,3…). A) MS/MS of [2M-2H+Na]$^-$ ($C_{14}H_{10}O_8Na^-$) *m/z* 329.02789. B) MS/MS of [3M-2H+Na-H_2O]$^-$ ($C_{21}H_{14}O_{11}Na^-$) *m/z* 465.04393. C) MS/MS of [5M-H-3H_2O]$^-$ ($C_{35}H_{23}O_{17}^-$) *m/z* 715.09407.

5.3 Third publication - Do Anti-tuberculosis Drugs Reach Their Target? – High Resolution Matrix-Assisted Laser Desorption/Ionization Mass Spectrometry Imaging Provides Information on Drug Penetration into Necrotic Granulomas

analytical chemistry

pubs.acs.org/ac Article

Do Anti-tuberculosis Drugs Reach Their Target?—High-Resolution Matrix-Assisted Laser Desorption/Ionization Mass Spectrometry Imaging Provides Information on Drug Penetration into Necrotic Granulomas

Julia Kokesch-Himmelreich, Axel Treu, Alan M. Race, Kerstin Walter, Christoph Hölscher, and Andreas Römpp*

Cite This: *Anal. Chem.* 2022, 94, 5483−5492 Read Online

ACCESS | Metrics & More | Article Recommendations | Supporting Information

ABSTRACT: Tuberculosis (TB) is characterized by mycobacteria-harboring centrally necrotizing granulomas. The efficacy of anti-TB drugs depends on their ability to reach the bacteria in the center of these lesions. Therefore, we developed a mass spectrometry (MS) imaging workflow to evaluate drug penetration in tissue. We employed a specific mouse model that—in contrast to regular inbred mice—strongly resembles human TB pathology. *Mycobacterium tuberculosis* was inactivated in lung sections of these mice by γ-irradiation using a protocol that was optimized to be compatible with high spatial resolution MS imaging. Different distributions in necrotic granulomas could be observed for the anti-TB drugs clofazimine, pyrazinamide, and rifampicin at a pixel size of 30 μm. Clofazimine, imaged here for the first time in necrotic granulomas of mice, showed higher intensities in the surrounding tissue than in necrotic granulomas, confirming data observed in TB patients. Using high spatial resolution drug and lipid imaging (5 μm pixel size) in combination with a newly developed data analysis tool, we found that clofazimine does penetrate to some extent into necrotic granulomas and accumulates in the macrophages inside the granulomas. These results demonstrate that our imaging platform improves the predictive power of preclinical animal models. Our workflow is currently being applied in preclinical studies for novel anti-TB drugs within the German Center for Infection Research (DZIF). It can also be extended to other applications in drug development and beyond. In particular, our data analysis approach can be used to investigate diffusion processes by MS imaging in general.

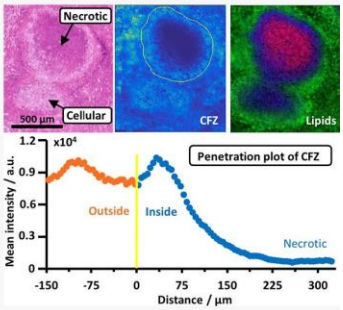

Tuberculosis (TB) is a common infectious disease caused by *Mycobacterium tuberculosis* (Mtb). According to the World Health Organization, TB ranks among the top ten causes of premature death worldwide and is responsible for more loss of life than HIV/AIDS with an estimated 9−11 million new active cases and 1.1−1.3 million deaths recorded in 2019.[1] TB treatment relies on antibiotic combination therapies, which can last for more than a year.[2] The long duration of TB drug regimens fosters the development of drug-resistant Mtb strains ultimately creating a demand for novel anti-TB drugs and the preclinical evaluation of drug candidates in vivo. TB infections in patients are characterized by the formation of necrotic granulomas in the affected organ, primarily the lungs. Necrotic granulomas are highly stratified: the necrotic center (caseum) consists of cell debris and contains a large number of extracellular bacteria. The caseum is surrounded by a cellular layer made up primarily by macrophages, which is encapsulated in a collagen-rich fibrous cuff.[3] Because Mtb persists in the caseum of these "necrotic granulomas", TB antibiotics must be able to penetrate into the center of necrotic granulomas in order to treat TB. Accordingly, for a comprehensive preclinical evaluation of novel anti-TB drugs, their distribution within the lesions and their capability to penetrate necrotic granulomas must be determined. With its unique combination of chemical and spatial information, mass spectrometry imaging (MS imaging) is an ideal tool to investigate the spatial distribution of drug compounds in tissue samples as it allows the identification and differentiation of multiple compounds, without (radioactive) labeling, in a single measurement.[4,5] Matrix-assisted laser desorption/ionization (MALDI) is the most commonly used method for MS imaging of drugs and has been successfully used to investigate the distribution of a number of drug compounds in thin tissue sections.[6−8] In TB research, MALDI MS imaging has been used previously to investigate the

Received: August 12, 2021
Accepted: February 16, 2022
Published: March 28, 2022

https://doi.org/10.1021/acs.analchem.1c03462
Anal. Chem. 2022, 94, 5483−5492

distribution of several anti-TB drugs in pulmonary granulomas, for example, in rabbit.[9] Bedaquiline (BDQ), pyrazinamide (PZA), and rifampicin (RIF) were investigated in a mouse model developing necrotizing granulomas after Mtb infection (C3HeB/FeJ) with a mass resolution of 60k [@m/z 400, full-width at half-maximum (FWHM)] and pixel sizes of 50 μm.[10,11] Two MALDI MS imaging studies have already been performed on human TB patients,[12,13] where different distributions for various drugs [clofazimine (CFZ), moxifloxacin (MXF), PZA, RIF, and linezolid] in necrotic granulomas were observed. These studies showed that not all therapeutically used anti-TB drugs are able to penetrate into necrotic granulomas. MXF, for example, could not achieve adequate therapeutic concentrations in the necrotic lesions but was readily present in cellular granulomas. This could explain the discrepancy between the efficacy of MXF in preclinical and clinical trials.[14−16] Preclinical evaluation for the activity of anti-TB drugs is almost exclusively based on regular inbred mouse strains such as BALB/c mice. However, after infection with Mtb, these mice do not develop any centrally necrotizing granulomas as they are present in TB patients requiring treatment.[17] The results for MXF show that MS imaging of anti-TB drugs in animal models exhibiting necrotizing granulomas could provide crucial predictive information for the further development of novel therapeutics in phase 2 and 3 clinical trials. IL-13-overexpressing (tg) mice represent an optimal model for the preclinical evaluation of anti-TB drugs not only because these mice strongly resemble the pathology of human TB.[18−20] As enhanced signal transduction by IL-13 is significantly linked to the degree of pathology in TB patients,[21] IL-13^{tg} mice also reflect the pathogenetic and immunological situation in the human lungs affected by TB. Hence, IL-13^{tg} mice are also an ideal tool for the analysis of the distribution of anti-TB therapeutics in necrotic granulomatous lesions by MS imaging after infection with Mtb and could improve the predictive value of preclinical drug testing and accelerate drug development. The overall small size of biological structures in mice requires high spatial resolution (better than 50 μm pixel size) to enable a direct correlation between the measured drug distribution and small histological structures such as airways, blood vessels, or different regions of necrotic granulomas. Therefore, we adapted our previously reported high-resolution AP MALDI MS imaging workflow[22] to study the penetration of anti-TB drugs in pulmonary granulomas of Mtb-infected IL-13^{tg} mice. This includes the inactivation of Mtb within the tissue of infected mice. We investigated the suitability of γ-irradiation for high-resolution MALDI MS imaging of anti-TB drugs. This workflow was developed in the framework of the German Center for Infection Research (DZIF) as a joint project of the University of Bayreuth and Research Center Borstel. Close interaction and coordination on each step of method development and application were crucial for project success. In the current manuscript, we describe this workflow focusing on MS imaging acquisition and data analysis. Tissue processing (including details of the irradiation protocol) and preclinical interpretation (including comparison of different mouse models) are discussed in a separate publication [Walter et al.].[23] After the development of necrotic granulomas was confirmed, mice were treated with a drug regimen of CFZ, PZA, and RIF. PZA and RIF are first-line drugs. CFZ is a second-line drug but has been used more frequently over the past years due to the rise of multidrug-resistant Mtb strains.[24] CFZ has not been investigated before in a mouse model with necrotizing granulomas. All three drugs showed different distributions with regard to necrotic granulomas in previous MS imaging studies.[11,12,25] Therefore, we used these drugs at therapeutic concentrations to investigate different drug penetration behaviors by high-resolution MALDI MS imaging and to further validate the IL-13^{tg} mouse model for preclinical anti-TB drug testing. We also investigated the distribution of lipids in granulomas and developed a new data analysis tool to compute the penetration properties of different drug compounds into different types of granuloma.

EXPERIMENTAL SECTION

An overview over the whole MS imaging workflow is given in Figure S1 in the Supporting Information. Details of each step are provided in the following subsections and in the Supporting Information.

Animal Experiments. IL-13^{tg} mice[26] on a BALB/c genetic background were infected with 263 cfu of Mtb H37Rv via aerosol infection. Treatment was started 9 weeks post-infection and mice received daily doses of PZA (150 mg/kg), CFZ (25 mg/kg), and RIF (10 mg/kg) for 10 days via gavage. Animals were euthanized 1 h after the last administration, organs were harvested, snap-frozen in liquid N_2, and stored at −80 °C. Uninfected BALB/c control mice received the same combination as infected IL-13^{tg} mice and were treated for 5 days. All animal experiments were performed in accordance with the German Animal Protection Law and were approved by the Animal Research Ethics Board of the Ministry of Energy, Agriculture, the Environment, Nature and Digitalization (approval number 3-1/15).

Cryosectioning and Mtb Inactivation. Serial lung sections with a thickness of 12−14 μm were cut from unembedded/uninflated lung lobes at −25 °C. Cryosectioning of lungs of infected IL-13^{tg} mice was performed in a biosafety level (BSL) 3 facility on a Leica CM1850 cryostat (Leica Biosystems GmbH, Wetzlar, Germany). Cryosectioning of uninfected BALB/c organs was performed outside the BSL 3 laboratory using a Leica CM3050 cryostat (Leica Biosystems GmbH). Sections were deposited onto precooled adhesive glass slides (Thermo Superfrost) as we have previously reported[22] and stored at −80 °C. For further processing outside of the BSL 3 facility, Mtb was inactivated by gamma (γ)-irradiation on dry ice—we have described the details in Walter et al.[23] Following microbiological examination by the National Reference Center for Mycobacteria (NRC, Borstel, Germany) of each sample batch, irradiated lung sections were shipped from the Research Center Borstel to the University of Bayreuth on dry ice and stored at −80 °C. Optical images were taken using a Keyence VHX-5000 digital microscope (Keyence Corporation, Osaka, Japan).

Matrix Application. Sections were transferred directly from the −80 °C storage into a desiccator for 15 min prior to matrix application. In the positive ion mode, 20 mg/mL 2,5-dihydroxybenzoic acid (DHB, ≥99.8%, Sigma-Aldrich) in 50% methanol and 5 mg/mL 4-nitroaniline (pNA, ≥99.8%, Sigma-Aldrich) in 75% acetone were used as matrices. Matrix solutions for the positive ion mode were acidified with 0.1% (v/v) trifluoroacetic acid. For the negative ion mode, 10 mg/mL 2,6-dihydroxyacetophenone (DHAP, ≥99.8%, Sigma-Aldrich) in 50% methanol was used. Matrices were applied using a semiautomatic pneumatic sprayer system built in-house.

https://doi.org/10.1021/acs.analchem.1c03462
Anal. Chem. 2022, 94, 5483−5492

MS Acquisition. MALDI MS imaging measurements were performed using the atmospheric pressure MALDI imaging source AP-SMALDI10 (TransMIT GmbH, Gießen, Germany) coupled to a Q Exactive HF (Thermo Fisher Scientific GmbH, Bremen, Germany).[27,28] Measurements were carried out in the positive and negative ion mode with a mass resolution of 240k @m/z 200 FWHM. Online mass calibration was performed using ubiquitous signals of the known sum formula, mostly matrix clusters[29] (Table S1, Supporting Information). Measurements featured either a single mass range or alternating mass ranges. Measurements with alternating mass ranges used step sizes of $x = y/n$ with n being the number of employed acquisition modes. Further information on the measurement setup for alternating acquisition modes can be found in the Supporting Information (Figure S2). Step sizes between 5 and 45 μm were chosen. The measurement parameters for each measurement shown in the following results and discussion part are summarized in Table S2, Supporting Information.

Data Analysis. Conversion of proprietary Thermo RAW files to imzML[30] was performed using the open access software "imzML Converter (Version 2.0.4)".[31] Further information on data processing can be found in the Supporting Information. Ion images and RGB composite images were generated in MSiReader Version 1.0.[32] Image generation parameters: bin width ±2.0 ppm, if normalization to the total ion count (TIC) was used, it is indicated in the figure captions. In the case of alternating measurements, the step size of 15 × 30 μm resulted in a pixel size of 30 × 30 μm in the MS images. Identification of all drug compounds was based on the accurate mass. To confirm the presence of the drugs, lung sections of IL-13^{tg} mice, which were not dosed with the drug cocktail (CFZ/PZA/RIF), were imaged under the same conditions, see Figure S7 (Supporting Information). Lipid compounds were tentatively identified by database search (lipidmaps.org) and MS/MS measurements (Figure S6, Supporting Information). Mass-to-charge ratios of all compounds are given as the theoretical mass. Mass accuracies across imaging data sets are given as the root mean square error (RMSE) of the Δ m/z values in ppm of each individual spectrum containing the targeted ion within a ±2.5 ppm window of the theoretical mass. RMSE values of all compounds are summarized in Table S3 (Supporting Information).

Penetration Analysis. Detailed penetration analysis of the drugs was performed using our newly developed penetration analysis tool, based on SpectralAnalysis[33] and MATLAB (R2016b), extending our work for food analysis[34] from one dimension (flat surface) to two dimensions and analyzing multiple features with arbitrary shape in a single image. The tool consists of two parts: (i) lipid-based edge detection to determine the interface and (ii) calculation of penetration plots based on distance maps. The whole data analysis workflow is described in detail in Figures S10 and S11 (Supporting Information). To compare the penetration results with the histology, we co-registered the MS imaging and H&E data, enabling transformation of data, such as the edge (interface) coordinates, between the modalities.[35]

Histopathological and Immunohistochemical Staining. Hematoxilin and eosin (H&E) staining according to Gill[36] was performed on consecutive sections to the sections subjected to MS imaging. To identify the cellular region of granulomas, macrophages were stained using anti-mouse CD68 antibodies (ab125212 or ab53444, clone FA-11, Abcam, Cambridge, U.K.), as we have described in Walter et al.[23] Sections were counterstained with methylene blue.

RESULTS AND DISCUSSION

Influence of γ-irradiation on Analyte Distribution. Sample preparation is the most crucial step in MALDI MS imaging of drugs in murine lung, as we have demonstrated in a previous study.[22] In the current study, we investigated the distribution of anti-TB drugs in the lung tissue of Mtb-infected mice by MS imaging in a standard MS laboratory, which requires inactivated Mtb in the sample material. Most of the commonly used inactivation procedures for Mtb-infected tissue are not suited for MS imaging. For example, immersion in organic solvents or PFA solutions[37] can cause severe analyte delocalization. In contrast, γ-irradiation was shown to be suitable to inactivate Mtb in rabbit lungs for MS imaging of drugs at 50 μm pixel size.[38] For our study, we needed to develop an irradiation protocol for the deactivation of Mtb-infected IL-13^{tg} mouse lung tissue that was compatible with MS imaging of drugs at high spatial resolution (5 μm pixel size). Initial irradiation experiments of whole lung lobes of IL-13^{tg} mice using energy doses up to 50 kGy were not effective and altered the organ structure such that reasonable sectioning was no longer possible. Instead of whole organs, we therefore optimized the inactivation of Mtb in lung sections of Mtb-infected IL-13^{tg} mice and found that Mtb could be inactivated by an energy dose of approx. 6 kGy as described in Walter et al.[23] Cryosectioning in the BSL 3 facility was performed without any embedding material to be compatible with the MS imaging experiments. The necrotic tissue makes sectioning even more challenging than it already is for fragile organs such as lung tissue. Our sectioning protocol was optimized based on our previous study on sectioning of lung tissue which included thaw mounting on cool glass slides using a finger from the back to warm up only a small area.[22] However, sectioning temperature had to be adapted to −25 °C. After γ-irradiation, one section of every batch was tested for viable Mtb (Figure 1A) and sections with inactivated Mtb were shipped to the MS imaging laboratory on dry ice.

It was crucial to rule out that this developed inactivation process has any influence on the drug distribution and integrity of the tissue section. For this reason, experiments were carried out with uninfected BALB/c mice, which received the drug regimen CFZ, PZA, and RIF. From the lung tissue of these mice, every second section was subjected to the inactivation process, providing pairs of neighboring nonirradiated and irradiated tissue (Figure 1B; for more details, also see Figure S3, Supporting Information). MALDI MS imaging measurements were performed on both sections in parallel to achieve a direct comparison of the drug distribution in nonirradiated and irradiated tissue. In Figure 1B, the optical image of one representative pair of nonirradiated (left side) and irradiated sections (right side) is shown. The morphology was still intact and prominent compartments of the lung such as airways and blood vessels were clearly visible (highlighted in the optical image with violet and red arrows). The cellular composition could also be preserved, which we have described in more detail in Walter et al.[23] The distribution of CFZ is shown in Figure 1C (for information about the identification of the compound, see chapter "drug distribution in IL-13^{tg} mice lung"). In both sections, CFZ was distributed homogenously in the lung parenchyma with abundant hot spots in lipid deposits located around a major airway, which is in accordance with our

https://doi.org/10.1021/acs.analchem.1c03462
Anal. Chem. 2022, 94, 5483−5492

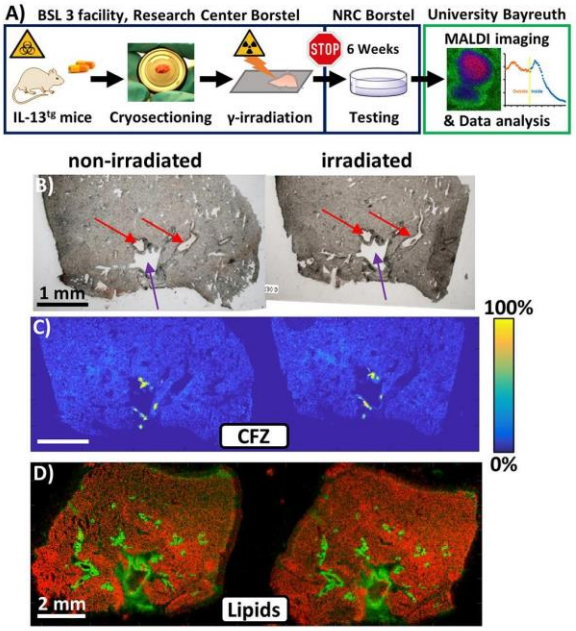

Figure 1. MS imaging of consecutive nonirradiated and irradiated noninfected BALB/c mouse lung sections: (A) short sample preparation workflow (detailed MS imaging workflow is shown in Figure S1, Supporting Information). (B) Optical image, violet arrow highlights large airway and red arrows point toward blood vessels. (C) MS image of CFZ ($[M + H]^+$, m/z 473.12942). The ion image is normalized to the TIC. (D) Distribution of lipids detected in neighboring sections, given in red is PC(32:2) ($[M + H]^+$, m/z 730.53813) and in green is PC(36:4) ($[M + K]^+$, m/z 820.5253). Lipid signals were normalized to the TIC.

previous results in noninfected mice lung tissue.[22] The influence of γ-irradiation on the PZA and RIF distributions was also investigated (Figure S4B,D, Supporting Information). No prominent difference was observed between the nonirradiated and irradiated lung sections. A second pair of irradiated and nonirradiated sections and directly neighboring sections to the sections in Figure 1B were measured in the positive ion mode in a mass range of m/z 460−900 to investigate the influence of γ-irradiation on the lipid distribution. The overlay of two lipid species shown in Figure 1D revealed no relevant difference between nonirradiated and irradiated lung sections. The H&E staining of all sections in Figure 1 are depicted in the Supporting Information (Figure S4A,C), showing intact morphologies of the sections after the irradiation process. As the γ-irradiation of our workflow had apparently no obvious impact on the distribution of either drugs or lipids, we proceeded with this inactivation protocol for the investigation of lung sections of Mtb-infected IL-13^{tg} mice dosed with CFZ, PZA, and RIF.

Drug Distribution in IL-13^{tg} Mice Lung. After inactivation by γ-irradiation, sections of Mtb-infected IL-13^{tg} mouse lung tissue were submitted to MS imaging (Figure 2). Each section contains two necrotic granulomas (as confirmed by H&E staining; Figure S5), which are visible in the optical image as dark gray almost black areas, highlighted by red arrows. Figure 2B,G provides the overlay of two lipid species, which are detected in both sections. The lipid PC(O-34:2) ($[M + Na]^+$, m/z 766.57211, red) was only detected within the granuloma area, whereas the lipid PC(36:4) ($[M + K]^+$, m/z 820.52532, green) is present in the surrounding tissue. The drug compounds CFZ (473 u) and PZA (123 u) could be detected in the same measurement as the lipids using alternating acquisition modes and employing two different mass range settings. For more details, please see Table S2 and Figure S2 in the Supporting Information. This alternating acquisition mode enabled the direct correlation of histological features (based on lipids) with the drug distribution and preserved scarce sample material. The MS images of CFZ are shown in Figure 2C,H. CFZ was mainly detected as the protonated molecular ion $[M + H]^+$ at m/z 473.12942 and the double protonated radical cation species $[M + 2H]^{+\cdot}$. The high mass resolution of the measurement [180k @m/z 473 (FWHM)] in conjunction with high mass accuracy allowed a differentiation of the isotopic patterns of both ion species as can be seen in the single pixel spectrum given in Figure S7A

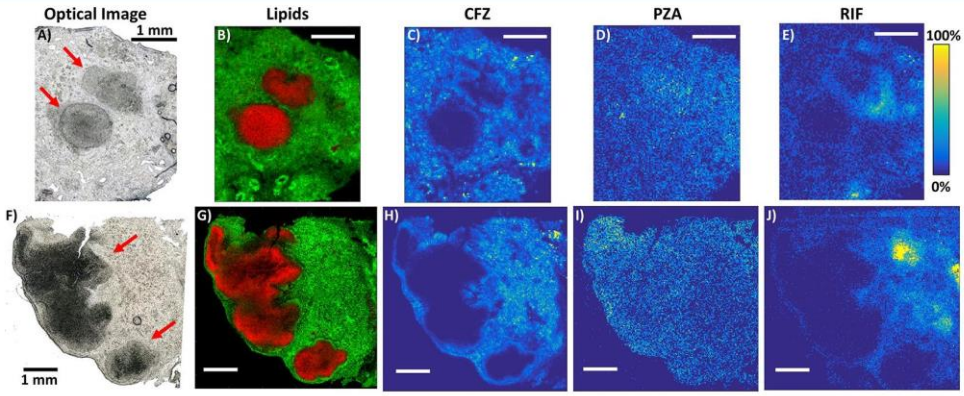

Figure 2. Lipid and drug distribution in TB granulomas: (A,F) sections of IL-13^{tg} mouse lung, red arrows indicate TB granulomas. (B,G) RGB images of PC(O-34:2) (red, $[M + Na]^+$, m/z 766.57211) and PC(36:4) (green, $[M + K]^+$, m/z 820.52531), lipid images are TIC-normalized. (C,H) Distributions of CFZ ($[M + H]^+$, m/z 473.12942). (D,I) Distributions of PZA ($[M + 2H]^{+\cdot}$, m/z 125.05831). Measurements were performed in the positive ion mode using the DHB matrix. (E,J) Distributions of RIF ($[M - H]^-$, m/z 821.39784). Measurements were conducted on neighboring sections in the negative ion mode using the DHAP matrix, see Figure S5C,D for optical images. All images were generated with 30 μm pixel size. RMSE values <1 ppm for all compounds (Table S3, Supporting Information).

https://doi.org/10.1021/acs.analchem.1c03462
Anal. Chem. 2022, 94, 5483−5492

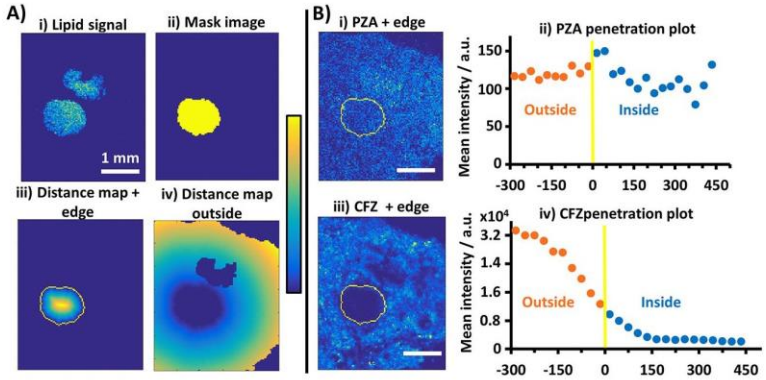

Figure 3. Data analysis workflow: (A) (i) ion image of m/z 766.57211 (PC(O-34:2), $[M + Na]^+$). (A) (ii) Binary image of round granuloma based on lipid in (A) (i). (A) (iii) Calculated edge for the round granuloma and distance map toward the center of the granuloma. (A) (iv) Distance map from the edge toward the outside of the tissue. For more details, see Figure S10 (Supporting Information). (B) Results of the data analysis: (B) (i,iii) ion images of PZA and CFZ with the calculated edge. (B) (ii,iv) Corresponding penetration plots for PZA and CFZ. Mean intensities of the drug for all pixels at a certain distance against the distance (μm). The vertical yellow line indicates the edge of the granuloma. Orange data points correspond to mean intensities of the drug outside the calculated edge and blue data points toward the inside.

(Supporting Information). The mass accuracies of the $[CFZ + H]^+$ peaks in Figure 2C,H were 0.29 and 0.81 ppm across the whole field of view. All compounds in this study were detected with an RMSE lower than 1 ppm and the calculated RMSE values for each measurement are compiled in Table S3 (Supporting Information). For confirmation, a lung section of Mtb-infected IL-13^{tg} mice not treated with CFZ was investigated as the negative control and no CFZ-related signal could be detected (Figure S8C, Supporting Information). The combination of high mass resolution, high mass accuracy, and control sample (Figure S8, Supporting Information) enabled the identification of all drug compounds in this study. PZA was solely detected as the radical ion $[M + 2H]^{+\cdot}$ at m/z 125.05836 (see the single pixel mass spectrum in Figure S7B, Supporting Information). We have proposed the molecular structure of this ion supported by MS/MS experiments in a previous study.[22] The third compound RIF was detected in neighboring sections (optical image in Figure S5C,D) of the sections shown in Figure 2A,F in the negative ion mode as the deprotonated molecular ion $[M - H]^-$ at m/z 821.39784 (see the Supporting Information Figure S7D for the single pixel mass spectrum). A comparison of the optical and MS images in Figure 2 clearly demonstrates that CFZ, PZA, and RIF exhibit different distribution patterns in distinct areas of the granulomas. For CFZ, a heterogeneous distribution can be observed. The intensity of CFZ was much higher in the surrounding tissue than in the area of the necrotic granuloma, indicating that CFZ is unable to penetrate into the necrotic core. In contrast, PZA is distributed evenly in the granuloma and the surrounding tissue, indicating that PZA is able to penetrate into necrotic granulomas. Additionally, the active metabolite of PZA, pyrazinoic acid (POA, $[M + 2H]^{+\cdot}$, m/z 126.04237), was co-detected in both measurements (Supporting Information Figure S9) and was mainly detected within the granulomas. Similar to CFZ, the intensity of RIF (Figure 2E,J) was also higher in the surrounding tissue than in the granuloma areas. The distributions of RIF, PZA, and POA have been imaged before in lung tissue of Mtb-infected C3HeB/FeJ mice, which also develop necrotic granulomas. RIF was imaged at 50 μm step size[10] and PZA and POA at 75 μm step size with a mass resolution of 60,000 @m/z 400 (FWHM).[11] Although a different mouse model was used, we detected the same distribution of RIF, PZA, and POA with a higher resolution (pixel size 30 μm) than previously reported. This shows that we have successfully established our high-resolution MALDI MS imaging workflow for a detailed investigation of the anti-TB drug penetration into necrotic granulomatous lesions in an animal model reflecting the typical pathogenesis in TB patients. CFZ was imaged in our studies for the first time in a mouse model with human-like TB pathology. Previously, the distributions of CFZ, PZA, and RIF were investigated in human TB patients in granulomatous lesions by MALDI MS imaging.[12] RIF could not be detected within granuloma regions after a single dose but accumulated in necrotic areas at the steady state. These results indicate that in our present mouse study, RIF had not reached steady state. Since we have observed in this and in our other study[23] the same distribution pattern for PZA (detectable inside and outside of necrotic lesions) and CFZ (only detectable outside of necrotic granulomas) as it was observed in TB patients, our results confirm that the IL-13^{tg} mouse model is suited for preclinical testing of anti-TB drugs.

Penetration Analysis. In drug development, it is important to be able to measure the penetration of pharmaceutical compounds into biological areas of interest to ensure that compounds are reaching the desired location. Previous studies using MS imaging to visualize the penetration of compounds into targeted structures include the work of Bonnel et al.[39] which proposed a method for measuring the penetration of pharmaceutical compounds in skin assuming a flat surface with the compound of interest only moving in one direction. Machálková et al.[40] presented a method for determining the penetration of compounds from circular shapes, which relied on additional laser scanning confocal microscopy experiments. To determine the penetration of compounds into granulomas, which do not have ideal circular shapes, a new analysis method was required. Our developed analysis tool, which is solely based on MS imaging data, consists of two main parts: (A) lipid-based edge detection of granuloma areas and (B) calculation of penetration plots based on distance maps. Our semiautomatic tool can determine the penetration of drug compounds into irregular, two-dimensional

https://doi.org/10.1021/acs.analchem.1c03462
Anal. Chem. 2022, 94, 5483−5492

shapes while assuming a movement of compounds within a plane. The analysis of multiple independent irregular shapes in one measurement is also possible.

The results and interim steps of the developed method are shown in Figure 3 using the measurement presented in Figure 2A−D as an example to briefly explain our approach. For more details about the data analysis approach, see Figures S10 and S11 (Supporting Information). The lipid PC(O-34:2) ([M + Na]$^+$, m/z 766.57211) from Figure 2B, which is only present within the granuloma area is depicted in Figure 3Ai. As a first step, this characteristic lipid was chosen as a mask for the granuloma area showing high intensities in both granulomas. While the whole data analysis workflow can be conducted on both granulomas in one run, the following steps are exemplified on the larger, round granuloma. The ion image of PC(O-34:2) ([M + Na]$^+$) was binarized and filtered and the remaining gaps were filled to generate a mask image (Figure 3Aii). Using this mask, the calculation of an "edge" was possible (yellow circle in Figure 3Aiii). For the granuloma mask image, a corresponding distance map (Figure 3Aiii) was then generated, where each intensity in the pixel of the mask was replaced by its distance to the "edge". The distance for every pixel from the "edge" toward the tissue border was calculated. Using the two distance maps (one to the inside of the calculated edge and one toward the tissue border from the edge), it is possible to determine the distance for each pixel in the measurement toward the calculated edge and to extract intensities (of given analytes) at each distance. In Figure 3Bi,iii, the ion images of PZA and CFZ are shown overlaid with the calculated edge. The mean intensities for each drug in all pixels at a certain distance can be calculated. These mean intensities plotted against the distance result in a penetration plot from the surrounding tissue, through the edge to the center of the granuloma. The plots for PZA and CFZ are depicted in Figure 3Bii,iv, respectively. The vertical yellow lines in the plots indicate the calculated edge (distance = 0 μm). The penetration curve of PZA (Figure 3Bii) shows a similar abundance of PZA in both regions, inside and outside of the granuloma. This confirms our observation that PZA is able to penetrate into necrotic granulomas and is homogenously distributed in the granuloma area and the surrounding tissue. In contrast, the penetration plot of CFZ (Figure 3Biv) shows a different penetration pattern. The intensities of CFZ are much lower inside the granuloma center than outside. The plot shows that this decline of CFZ intensity from the edge toward the center of the granuloma is a gradual process. However, within the granuloma, the abundance of CFZ does not drop to zero (not obvious in the MS image in Figure 2C), indicating that CFZ is able to reach the granuloma center to some extent. Furthermore, the intensity decline begins already in the surrounding tissue outside of the determined edge. The penetration plot of RIF in this granuloma is given in Figure S13A and shows a similar trend as the CFZ plot. The mean RIF intensity begins to decrease toward the edge and declines further toward the center of the granuloma. In summary, our developed penetration analysis tool provides detailed information about the penetration profiles of drugs and is a useful tool to compare the penetration behavior of different drugs and samples.

Penetration Behavior of CFZ. To further investigate the penetration behavior of CZF, the penetration analysis was conducted on all the remaining granulomas from both sections shown in Figure 2. In Figure 4B,E, the H&E staining of the

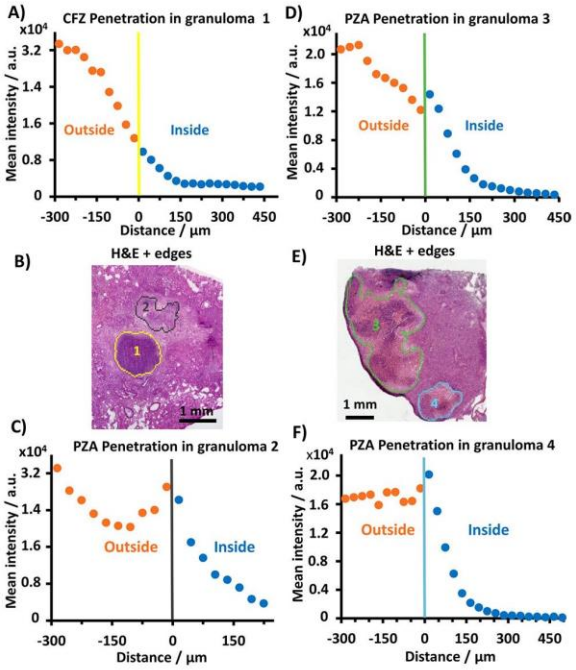

Figure 4. Comparison of penetration plots of CFZ in different granulomas: (A,C) penetration curves of CFZ for granuloma 1 and 2 in (B). (B,E) H&E staining of neighboring sections of sections in Figure 2 with calculated edges from the penetration tool. (D,F) Penetration curves of CFZ for granuloma 3 and 4 in (E). In all penetration plots, the mean intensities of CFZ for a certain distance are shown against the distance in μm. The colored vertical lines represent the calculated "colored edges" of the granulomas in (B,E).

neighboring sections of both imaged sections is shown with the calculated edge for each granuloma. The colored edges correspond to the colored vertical lines in the penetration plots. In Figure 4A, the penetration plot of the round granuloma (granuloma 1) from Figure 3 is depicted again, and in Figure 4C, the plot of granuloma 2 in the same section is shown. The penetration plots of Figure 4D,F correspond to the granulomas 3 and 4 in the second section. All four penetration plots follow a similar trend, and the intensity of CFZ is higher in the outside region than within the granuloma area and the CFZ signal from the calculated edge toward the center of the granuloma gradually declines. The penetration plot of granuloma 2 in Figure 4C shows the same pattern as granuloma 1 in Figure 4A. In both granulomas, CFZ signal intensity was found inside the necrotic center but with much lower intensity than in the surrounding tissue. In Figure 4C,D, the decline of the CFZ signal starts outside of the calculated edge as observed for granuloma 1 (Figure 4A). This penetration behavior may be caused by the structure of the granulomas, which are encapsulated in a collagen-rich fibrous cuff. This fibrous cuff is very prominent in granuloma 1 (Figure 4B) and can be observed as a fine red line in the H&E-stained section (also see Figure S5A, Supporting Information). In Figure 4B, it can be seen that the fibrous cuff lies close to the determined yellow edge of granuloma 1. A layer of fibroblasts, epithelioid macrophages, and other immune cells surround the fibrous cuff. These cellular components of the surrounding tissue and the fibrous cuff itself might hinder the diffusion of

https://doi.org/10.1021/acs.analchem.1c03462
Anal. Chem. 2022, 94, 5483−5492

CFZ and can therefore explain the decrease in CFZ before the calculated edge. Furthermore, the plots in Figure 4C,D,F show a maximum of the CFZ intensity around the calculated edges. A comparison of the H&E stains of all four granulomas in Figure 4 shows that granuloma 1 in Figure 4B (yellow edge) displays a more stratified structure and a solely necrotic core. The other three granulomas exhibited a higher proportion of cellular quantities, indicated by white regions in the H&E staining (detailed annotation in Figure S5).

The necrotic areas of granuloma 3 (green edge) in Figure 4E are surrounded by a thick cellular layer (detailed description in Figure S5B). The maxima in these penetration plots (Figure 4C,D,F) indicate that CFZ accumulates in these cellular regions. As CFZ was given in combination with PZA and RIF in this study, these drugs could change the environment and therefore have an influence on the penetration behavior. However, since CFZ was less abundant in the necrotic core, these findings can explain the limited activity of a CFZ monotherapy in necrotic lung lesions of C3HeB/FeJ mice in a previous study.[41] The penetration analysis was also carried out for PZA and RIF. PZA shows in the three additional penetration plots the same behavior as before. This confirms the homogeneous distribution of PZA over the whole tissue sections including the necrotic core (Figure S12, Supporting Information). RIF, on the other hand, showed as expected a similar behavior as CFZ. In all four plots, the intensities of RIF showed a gradual decline, withhigher intensities in the surrounding tissue than within the granuloma area (Figure S13, Supporting Information). In comparison to CFZ, the RIF penetration plots did not reveal any maximum around the calculated edges, indicating that RIF did not accumulate in the cellular regions.

High-Resolution MS Imaging. To determine the influence of the internal structure of a granuloma on the penetration behavior of CFZ, imaging was performed with a pixel size of 5 μm to gain more detailed information than in Figure 2. MS imaging was performed on a small (0.5 × 1 mm) dumbbell-shaped granuloma exhibiting a very clearly defined internal structure (Figure 5) to examine which parts of the granuloma are effectively reached by this antibiotic. H&E staining of the lesion allowed a preliminary differentiation of the granuloma regions (Figure 5A). The darker violet area in the (larger) upper half of the granuloma indicates a central necrosis. The lighter almost white areas indicate the more cellular regions, showing that the necrotic core is surrounded by an approx. 100 μm-thick cellular layer. The smaller lower half of the granuloma appeared to be mainly cellular without a central necrosis. The entirety of the granuloma is encapsulated in a fibrous cuff and surrounded by fibroblasts, which are indicated with asterisks (*) (Figure 5A). One prominent cell type in granulomas are macrophages, which can be stained using CD68 antibodies and appear afterward in yellow. The CD68 staining in Figure 5B shows that the cellular regions adjacent to the necrotic core and the smaller lower, cellular half of the granuloma have a high content of macrophages. Outside the granuloma, a few smaller CD68-positive macrophage clusters can be found (Figure 5B; black arrows). The MS imaging experiment with 5 μm step size was performed on a neighboring section to Figure 5A,B with a mass range of m/z 400−900 in the positive ion mode to be able to detect CFZ and lipids. This is the lowest reported step size for lipids and anti-TB drugs in Mtb-infected tissue, so far. Analogous to Figure 2B,E, the lipid PC(36:4) ([M + K]$^+$, m/z 820.52531) is present in the surrounding area (Figure 5D, green) and shows a higher intensity in the regions of the fibroblasts and epithelioid macrophages. Due to the smaller pixel size and the distinct histological structure of the granuloma, we can now expand upon the results of Figure 2 and differentiate between characteristic lipids for the different tissue types of the granuloma. In Figure 5D, the lipid PC(O-36:3) ([M + K]$^+$, red, m/z 808.56170) is mainly present in the central necrosis located in the upper half of the granuloma. The lipid PC(O-36:4) ([M + K]$^+$, m/z 806.54604) is given in blue as representative lipid for the cellular areas inside the granuloma. The distribution of CFZ ([M + H]$^+$, m/z 473.12942) is shown in Figure 5C. It can be observed not only in the surrounding tissue but also in the granuloma area. The comparison between the MS image and the H&E staining revealed that the drug is detected in the cellular regions (surrounding the necrotic core in the upper part of the granuloma and in the intact cellular

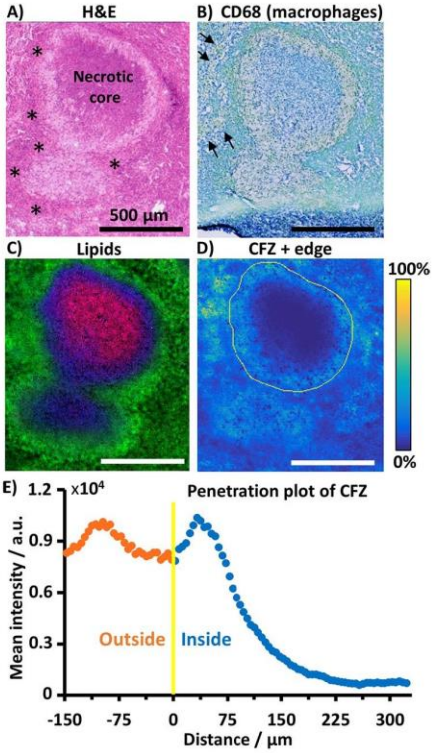

Figure 5. High-resolution MS imaging of distinct structured granuloma: (A) H&E stain, * indicates fibroblast- and epitheloid macrophage-rich regions. (B) CD68 antibody stain, arrows indicate macrophage clusters outside of the granuloma area. (C) RGB overlay of three lipids, PC(O-36:3) (red, [M + K]$^+$, m/z 808.56170), PC(36:4) (green, [M + K]$^+$, m/z 820.52531), and PC(O-36:4) (blue, [M + K]$^+$, m/z 806.54604). Lipid ion signals are normalized to the TIC. (D) Distribution of CFZ ([M + H]$^+$, m/z 473.12942) with drawn ROI. MS imaging measurement was acquired in the positive ion mode using pNA matrix, step size, and pixel size was 5 μm. RMSE <1.0 ppm (Table S3). MS imaging experiment and staining methods were performed on adjacent sections. (E) Penetration plot of CFZ for the ion image in (D). Mean intensities of the drug for a certain distance against the distance (μm). The vertical yellow line indicates the drawn ROI edge. For more details for the penetration workflow, see the Supporting Information (Figure S14, Supporting Information).

https://doi.org/10.1021/acs.analchem.1c03462
Anal. Chem. 2022, 94, 5483−5492

part of the lower part of the granuloma). As expected, the intensity of CFZ was very low in the central necrotic area. By comparing the CFZ distribution with the CD68-positive areas, it can be observed that CFZ was detected in the macrophage-rich areas, inside the granuloma but also in the macrophages in the surrounding tissue (black arrows in Figure 5B). The intensity of CFZ was higher in some of the macrophage clusters in the surrounding tissue than within the granuloma. These macrophages are not encapsulated by a collagen rim and could represent a different type of macrophage. The presence of CFZ in the cellular areas of the granuloma is in accordance with our findings of the CFZ distribution in Mtb-infected wildtype mice (BALB/c) in Walter et al.[23] Here, a higher intensity was detected in cellular granulomas, which contain a high amount of macrophages, as compared to necrotic granulomas of IL-13^{tg} mice. Previous studies in mice indicated that CFZ accumulates in macrophages of different tissues.[42,43] To confirm the identity of CFZ, Aplin et al. extracted crystals from macrophages and analyzed the homogenate by MS.[42] In our study, the combination of immunohistochemistry and MS imaging in tissue sections provides a direct link between the histological structure and the specific molecular information and enables the in situ identification of CFZ. In comparison with the MS imaging study of CFZ in lung sections of TB patients,[12] our approach with 5 μm pixel size provides a 225-fold increase in the number of data points (pixels) per unit area. This enables a better correlation of the drug and lipid distributions with small histological features such as the macrophage clusters or rim of foamy macrophages in mice lung tissue. The smaller step size also provides more data points for the penetration plot and makes a more detailed investigation of the CFZ penetration possible. The interface between the necrotic region and the surrounding tissue appears to play an important role for the drug penetration behavior. To investigate the CFZ penetration profile specifically along the different parts of the granuloma, a region of interest (ROI) in the upper part of the granuloma in Figure 5A was manually generated in Spectral Analysis.[33] This ROI was chosen based on the distribution of PC(O-36:4) ($[M + K]^+$, m/z 806.54604, Figure S14B), which was detected with higher abundance in the cellular regions of the granuloma. The overlay of this ROI with the CFZ signal and the H&E staining is presented in Figures 5C and in S14A (Supporting Information), respectively. The ROI was subsequently imported into our penetration tool and all steps as described in Figure 3Aiii−B were performed, resulting in the penetration plot of CFZ in Figure 5E (see Figure S14D−F for the detailed data analysis workflow in the Supporting Information). This penetration plot shows a similar trend as before. The maximum of the mean CFZ intensities in the outside region (orange data points) corresponds to the macrophage clusters in the surrounding tissue. In accordance with Figure 4, the maximum within the granuloma (blue data points) is located in the cellular layer surrounding the necrotic core before the CFZ declines toward the necrotic core. After this decline, the CFZ intensity does not completely vanish but is much lower in comparison with the maximum in the cellular layer. We reproduced these findings in a granuloma which comprises a similar distinct macrophage rim (Figure S15, Supporting Information), confirming that CFZ accumulates in macrophages. Combining data from all penetration plots, our results indicate that CFZ is located in the lung tissue outside of centrally necrotized granulomas and its penetration might be hindered by the fibrous cuff and other cell agglomerates walling off the mycobacteria-containing inside. However, CFZ is able to reach the cellular regions of the granulomas, probably by blood vessels and accumulates in macrophages inside the granulomas. The CFZ intensity decreases toward the necrotic center, which is entirely acellular and thus free of a vascular supply. In addition, CFZ and other drugs can bind to caseum macromolecules, which hamper the passive diffusion toward the center of the necrotic core.[44] This in-depth investigation of the CFZ penetration behavior in different compartments of the lung tissue and granuloma was only possible because of the high-resolution MS imaging workflow and data analysis approach developed in this study. This approach could also be applied to other diseases whose treatment requires the penetration of drug compounds into defined pathological structures such as tumors or parasitic cysts caused by the larvae of various tape worms.

CONCLUSIONS

We have developed a MALDI MS imaging workflow to investigate the distribution and penetration behavior of anti-TB drugs in mouse lung tissue. In accordance with the literature, different distributions for PZA and RIF could be observed in the necrotic granulomas of Mtb-infected IL-13^{tg} mice. Both drugs were detected here with a lower pixel size (30 μm) than previously reported (PZA: 75 μm, RIF: 50 μm) providing more data points for the small histological features of mouse granulomas. CFZ was imaged in our studies for the first time in a mouse model with necrotizing granulomas. Our study confirms the distribution patterns of CFZ and PZA in granulomatous lesions of TB patients and thus verifies the suitability of the IL-13^{tg} mouse model for preclinical anti-TB drug testing. From a methodological point of view, it was important to ensure that inactivation of Mtb in infected lung sections by γ-irradiation did not influence the distribution of the analyzed drugs and lipids and that the tissue morphology was still intact. MS imaging data were based on high mass resolution (240k @m/z 200, FWHM) and mass accuracy (better than 1 ppm) ensuring confident identification of all analyzed compounds. To gain more detailed information about the drug penetration and to visualize it better, we have developed a new data analysis approach representing a highly flexible tool to investigate multiple ROIs and drugs in one run. This tool allowed an in-depth investigation of the drug penetration behaviors. To investigate the CFZ penetration and lipid pattern of granulomas in more detail, an MS imaging experiment with a step size of 5 μm on a histologically distinct structured granuloma was conducted. This is the lowest reported step size for lipids and anti-TB drugs in Mtb-infected tissue so far. Characteristic lipids could be identified for the surrounding lung tissue and for the cellular and necrotic structures of granulomas in Mtb-infected IL-13^{tg} mice. Our measurements show that CFZ can actually reach the granuloma to some extent and accumulates in macrophages in the cellular regions. Since the efficacy of anti-TB drugs depends on their ability to breach the fibrous cuff and cellular macrophage zone to reach the mycobacteria-containing necrotic core of granulomas, the information provided by our penetration analysis methodology can advance the development of novel anti-TB drugs. The combination of the suitable, human-like IL-13^{tg} mouse model and the developed MS imaging workflow is therefore currently being applied in preclinical studies for novel anti-TB drugs within the German

https://doi.org/10.1021/acs.analchem.1c03462
Anal. Chem. 2022, 94, 5483−5492

Center for Infection Research (DZIF). Apart from this application, the combination of the high-resolution MALDI imaging workflow and penetration analysis tool can be used to study penetration behaviors of any drugs in different diseased tissues or diffusion processes in general.

■ ASSOCIATED CONTENT

Supporting Information

The Supporting Information is available free of charge at https://pubs.acs.org/doi/10.1021/acs.analchem.1c03462.

Further details on the MALDI imaging workflow, including instrument settings; additional microscope and MS images for all samples; corresponding mass spectra; results for negative control samples and repeat measurement; and details about the data analysis workflow (PDF)

■ AUTHOR INFORMATION

Corresponding Author

Andreas Römpp − *Bioanalytical Sciences and Food Analysis, University of Bayreuth, Bayreuth 95447, Germany; German Center for Infection Research (DZIF), Braunschweig 38124, Germany;* orcid.org/0000-0001-8384-9250; Email: Andreas.roempp@uni-bayreuth.de

Authors

Julia Kokesch-Himmelreich − *Bioanalytical Sciences and Food Analysis, University of Bayreuth, Bayreuth 95447, Germany; German Center for Infection Research (DZIF), Braunschweig 38124, Germany*

Axel Treu − *Bioanalytical Sciences and Food Analysis, University of Bayreuth, Bayreuth 95447, Germany; German Center for Infection Research (DZIF), Braunschweig 38124, Germany*

Alan M. Race − *Bioanalytical Sciences and Food Analysis, University of Bayreuth, Bayreuth 95447, Germany;* Present Address: Institute of Medical Bioinformatics and Biostatistics, Philipps University of Marburg, Marburg, Germany; orcid.org/0000-0001-8996-2641

Kerstin Walter − *Infection Immunology, Leibniz Lung Center, Research Center Borstel, Borstel 23845, Germany; German Center for Infection Research (DZIF), Braunschweig 38124, Germany*

Christoph Hölscher − *Infection Immunology, Leibniz Lung Center, Research Center Borstel, Borstel 23845, Germany; German Center for Infection Research (DZIF), Braunschweig 38124, Germany*

Complete contact information is available at: https://pubs.acs.org/10.1021/acs.analchem.1c03462

Author Contributions

The manuscript was written through contributions of all authors. All authors have given approval to the final version of the manuscript. J.K.-H. and A.T. contributed equally.

Notes

The authors declare no competing financial interest.

■ ACKNOWLEDGMENTS

Financial support from the German Center for Infection Research (DZIF) TTU 02.806, TTU 02.810, and TTU 02.814, the Deutsche Forschungsgemeinschaft (DFG) INST 91/373-1-FUGG and the TechnologieAllianzOberfranken (TAO) is gratefully acknowledged. We would like to thank Alexandra Hölscher and Johanna Volz for technical assistance during animal experiments, Ann-Kathrin Lemm for infection, dosing, and sectioning the lung samples, and Elena Roman-Paucar and Nils Weidner for their support with the MALDI sample preparation. We are also grateful to Marion Schuldt for supplying and cleaning the lab and to Ilka Monath, Christine Keller, Sarah Vieten, and Gerhard Schultheiß for organizing the animal facilities in Borstel and Kiel. We would like to thank the National Reference Center for Mycobacteria in Borstel for the microbial testing. Furthermore, the authors would like to thank Norbert Heinrich and Julia Dreisbach for fruitful discussions.

■ REFERENCES

(1) World Health Organization. *Global Tuberculosis Report—Executive Summary*, 2020.
(2) Horsburgh, C. R., Jr.; Barry, C. E., 3rd; Lange, C. *N. Engl. J. Med.* **2015**, *373*, 2149−2160.
(3) Dartois, V. *Nat. Rev. Microbiol.* **2014**, *12*, 159.
(4) Spengler, B. *Anal. Chem.* **2015**, *87*, 64−82.
(5) Römpp, A.; Spengler, B. *Histochem. Cell Biol.* **2013**, *139*, 759−783.
(6) Prideaux, B.; Stoeckli, M. *J. Proteomics* **2012**, *75*, 4999−5013.
(7) Schulz, S.; Becker, M.; Groseclose, M. R.; Schadt, S.; Hopf, C. *Curr. Opin. Biotechnol.* **2019**, *55*, 51−59.
(8) Römpp, A.; Guenther, S.; Takats, Z.; Spengler, B. *Anal. Bioanal. Chem.* **2011**, *401*, 65−73.
(9) Manier, M. L.; Reyzer, M. L.; Goh, A.; Dartois, V.; Via, L. E.; Barry, C. E.; Caprioli, R. M. *J. Am. Soc. Mass Spectrom.* **2011**, *22*, 1409−1419.
(10) DeMarco, V. P.; Ordonez, A. A.; Klunk, M.; Prideaux, B.; Wang, H.; Zhuo, Z.; Tonge, P. J.; Dannals, R. F.; Holt, D. P.; Lee, C. K. K.; Weinstein, E. A.; Dartois, V.; Dooley, K. E.; Jain, S. K. *Antimicrob. Agents Chemother.* **2015**, *59*, 5768−5774.
(11) Irwin, S. M.; Prideaux, B.; Lyon, E. R.; Zimmerman, M. D.; Brooks, E. J.; Schrupp, C. A.; Chen, C.; Reichlen, M. J.; Asay, B. C.; Voskuil, M. I.; Nuermberger, E. L.; Andries, K.; Lyons, M. A.; Dartois, V.; Lenaerts, A. J. *ACS Infect. Dis.* **2016**, *2*, 251−267.
(12) Prideaux, B.; Via, L. E.; Zimmerman, M. D.; Eum, S.; Sarathy, J.; O'Brien, P.; Chen, C.; Kaya, F.; Weiner, D. M.; Chen, P.-Y.; Song, T.; Lee, M.; Shim, T. S.; Cho, J. S.; Kim, W.; Cho, S. N.; Olivier, K. N.; Barry, C. E.; Dartois, V. *Nat. Med.* **2015**, *21*, 1223.
(13) Strydom, N.; Gupta, S. V.; Fox, W. S.; Via, L. E.; Bang, H.; Lee, M.; Eum, S.; Shim, T.; Barry, C. E., 3rd; Zimmerman, M.; Dartois, V.; Savic, R. M. *PLoS Med.* **2019**, *16*, No. e1002773.
(14) Nuermberger, E. L.; Yoshimatsu, T.; Tyagi, S.; O'Brien, R. J.; Vernon, A. N.; Chaisson, R. E.; Bishai, W. R.; Grosset, J. H. *Am. J. Respir. Crit. Care Med.* **2004**, *169*, 421−426.
(15) Gillespie, S. H.; Crook, A. M.; McHugh, T. D.; Mendel, C. M.; Meredith, S. K.; Murray, S. R.; Pappas, F.; Phillips, P. P. J.; Nunn, A. J.; Consortium, R. E. *N. Engl. J. Med.* **2014**, *371*, 1577−1587.
(16) Jindani, A.; Harrison, T. S.; Nunn, A. J.; Phillips, P. P. J.; Churchyard, G. J.; Charalambous, S.; Hatherill, M.; Geldenhuys, H.; McIlleron, H. M.; Zvada, S. P.; Mungofa, S.; Shah, N. A.; Zizhou, S.; Magweta, L.; Shepherd, J.; Nyirenda, S.; van Dijk, J. H.; Clouting, H. E.; Coleman, D.; Bateson, A. L. E.; McHugh, T. D.; Butcher, P. D.; Mitchison, D. A.; Team, R. T. *N. Engl. J. Med.* **2014**, *371*, 1599−1608.
(17) Basaraba, R. J.; Hunter, R. L. *Microbiol. Spectrum* **2017**, *5*, 5.
(18) Heitmann, L.; Abad Dar, M.; Schreiber, T.; Erdmann, H.; Behrends, J.; McKenzie, A. N.; Brombacher, F.; Ehlers, S.; Hölscher, C. *J. Pathol.* **2014**, *234*, 338−350.
(19) Herrtwich, L.; Nanda, I.; Evangelou, K.; Nikolova, T.; Horn, V.; Sagar; Erny, D.; Stefanowski, J.; Rogell, L.; Klein, C.; Gharun, K.; Follo, M.; Seidl, M.; Kremer, B.; Münke, N.; Senges, J.; Fliegauf, M.; Aschman, T.; Pfeifer, D.; Sarrazin, S.; Sieweke, M. H.; Wagner, D.; Dierks, C.; Haaf, T.; Ness, T.; Zaiss, M. M.; Voll, R. E.; Deshmukh, S.

D.; Prinz, M.; Goldmann, T.; Hölscher, C.; Hauser, A. E.; Lopez-Contreras, A. J.; Grün, D.; Gorgoulis, V.; Diefenbach, A.; Henneke, P.; Triantafyllopoulou, A. *Cell* **2016**, *167*, 1264−1280.
(20) Lösslein, A. K.; Lohrmann, F.; Scheuermann, L.; Gharun, K.; Neuber, J.; Kolter, J.; Forde, A. J.; Kleimeyer, C.; Poh, Y. Y.; Mack, M.; Triantafyllopoulou, A.; Dunlap, M. D.; Khader, S. A.; Seidl, M.; Hölscher, A.; Hölscher, C.; Guan, X. L.; Dorhoi, A.; Henneke, P. *Nat. Commun.* **2021**, *12*, 2027.
(21) Holscher, C.; Heitmann, L.; Owusu-Dabo, E.; Horstmann, R. D.; Meyer, C. G.; Ehlers, S.; Thye, T. *Mediators Inflammation* **2016**, *2016*, 4245028.
(22) Treu, A.; Kokesch-Himmelreich, J.; Walter, K.; Hölscher, C.; Römpp, A. *J. Am. Soc. Mass Spectrom.* **2020**, *31*, 2277−2286.
(23) Walter, K.; Kokesch-Himmelreich, J.; Treu, A.; Waldow, F.; Hillemann, D.; Jakobs, N.; Lemm, A.-K.; Schwudke, D.; Römpp, A.; Hölscher, C. *Antimicrob. Agents Chemother.* **2021**.
(24) Lange, C.; Chesov, D.; Heyckendorf, J.; Leung, C. C.; Udwadia, Z.; Dheda, K. *Respirology* **2018**, *23*, 656−673.
(25) Blanc, L.; Sarathy, J. P.; Alvarez Cabrera, N.; O'Brien, P.; Dias-Freedman, I.; Mina, M.; Sacchettini, J.; Savic, R. M.; Gengenbacher, M.; Podell, B. K.; Prideaux, B.; Ioerger, T.; Dick, T.; Dartois, V. *J. Exp. Med.* **2018**, *215*, 1975−1986.
(26) Emson, C. L.; Bell, S. E.; Jones, A.; Wisden, W.; McKenzie, A. N. J. *J. Exp. Med.* **1998**, *188*, 399−404.
(27) Koestler, M.; Kirsch, D.; Hester, A.; Leisner, A.; Guenther, S.; Spengler, B. *Rapid Commun. Mass Spectrom.* **2008**, *22*, 3275−3285.
(28) Römpp, A.; Guenther, S.; Schober, Y.; Schulz, O.; Takats, Z.; Kummer, W.; Spengler, B. *Angew. Chem., Int. Ed.* **2010**, *49*, 3834−3838.
(29) Treu, A.; Römpp, A. *Rapid Commun. Mass Spectrom.* **2021**, *35*, 9110.
(30) Schramm, T.; Hester, Z.; Klinkert, I.; Both, J.-P.; Heeren, R. M. A.; Brunelle, A.; Laprévote, O.; Desbenoit, N.; Robbe, M.-F.; Stoeckli, M.; Spengler, B.; Römpp, A. *J. Proteomics* **2012**, *75*, 5106−5110.
(31) Race, A. M.; Styles, I. B.; Bunch, J. *J. Proteomics* **2012**, *75*, 5111−5112.
(32) Bokhart, M. T.; Nazari, M.; Garrard, K. P.; Muddiman, D. C. *J. Am. Soc. Mass Spectrom.* **2018**, *29*, 8−16.
(33) Race, A. M.; Palmer, A. D.; Dexter, A.; Steven, R. T.; Styles, I. B.; Bunch, J. *Anal. Chem.* **2016**, *88*, 9451−9458.
(34) Kokesch-Himmelreich, J.; Wittek, O.; Race, A. M.; Rakete, S.; Schlicht, C.; Busch, U.; Römpp, A. *Food Chemistry* **2022**, DOI: 10.1016/j.foodchem.2022.132529.
(35) Race, A. M.; Sutton, D.; Hamm, G.; Maglennon, G.; Morton, J. P.; Strittmatter, N.; Campbell, A.; Sansom, O. J.; Wang, Y.; Barry, S. T.; Takáts, Z.; Goodwin, R. J. A.; Bunch, J. *Anal. Chem.* **2021**, *93*, 3061−3071.
(36) Bancroft, J. D. G. M. The Hematoxylins and Eosin. *Theory and Practice of Histology Techniques*; Churchill Livingstone, 2008.
(37) Schwebach, J. R.; Jacobs, W. R., Jr.; Casadevall, A. *J. Clin. Microbiol.* **2001**, *39*, 769−771.
(38) Zimmerman, M.; Lestner, J.; Prideaux, B.; O'Brien, P.; Dias-Freedman, I.; Chen, C.; Dietzold, J.; Daudelin, I.; Kaya, F.; Blanc, L.; Chen, P. Y.; Park, S.; Salgame, P.; Sarathy, J.; Dartois, V. *Antimicrob. Agents Chemother.* **2017**, *61*, No. e00924.
(39) Bonnel, D.; Legouffe, R.; Eriksson, A. H.; Mortensen, R. W.; Pamelard, F.; Stauber, J.; Nielsen, K. T. *Anal. Bioanal. Chem.* **2018**, *410*, 2815−2828.
(40) Machálková, M.; Pavlatovská, B.; Michálek, J.; Pruška, A.; Štěpka, K.; Nečasová, T.; Radaszkiewicz, K. A.; Kozubek, M.; Šmarda, J.; Preisler, J.; Navrátilová, J. *Anal. Chem.* **2019**, *91*, 13475−13484.
(41) Irwin, S. M.; Gruppo, V.; Brooks, E.; Gilliland, J.; Scherman, M.; Reichlen, M. J.; Leistikow, R.; Kramnik, I.; Nuermberger, E. L.; Voskuil, M. I.; Lenaerts, A. J. *Antimicrob. Agents Chemother.* **2014**, *58*, 4026−4034.
(42) Aplin, R. T.; McDougall, A. C. *Experientia* **1975**, *31*, 468−469.
(43) Baik, J.; Rosania, G. R. *PLoS One* **2012**, *7*, No. e47494.
(44) Sarathy, J. P.; Zuccotto, F.; Hsinpin, H.; Sandberg, L.; Via, L. E.; Marriner, G. A.; Masquelin, T.; Wyatt, P.; Ray, P.; Dartois, V. *ACS Infect. Dis.* **2016**, *2*, 552−563.

https://doi.org/10.1021/acs.analchem.1c03462
Anal. Chem. 2022, 94, 5483−5492

Supporting Information

Do anti-TB drugs reach their target? – High resolution MALDI MS imaging provides information on drug penetration into necrotic granulomas

Julia Kokesch-Himmelreich[a,+] ‡, Axel Treu[a,+] ‡, Alan M. Race[a], Kerstin Walter[b,+], Christoph Hölscher[b,+] and Andreas Römpp[a,+,*]

a Bioanalytical Sciences and Food Analysis, University of Bayreuth, Bayreuth, Germany

b Infection Immunology, Leibniz Lung Center, Research Center Borstel, Borstel, Germany

+ German Center for Infection Research (DZIF)

‡ Authors contributed equally

* Correspondence to this author:

Andreas Römpp, Bioanalytical Sciences and Food Analysis, University of Bayreuth, 95447 Bayreuth, Germany,
Andreas.roempp@uni-bayreuth.de

MALDI MS imaging workflow

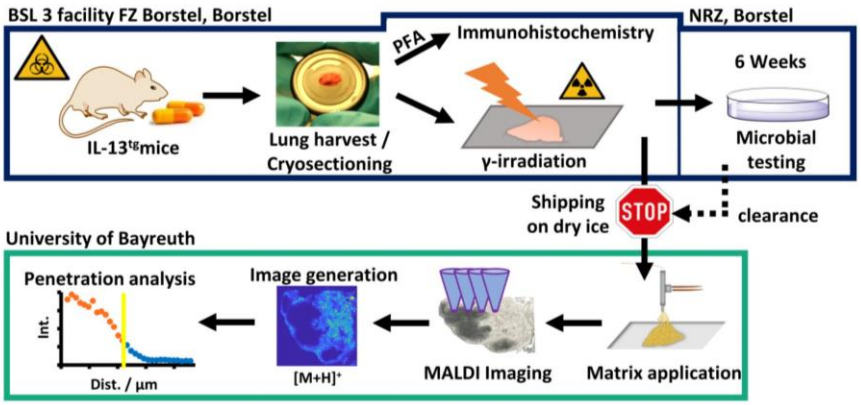

Figure S1. MS Imaging workflow for lung tissue of Mtb infected mice.

Animal studies, lung harvesting and cryosectioning had to be performed in a BSL 3 facility (Research Center Borstel). Inactivation of bacteria is commonly done by incubation in PFA for 1 h. These sections were used for histological staining and immunohistochemistry. For MS imaging measurements, inactivation of bacteria was achieved by γ-irradiation. Sections of each batch were tested for Mtb (MGIT) by the National Reference Center (NRZ) in Borstel. After clearance, the inactivated sections were shipped to our lab in Bayreuth on dry ice and stored at -80 °C until measurement. Sections were dehydrated in a desiccator for 15 min prior to matrix application. MALDI matrices were applied using a pneumatic sprayer. All data were acquired using the AP-SMALDI10 high-resolution MALDI MS imaging ion source (TransMIT GmbH) which was coupled to a Q Exactive HF orbital trapping mass spectrometer (Thermo Fisher). MS Imaging data was converted to the open file format imzML[1] using the jimzml converter (Version 2.0.4)[2]. MSiReader 1.0[3] was used to generate MS images and *m/z* windows of 2.0 ppm were chosen to generate all shown MS images. Detailed penetration analysis of the drugs was performed using our newly developed semiautomatic penetration tool based on MATLAB (3.2.64.12).

Animal Samples

IL-13^{tg} mice[4] on a BALB/c genetic background were bred under specific-pathogen-free conditions at the animal facility of the Christian-Albrechts-University Kiel (Kiel, Germany). BALB/c mice were purchased from Charles River (Sulzfeld, Germany). Mtb infection of IL-13^{tg} mice were conducted in the biosafety level 3 (BSL 3) facility at the Research Center Borstel (Borstel, Germany). Mice were infected with approx. 100 CFU of the Mtb strain H37Rv via the aerosol route using a Glas-Col Model 099C A4224 inhalation system (Glas-Col LLC, Terre Haute, USA). As soon as IL-13^{tg} mice formed centrally necrotizing granulomas after 10 weeks of infection antibiotic treatment was started. We have described more details on aerosol infection and drug administration in Walter *et al*[5].

MS Acquisition

Table S1. Compounds used as lock masses *for internal calibration.*

Compound (polarity)	**Exact mass**	**Composition**	**Sum formula**
DHB (pos)	137.02332	$M+H-H_2O^+$	$C_7H_5O_3^+$
DHB (pos)	716.12461	$5M+NH_4-4H_2O^+$	$C_{35}H_{26}NO_{16}^+$
PS (38:4) (neg)	810.52905	$M-H^-$	$C_{44}H_{77}O_{10}NP^-$

***Table S2. Measurement parameters for all measurements shown in this paper and the Supporting Information**. The samples labeled with an asterisk (first column) are sections of non- infected BALB/C mice. All other samples are sections of Mtb infected IL-13^{tg} mice. The second column gives the targeted analytes for the measurement and the third column 'Figure' gives the reference to the corresponding ion images in the main paper and the Supporting Information. The acquisition mode column describes if full scan (FS) or single ion monitoring (SIM) mode was used. For the alternating measurements two acquisition modes and two mass ranges were applied, one for each scan event. These measurements can be recognized by their step size x=y/2.*

Sample	Analytes	Figure	Matrix	Polarity	Acquisition mode	mass range/m/z	step size/µm	raster size/pixel
A*	CFZ/PZA	1C/D	DHB	positive	Full scan	120 - 500	35x35	500x150
B*	RIF Lipids	1F 1G	DHAP	negative positive	SIM Full scan	805-825 450-900	45x45	410x150
1	CFZ/Lipids PZA/POA	2C/B 2D/S9B	DHB	positive	Full scan SIM	450-900 120-140	15x30	108x130
2	RIF	2E	DHAP	negative	SIM	805-825	30x30	111x128
3	CFZ/Lipids PZA/POA	2H/G 2I/S9D	DHB	positive	Full scan SIM	450-900 120-140	15x30	360x180
4	RIF	2J	DHAP	negative	Full scan	800-900	30x30	177x167
5	CFZ/Lipids	5 C/D	pNA	positive	Full scan	450-900	5x5	238x270
6	CFZ/Lipids	S14C/D	DHB	positive	Full scan	450-1000	10x10	200x200
7	CFZ/Lipids PZA	S8C/B S8D	DHB	positive	Full scan SIM	450-900 120-140	30x30 30x30	304x172 304x172
8	Lipids/RIF	S8F/G	DHAP	negative	Full scan	800-900	30x30	307x174

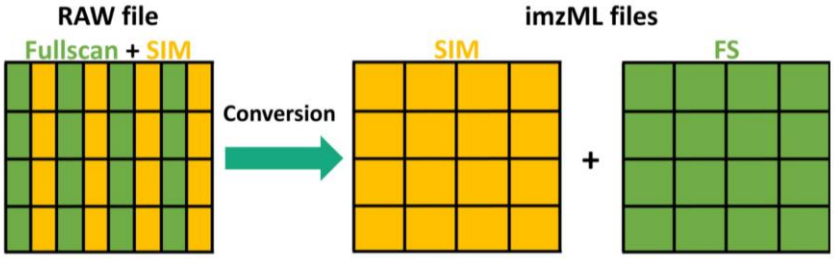

Figure S2. Schematic depicting the conversion of RAW files containing alternating SIM and fullscan acquisistion windows.

Ion images generated directly from measurements with alternating SIM and FS acquisition will contain empty pixels. This can be prevented by converting rawdata into individual imzML files for each modality. To enable this operation, the number of pixels in *x* direction must be a common multiple of the number of employed acquisition modes (*n*) to ensure that pixel of the same modality are arranged in vertical lines and not in a chessboard pattern. Tools for converting rawdata containing multiple mass ranges directly into separate imzML files are available on www.imzml.org. To avoid rectangular shaped pixel in measurements with alternating SIM and FS acquisition, the step size in *x* direction is defined as *y/n* with *y* as the step size in *y* direction and *n* the number of employed acquisition modes. It is important to note that the resulting MS images still have square pixels and the pixel size is equal to the step size in y direction. A measurement of two alternating events with a step size of 15 µm x 30 µm for example will lead to a pixel size of 30 µm in the MS images.

Influence of irradiation on analyte distribution

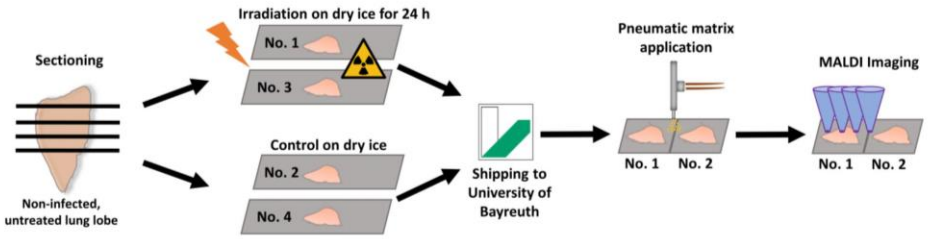

Figure S3. Schematic showing the irradiation procedure for measurements on directly neighboring irradiated and non-irradiated sections.

Sections were cut from whole lung lobes of uninfected control (BALB/c) mice which received the drugs CFZ, PZA and RIF. Only one section was deposited onto each slide. Every second slide received a dose of approx. 6 kGy on dry ice with the same parameters as the IL-13^{tg} sections, shown in the workflow. The adjacent sections were stored for the same time period on dry ice but not irradiated. This procedure resulted in pairs of directly neighboring irradiated and non-irradiated sections. Sections were shipped to our laboratory on dry ice. The section pairs were mounted on the same sample holder. The sample preparation and MALDI MS imaging measurement were performed on both sections in parallel to achieve a direct comparison of the drug distribution in non-irradiated and irradiated tissue.

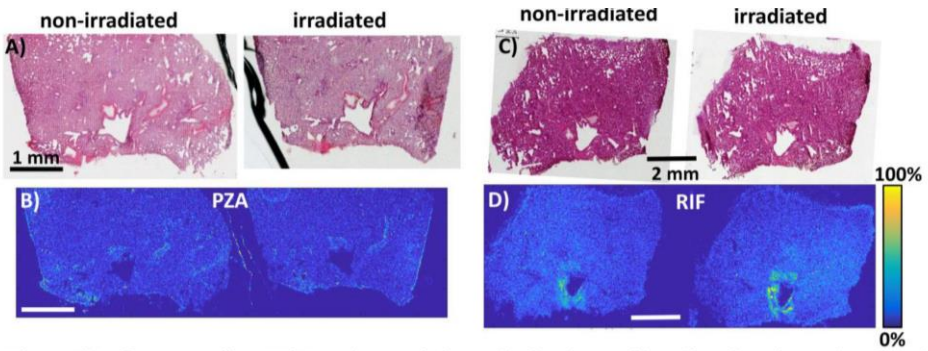

Figure S4. Corresponding H&E stains and drug distributions of irradiated and non-irradiated sections in Figure 1*. A) H&E stainings of sections in Figure 1B and C. B) Distribution of PZA ($[M+2H]^+$, m/z 125.05831), ion image is normalized to the TIC. The measurement was performed in positive ion mode using DHB matrix at 35 µm pixel size. C) H&E staining of sections in Figure 1D. D) Distribution of RIF ($[M-H]^-$, m/z 821.39784). The measurement was conducted in the negative ion mode with DHAP matrix and a step size of 45 µm.*

The H&E stained sections show again the intact morphology of the section after the irradiation process (right panels). The distribution of the readily water soluble PZA (150 mg/mL[6] in Figure S4B was identical in both sections. PZA did not leak out of the sections or into the large airway (Figure 1B, violet arrows). It was contained in the section and was only detected on tissue or blood vessels (Figure 1B, red arrows). RIF was detected in negative ion with a distribution similar to CFZ (Figure. 1C). No prominent difference was observed between the non-irradiated and irradiated lung sections.

Drug detection in IL-13tg mice lung

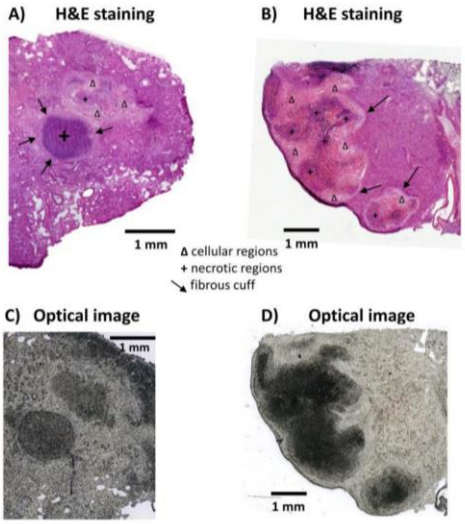

Figure S5. Neighboring sections of the sections in Figure 2A, F*. Each section contains two granulomas. A, B) H&E staining, darker violet regions inside the granuloma area indicate a necrotic state of the tissue (indicated with '+'). White regions (Δ) are more cellular regions of the granuloma. The granuloma are encapsulated in a fibrous cuff (indicated by black arrows) and surrounded by fibroblasts ('*'). The collagen ring is most prominent in the Figure S5A, as a fine red line. C, D) Optical images of sections before the RIF measurements in 2 E and J.*

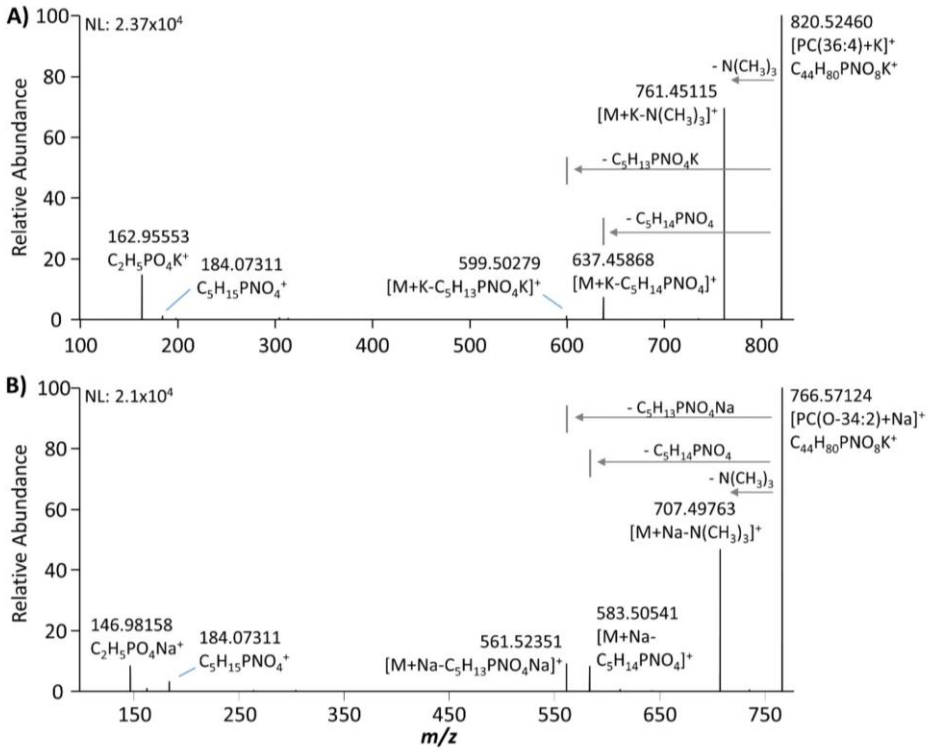

Figure S6. MS/MS of the lipids used for edge generation during penetration analysis in this work. *MS/MS parameters: Precursor isolation width ± 0.2 m/z, HCD setting 10 – 30, scan width (A) m/z 100 – 825 and (B) m/z 100 – 770. Spectra were average across 60 scans to account for signal fluctuations.*

Lipids were pre-identified based on accurate mass data and data base search (lipidmaps.org). MS/MS data was used to confirm the pre-identification. A) MS/MS of the lipid 820.525 pre-identified as PC(36:4) $[M+K]^+$. The fragment spectrum shows the typical fragments and neutral losses of a potassiated phosphatidylcholine in the positive ion mode. B) MS/MS of the lipid 766.572 pre-identified as PC(O-34:2), $[M+Na]^+$ or PC(P-34:1), $[M+Na]^+$. The MS/MS spectrum shows the characteristic fragments and neutral losses of a sodiated phosphatidylcholine in the positive ion mode. Additional information from full MS spectra and MS/MS of similar lipid precursors lead to the tentative assignment of PC(O-34:2), $[M+Na]^+$.

.

Mass spectra of drug compounds

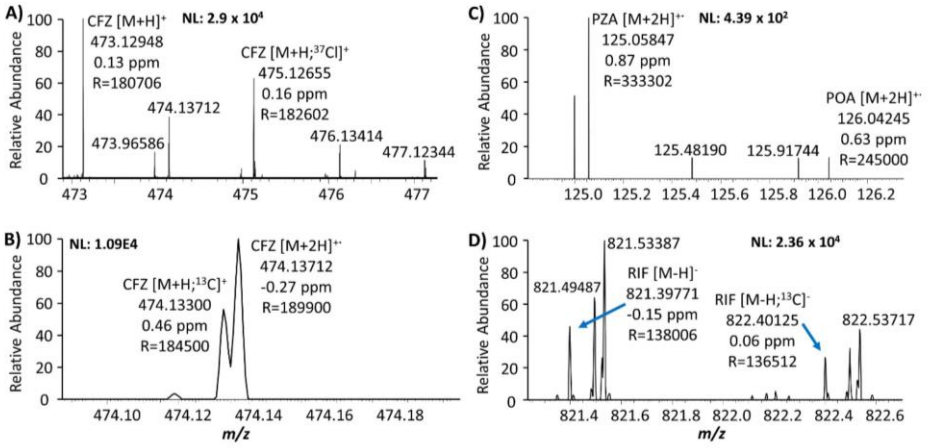

***Figure S7. Single pixel on tissue mass spectra of drug compounds**. All drug signals are shown with their corresponding mass resolution (FWHM) and mass accuracy in ppm. A) Isotopic pattern of CFZ in mass spectrum of the measurement in Figure 2 C in positive ion mode. B) Enlargement of the mass spectrum in Figure S7A. C) Single pixel mass spectrum of the SIM measurement in Figure 2D. PZA and POA are both detected as double protonated odd electron molecular ions ($[M+2H]^{+\cdot}$). D) Single pixel mass spectrum of the SIM measurement in Figure 2 E in negative ion mode showing the isotopic pattern of RIF ($[M-H]^-$).*

In addition to the single protonated molecular ion $[M+H]^+$ *m/z* 473.12948, the compound CFZ also forms a double protonated odd electron molecular ion $[M+2H]^{+\cdot}$ *m/z* 474.13712, similar to PZA. To distinguish the overlapping isotopic patterns of the two molecular ion species, high mass resolution is needed. In this case a mass resolution higher than 180k (FWHM) could be achieved for the double protonated odd electron molecular ion $[M+2H]^{+\cdot}$ *m/z* 474.13712.

***Table S3. Calculated RMSE values (ppm) for all investigated compounds**. The figure of the corresponding MS image is given in the first column. The theoretical m/z ratio of the analyte is shown in the third column. The number of spectra in which the analyte was detected is given in the fourth column. The root mean square error (RMSE) of the δm/z values in ppm of all spectra containing the targeted ion was calculated (last column).*

Figure	Analyte/Ion	*m/z*	Number of spectra	RMSE value/ppm
1C	$[CFZ+H]^+$	473.12942	48168	0.82
1D	$[PZA+2H]^{++}$	125.05831	47762	0.36
1F	$[RIF-H]^-$	821.39784	36170	0.66
1G	$[PC(32:2)+H]^+$	730.53813	38983	0.53
1G	$[PC(36:4)+K]^+$	820.52531	64094	0.35
2B	$[PC(O-34:2)+Na]^+$	766.57211	11306	0.90
2B	$[PC(36:4)+K]^+$	820.52531	13657	0.20
2C	$[CFZ+H]^+$	473.12942	13933	0.29
2D	$[PZA+2H]^{++}$	125.05831	10633	0.87
2E	$[RIF-H]^-$	821.39784	7551	0.78
2G	$[PC(O-34:2)+Na]^+$	766.57211	19242	0.65
2G	$[PC(36:4)+K]^+$	820.52531	25067	0.38
2H	$[CFZ+H]^+$	473.12942	25890	0.81
2I	$[PZA+2H]^{++}$	125.05831	11984	0.36
2J	$[RIF-H]^-$	821.39784	12913	0.68
5C	$[CFZ+H]^+$	473.12942	65096	0.3
5D	$[PC(O-36:3)+K]^+$	808.56170	28281	0.45
5D	$[PC(36:4)+K]^+$	820.52531	64083	0.34
5D	$[PC(O-36:4)+K]^+$	806.54604	52070	0.54
S9B	$[POA+2H]^{++}$	126.04237	821	0.95
S9D	$[POA+2H]^{++}$	126.04237	884	0.98
S14D	$[PC(O-36:3)+K]^+$	808.56170	32740	0.5
S14D	$[PC(36:4)+K]^+$	820.52531	39998	0.2
S14D	$[PC(O-36:4)+K]^+$	806.54604	39913	0.46
S14C	$[CFZ+H]^+$	473.12942	39997	0.14
S8B	$[PC(36:4)+K]^+$	820.52531	37089	0.26
S8B	$[PC(O-34:2)+Na]^+$	766.57211	11253	0.75
S8F	$[PS(39:6)-H]^-$	820.51340	32701	0.51

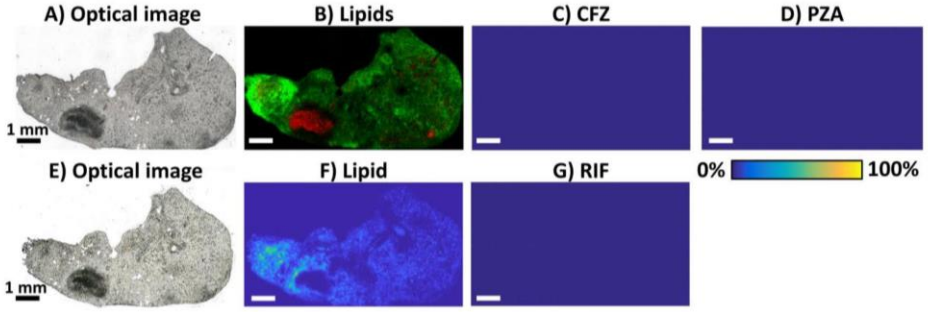

Figure S8. Negative control measurements conducted on Mtb-infected IL-13^{tg} mice which did not receive PZA, CFZ or RIF. *Measurements were conducted with the same conditions as described in Figure 2. A) Optical image. B) Overlay of PC(O-34:2), (red, $[M+Na]^+$, m/z 766.5721) and PC(36:4) (green, $[M+K]^+$, m/z 820.5253), lipid images are TIC normalized, RMSE < 1 ppm (see Table S3). C) Ion image of the exact mass of Clofazimine $[M+H]^+$ m/z 473.12942 ±2 ppm. D) Ion image of the exact mass of Pyrazinamide $[M+2H]^{++}$ m/z 125.05836 ±2 ppm. E) Optical image. F) Distribution of PS(39:6) ($[M-H]^-$, m/z 820.52177) detected in negative ion mode, RMSE<1 ppm (see Table S2). G) Ion image of the exact mass of Rifampicin $[M-H]^-$ m/z 821.39784 ±2 ppm.*

Measurements were conducted with the same conditions as the measurements in Figure 2, see also Table S2. In both measurements, lipid signals could be detected with high mass accuracy and their distribution match the optical images. The ion images of the exact masses of the drug compounds CFZ, PZA and RIF do not show significant signal intensities, as expected. This confirms the identity of the drug signals in Figure 2 and S6.

Pyrazinoic acid (POA) in TB infected IL-13^{tg} lung tissue

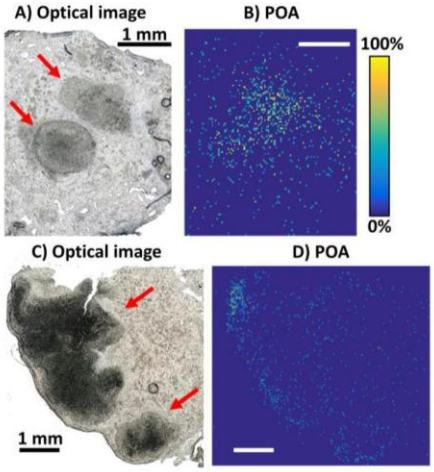

***Figure S9. Distribution of pyrazinoic acid (POA) in the measurements shown in Figure 2**. A and C) Optical images of tissue sections, which are also shown in Figure 2 A and E. B) Distribution of POA ($[M+2H]^{+\cdot}$, m/z 126.04237.) in the measurement shown in Figure 2 A-D. D) Distribution of POA) in the measurement shown in Figure 2 F-I.*

POA is detected alongside PZA in the SIM acquisition window. For image generation a pixel size of 30 µm and a bin width of 2.0 ppm was used. POA is the main active metabolite of PZA and is generated by the bacteria (Mtb) inside the granulomas. POA can also be formed during the MS imaging experiment by in source transformation.

Penetration Analysis

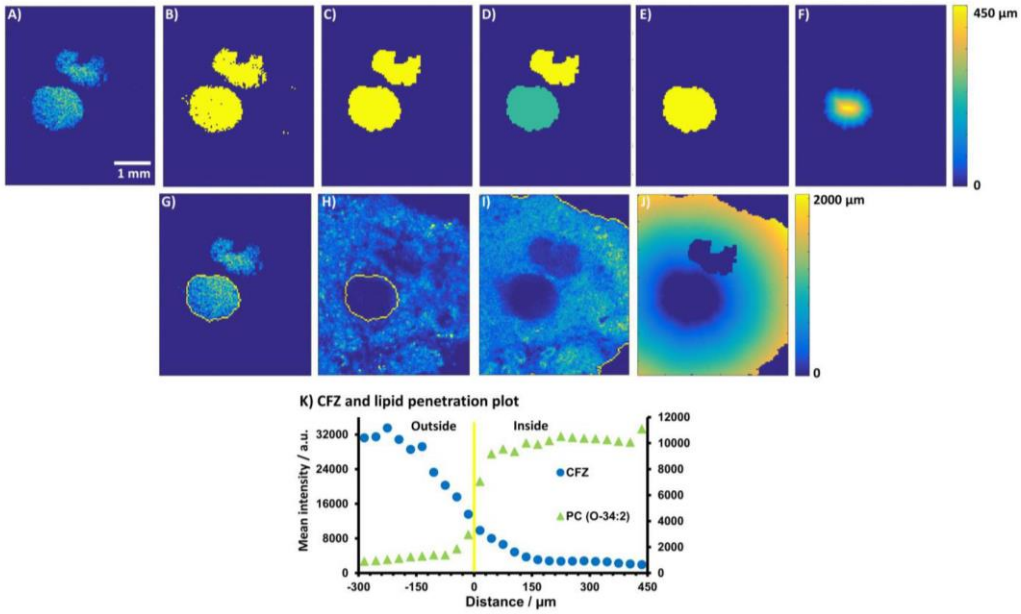

Figure S10. Detailed penetration analysis workflow. All shown images are generated by the semi-automatic tool. *A) Selected ion image of a lipid compound present in granulomas. B) Binarized image of A. C) Mask image generated by filtering and filling remaining wholes of B. D) Separate masks for each granuloma (yellow and green). E) Mask image of selected granuloma. F) Distance map for inside of granuloma. G) Display of edge of granuloma in lipid ion image (A). H) Display of edge of granuloma in CFZ ion image. I) Edge of tissue section displayed in selected ion image of lipid present outside of granulomas. J) Distance map of pixels outside of granuloma. See text for more details.*

The newly developed penetration analysis tool was written in MATLAB (R2016b), and is extending the work by Kokesch-Himmelreich *et al.*[7] from one dimension to two dimensions with arbitrary shape. The workflow consists of the following steps:

i) A user selected ion image (ideally where signal is only present within the granulomas) was generated (Figure S10A), binarized (Figure S10B), filtered and remaining holes filled to generate a mask image (Figure S10C). Sets of connected pixels (each granuloma) from the mask image were extracted and sorted by the number of pixels they consist of (Figure S10D), creating a set of granuloma mask images. For each granuloma mask image (Figure S10E), a corresponding distance image is generated (Figure S10F), where each pixel in the mask is replaced by its

distance to the nearest pixel outside of the mask. This allows the calculation of the 'edge' of the granuloma. The calculated edge is shown with the lipid image in Figure S10G and with the analyte (CFZ) ion image in Figure S10H.

ii) A user selected ion image (ideally where signal is present within the entire tissue) was generated (Figure S10I), filtered and remaining holes filled to generate a mask image. This formed the 'on tissue' mask image. For each granuloma mask image, a second distance image was created (Figure S10J), calculating the distance for every pixel in the 'on tissue' mask, but not in the granuloma mask to the nearest pixel within the granuloma.

Using the two distance maps (one to the inside of the granuloma, and the other away from the granuloma), or by expanding or contracting the granuloma edge by a single pixel, it is possible to extract the intensities of analytes at each distance to calculate a mean intensity for a given distance from the granuloma edge. The pixels which are incorporated into the mean calculation at a distance of 150 μm outside and inside of the granuloma edge are shown as an example in Figure S11. Repeating this for all possible distances, one can form a penetration curve from the edge of the tissue, through the edge of the granuloma to the centre of the granuloma (Figure S10K). Here, the penetration of CFZ and the lipid signal is shown. The yellow line corresponds to the calculated edge.

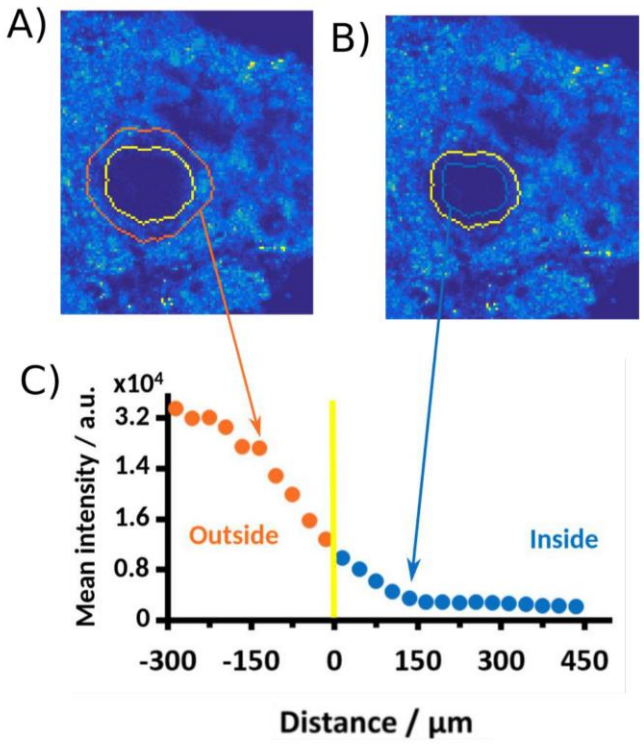

Figure S11. Pixels used in the calculation of average intensity as a function of distance: A) ion image showing edge of granuloma (yellow) and pixels which are 150 µm outside of the granuloma (orange). B) ion image showing edge of granuloma (yellow) and pixels which are 150 µm inside the granuloma. C) intensity as a function of distance to the edge of granuloma plot (corresponding to Figure 3Biv). Arrows indicate the corresponding data points which correspond to the orange and blue pixels in A) and B, respectively.

Penetration behavior of PZA und RIF

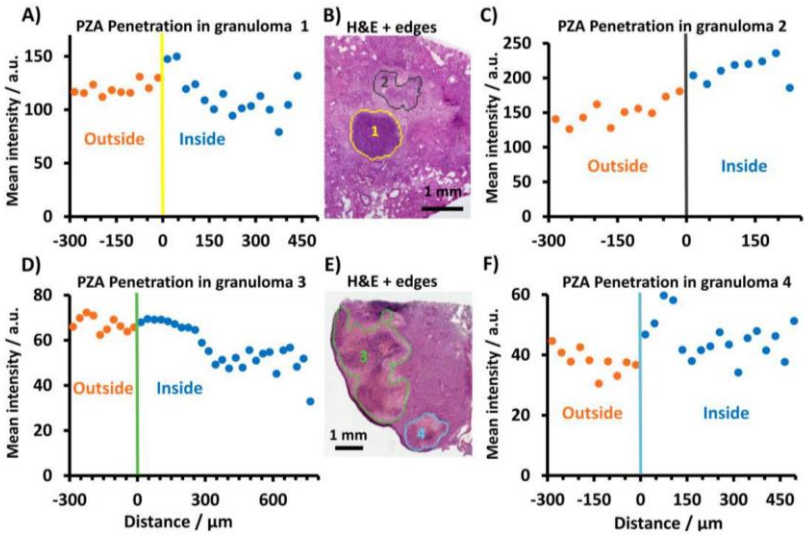

Figure S12. Comparison of penetration curves of PZA in different granulomas: *B, E) H&E staining of sections neighboring those in Figure 2 with calculated edges from the penetration tool. A, C) Penetration curves of PZA for granulomas 1 and 2 in Figure S11B. D, F) Penetration curves of PZA for granulomas 3 and 4 in Figure S11E.*

In all penetration plots the mean intensities of PZA for a certain distance is shown against the distance in µm. The colored vertical lines represent the calculated 'colored edges' of the granulomas in Figure S11B and E. Orange data points correspond to mean intensities of the drug outside the calculated edge and blue data points towards the inside. PZA shows in all four penetration plots similar mean intensities for the granuloma region areas and the outside regions meaning it is homogenously distributed over the whole tissue sections including the necrotic core. In Figure S11C and F the intensities of PZA seem even a little bit higher in the granuloma area than in the surrounding tissue.

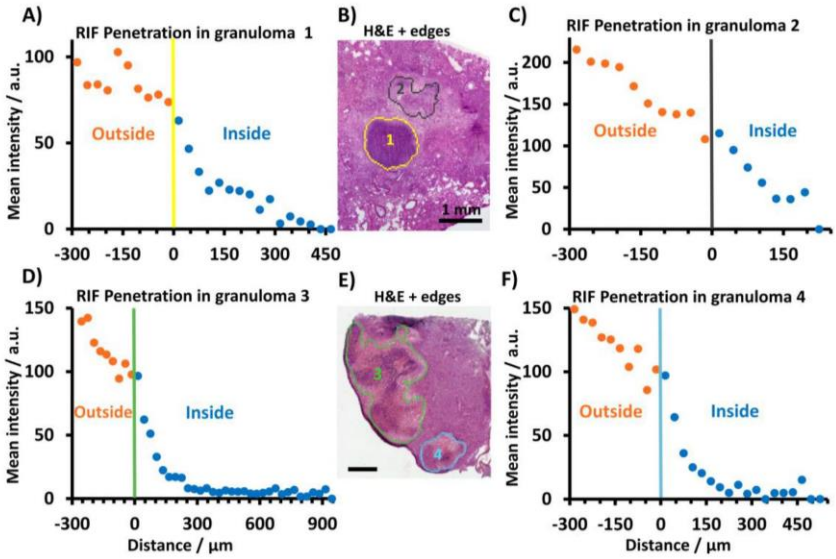

Figure S13. Comparison of penetration curves of RIF in different granulomas. *B, E) H&E staining of sections neighboring those in Figure 2 with calculated edges from the penetration tool. A, C) Penetration curves of RIF for granuloma 1 and 2 in Figure S12 B. D, F) Penetration curves of RIF for granuloma 3 and 4 in Figure S12 E.*

In all penetration plots the mean intensities of RIF for a certain distance is shown against the distance in µm. The colored vertical lines represent the calculated 'colored edges' of the granulomas in Figure S12B and E. Orange data points correspond to mean intensities of the drug outside the calculated edge and blue data points towards the inside. In all four plots, the intensities of RIF are higher in the outside regions than in the granuloma areas. The RIF intensities decrease before and after reaching the edge, but in comparison to CFZ the RIF penetration plots do not show any maximum around the edge.

High resolution MS imaging

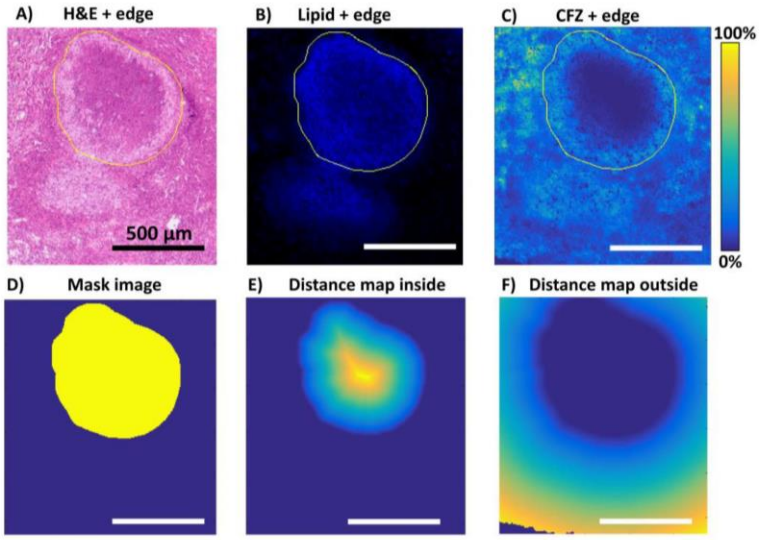

Figure S14. Penetration analysis of CFZ in 5 µm step size measurement of Figure 5. *A) H&E staining and manually drawn ROI in yellow, B) Lipid PC(O-36:4) ($[M+K]^+$, m/z 806.54604) with manually drawn ROI in yellow. C) Distribution of CFZ ($[M+H]^+$, m/z 473.12942) with yellow ROI. D) Mask used for distance calculation. E) Distance map towards the center of the granuloma. F) Distance map from the edge towards the outside of the tissue.*

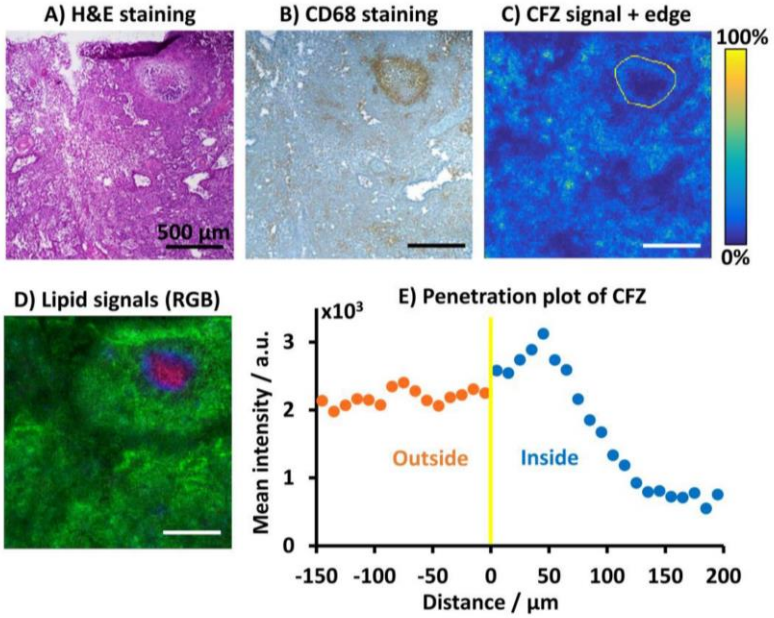

Figure S15. Reproduction of Figure 5: High resolution MS imaging of distinct structured granuloma: *A) H&E stain. B) CD68 antibody stain, visualizes macrophages. The small granuloma in upper half of the H&E image consists of a necrotic core, which is surrounded by a cellular ring, which consists mainly of macrophages. C) Distribution of CFZ ($[M+H]^+$, m/z 473.12942) with manually drawn ROI in yellow. CFZ shows higher intensities in the surrounding tissue and in the macrophage rich areas than in the necrotic regions. D) RGB overlay of three lipids, PC(O-36:3) (red, $[M+K]^+$, m/z 808.56170), PC(36:4) (green, $[M+K]^+$, m/z 820.52531,) and PC(O-36:4) (blue, $[M+K]^+$ m/z 806.54604). Lipid images are normalized to the TIC. MS imaging measurement was acquired in positive ion mode using DHB matrix, step size and pixel size was 10 µm. RMSE < 1.0 ppm (Table S3). All three lipids are present in the same tissue type as in Figure 5 C. E) Penetration plot of CFZ for the ion image in Figure S14 D.*

Similar trend of the mean CFZ intensities per distance can be observed as in Figure 5. The mean intensities are decreasing towards the center of the granuloma, but a maximum can be seen around the drawn edge corresponding to the ring of macrophages surrounding the necrotic core. This confirms the former observation that CFZ can accumulate in the macrophages.

References

(1) Schramm, T.; Hester, A.; Klinkert, I.; Both, J. P.; Heeren, R. M.; Brunelle, A.; Laprevote, O.; Desbenoit, N.; Robbe, M. F.; Stoeckli, M.; Spengler, B.; Römpp, A. *J Proteomics* **2012**, *75*, 5106-5110.
(2) Race, A. M.; Styles, I. B.; Bunch, J. *Journal of Proteomics* **2012**, *75*, 5111-5112.
(3) Bokhart, M. T.; Nazari, M.; Garrard, K. P.; Muddiman, D. C. *Journal of The American Society for Mass Spectrometry* **2018**, *29*, 8-16.
(4) Emson, C. L.; Bell, S. E.; Jones, A.; Wisden, W.; McKenzie, A. N. *The Journal of experimental medicine* **1998**, *188*, 399-404.
(5) Walter, K.; Kokesch-Himmelreich, J.; Treu, A.; Waldow, F.; Hillemann, D.; Jakobs, N.; Lemm, A.-K.; Schwudke, D.; Römpp, A.; Hölscher, C. *Antimicrob Agents Chemother* **2021**, 10.1128/AAC.01588-21.
(6) Wishart, D. S.; Feunang, Y. D.; Guo, A. C.; Lo, E. J.; Marcu, A.; Grant, J. R.; Sajed, T.; Johnson, D.; Li, C.; Sayeeda, Z.; Assempour, N.; Iynkkaran, I.; Liu, Y.; Maciejewski, A.; Gale, N.; Wilson, A.; Chin, L.; Cummings, R.; Le, D.; Pon, A.; Knox, C.; Wilson, M. *Nucleic Acids Research* **2018**, *46*, D1074-D1082.
(7) Kokesch-Himmelreich, J.; Wittek, O.; Race, A. M.; Rakete, S.; Schlicht, C.; Busch, U.; Römpp, A. *Food Chemistry* **2022**, https://doi.org/10.1016/j.foodchem.2022.132529

5.4 Manuscript for a fourth publication - The efficacy of the novel antitubercular agent BTZ-043 in preclinical Tuberculosis mouse models

At the time this thesis was submitted, the manuscript for a fourth publication was in preparation for submission.

The efficacy of the novel antitubercular agent BTZ-043 in preclinical Tuberculosis mouse models

Axel Treu[a,e,*], Kerstin Walter[b,e,*], Julia Kokesch-Himmelreich[a,e], Franziska Waldow[c,e], Julia Dreisbach[d,e], Dominik Schwudke[c,e], Michael Hölscher[d,e], Christoph Hölscher[b,e], Andreas Römpp[a,e].

Affiliations

[a] Bioanalytical Sciences and Food Analysis, University of Bayreuth, Bayreuth, Germany.
[b] Infection Immunology, Leibniz Lung Center, Research Center Borstel, Borstel, Germany.
[c] Bioanalytical Chemistry, Leibniz Lung Center, Research Center Borstel, Borstel, Germany.
[d] Division of Infectious Diseases and Tropical Medicine, Ludwig Maximilians Universität München, München, Germany.
[e] German Center for Infection Research (DZIF), Braunschweig, Germany
* Authors contributed equally.

Abstract

Tuberculosis remains as one of the deadliest infectious diseases and poses a serious threat to public health worldwide. The increasing prevalence of drug resistant mycobacterial strains makes future efforts towards the eradication of TB dependent on the development of novel drug compounds. BTZ-043 is a chemotherapeutic agent inhibiting cell wall formation of *Mycobacterium tuberculosis* (Mtb) by selectively blocking the DprE1 enzyme. Herein we report upon the efficacy of BTZ-043 in the mouse models BALB/c and IL-13^{tg}. Dose ranging on BALB/c mice showed that BTZ-043 monotherapy at a dose of 250 mg/kg/day is more effective than isoniazid in BALB/c mice and comparable to a combination of pyrazinamide, clofazimine and rifampicin in IL-13^{tg} mice which mimic human TB pathology. CFU reduction and PK curves indicate that the AUC is the driver of the BTZ-043 efficacy. Ziehl-Neelsen stainings of IL-13^{tg} mice treated with BTZ-043 show that the drug causes a loss of acid fastness in Mtb, which is in accordance with its mechanism of action. For MALDI imaging, lung sections of IL-13^{tg} mice were inactivated via γ irradiation. LC-MS/MS showed that the irradiation procedure has no influence on the concentration of BTZ-043 and that from 0.5 to 8 h post-dose the tissue concentration of BTZ-043 drops from 6.71 to 0.27 ng/mg, which is still significantly above the MIC of Mtb reported in the literature. High resolution MALDI MSI was used to investigate the penetration of BTZ-043 into granuloma of IL-13^{tg} mice, constituting the first time this compound was investigated with MSI. Measurements with 10 µm pixel size in correlation with histological data showed an accumulation of BTZ-043 in the cellular regions of TB granuloma. Imaging measurements 4 and 8 h post-dose showed a penetration of BTZ-043 into the caseum of necrotic granuloma of IL-13^{tg} mice.

Introduction

Tuberculosis (TB) is a common infectious disease of the pulmonary system with *Mycobacterium tuberculosis* (Mtb) as its main causative agent. TB is a global threat to public health responsible for more than a million recorded deaths and around ten million new active cases every year.[1]
Treatment of TB relies on long term antibiotic combination therapies with drugs such as pyrazinamide, isoniazid, rifampicin or ethambutol which are the current WHO recommend first line drugs for treatment of new active cases[2]. While some of these drugs have been in use for over 50 years, the emergence of drug resistant Mtb strains[3] lead to a demand for novel anti-TB drugs.
Pre-clinical screening and testing of drug candidates is the crucial element to keep the development pipeline for novel anti-TB drugs filled. Especially for TB, the predictive power of pre-clinical tests depends on the ability of pre-clinical models to reflect the specific human TB pathology[4]. Regular inbred mice (BALB/c or SWISS) are the most commonly used models for pre-clinical testing[5-6] which, at the same time, fail to replicate human TB pathology. In particular, pulmonary granuloma of these mice lack the non-vascularized central caseum observed in humans, which has a significant impact on drug penetration.[4]

BTZ-043 is a novel compound of the benzothiazinone class. Benzothiazinones are sulfur containing nitroaromatic spiro compounds which were found capable of killing Mtb *in vivo*, *ex vivo* and in animal models.[7] BTZ-043 interferes with the cell wall formation by bonding to the active pocket Cys387 of decaprenylphosphoryl-β-D-ribofuranose-2'-epimerase thus blocking the formation of decaprenylphosphoryl arabinose, which is an arabinose donor for the synthesis of arabinogalactan and lipoarabinomannan.[8] The absence of these polysaccharides in the cell wall subsequently promotes cell wall lysis and cell death.

Here we investigated the efficacy of BTZ-043 in pre-clinical TB mouse models. BALB/c mice were used for dose ranging / dose escalation and pharmacokinetic (PK) studies to determine the driver of the BTZ-043 efficacy. Colony forming unit (CFU) reduction and histological investigations were conducted with interleukin 13 overexpressing (IL-13^{tg}) mice to determine the efficacy of BTZ-043 in a mouse model which strongly resembles human TB pathology.[9] In IL-13^{tg} mice, TB infection leads to the formation of centrally necrotic granuloma, very similar to those found in humans. High resolution MALDI MSI was performed on γ ray inactivated lung sections to investigate if BTZ-043 is able to penetrate into necrotic granuloma of IL-13^{tg} mice in conjunction with LC-MS/MS to determine the tissue concentration of BTZ-043 and to rule out an influence of the γ irradiation on the drug concentration.

Results and discussion

Dose ranging

To determine the efficacy of BTZ-043 and a suitable dose for follow up animal trials, dose ranging was conducted on BALB/c mice, Figure 1. Treatment with several BTZ-043 doses was started 22 days post infection and CFU reduction investigated 47, 61 and 75 days post infection. The results were evaluated against an untreated control group which received only the drug vehicle and a positive control group which received isoniazid (INH), a current first line anti-TB drug, at 25 mg/kg/day. 47 days post infection, all administered BTZ-043 doses show a lower CFU value than the vehicle group and the before treatment value. The 500 and 1000 mg/kg/day BTZ-043 doses have a higher efficacy than the INH

positive control. The efficacy of the 250 and 100 mg/kg/day BTZ-043 dose is similar to INH. The 50 mg/kg/day BTZ-043 doses exhibit a lower efficacy than INH. 61 days post infection, the 250, 500 and 1000 mg/kg/day doses exhibit a higher efficacy than INH while the 100 mg/kg/day dose has similar and the 50 mg/kg/day dose has a lower efficacy than INH. This trend is continued 75 days post infection which shows that the efficacy of the 250, 500 and 1000 mg/kg/day dose have a substantially higher efficacy than the INH control. As the efficacy between these doses is not significantly different, the 250 mg/kg/day dose was chosen as the lowest possible dose that still achieves maximum efficacy for further animal trials on TB infected IL-13^{tg} mice.

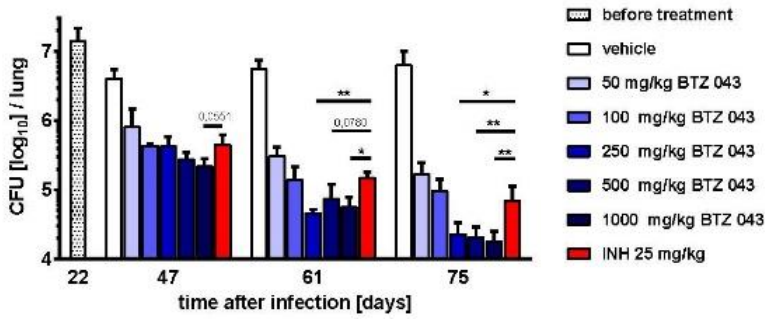

Figure 1. Dose ranging CFU reduction in BALB/c mice. Treatment started 22 days post infection and CFU reduction was investigated 47, 61 and 75 days post infection. Animals received a single dose daily. For every time point and dose n = 3. Vehicle = Mice that received only the drug vehicle.

Pharmacokinetics of BTZ-043

Plasma pharmacokinetics of BTZ-043 were investigated in uninfected BALB/c mice which received four different BTZ-043 doses (2.5, 5, 50, 250 mg/kg/day) for five consecutive days. Plasma concentrations were determined 0.5, 1, 2, 4 and 8 h post-dose via LC-MS/MS, Figure 2. In the investigated doses, BTZ-043 resorbs quickly and reaches a dose independent plasma C_{max} after 0.5 h. A dose increase from 2.5 to 5 mg/kg/day leads to a dose proportional increase of C_{max} (520 to 1050 ng/mL). The C_{max} increase observed for a dose increase from 5 to 50 mg/kg/day is lower than dose proportional (1050 to 8070 ng/mL). From 50 mg/kg/day upwards a dose increase to 250 mg/kg/day does not cause an increase of C_{max}. Instead, both doses lead to a similar C_{max} around 8000 ng/mL. The reason for this might be a solubility limited absorption limit of BTZ-043, which is a highly lipophilic[10] compound. Following C_{max}, BTZ-043 is eliminated in a biphasic manner in all four concentrations. The first rapid phase of decline ends 2 h post-dose and transitions into a slower second elimination phase. The elimination half-life of BTZ-043 is around 4 h for the 250 mg/kg/dose. While the 50 and 250 mg/kg/day doses lead to a similar C_{max}, the dose ranging data of Figure 1 shows that the efficacy of the 250 mg/kg/day dose is superior to the 50 mg/kg/day dose. A possible reason for this may be that at the onset of the second elimination phase 2 h post-dose the plasma concentration of the 250 mg/kg/day dose (3550 ng/mL) is much higher than that of the 50 mg/kg/day dose (2070 ng/mL). So despite the similar C_{max}, total exposition is higher for the 250 mg/kg/dose indicating that the driver of the BTZ-043 efficacy is the area under the curve (AUC), i.e. the exposure.

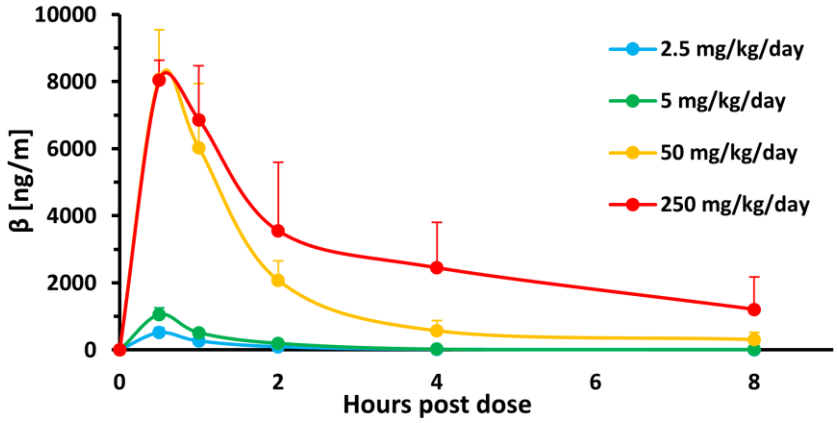

Figure 2. Pharmacokinetics of BTZ-043 in BALB/c mice. Plasma concentration curves of four different BTZ-043 doses measured 0.5, 1, 2, 4 and 8 h post-dose. For every dose and time point n = 3.

Efficacy of BTZ-043 in IL-13tg mice

CFU reduction was investigated in infected IL-13^{tg} mice to evaluate the efficacy of BTZ-043 in an animal model that closely resembles human TB pathology. The efficacy of BTZ-043 was compared against the CFU value at the onset of treatment and positive control group which received a cocktail of pyrazinamide (PZA, 150 mg/kg/day), clofazimine (CFZ, 25 mg/kg/day) and rifampicin (RIF, 10 mg/kg/day), Figure 3. Treatment was started 60 days post infection, i.e. at the onset of granuloma formation, and carried out for 10 days. As the animals of this study were mainly intended for MALDI MSI and LC-MS/MS of tissue, only one time point was investigated. After 10 days of treatment the CFU reduction in BTZ-043 treated animals was around 1 log unit, in PZA/CFZ/RIF treated animals around 1.7 log units. Considering the short treatment duration, the efficacy of BTZ-043, even in monotherapy, is comparable to that of the established first and second line drugs PZA/CFZ/RIF. The effect of BTZ-043 on Mtb in TB granuloma can be observed in the Ziel-Neelsen (ZN) stain.

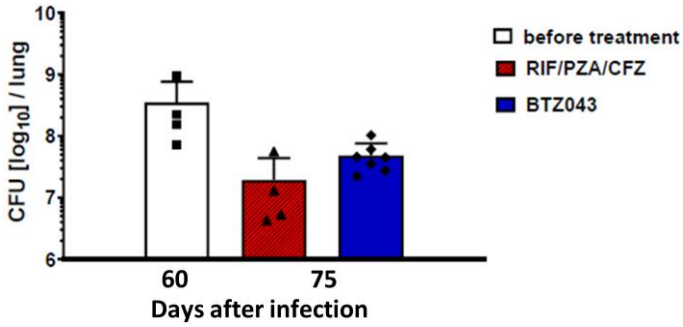

Figure 3. CFU reduction of BTZ-043 and a cocktail of PZA (150 mg/kg/day), CFZ (25 mg/kg/day) and RIF (10 mg/kg/day) in IL-13tg mice.

Mtb is visible in the ZN stain as a bright red acid fast rod, however in the ZN stain of necrotic granuloma from IL-13^{tg} mice treated with BTZ-043, almost no acid fast rods are visible, Figure 4 A,B. The ZN stain of PZA/CFZ/RIF treated animals on the other hand shows large numbers of extracellular acid fast rods in the cellular zone of the granuloma Figure 4 C,D. The basis of the acid fast staining of Mtb is the high affinity of the carbol fuchsin dye to the mycolic acids in the cell wall of Mtb which are responsible for its acid fastness. BTZ-043 acts upon the cell wall formation of Mtb and inhibits the synthesis of

arabinogalactan and lipoarabinomannan which are located below the mycolic acid layer[8] in the Mtb cell wall. A lack of these polysaccharides may lead to an improperly formed or missing mycolic acid layer, i.e. a loss of acid fastness, rendering them undetectable in the ZN stain. Also, the loss of acid fastness may make Mtb more susceptible to other anti-TB drugs which would usually struggle to penetrate the mycolic acid layer. While the BTZ-043 treated Mtb have lost their acid fastness, CFU data (Figure 3) shows they are still present within the tissue, indicating that BTZ-043 is able to penetrate into TB granuloma at least to some extent.

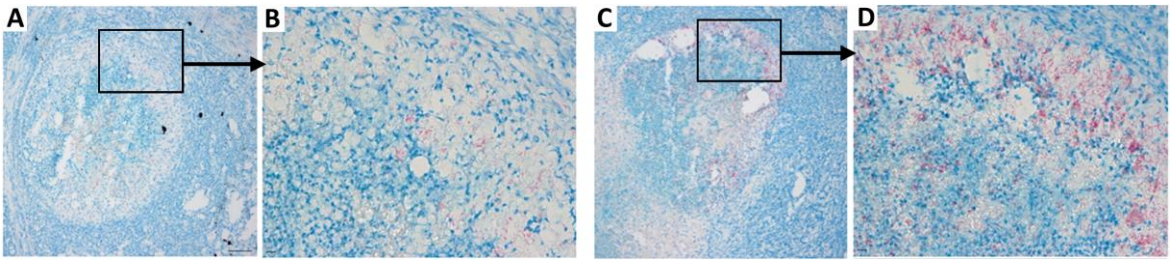

Figure 4. Ziehl-Neelsen stain of necrotic granuloma in IL-13^{tg} mice treated with PZA/CFZ/RIF and BTZ-043. **A)** Granuloma overview of an animal treated with BTZ-043. **B)** Enlargement of the area highlighted in A showing a section of the cellular zone of the granuloma with only a small number of acid fast rods, i.e. Mtb. **C)** Granuloma overview of an animal treated with BTZ-043. **D)** Enlargement of the area highlighted in C showing a section of the cellular zone of the granuloma with a large number of acid fast rods, i.e. Mtb.

Tissue concentration of BTZ-043

MALDI MSI of sections to investigate the penetration of BTZ-043 is conducted in a regular laboratory without a biological safety level. Accordingly, sections of infected IL-13^{tg} mice treated with BTZ-043 were inactivated using γ irradiation according to an earlier reported method.[11] Here the influence of the irradiation on the BTZ-043 concertation in sections was determined by LC-MS/MS of neighboring irradiated/non-irradiated homogenated sections of uninfected BALB/c mice (1 h post dose) which received the same treatment as infected IL-13^{tg} mice. These measurements showed that the BTZ-043 concentration is not significantly different in irradiated and non-irradiated sections meaning the irradiation procedure has no influence on the BTZ-043 concentration, Figure 5 left panel.

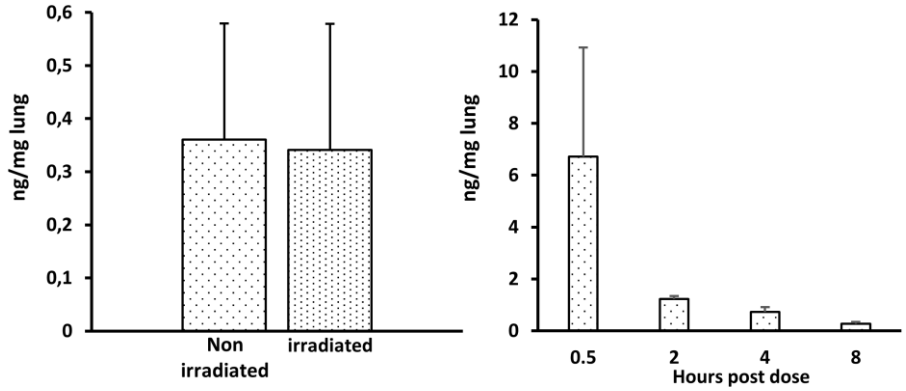

Figure 5. LC-MS/MS quantification of BTZ-043 in tissue sections. **Left panel)** BTZ-043 concentration in non-irradiated and irradiated sections of BALB/c mice. **Right panel)** BTZ-043 concentration in sections of irradiated IL-13^{tg} mice 0.5, 2, 4 and 8 h post dose.

In inactivated and homogenated sections of IL-13^{tg} mice, the BTZ-043 concentration was determined 0.5, 2, 4 and 8 h post-dose, Figure 5 right panel. The highest tissue concentration was determined 0.5 h

post-dose at 6.71 ng/mg lung tissue, likely due to the high level of blood perfusion of lung tissue. After 2 h the BTZ-043 concentration has dropped to 1.23 ng/mg lung. Between 4 and 8 h post-dose, the concentration drops from 0.73 to 0.27 ng/mg lung tissue. The plasma MIC of BTZ-043 for the H37Rv strain, the same strain as used in this work, was determined at 1 ng/mL.[7] While the plasma concentration cannot be correlated directly with the tissue concentration this still provides a good point of reference considering that 8 h post-dose the tissue concentration of BTZ-043 is still two hundred times the plasma MIC. To put these values into context, is must be determined if BTZ-043 is able to penetrate into all areas of TB granuloma.

MALDI MSI

As the irradiation does not influence the BTZ-043 concentration in tissue sections, MALDI MSI was used on inactivated sections to determine if BTZ-043 is able to penetrate into the caseum. Imaging was performed with a step size of 10 x 10 µm on a section collected 2 h post-dose containing two well-stratified centrally necrotic round shaped granuloma roughly 0.7 – 0.9 mm in diameter, Figure 6 A . Both granuloma are encased by a prominent fibrous capsule visible in blue in the AZAN trichrome stain (Figure 6 B). Inside of the fibrous capsule both granuloma possess a layer of macrophage rich tissue visible in yellow in the CD68 stain and highlighted by arrows in Figure 6 C (CD68 stain). As shown by the oil red staining (Figure 6 D) performed on a neighboring section, the macrophage rich areas visible in the CD68 stain have a high lipid content indicating the presence of foamy macrophages.[12] Both granuloma contain a central caseum which are highlighted in the HE staining.

The protonated molecule of BTZ-043 ($[M+H]^+$,$C_{17}H_{17}F_3N_3O_5S^+$) was detected at *m/z* 432.08355 with an RMSE of 0.54 ppm (47524 spectra). BTZ-043 is detected in the entire tissue section with a higher abundance in the granuloma areas, Figure 6 E. Comparison with the histological stainings given in Figure 6 A-D indicates that the area of high BTZ-043 abundance is located inside the fibrous capsules of the granuloma and coincides with the macrophage layers. Using our previously reported penetration analysis tool[13], granuloma edges and BTZ-043 penetration plots were generated for both granuloma based on the distribution of the endogenous signals *m/z* 482.36050 assigned as lysophosphatidylcholine(O-16:0) demarcating the granuloma area and *m/z* 488.44620 assigned as *N*-acylethanolamine(30:4) demarcating the surrounding area, Figure 6 F. The generated plots (Figure 6 G) show the average intensity of BTZ-043 in all pixels with the same distance to the granuloma edge indicated by the zero value on the x axis. The determined granuloma edges which here are located between the fibrous capsule and the macrophage layer are given in Figure 6 E as blue and green lines. In both granuloma, the BTZ-043 intensity shows a steep increase directly inside the edge, i.e. the macrophage layer. Following this, the BTZ-043 intensity transitions into a steep decline towards the center of the granuloma, i.e. the caseum. Due to the thicker macrophage layer in the left granuloma, the BTZ-043 abundance reaches a plateau before decreasing towards the center. Although expected, this shows that even in granuloma contained in the same lung section there is significant biological variation.

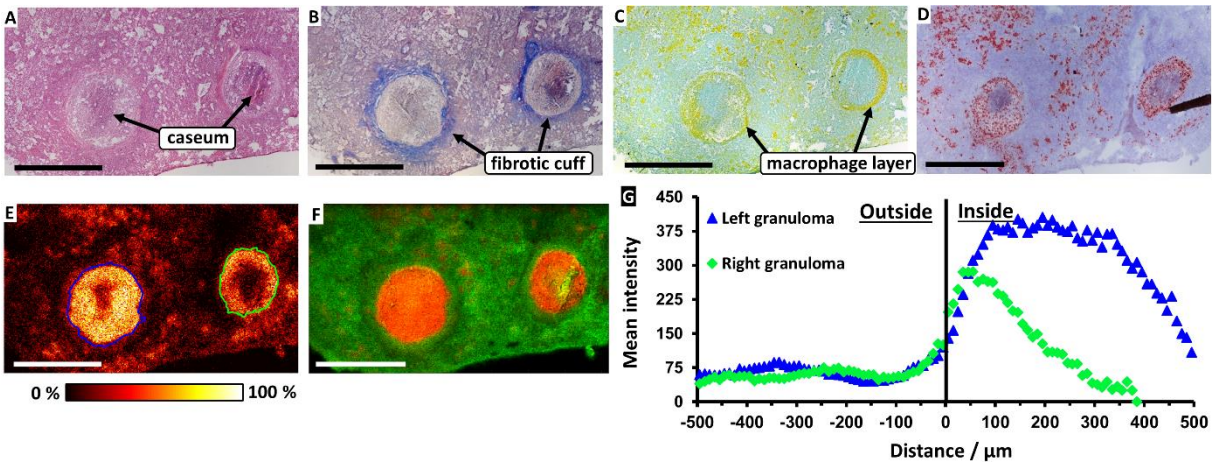

Figure 6. MALDI MSI of BTZ-043 2 h post-dose with a pixel size of 10 x 10 µm on two granuloma with a well-defined histology. Histological stainings were conducted on neighboring sections. **A)** HE stain. **B)** AZAN trichrome stain. **C)** CD68 stain. **D)** Oil red stain. **E)** Distribution of BTZ-043 $[M+H]^+$, $C_{17}H_{17}F_3N_3O_5S^+$, *m/z* 432.08355, RMSE 0.54 ppm (47525 spectra) *m/z* 420 – 550 raster size 410 x 235 pixel. The blue line demarcated the edge of the left granuloma. The green line demarcated the edge of the right granuloma. **F)** Overlay of lysophosphatidylcholine(O-16:0) $[M+H]^+$, $C_{24}H_{53}NO_6P^+$, $[M+H]^+$ *m/z* 482.36050 in red and *N*-acylethanolamine(30:4) $C_{32}H_{58}NO_2^+$, $[M+H]^+$ *m/z* 488.44620 in green. **G)** Penetration plots showing the penetration of BTZ-043 into both granuloma present in the section. The color schemes of the data points correspond the color of the respective granuloma edges in panel E. Scale bars = 1 mm.

These results show that BTZ-043 is able to penetrate into necrotic tuberculous granuloma. Two hours post-dose it has penetrated the fibrous cuff of the granuloma and is detected with higher abundance in the macrophage layer. BTZ-043 is a highly lipophilic compound[10] and may accumulate in lipid rich foamy macrophages, which could explain the intensity increase in the macrophage layer.

While it remains above the MIC 8 h post-dose, the overall tissue concentration of BTZ-043 decreases by roughly 95 % from 0.5 h to 8 h post-dose. To investigate the course of the BTZ-043 distribution over this timeframe, lung sections of mice sacrificed 0.5, 2, 4 and 8 h post-dose were investigated with MALDI MSI. Granuloma are subject to significant biological variation, even if they originate from the same animal and are in close proximity to another – as shown above. Therefore, to enable a reasonable comparison of the BTZ-043 distribution between post-dose time points only sections containing granuloma with a similar histology, i.e. granuloma containing a clear/prominent central caseum surrounded by a macrophage layer, were selected for this investigation. Post-measurement haematoxylin and eosin stains showing the histology of the investigated sections for each time point are given in Figure 7 A-D. In the presented stains, the granuloma caseum is visible in dark violet. The lighter violet area surrounding the caseum represents the macrophage layer. The MALDI MSI measured distributions of BTZ-043 $[M+H]^+$ are given in Figure 7 E-H. All measurements were conducted with a step size of 30 x 30 µm.

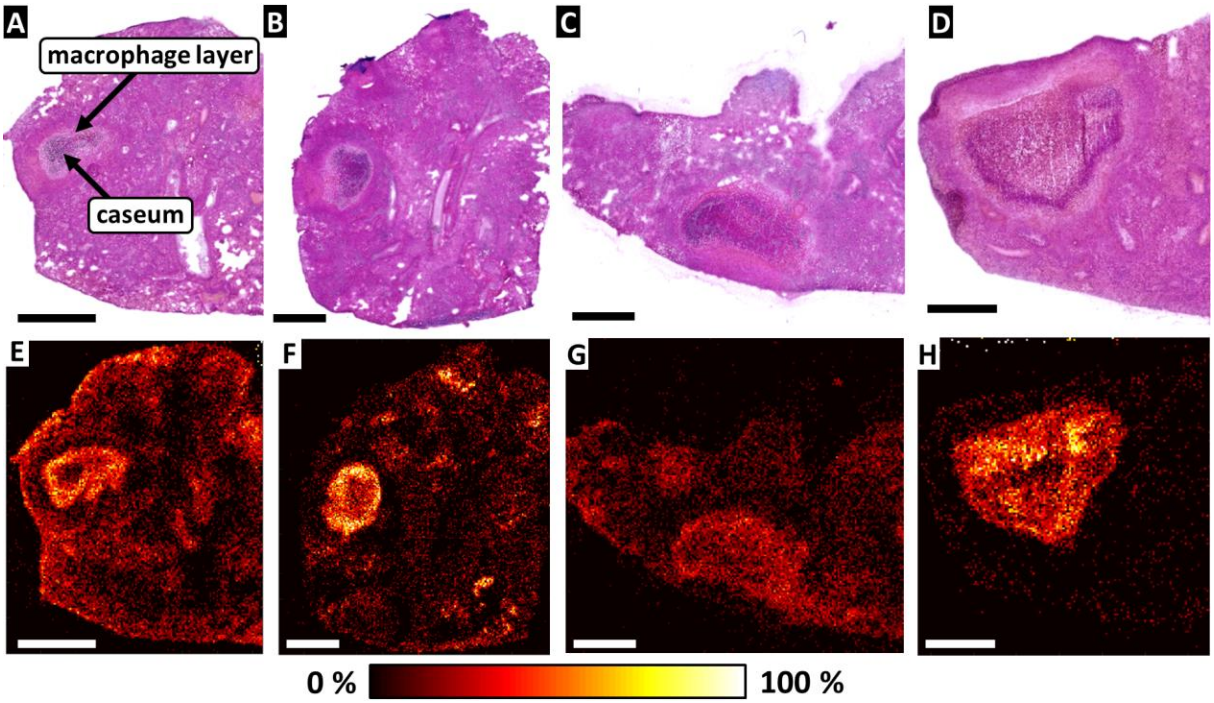

Figure 7. MALDI MSI of BTZ-043 0.5, 2, 4 and 8 h post-dose with a piexl size of 30 x 30 µm and a mass range of *m/z* 420-550. **A-D)** Post-measurement HE stains of the imaged sections showing that all granuloma investiagted in this timeline posess a central caseum surrounded by a layer of macrophages. Time points are A = 0.5 h, B = 2 h, C = 4 h and D = 8 h. **E-H)** Corresponding ion images of BTZ-043 $[M+H]^+$, $C_{17}H_{17}F_3N_3O_5S^+$, *m/z* 432.08355. **E)** 0.5 h post-dose, RMSE 0.55 ppm (11014 spectra), raster size 175 x 160 pixel **F)** 2 h post-dose, RMSE 0.49 ppm (11380 spectra), raster size 210 x 242 pixel. **G)** 4 h post-dose, RMSE 0.17 ppm (5690 spectra),raster size 160 x 175 pixel. H) 8 h post-dose, RMSE 0.63 ppm (4460 spectra), raster size 175 x 165 pixel. Scale bars = 1 mm.

After 0.5 and 2 h, BTZ-043 is detected in the entire section and shows a higher intensity in the macrophage layer of the granuloma which drops towards the caseum, Figure 7 E, F. After 4 h, BTZ-043 is still detectable in the entire section and is evenly distributed in the granuloma area, including the caseum, Figure 7 G. Eight hours post-dose, BTZ-043 is still detectable in the cellular layer and caseum with similar intensity while the intensity in the surrounding tissue has dropped substantially. A biological replicate for each time point has been measured. These results show that BTZ-043 is able to penetrate into the caseum of tuberculous granuloma following an accumulation in the macrophage layer, despite the overall decreasing tissue concentration. BTZ-043 retains a higher intensity in the granuloma than in the surrounding tissue 8 h post-dose. As the AUC is the likely driver for the BTZ-043 efficacy this may also increases the efficacy of BTZ-043 in the granuloma itself.

Conclusions

CFU reduction and dose ranging showed that BTZ-043 has a higher efficacy than INH in TB infected BALB/c mice. It could be shown that the efficacy of BTZ-043 depends on the AUC. In IL-13^{tg} mice, the efficacy of BTZ-043 is comparable to that of current first and second line anti-TB drugs. ZN stainings of mice treated with BTZ-043 show that the drug causes a loss of acid fastness in Mtb. This may make Mtb more susceptible to other drug compounds and therapy approaches, when used in combination with other drug compounds which are not able to reach past the mycolic acid layer responsible for the acid fastness. LC-MS/MS of tissue sections showed that the γ ray inactivation has no influence on the drug concentration and that 8 h post-dose the BTZ-043 concentration is still several hundred times above the MIC. High resolution MALDI MSI in conjunction with histochemical methods shows an

accumulation of BTZ-043 in the macrophage layers of the granuloma. Investigation of further post-dose time points reveals that BTZ-043 is able to penetrate into the caseum of tuberculous granuloma thus reaching the main point of action for anti-TB drugs. Considering that the BTZ-043 efficacy depends on the AUC, the fact that BTZ-043 remains detectable inside the granuloma longer than in the surrounding area may also mean an increased efficacy inside the granuloma.

Methods

BALB/c and IL-13tg CFU reduction and drug dosing: BALB/c mice were exposed to a low or intermediate dose aerosol infection with the Mtb H37Rv strain in a Glas-Col aerosol chamber, as previously described[14]. Treatment was initiated 22 days after infection. BTZ-043 and INH were administered in the same fashion. Drug treatment was initiated 60 days after infection for ten consecutive days, and the CFZ/PZA/RIF drug combination and BTZ-043 was administered by oral gavage for 10 consecutive days. 1 h after the last administration mice were euthanized by CO_2 inhalation, lungs were aseptically removed and lung tissue containing macroscopically visible lesions was snap frozen in liquid nitrogen. Mice were sacrificed 0.5 h or 1 h after the last administration, individual lung lobes were isolated and snap frozen in liquid nitrogen. All animal experimentation was in accordance with the German Animal Protection Law and was approved by the animal research ethics committee of the federal state of Schleswig-Holstein (Germany) prior to permission by the Ministry of Energy, Agriculture, the Environment, Nature and Digitalization.

PK study. Sample preparation: In a 1.5 mL test tube, 20 µL of plasma were mixed with 2 µL of methanol (Merck, LC-MS grade). 200 µL of 7:3 hexane / ethyl acetate (hexane: (analytical reagent grade, Fisher, ethyl acetate: LiChrosolv, Merck) internal standard solution of 0.333 µg/mL BTZ10726040 for the high concentration range and 0.0333 µg/mL for the low concentration range were added. After centrifugation (5 min at 10000 *x g* and 4°C), 150 µL of the organic supernatant was evaporated at RT with N_2 using a TurboVap evaporator. The residue was reconstituted with 40 µL methanol, vortexed and transferred into an autosampler vial. For every dose and time point n=3. LC-MS/MS was performed on an Agilent 1100 Series HPLC (Agilent Technologies, Santa Clara, CA, USA) using a Inertsil ODS-4 C_{18} column (GL Sciences Inc. 2.1 x 75 mm, 3 µm particle size) with an Inertsil ODS-4 guard column (1.5 x 10 mm, 3 µm particle size) at a column temperature of 25°C. Mobile phase solvent A: 0.1 % formic acid (Suprapur, Merck). Solvent B: methanol with 0.1 % formic acid. Gradient start with 50 % B increased to 75 % until minute 1 which is then held until minute 3. B is raised to 100 % at 3.1 minutes and held until minute 6. At 6.1 min B is dropped to 50 and held until minute 10 resulting in a total runtime of 10 minutes. Injection volume was 1 µL at high concentration (20 – 7000 ng/mL) and 2 µL at low concentration levels (5 – 2000 ng/mL). Autosampler temperature was set at 5°C. ESI MRM MS/MS on a API 3000 (Applied Biosystems, Waltham, MA, USA) triple quadrupole mass spectrometer. The transition 432.1 → 82.9 in positive ion mode was used for quantification. Spray voltage 4.5 kV, source temperature 400°C. Data analysis was performed in Analyst 1.4.2.

ZN staining. Resected lung lobes of IL-13^{tg} mice were fixed in 4 % formalin-PBS, set in paraffin blocks and sectioned (2–3 µm). ZN staining was conducted using a ready for use carbol fuchsin solution (Merck, Darmstadt, Germany).

LC-MS/MS of sections. Sample preparation: After drying lung cryosections in a SpeedVac, samples were reconstituted with 25 µL LC-MS-grade water, 200 µL ACN (reserpine concentration: 12.5 ng/mL) and 25 µL 1 % formic acid. Samples were vortexed and afterwards centrifuged for 10 min at 15 000 ×

g, room temperature. Approximately 200 µl of the resulting supernatant were transferred in a 1.5 mL Eppendorf tube and re-centrifuged under the same conditions. LC-MS/MS: Liquid chromatography was performed on an Agilent 1100 Series HPLC (Agilent Technologies, Santa Clara, CA, USA) using a SeQuant® ZIC®-HILIC column (Merck Millipore SeQuant, 2.1 inner diameter x 150 mm length with 5 µm particle size, pore-size 200 Å) at a column temperature of 30 °C. The mobile phase consisted of 1 % formic acid (FA, solvent A) and acetonitrile (ACN, solvent B). The gradient started at 90 % B at a flowrate of 0.5 mL/min. After one minute of isocratic conditions, the percentage of acetonitrile was decreased to 2 % B until minute four. At minute four, the flowrate was increased to 0.8 ml/min. The gradient was kept isocratic at 2 % B with a flowrate of 0.8 mL/min for 6 minutes until minute 10. Afterwards, the percentage of acetonitrile was re-increased to 90 % B until minute 15 and the flowrate re-decreased to 0.5 ml/min until minute 19. These conditions were maintained for one minute, so that the total run time was 20 minutes. The autosampler temperature was set to 4 °C and sample injection volume was 5 µL. The Waters Micromass Quattro Premier XE triple quadrupole mass spectrometer (Waters Corporation, Milford, MA, USA) using electrospray ionization (ESI) was operated in positive ion mode using multiple reaction monitoring (MRM). The transition *m/z* 432 → 292 was used to quantify the BTZ-043. The cone gas- and desolvation gas flow were set to 100 l/h and 800 l/h, respectively. The extractor voltage was 3.0 V. We optimized the capillary voltage, the source-, and the desolvation gas temperature and chose 3.0 kV, 450 °C, and 90 °C, respectively. MassLynx 4.1 and TargetLynx (Waters Corporation, Milford, Massachusetts, USA) were used for operating the platform and quantifying the samples, respectively.

MALDI MSI Gamma inactivation of IL-13tg lung sections: Sections were sterilized using a Biobeam 8000 (Gamma-Service-Medical, Leipzig/Germany) γ irradiation device equipped with ^{137}Cs source as reported previously by Walter et al[11]. Sections were stored at -80°C, and shipped to our laboratory on dry ice. MALDI MS imaging: Sections were brought to room temperature inside a desiccator for 15 min. Matrix was applied using a pneumatic sprayer system built in house. Imaging measurements were performed using a AP-SMALDI 10 (TransMIT GmbH, Gießen/Germany) atmospheric pressure MALDI imaging source equipped with a λ = 337 nm N_2 laser operating at repetition rate of 60 Hz coupled to a Q Exactive HF (Thermo Fisher Scientific, Bremen/Germany) orbital trapping mass spectrometer. Measurements were conducted with 30 laser shots per pixel and a mass range of *m/z* 420-540 with a step size of 10 x 10 µm and 30 x 30 µm.Ion images and RGB overlays were generated in MSiResder Version 1.0[15] with a bin with of 2 ppm. Penetration plots were generated using our previously reported penetration analysis tool.[13] Mass accuracies across imaging datasets are given as the root mean square error (RMSE) of the δ*m/z* values in ppm of all pixels containing the targeted ion within a ±3 ppm window of the theoretical *m/z*.

References

1. WHO Global Tuberculosis Report 2020; 2020.
2. Consortium, C. R.; the, G. P.; Allix-Beguec, C.; Arandjelovic, I.; Bi, L.; Beckert, P.; Bonnet, M.; Bradley, P.; Cabibbe, A. M.; Cancino-Munoz, I.; Caulfield, M. J.; Chaiprasert, A.; Cirillo, D. M.; Clifton, D. A.; Comas, I.; Crook, D. W.; De Filippo, M. R.; de Neeling, H.; Diel, R.; Drobniewski, F. A.; Faksri, K.; Farhat, M. R.; Fleming, J.; Fowler, P.; Fowler, T. A.; Gao, Q.; Gardy, J.; Gascoyne-Binzi, D.; Gibertoni-Cruz, A. L.; Gil-Brusola, A.; Golubchik, T.; Gonzalo, X.; Grandjean, L.; He, G.; Guthrie, J. L.; Hoosdally, S.; Hunt, M.; Iqbal, Z.; Ismail, N.; Johnston, J.; Khanzada, F. M.; Khor, C. C.; Kohl, T. A.; Kong, C.; Lipworth, S.; Liu, Q.; Maphalala, G.; Martinez, E.; Mathys, V.; Merker, M.; Miotto, P.; Mistry, N.; Moore, D. A. J.; Murray, M.; Niemann, S.; Omar, S. V.; Ong, R. T.; Peto, T. E. A.; Posey, J. E.; Prammananan, T.; Pym, A.; Rodrigues, C.;

Rodrigues, M.; Rodwell, T.; Rossolini, G. M.; Sanchez Padilla, E.; Schito, M.; Shen, X.; Shendure, J.; Sintchenko, V.; Sloutsky, A.; Smith, E. G.; Snyder, M.; Soetaert, K.; Starks, A. M.; Supply, P.; Suriyapol, P.; Tahseen, S.; Tang, P.; Teo, Y. Y.; Thuong, T. N. T.; Thwaites, G.; Tortoli, E.; van Soolingen, D.; Walker, A. S.; Walker, T. M.; Wilcox, M.; Wilson, D. J.; Wyllie, D.; Yang, Y.; Zhang, H.; Zhao, Y.; Zhu, B., Prediction of Susceptibility to First-Line Tuberculosis Drugs by DNA Sequencing. N Engl J Med 2018, 379 (15), 1403-1415.

3. Zager, E. M.; McNerney, R., Multidrug-resistant tuberculosis. BMC Infect Dis 2008, 8, 10.
4. Dartois, V., The path of anti-tuberculosis drugs: from blood to lesions to mycobacterial cells. Nature Reviews Microbiology 2014, 12, 159.
5. Ericsson, A. C.; Crim, M. J.; Franklin, C. L., A brief history of animal modeling. Mo Med 2013, 110 (3), 201-205.
6. Kim, W. Y.; Sharpless, N. E., Drug efficacy testing in mice. Curr Top Microbiol Immunol 2012, 355, 19-38.
7. Makarov, V.; Manina, G.; Mikusova, K.; Möllmann, U.; Ryabova, O.; Saint-Joanis, B.; Dhar, N.; Pasca, M. R.; Buroni, S.; Lucarelli, A. P.; Milano, A.; De Rossi, E.; Belanova, M.; Bobovska, A.; Dianiskova, P.; Kordulakova, J.; Sala, C.; Fullam, E.; Schneider, P.; McKinney, J. D.; Brodin, P.; Christophe, T.; Waddell, S.; Butcher, P.; Albrethsen, J.; Rosenkrands, I.; Brosch, R.; Nandi, V.; Bharath, S.; Gaonkar, S.; Shandil, R. K.; Balasubramanian, V.; Balganesh, T.; Tyagi, S.; Grosset, J.; Riccardi, G.; Cole, S. T., Benzothiazinones Kill Mycobacterium tuberculosis by Blocking Arabinan Synthesis. Science 2009, 324 (5928), 801.
8. Crellin, P. K.; Brammananth, R.; Coppel, R. L., Decaprenylphosphoryl-beta-D-ribose 2'-epimerase, the target of benzothiazinones and dinitrobenzamides, is an essential enzyme in Mycobacterium smegmatis. PLoS One 2011, 6 (2), e16869.
9. Heitmann, L.; Abad Dar, M.; Schreiber, T.; Erdmann, H.; Behrends, J.; McKenzie, A. N.; Brombacher, F.; Ehlers, S.; Holscher, C., The IL-13/IL-4Ralpha axis is involved in tuberculosis-associated pathology. J Pathol 2014, 234 (3), 338-50.
10. Rudolph, D.; Redinger, N.; Schaible, U. E.; Feldmann, C., Transport of Lipophilic Anti-Tuberculosis Drug Benzothiazone-043 in Ca3(PO4)2 Nanocontainers. ChemNanoMat 2020, 7 (1), 7-16.
11. Kerstin Walter, Julia Kokesch-Himmelreich, Axel Treu, Franziska Waldow, Doris Hillemann, Nikolas Jakobs, Ann-Kathrin Lemm, Dominik Schwudke, Andreas Römpp, Christoph Hölscher. Interleukin-13 overexpressing mice represent an advanced pre-clincial model for detecting the distribution of anti-mycobacterial drugs within centrally necrotizing granulomas. Antimicrobial Agents and Chemotherapy, DOI: https://doi.org/10.1128/AAC.01588-21.
12. Yuan, Y.; Li, P.; Ye, J., Lipid homeostasis and the formation of macrophage-derived foam cells in atherosclerosis. Protein Cell 2012, 3 (3), 173-81.
13. Kokesch-Himmelreich, J.; Treu, A.; Race, A. M.; Walter, K.; Hoelscher, C.; Roemmp, A., Do anti-TB drugs reach their target? – High resolution MALDI MS imaging provides information of drug penetration into necrotic granulomas during pre-clinical research. Submitted 2021.
14. Walter, K.; Steinwede, K.; Aly, S.; Reinheckel, T.; Bohling, J.; Maus, U. A.; Ehlers, S., Cathepsin G in Experimental Tuberculosis: Relevance for Antibacterial Protection and Potential for Immunotherapy. J Immunol 2015, 195 (7), 3325-33.
15. Bokhart, M. T.; Nazari, M.; Garrard, K. P.; Muddiman, D. C., MSiReader v1.0: Evolving Open-Source Mass Spectrometry Imaging Software for Targeted and Untargeted Analyses. Journal of The American Society for Mass Spectrometry 2018, 29 (1), 8-16

6 References

1. McDonnell, L. A.; Heeren, R. M. A., Imaging mass spectrometry. *Mass Spectrometry Reviews* **2007,** *26* (4), 606-643.
2. Römpp, A.; Spengler, B., Mass spectrometry imaging with high resolution in mass and space. *Histochemistry and Cell Biology* **2013,** *139* (6), 759-783.
3. Prideaux, B.; Stoeckli, M., Mass spectrometry imaging for drug distribution studies. *Journal of Proteomics* **2012,** *75* (16), 4999-5013.
4. Schulz, S.; Becker, M.; Groseclose, M. R.; Schadt, S.; Hopf, C., Advanced MALDI mass spectrometry imaging in pharmaceutical research and drug development. *Curr Opin Biotechnol* **2019,** *55*, 51-59.
5. WHO *Global Tuberculosis Report 2020: executive summary*; Geneva, Switzerland, 2020.
6. WHO, *Treatment of tuberculosis: Guidelines*. 4 ed.; Geneva, Switzerland, 2010.
7. Horsburgh, C. R., Jr.; Barry, C. E., 3rd; Lange, C., Treatment of Tuberculosis. *N Engl J Med* **2015,** *373* (22), 2149-60.
8. Prideaux, B.; Dartois, V.; Staab, D.; Weiner, D. M.; Goh, A.; Via, L. E.; Barry, C. E.; Stoeckli, M., High-Sensitivity MALDI-MRM-MS Imaging of Moxifloxacin Distribution in Tuberculosis-Infected Rabbit Lungs and Granulomatous Lesions. *Analytical Chemistry* **2011,** *83* (6), 2112-2118.
9. Kim, W. Y.; Sharpless, N. E., Drug efficacy testing in mice. *Curr Top Microbiol Immunol* **2012,** *355*, 19-38.
10. Ericsson, A. C.; Crim, M. J.; Franklin, C. L., A brief history of animal modeling. *Mo Med* **2013,** *110* (3), 201-205.
11. Heitmann, L.; Abad Dar, M.; Schreiber, T.; Erdmann, H.; Behrends, J.; McKenzie, A. N.; Brombacher, F.; Ehlers, S.; Holscher, C., The IL-13/IL-4Ralpha axis is involved in tuberculosis-associated pathology. *J Pathol* **2014,** *234* (3), 338-50.
12. Griffiths, J., A Brief History of Mass Spectrometry. *Analytical Chemistry* **2008,** *80* (15), 5678-5683.
13. Thomson, J. J., *Rays of Positive Electricity and Their Applicatioin to Chemical Analysis*. Longmans, Green and Co.: London, 1913.
14. Wollnik, H., Ion optics in mass spectrometers. *Journal of Mass Spectrometry* **1999,** *34* (10), 991-1006.
15. Hoffmann, E. d.; Stroobant, V., Ion Sources. In *Mass Spectrometry Principles and Applications*, 3 ed.; John Wiley & Sons Ltd.: Chichester, England, 2007; pp 16-17.
16. McLaffety, F. W.; Turecek, F., *Interpretation of Mass Spectra*. 4 ed.; University Science Books: Mill Valley, CA, USA, 1993.
17. Awad, H.; Khamis, M. M.; El-Aneed, A., Mass Spectrometry, Review of the Basics: Ionization. *Applied Spectroscopy Reviews* **2015,** *50* (2), 158-175.
18. Gross, J. H., Instrumentation. In *Mass Spectrometry A Textbook*, 3 ed.; Springer International Publishing AG: Cham, Switzerland, 2017; pp 151-292.
19. Hoffmann, E. d.; Stroobant, V., Limitation of Ion Current from the Source by the Electrochemical Process. In *Mass Spectrometry Principles and Applications*, 3 ed.; John Wiley & Sons Ltd.: Chichester, England, 2007.
20. David W. Koppenaal, C. J. B., M. Bonner Denton, Roger P. Sperline, Gary M. Hieftje, Gregory D. Schilling, Francisco J. Andrade, James H. Barnes, MS Detectors. *Analytical Chemistry* **2005,** *77* (21), 418 A-427 A.
21. Kingdon, K. H., A Method for the Neutralization of Electron Space Charge by Positive Ionization at Very Low Gas Pressures. *Physical Review* **1923,** *21* (4), 408-418.
22. Hu, Q.; Noll, R. J.; Li, H.; Makarov, A.; Hardman, M.; Graham Cooks, R., The Orbitrap: a new mass spectrometer. *J Mass Spectrom* **2005,** *40* (4), 430-43.
23. Makarov, A., Electrostatic Axially Harmonic Orbital Trapping: A High-Performance Technique of Mass Analysis. *Analytical Chemistry* **2000,** *72* (6), 1156-1162.

24. Zubarev, R. A.; Makarov, A., Orbitrap Mass Spectrometry. *Analytical Chemistry* **2013,** *85* (11), 5288-5296.
25. Makarov, A.; Denisov, E.; Kholomeev, A.; Balschun, W.; Lange, O.; Strupat, K.; Horning, S., Performance Evaluation of a Hybrid Linear Ion Trap/Orbitrap Mass Spectrometer. *Analytical Chemistry* **2006,** *78* (7), 2113-2120.
26. Scigelova, M.; Makarov, A., Orbitrap mass analyzer--overview and applications in proteomics. *Proteomics* **2006,** *6 Suppl 2*, 16-21.
27. Makarov, A.; Denisov, E.; Lange, O.; Horning, S., Dynamic range of mass accuracy in LTQ Orbitrap hybrid mass spectrometer. *J Am Soc Mass Spectrom* **2006,** *17* (7), 977-982.
28. Fenner, N. C.; Daly, N. R., Laser Used for Mass Analysis. *Review of Scientific Instruments* **1966,** *37* (8), 1068-1070.
29. Gross, J. H., Matrix-Assisted Laser Desorption/Ionization. In *Mass Spectrometry A Textbook*

3ed.; Cham, Switzerland, 2017; Vol. Springer International Publishing AG.
30. Yoshimura, Y.; Enomoto, H.; Moriyama, T.; Kawamura, Y.; Setou, M.; Zaima, N., Visualization of anthocyanin species in rabbiteye blueberry Vaccinium ashei by matrix-assisted laser desorption/ionization imaging mass spectrometry. *Anal Bioanal Chem* **2012,** *403* (7), 1885-95.
31. Dreisewerd, K., The Desorption Process in MALDI. *Chemical Reviews* **2003,** *103* (2), 395-426.
32. Westmacott, G.; Ens, W.; Hillenkamp, F.; Dreisewerd, K.; Schürenberg, M., The influence of laser fluence on ion yield in matrix-assisted laser desorption ionization mass spectrometry. *International Journal of Mass Spectrometry* **2002,** *221* (1), 67-81.
33. Karas, M.; Glückmann, M.; Schäfer, J., Ionization in matrix-assisted laser desorption/ionization: singly charged molecular ions are the lucky survivors. *Journal of Mass Spectrometry* **2000,** *35* (1), 1-12.
34. Knochenmuss, R., Photoionization Pathways and Free Electrons in UV-MALDI. *Analytical Chemistry* **2004,** *76* (11), 3179-3184.
35. Knochenmuss, R., Energetics and Kinetics of Thermal Ionization Models of MALDI. *Journal of The American Society for Mass Spectrometry* **2014,** *25* (9), 1521-1527.
36. Knochenmuss, R., A Quantitative Model of Ultraviolet Matrix-Assisted Laser Desorption/Ionization Including Analyte Ion Generation. *Analytical Chemistry* **2003,** *75* (10), 2199-2207.
37. Knochenmuss, R., MALDI mechanisms: wavelength and matrix dependence of the coupled photophysical and chemical dynamics model. *Analyst* **2014,** *139* (1), 147-56.
38. Spengler, B., Mass spectrometry imaging of biomolecular information. *Analytical Chemistry* **2015,** *87* (1), 64-82.
39. Soltwisch, J.; Göritz, G.; Jungmann, J. H.; Kiss, A.; Smith, D. F.; Ellis, S. R.; Heeren, R. M. A., MALDI Mass Spectrometry Imaging in Microscope Mode with Infrared Lasers: Bypassing the Diffraction Limits. *Analytical Chemistry* **2014,** *86* (1), 321-325.
40. Luxembourg, S. L.; Mize, T. H.; McDonnell, L. A.; Heeren, R. M. A., High-Spatial Resolution Mass Spectrometric Imaging of Peptide and Protein Distributions on a Surface. *Analytical Chemistry* **2004,** *76* (18), 5339-5344.
41. Koestler, M.; Kirsch, D.; Hester, A.; Leisner, A.; Guenther, S.; Spengler, B., A high-resolution scanning microprobe matrix-assisted laser desorption/ionization ion source for imaging analysis on an ion trap/Fourier transform ion cyclotron resonance mass spectrometer. *Rapid Communications in Mass Spectrometry* **2008,** *22* (20), 3275-3285.
42. Bokhart, M. T.; Nazari, M.; Garrard, K. P.; Muddiman, D. C., MSiReader v1.0: Evolving Open-Source Mass Spectrometry Imaging Software for Targeted and Untargeted Analyses. *Journal of The American Society for Mass Spectrometry* **2018,** *29* (1), 8-16.
43. Paschke, C.; Leisner, A.; Hester, A.; Maass, K.; Guenther, S.; Bouschen, W.; Spengler, B., Mirion--a software package for automatic processing of mass spectrometric images. *J Am Soc Mass Spectrom* **2013,** *24* (8), 1296-306.
44. Pachuta, S. J.; Cooks, R. G., Mechanisms in molecular SIMS. *Chemical Reviews* **1987,** *87* (3), 647-669.

45. Asher, S. E., Secondary Ion Mass Spectrometry. In *Microanalysis of Solids*, Yacobi, B. G.; Holt, D. B.; Kazmerski, L. L., Eds. Springer US: Boston, MA, 1994; pp 149-177.
46. Massonnet, P.; Heeren, R. M. A., A concise tutorial review of TOF-SIMS based molecular and cellular imaging. *Journal of Analytical Atomic Spectrometry* **2019,** *34* (11), 2217-2228.
47. Fletcher, J. S.; Lockyer, N. P.; Vickerman, J. C., Developments in molecular SIMS depth profiling and 3D imaging of biological systems using polyatomic primary ions. *Mass Spectrom Rev* **2011,** *30* (1), 142-74.
48. Singh, A. V.; Jungnickel, H.; Leibrock, L.; Tentschert, J.; Reichardt, P.; Katz, A.; Laux, P.; Luch, A., ToF-SIMS 3D imaging unveils important insights on the cellular microenvironment during biomineralization of gold nanostructures. *Sci Rep* **2020,** *10* (1), 261.
49. Bodzon-Kulakowska, A.; Suder, P., Imaging mass spectrometry: Instrumentation, applications, and combination with other visualization techniques. *Mass Spectrometry Reviews* **2016,** *35* (1), 147-169.
50. Liebl, H., Ion Microprobe Mass Analyzer. *Journal of Applied Physics* **1967,** *38* (13), 5277-5283.
51. Svensson, B. G.; Linnarsson, M. K.; Mohadjeri, B.; Petravić, M.; Williams, J. S., SIMS and depth profiling of semiconductor structures. *Nuclear Instruments and Methods in Physics Research Section B: Beam Interactions with Materials and Atoms* **1994,** *85* (1), 363-369.
52. Fearn, S., Characterisation of biological material with ToF-SIMS: a review. *Materials Science and Technology* **2014,** *31* (2), 148-161.
53. Kollmer, F.; Paul, W.; Krehl, M.; Niehuis, E., Ultra high spatial resolution SIMS with cluster ions — approaching the physical limits. *Surface and Interface Analysis* **2013,** *45* (1), 312-314.
54. Gross, J. H., Ambient Desorption/Ionization. In *Mass Spectrometry A Textbook*, 3 ed.; Springer International Publishing AG: Cham, Switzerland, 2017; pp 782-783.
55. Hoffmann, E. d.; Stroobant, V., Electrospray. In *Mass Spectrometry Principles and Applications*, John Wiley & Sons Ltd.: Chichester, England, 2007.
56. Wiseman, J. M.; Ifa, D. R.; Zhu, Y.; Kissinger, C. B.; Manicke, N. E.; Kissinger, P. T.; Cooks, R. G., Desorption electrospray ionization mass spectrometry: Imaging drugs and metabolites in tissues. *Proceedings of the National Academy of Sciences* **2008,** *105* (47), 18120.
57. Pirro, V.; Guffey, S. C.; Sepulveda, M. S.; Mahapatra, C. T.; Ferreira, C. R.; Jarmusch, A. K.; Cooks, R. G., Lipid dynamics in zebrafish embryonic development observed by DESI-MS imaging and nanoelectrospray-MS. *Mol Biosyst* **2016,** *12* (7), 2069-79.
58. Towers, M. W.; Karancsi, T.; Jones, E. A.; Pringle, S. D.; Claude, E., Optimised Desorption Electrospray Ionisation Mass Spectrometry Imaging (DESI-MSI) for the Analysis of Proteins/Peptides Directly from Tissue Sections on a Travelling Wave Ion Mobility Q-ToF. *J Am Soc Mass Spectrom* **2018,** *29* (12), 2456-2466.
59. Campbell, D. I.; Ferreira, C. R.; Eberlin, L. S.; Cooks, R. G., Improved spatial resolution in the imaging of biological tissue using desorption electrospray ionization. *Anal Bioanal Chem* **2012,** *404* (2), 389-98.
60. Kompauer, M.; Heiles, S.; Spengler, B., Atmospheric pressure MALDI mass spectrometry imaging of tissues and cells at 1.4-µm lateral resolution. *Nature Methods* **2016,** *14*, 90.
61. Niehaus, M.; Soltwisch, J.; Belov, M. E.; Dreisewerd, K., Transmission-mode MALDI-2 mass spectrometry imaging of cells and tissues at subcellular resolution. *Nat Methods* **2019,** *16* (9), 925-931.
62. Römpp, A.; Guenther, S.; Schober, Y.; Schulz, O.; Takats, Z.; Kummer, W.; Spengler, B., Histology by Mass Spectrometry: Label-Free Tissue Characterization Obtained from High-Accuracy Bioanalytical Imaging. *Angewandte Chemie International Edition* **2010,** *49* (22), 3834-3838.
63. Yang, J.; Caprioli, R. M., Matrix sublimation/recrystallization for imaging proteins by mass spectrometry at high spatial resolution. *Anal Chem* **2011,** *83* (14), 5728-34.
64. Huber, K.; Khamehgir-Silz, P.; Schramm, T.; Gorshkov, V.; Spengler, B.; Römpp, A., Approaching cellular resolution and reliable identification in mass spectrometry imaging of tryptic peptides. *Anal Bioanal Chem* **2018,** *410* (23), 5825-5837.
65. Giordano, S.; Zucchetti, M.; Decio, A.; Cesca, M.; Fuso Nerini, I.; Maiezza, M.; Ferrari, M.; Licandro, S. A.; Frapolli, R.; Giavazzi, R.; Maurizio, D.; Davoli, E.; Morosi, L., Heterogeneity of paclitaxel

distribution in different tumor models assessed by MALDI mass spectrometry imaging. *Sci Rep* **2016,** *6*, 39284.
66. Seneviratne, H. K.; Hendrix, C. W.; Fuchs, E. J.; Bumpus, N. N., MALDI Mass Spectrometry Imaging Reveals Heterogeneous Distribution of Tenofovir and Tenofovir Diphosphate in Colorectal Tissue of Subjects Receiving a Tenofovir-Containing Enema. *J Pharmacol Exp Ther* **2018,** *367* (1), 40-48.
67. Grove, K. J.; Hoque, S.; Rudewicz, P. J., Investigation of amodiaquine localization in liver lobules using matrix-assisted laser desorption/ionization imaging mass spectrometry. *Rapid Commun Mass Spectrom* **2019,** *33* (3), 252-258.
68. Römpp, A.; Guenther, S.; Takats, Z.; Spengler, B., Mass spectrometry imaging with high resolution in mass and space (HR2 MSI) for reliable investigation of drug compound distributions on the cellular level. *Analytical and Bioanalytical Chemistry* **2011,** *401* (1), 65-73.
69. Groseclose, M. R.; Castellino, S., An Investigation into Retigabine (Ezogabine) Associated Dyspigmentation in Rat Eyes by MALDI Imaging Mass Spectrometry. *Chemical Research in Toxicology* **2019,** *32* (2), 294-303.
70. Groseclose, M. R.; Castellino, S., Intramuscular and subcutaneous drug depot characterization of a long-acting cabotegravir nanoformulation by MALDI IMS. *International Journal of Mass Spectrometry* **2019,** *437*, 92-98.
71. Bäckström, E.; Hamm, G.; Nilsson, A.; Fihn, B.-M.; Strittmatter, N.; Andrén, P.; Goodwin, R. J. A.; Fridén, M., Uncovering the regional localization of inhaled salmeterol retention in the lung. *Drug Delivery* **2018,** *25* (1), 838-845.
72. Römpp, A.; Schramm, T.; Hester, A.; Klinkert, I.; Both, J.-P.; Heeren, R. M. A.; Stöckli, M.; Spengler, B., imzML: Imaging Mass Spectrometry Markup Language: A Common Data Format for Mass Spectrometry Imaging. In *Data Mining in Proteomics: From Standards to Applications*, Hamacher, M.; Eisenacher, M.; Stephan, C., Eds. Humana Press: Totowa, NJ, 2011; pp 205-224.
73. Schramm, T.; Hester, Z.; Klinkert, I.; Both, J.-P.; Heeren, R. M. A.; Brunelle, A.; Laprévote, O.; Desbenoit, N.; Robbe, M.-F.; Stoeckli, M.; Spengler, B.; Römpp, A., imzML — A common data format for the flexible exchange and processing of mass spectrometry imaging data. *Journal of Proteomics* **2012,** *75* (16), 5106-5110.
74. MS-imaging.org - Software tools. https://ms-imaging.org/wp/imzml/software-tools/.
75. Guenther, S.; Römpp, A.; Kummer, W.; Spengler, B., AP-MALDI imaging of neuropeptides in mouse pituitary gland with 5µm spatial resolution and high mass accuracy. *International Journal of Mass Spectrometry* **2011,** *305* (2-3), 228-237.
76. Desbenoit, N.; Walch, A.; Spengler, B.; Brunelle, A.; Römpp, A., Correlative mass spectrometry imaging, applying time-of-flight secondary ion mass spectrometry and atmospheric pressure matrix-assisted laser desorption/ionization to a single tissue section. *Rapid Communications in Mass Spectrometry* **2017,** *32* (2), 159-166.
77. Bhandari, D. R.; Wang, Q.; Friedt, W.; Spengler, B.; Gottwald, S.; Römpp, A., High resolution mass spectrometry imaging of plant tissues: towards a plant metabolite atlas. *Analyst* **2015,** *140* (22), 7696-709.
78. Khalil, S. M.; Römpp, A.; Pretzel, J.; Becker, K.; Spengler, B., Phospholipid Topography of Whole-Body Sections of the Anopheles stephensi Mosquito, Characterized by High-Resolution Atmospheric-Pressure Scanning Microprobe Matrix-Assisted Laser Desorption/Ionization Mass Spectrometry Imaging. *Anal Chem* **2015,** *87* (22), 11309-16.
79. Carter, C. L.; Jones, J. W.; Farese, A. M.; MacVittie, T. J.; Kane, M. A., Inflation-Fixation Method for Lipidomic Mapping of Lung Biopsies by Matrix Assisted Laser Desorption/Ionization-Mass Spectrometry Imaging. *Analytical Chemistry* **2016,** *88* (9), 4788-4794.
80. Scott, A. J.; Chandler, C. E.; Ellis, S. R.; Heeren, R. M. A.; Ernst, R. K., Maintenance of Deep Lung Architecture and Automated Airway Segmentation for 3D Mass Spectrometry Imaging. *Scientific Reports* **2019,** *9* (1), 20160.
81. Berry, K. A. Z.; Li, B.; Reynolds, S. D.; Barkley, R. M.; Gijón, M. A.; Hankin, J. A.; Henson, P. M.; Murphy, R. C., MALDI imaging MS of phospholipids in the mouse lung. *Journal of Lipid Research* **2011,** *52* (8), 1551-1560.

82. Hankin, J. A.; Barkley, R. M.; Murphy, R. C., Sublimation as a method of matrix application for mass spectrometric imaging. *Journal of the American Society for Mass Spectrometry* **2007,** *18* (9), 1646-1652.
83. Gemperline, E.; Rawson, S.; Li, L., Optimization and Comparison of Multiple MALDI Matrix Application Methods for Small Molecule Mass Spectrometric Imaging. *Analytical Chemistry* **2014,** *86* (20), 10030-10035.
84. Buchberger, A. R.; DeLaney, K.; Johnson, J.; Li, L., Mass Spectrometry Imaging: A Review of Emerging Advancements and Future Insights. *Analytical Chemistry* **2018,** *90* (1), 240-265.
85. Stock, N. L., Introducing Graduate Students to High-Resolution Mass Spectrometry (HRMS) Using a Hands-On Approach. *Journal of Chemical Education* **2017,** *94* (12), 1978-1982.
86. Xian, F.; Hendrickson, C. L.; Marshall, A. G., High resolution mass spectrometry. *Anal Chem* **2012,** *84* (2), 708-19.
87. Gross, J. H., Resolution and Resolving Power. In *Mass Spectrometry A Textbook*, 3 ed.; Springer International Publishing AG: Cham, Switzerland, 2017; p 113.
88. Gross, J. H., Applied High-Resolution Mass Spectrometry. In *Mass Spectrometry A Textbook*, 3 ed.; Springer International Publishing AG: Cham, Switzerland, 2017; pp 123-132.
89. Mohan, K. R.; Bartlett, M. G.; Busch, K. L.; Schoen, A. E.; Gore, N., Calibration Point for Electron Ionization MS / MS spectra measured with multiquadrupole mass spectrometers. *Journal of the American Society for Mass Spectrometry* **1994,** *5* (6), 576-582.
90. Jiang, L.; Moini, M., Ultramark 1621 as a reference compound for positive and negative ion fast-atom bombardment high-resolution mass spectrometry. *Journal of the American Society for Mass Spectrometry* **1992,** *3* (8), 842-846.
91. Kolarova, L.; Prokes, L.; Kucera, L.; Hampl, A.; Pena-Mendez, E.; Vanhara, P.; Havel, J., Clusters of Monoisotopic Elements for Calibration in (TOF) Mass Spectrometry. *J Am Soc Mass Spectrom* **2017,** *28* (3), 419-427.
92. Lou, X.; van Dongen, J. L.; Meijer, E. W., Generation of CsI cluster ions for mass calibration in matrix-assisted laser desorption/ionization mass spectrometry. *J Am Soc Mass Spectrom* **2010,** *21* (7), 1223-6.
93. Kim, J. W.; Ramaswamy, B. R.; Chang, K. H.; Isobe, T.; Tanabe, S., Multiresidue analytical method for the determination of antimicrobials, preservatives, benzotriazole UV stabilizers, flame retardants and plasticizers in fish using ultra high performance liquid chromatography coupled with tandem mass spectrometry. *J Chromatogr A* **2011,** *1218* (22), 3511-20.
94. Heiles, S.; Kompauer, M.; Muller, M. A.; Spengler, B., Atmospheric-Pressure MALDI Mass Spectrometry Imaging at 213 nm Laser Wavelength. *J Am Soc Mass Spectrom* **2020,** *31* (2), 326-335.
95. Fu, T.; Oetjen, J.; Chapelle, M.; Verdu, A.; Szesny, M.; Chaumot, A.; Degli-Esposti, D.; Geffard, O.; Clement, Y.; Salvador, A.; Ayciriex, S., In situ isobaric lipid mapping by MALDI-ion mobility separation-mass spectrometry imaging. *J Mass Spectrom* **2020,** *55* (9), e4531.
96. WHO, World Health Organization (WHO) Information Note Tuberculosis and COVID-19. In *COVID-19: Considerations for tuberculosis (TB) care*, 2020.
97. Organization, W. H., WHO: Global TB progress at risk. WHO: Geneva, Switzerland, 2020.
98. Dartois, V., The path of anti-tuberculosis drugs: from blood to lesions to mycobacterial cells. *Nature Reviews Microbiology* **2014,** *12*, 159.
99. Orme, I. M.; Basaraba, R. J., The formation of the granuloma in tuberculosis infection. *Seminars in Immunology* **2014,** *26* (6), 601-609.
100. Russell, D. G.; Cardona, P. J.; Kim, M. J.; Allain, S.; Altare, F., Foamy macrophages and the progression of the human tuberculosis granuloma. *Nat Immunol* **2009,** *10* (9), 943-8.
101. Iacobino, A.; Piccaro, G.; Giannoni, F.; Mustazzolu, A.; Fattorini, L., Mycobacterium tuberculosis Is Selectively Killed by Rifampin and Rifapentine in Hypoxia at Neutral pH. *Antimicrob Agents Chemother* **2017,** *61* (3).
102. Keshavjee, S.; Farmer, P. E., Tuberculosis, drug resistance, and the history of modern medicine. *N Engl J Med* **2012,** *367* (10), 931-6.

103. Gotham, D.; Fortunak, J.; Pozniak, A.; Khoo, S.; Cooke, G.; Nytko, F. E.; Hill, A., Estimated generic prices for novel treatments for drug-resistant tuberculosis. *Journal of Antimicrobial Chemotherapy* **2017**.
104. Blanc, L.; Sarathy, J. P.; Alvarez Cabrera, N.; O'Brien, P.; Dias-Freedman, I.; Mina, M.; Sacchettini, J.; Savic, R. M.; Gengenbacher, M.; Podell, B. K.; Prideaux, B.; Ioerger, T.; Dick, T.; Dartois, V., Impact of immunopathology on the antituberculous activity of pyrazinamide. *Journal of Experimental Medicine* **2018,** *215* (8), 1975-1986.
105. Blanc, L.; Lenaerts, A.; Dartois, V.; Prideaux, B., Visualization of Mycobacterial Biomarkers and Tuberculosis Drugs in Infected Tissue by MALDI-MS Imaging. *Analytical Chemistry* **2018,** *90* (10), 6275-6282.
106. Rifat, D.; Prideaux, B.; Savic, R. M.; Urbanowski, M. E.; Parsons, T. L.; Luna, B.; Marzinke, M. A.; Ordonez, A. A.; DeMarco, V. P.; Jain, S. K.; Dartois, V.; Bishai, W. R.; Dooley, K. E., Pharmacokinetics of rifapentine and rifampin in a rabbit model of tuberculosis and correlation with clinical trial data. *Science Translational Medicine* **2018,** *10* (435), eaai7786.
107. Prideaux, B.; ElNaggar, M. S.; Zimmerman, M.; Wiseman, J. M.; Li, X.; Dartois, V., Mass spectrometry imaging of levofloxacin distribution in TB-infected pulmonary lesions by MALDI-MSI and continuous liquid microjunction surface sampling. *International Journal of Mass Spectrometry* **2015,** *377*, 699-708.
108. Blanc, L.; Daudelin, I. B.; Podell, B. K.; Chen, P.-Y.; Zimmerman, M.; Martinot, A. J.; Savic, R. M.; Prideaux, B.; Dartois, V., High-resolution mapping of fluoroquinolones in TB rabbit lesions reveals specific distribution in immune cell types. *eLife* **2018,** *7*, e41115.
109. Zimmerman, M.; Lestner, J.; Prideaux, B.; O'Brien, P.; Dias-Freedman, I.; Chen, C.; Dietzold, J.; Daudelin, I.; Kaya, F.; Blanc, L.; Chen, P.-Y.; Park, S.; Salgame, P.; Sarathy, J.; Dartois, V., Ethambutol Partitioning in Tuberculous Pulmonary Lesions Explains Its Clinical Efficacy. *Antimicrobial Agents and Chemotherapy* **2017,** *61* (9), e00924-17.
110. Prideaux, B.; Via, L. E.; Zimmerman, M. D.; Eum, S.; Sarathy, J.; O'Brien, P.; Chen, C.; Kaya, F.; Weiner, D. M.; Chen, P.-Y.; Song, T.; Lee, M.; Shim, T. S.; Cho, J. S.; Kim, W.; Cho, S. N.; Olivier, K. N.; Barry Iii, C. E.; Dartois, V., The association between sterilizing activity and drug distribution into tuberculosis lesions. *Nature Medicine* **2015,** *21*, 1223.
111. Strydom, N.; Gupta, S. V.; Fox, W. S.; Via, L. E.; Bang, H.; Lee, M.; Eum, S.; Shim, T.; Barry, C. E., 3rd; Zimmerman, M.; Dartois, V.; Savic, R. M., Tuberculosis drugs' distribution and emergence of resistance in patient's lung lesions: A mechanistic model and tool for regimen and dose optimization. *PLoS Med* **2019,** *16* (4), e1002773.
112. Basaraba, R. J.; Hunter, R. L., Pathology of Tuberculosis: How the Pathology of Human Tuberculosis Informs and Directs Animal Models. *Microbiology Spectrum* **2017,** *5* (3).
113. Zuberi, A.; Lutz, C., Mouse Models for Drug Discovery. Can New Tools and Technology Improve Translational Power? *Journal of the Institute for Laboratory Animal Research* **2017,** *57* (2), 178-185.
114. Driver, E. R.; Ryan, G. J.; Hoff, D. R.; Irwin, S. M.; Basaraba, R. J.; Kramnik, I.; Lenaerts, A. J., Evaluation of a Mouse Model of Necrotic Granuloma Formation Using C3HeB/FeJ Mice for Testing of Drugs against <span class="named-content genus-species" id="named-content-1">Mycobacterium tuberculosis</span&gt. *Antimicrobial Agents and Chemotherapy* **2012,** *56* (6), 3181.
115. Irwin, S. M.; Prideaux, B.; Lyon, E. R.; Zimmerman, M. D.; Brooks, E. J.; Schrupp, C. A.; Chen, C.; Reichlen, M. J.; Asay, B. C.; Voskuil, M. I.; Nuermberger, E. L.; Andries, K.; Lyons, M. A.; Dartois, V.; Lenaerts, A. J., Bedaquiline and Pyrazinamide Treatment Responses Are Affected by Pulmonary Lesion Heterogeneity in Mycobacterium tuberculosis Infected C3HeB/FeJ Mice. *ACS Infectious Diseases* **2016,** *2* (4), 251-267.
116. DeMarco, V. P.; Ordonez, A. A.; Klunk, M.; Prideaux, B.; Wang, H.; Zhuo, Z.; Tonge, P. J.; Dannals, R. F.; Holt, D. P.; Lee, C. K.; Weinstein, E. A.; Dartois, V.; Dooley, K. E.; Jain, S. K., Determination of [11C]rifampin pharmacokinetics within Mycobacterium tuberculosis-infected mice by using dynamic positron emission tomography bioimaging. *Antimicrobial Agents and Chemotherapy* **2015,** *59* (9), 5768-5774.

117. Liu, X.; Weaver, E. M.; Hummon, A. B., Evaluation of therapeutics in three-dimensional cell culture systems by MALDI imaging mass spectrometry. *Anal Chem* **2013,** *85* (13), 6295-302.
118. Bonnel, D.; Legouffe, R.; Eriksson, A. H.; Mortensen, R. W.; Pamelard, F.; Stauber, J.; Nielsen, K. T., MALDI imaging facilitates new topical drug development process by determining quantitative skin distribution profiles. *Analytical and Bioanalytical Chemistry* **2018,** *410* (11), 2815-2828.
119. Machálková, M.; Pavlatovská, B.; Michálek, J.; Pruška, A.; Štěpka, K.; Nečasová, T.; Radaszkiewicz, K. A.; Kozubek, M.; Šmarda, J.; Preisler, J.; Navrátilová, J., Drug Penetration Analysis in 3D Cell Cultures Using Fiducial-Based Semiautomatic Coregistration of MALDI MSI and Immunofluorescence Images. *Analytical Chemistry* **2019,** *91* (21), 13475-13484.
120. Kokesch-Himmelreich, J.; Wittek, O.; Race, A. M.; Rakete, S.; Schlicht, C.; Busch, U.; Römmp, A., MALDI mass spectrometry imaging of fresh and processed food: constituents, ingredients, contaminants and additives. *To be submitted*.
121. Sato, S.; Bartolák-Suki, E.; Parameswaran, H.; Hamakawa, H.; Suki, B., Scale dependence of structure-function relationship in the emphysematous mouse lung. *Front Physiol* **2015,** *6*, 146-146.
122. Wishart, D. S.; Feunang, Y. D.; Guo, A. C.; Lo, E. J.; Marcu, A.; Grant, J. R.; Sajed, T.; Johnson, D.; Li, C.; Sayeeda, Z.; Assempour, N.; Iynkkaran, I.; Liu, Y.; Maciejewski, A.; Gale, N.; Wilson, A.; Chin, L.; Cummings, R.; Le, D.; Pon, A.; Knox, C.; Wilson, M., DrugBank 5.0: a major update to the DrugBank database for 2018. *Nucleic Acids Research* **2018,** *46* (D1), D1074-D1082.
123. Lappin, G.; Rowland, M.; Garner, R. C., The use of isotopes in the determination of absolute bioavailability of drugs in humans. *Expert Opinion on Drug Metabolism & Toxicology* **2006,** *2* (3), 419-427.
124. Kaufmann, A., Analytical performance of the various acquisition modes in Orbitrap MS and MS/MS. *Journal of Mass Spectrometry* **2018,** *53* (8), ii-ii.
125. CIAAW http://www.ciaaw.org/atomic-masses.htm (accessed 10.02).
126. Lam, A. P.; Gottardi, C. J., Fat in fibrosis. *American Journal of Respiratory and Critical Care Medicine* **2013,** *188* (10), 1268-1269.
127. Bahuguna, A.; Rawat, D. S., An overview of new antitubercular drugs, drug candidates, and their targets. *Medicinal Research Reviews* **2019,** *40* (1), 236-292.
128. Guenther, S.; Römpp, A.; Kummer, W.; Spengler, B., AP-MALDI imaging of neuropeptides in mouse pituitary gland with 5µm spatial resolution and high mass accuracy. *International Journal of Mass Spectrometry* **2011,** *305* (2), 228-237.
129. Aplin, R. T.; McDougall, A. C., Identification of crystals of the rimino-phenazine compound B663 (lamprene: Clofazimine) in mouse spleen macrophages by thin layer chromatography and mass spectrum analysis. *Experientia* **1975,** *31* (4), 468-469.
130. Urtti, A.; Baik, J.; Rosania, G. R., Macrophages Sequester Clofazimine in an Intracellular Liquid Crystal-Like Supramolecular Organization. *PLoS ONE* **2012,** *7* (10).
131. Race, A. M.; Palmer, A. D.; Dexter, A.; Steven, R. T.; Styles, I. B.; Bunch, J., SpectralAnalysis: Software for the Masses. *Analytical Chemistry* **2016,** *88* (19), 9451-9458.
132. Manier, M. L.; Reyzer, M. L.; Goh, A.; Dartois, V.; Via, L. E.; Barry, C. E.; Caprioli, R. M., Reagent Precoated Targets for Rapid In-Tissue Derivatization of the Anti-Tuberculosis Drug Isoniazid Followed by MALDI Imaging Mass Spectrometry. *Journal of The American Society for Mass Spectrometry* **2011,** *22* (8), 1409-1419.
133. Baijnath, S.; Moodley, C.; Ngcobo, B.; Singh, S. D.; Kruger, H. G.; Arvidsson, P. I.; Naicker, T.; Pym, A.; Govender, T., Clofazimine protects against Mycobacterium tuberculosis dissemination in the central nervous system following aerosol challenge in a murine model. *Int J Antimicrob Agents* **2018,** *51* (1), 77-81.
134. Makarov, V.; Manina, G.; Mikusova, K.; Möllmann, U.; Ryabova, O.; Saint-Joanis, B.; Dhar, N.; Pasca, M. R.; Buroni, S.; Lucarelli, A. P.; Milano, A.; De Rossi, E.; Belanova, M.; Bobovska, A.; Dianiskova, P.; Kordulakova, J.; Sala, C.; Fullam, E.; Schneider, P.; McKinney, J. D.; Brodin, P.; Christophe, T.; Waddell, S.; Butcher, P.; Albrethsen, J.; Rosenkrands, I.; Brosch, R.; Nandi, V.; Bharath, S.; Gaonkar, S.; Shandil, R. K.; Balasubramanian, V.; Balganesh, T.; Tyagi, S.; Grosset, J.;

Riccardi, G.; Cole, S. T., Benzothiazinones kill Mycobacterium tuberculosis by blocking arabinan synthesis. *Science* **2009,** *324* (5928), 801.
135. Crellin, P. K.; Brammananth, R.; Coppel, R. L., Decaprenylphosphoryl-beta-D-ribose 2'-epimerase, the target of benzothiazinones and dinitrobenzamides, is an essential enzyme in Mycobacterium smegmatis. *PLoS One* **2011,** *6* (2), e16869.
136. Yuan, Y.; Li, P.; Ye, J., Lipid homeostasis and the formation of macrophage-derived foam cells in atherosclerosis. *Protein Cell* **2012,** *3* (3), 173-81.
137. Rudolph, D.; Redinger, N.; Schaible, U. E.; Feldmann, C., Transport of Lipophilic Anti-Tuberculosis Drug Benzothiazone-043 in Ca3(PO4)2 Nanocontainers. *ChemNanoMat* **2021,** *7* (1), 7-16.

7 Publication list

Presented in following is a list of all publications and manuscripts in which I am or will be listed as an author.

Publications and manuscripts included in this dissertation

Axel Treu, Julia Kokesch-Himmelreich, Kerstin Walter, Christoph Hölscher, Andreas Römpp. Integrating High-Resolution MALDI Imaging into the Development Pipeline of Anti-Tuberculosis Drugs. *Journal of the American Society for Mass Spectrometry.* 2020, 31, 11, 2277–2286

Axel Treu, Andreas Römpp. Matrix ions as internal standard for high mass accuracy matrix assisted laser desorption/ionization mass spectrometry imaging. *Rapid Communications in Mass Spectrometry*. 2021, 35 (16), e9110

Julia Kokesch-Himmelreich, Axel Treu, Alan Mark Race, Kerstin Walter, Christoph Hölscher, Andreas Römpp. Do Anti-tuberculosis Drugs Reach Their Target? – High Resolution Matrix-Assisted Laser Desorption/Ionization Mass Spectrometry Imaging Provides Information on Drug Penetration into Necrotic Granulomas. *Analytical Chemistry.* 2022, 94, 14, 5483–5492.

Axel Treu, Kerstin Walter, Julia Kokesch-Himmelreich, Franziska Waldow, Julia Dreisbach, Dominik Schwudke, Michael Hölscher, Christoph Hölscher, Andreas Römpp. The efficacy of the novel antitubercular agent BTZ-043 in preclinical Tuberculosis mouse models. *Manuscript in preparation for submission.*

Publications not included in this dissertation

Axal Treu, Miriam Rittner, Dorit Kemken, Hans-Martin Schiebel, Peter Spiteller,Thomas Dülcks. Loss of atmic nitrogen from even electrons? A study on benzodiazepines. *Journal of Mass Spectrometry*. 2015, 50, 8, 978-986.

Kerstin Walter, Julia Kokesch-Himmelreich, Axel Treu, Franziska Waldow, Doris Hillemann, Nikolas Jakobs, Ann-Kathrin Lemm, Dominik Schwudke, Andreas Römpp, Christoph Hölscher. Interleukin-13 overexpressing mice represent an advanced pre-clincial model for detecting the distribution of anti-mycobacterial drugs within centrally necrotizing granulomas. *Antimicrobial Agents and Chemotherapy*, DOI: https://doi.org/10.1128/AAC.01588-21.

8 Acknowledgements

This thesis would not have been possible without the help and support of a number of people. In particular I would like to thank…

…my supervisor Prof. Dr. Andreas Römpp for his help and advice, the numerous fruitful discussions and for giving me the opportunity to work on the DZIF project enabling me to earn my PhD at his workgroup,

…Dr. Julia Kokesch-Himmelreich with whom I worked closely on the DZIF project for her help and advice and the very good working relationship,

…our cooperation partners Dr. Kerstin Walter and Prof. Christoph Hölscher from the Infection Immunology group at the Research Center Borstel for providing the murine sample material required for this work and the productive working relationship,

…our cooperation partner Dr. Franziska Waldow and PD Dr. Domninik Schwudke of the Bioanalytical Chemistry group at the Research Center Borstel for providing LC-MS data,

… my office colleagues Elisabeth Schirmer, Jasmin Kniese and Christina Grimmler for making our office the best office in the world and for always ‘Locker durch die Hose atmen’,

…Oliver Wittek for proof reading,

…PD Dr. Heinar Schmidt for many fruitful and helpful discussions,

…Gudrun Brauner for her assistance in organizational matters,

…the rest of the AK Römpp for the very friendly atmosphere and companionship,

…my entire family and friends, especially my mom, dad and grandmother, for their support during the ups and downs of the past years.

9 Declarations

(§ 9 Satz 2 Nr. 3 PromO BayNAT)

Hiermit versichere ich eidesstattlich, dass ich die Arbeit selbstständig verfasst und keine anderen als die von mir angegebenen Quellen und Hilfsmittel benutzt habe (vgl. Art. 64 Abs. 1 Satz 6 BayHSchG).

(§ 9 Satz 2 Nr. 3 PromO BayNAT)

Hiermit erkläre ich, dass ich die Dissertation nicht bereits zur Erlangung eines akademischen Grades eingereicht habe und dass ich nicht bereits diese oder eine gleichartige Doktorprüfung endgültig nicht bestanden habe.

(§ 9 Satz 2 Nr. 4 PromO BayNAT)

Hiermit erkläre ich, dass ich Hilfe von gewerblichen Promotionsberatern bzw. -vermittlern oder ähnlichen Dienstleistern weder bisher in Anspruch genommen habe noch künftig in Anspruch nehmen werde.

(§ 9 Satz 2 Nr. 7 PromO BayNAT)

Hiermit erkläre ich mein Einverständnis, dass die elektronische Fassung meiner Dissertation unter Wahrung meiner Urheberrechte und des Datenschutzes einer gesonderten Überprüfung unterzogen werden kann.

(§ 9 Satz 2 Nr. 8 PromO BayNAT)

Hiermit erkläre ich mein Einverständnis, dass bei Verdacht wissenschaftlichen Fehlverhaltens Ermittlungen durch universitätsinterne Organe der wissenschaftlichen Selbstkontrolle stattfinden können.

…….

Ort, Datum, Unterschrift